# THE EFFECTS OF PERFLUOROOCTANOIC ACID, PERFLUOROBUTANESULFONIC ACID, AND PERFLUOROOCTANESULFONIC ACID ON MODEL BIOLOGICAL MEMBRANES AND MONOLAYERS

by

Tess Noelle Sobolewski

A dissertation submitted in partial fulfillment
of the requirements for the degree

of

Doctor of Philosophy

in

Chemistry

MONTANA STATE UNIVERSITY
Bozeman, Montana

May 2025

©COPYRIGHT

by

Tess Noelle Sobolewski

2025

All Rights Reserved

# DEDICATION

This dissertation is dedicated to my parents, grandmother, wife, colleagues, and friends. Your constant support has been instrumental in shaping me into the chemist I am today. To my grandmother, thank you for diligently sending me over five hundred PFAS articles during my time at MSU, keeping me informed about the global impact of PFAS on various communities. To my parents, thank you for being present at every key moment of my PhD journey and for your steadfast support throughout my life. And to my wife, thank you for listening to every practice talk, helping me navigate challenges, and for your unwavering encouragement. Your love and support have meant the world to me.

# ACKNOWLEDGEMENTS

I would like to express my deepest gratitude to Dr. Rob Walker and the Walker Research Group for their unwavering support throughout the course of my research. In particular, I would like to thank Rhys Trousdale for his invaluable collaboration in data collection and analysis, which formed the foundation for several of the manuscripts included in this dissertation.

I am also deeply grateful to my committee members—Dr. Erik Grumstrup, Dr. Nick Stadie, Dr. Martin Mosquera, and Dr. Mari Eggers—for their thoughtful guidance and encouragement throughout my four years at Montana State University. Their expertise and feedback have been critical in shaping the direction of my work.

A special thank you goes to Dr. Doreen Brown for her continuous support and mentorship throughout my graduate studies. Her advice and assistance have been indispensable as I navigated the challenges of the program.

This research was made possible by the generous funding provided by the National Science Foundation through the EPSCoR Cooperative Agreement OIA-1757351. Additionally, I would like to acknowledge the Montana Water Center (MWC) for its support, which was made possible through base funding from the U.S. Geological Survey (USGS) Water Research Act, section 104b.

Chapter 5 of this dissertation, which focuses on the outreach component examining private wells across rural Montana counties, was supported by the United States Geological Survey and the Montana Water Center. I would like to thank Kelly Smalling and Paul Bradley for their mentorship and guidance throughout this process.

TABLE OF CONTENTS

1. INTRODUCTION ..... 1

1.1 Motivation ..... 2
1.1.1 Poly and Perfluoroalkyl Substances ..... 2
1.1.2 Health Effects and Bioaccumulation of PFAS ..... 4
1.1.3 PFAS Drinking Water Standards ..... 5
1.1.4 Model Biomembranes and Monolayers ..... 6
1.1.5 Cooperative Adsorption and the Air-Water Interface ..... 10
1.1.6 Hypotheses ..... 11
1.2 Methods and Techniques ..... 12
1.2.1 Differential Scanning Calorimetry ..... 12
1.2.2 Dynamic Light Scattering ..... 14
1.2.3 Surface Activity and Micelle Formation ..... 15
1.2.4 Langmuir Surface Pressure – Area Isotherms ..... 19
1.2.5 Vibrational Sum Frequency Generation (VSFG) ..... 23
1.3 Thesis Organization ..... 29
Chapter 2: ..... 29
Chapter 3: ..... 29
Chapter 4: ..... 30
Chapter 5: ..... 30
Chapter 6: ..... 31

2. AGGREGATION NOT MICELLIZATION: PERFLUOROOCTANOIC ACID, PERFLUOROBUTANESULFONIC ACID, AND POTASSIUM PERFLUOROOCTANESULFONATE BEHAVIOR IN AQUEOUS SOLUTION ..... 32

Contribution of Authors and Co-Authors ..... 32
Manuscript Information ..... 33
2.0 Abstract ..... 34
2.1 Introduction ..... 35
2.2 Experimental Materials and Methods ..... 37
2.2.1 Materials ..... 37
2.2.2 Sample Preparation. ..... 38
2.2.2.1 Preparation of Variable pH Solutions: ..... 38
2.2.2.2 Preparation of pH 8 Solutions: ..... 39
2.2.3 Experimental Techniques ..... 40
2.2.3.1 Surface Tensiometry: ..... 40
2.2.3.2 Conductivity: ..... 40
2.2.3.3 Dynamic Light Scattering: ..... 41
2.2.3.4 Cryo-EM: ..... 42
2.3 Results and Discussion ..... 42

TABLE OF CONTENTS CONTINUED

2.3.1 Surface Tension. ..... 42
2.3.2 Dynamic Light Scattering. ..... 48
2.3.3 Cryo-EM. ..... 51
2.3.4 Impact and Consequences. ..... 57
2.4 Conclusions ..... 61

3. NANOMOLAR PFOA CONCENTRATIONS AFFECT LIPID MEMBRANE STRUCTURE: CONSEQUENCES FOR BIOCONCENTRATION MECHANISMS ..... 63

Contribution of Authors and Co-Authors ..... 63
Manuscript Information ..... 64
3.0 Abstract ..... 65
3.1 Introduction ..... 65
3.2 Experimental Materials and Methods. ..... 70
3.2.1 Materials. ..... 70
3.2.2 Processing ..... 71
3.2.2.1 Vesicle Preparation. ..... 71
3.2.3 Methods ..... 71
3.2.3.1 Differential Scanning Calorimetry. ..... 71
3.2.3.2 Dynamic Light Scattering. ..... 72
3.2.3.3 Cryo-Electron Microscopy. ..... 72
3.2.3.4 Time-Correlated Single Photon Counting. ..... 73
3.3 Results ..... 74
3.3.1 Differential Scanning Calorimetry. ..... 74
3.3.2 Dynamic Light Scattering ..... 77
3.3.3 Cryo-EM ..... 80
3.3.4 PFOA Effects on Secondary Solute Partitioning ..... 83

4. PFOA COOPERATIVE ADSORPTION TO DPPC MONOLAYERS AND ORDERING OF INTERFACIAL WATER ..... 90

Contribution of Authors and Co-Authors ..... 90
Manuscript Information ..... 91
4.0 Abstract ..... 92
4.1 Introduction ..... 92
4.2 Experimental Materials and Methods ..... 95
4.2.1 Materials and Sample Preparation ..... 95
4.2.2 Vibrational Sum Frequency Generation (VSFG) ..... 96
4.2.3 Langmuir Area-Pressure Isotherms ..... 98
4.3 Results ..... 99
4.3.1 VSFG CH Region Results ..... 99

TABLE OF CONTENTS CONTINUED

4.3.2 VSFG OH Region Results ..... 103
4.3.3 Langmuir Area-Pressure Isotherms ..... 110
4.4 Conclusion ..... 113

5. CUMULATIVE RISK ASSESSMENT: PER- AND POLYFLUOROALKYL SUBSTANCES (PFAS) IN MONTANA RURAL AND DEVELOPING PRIVATE WELLS ..... 115

Contribution of Authors and Co-Authors ..... 115
Manuscript Information ..... 117
5.0 Abstract ..... 118
5.1 Introduction ..... 119
5.2 Experimental Materials and Methods ..... 122
5.2.1 Sample Collection and Participant Instructions ..... 122
5.2.2 Analytical Methods and Quality Assurance ..... 123
5.2.3 Cumulative Risk Assessments ..... 125
5.3 Results and Discussion ..... 127
5.3.1 PFAS Detected in Private Well Samples ..... 127
5.3.2 PFAS Detection by Property Size ..... 132
5.3.3 PFAS Detection by Well Depth ..... 134
5.3.4 Cumulative Risk Assessment ..... 135
5.4 Conclusions ..... 138

6. CONCLUSION AND FUTURE DIRECTIONS ..... 139

6.1 Summary of Research ..... 139
6.2 Future Directions ..... 141
6.2.1 Accurate Modeling of Membranes and Surfactant ..... 142
6.2.1.1 Cell Membranes. ..... 142
6.2.1.2 Lung Surfactant. ..... 142
6.2.2 Coexistence of PFAS ..... 143

CUMULATIVE REFERENCES CITED ..... 145

APPENDICES ..... 173

A. SUPPORTING INFORMATION FOR CHAPTER 2 ..... 174

B. SUPPORTING INFORMATION FOR CHAPTER 3 ..... 187

C. SUPPORTING INFORMATION FOR CHAPTER 4 ..... 192

D. SUPPORTING INFORMATION FOR CHAPTER 5 ..... 201

# LIST OF TABLES

Table Page

1. Table 1.1. EPA Maximum Contaminant Levels (MCL) for 6 PFAS and mixtures ..... 6

2. Table 2.1. Parts per trillion (ppt) conversion to nanomolar (nM) concentrations ..... 39

3. Table 2.2. Terminal surface excess concentrations, $\Gamma_{max}$ (molecules/cm$^2$), bulk concentration when $\Gamma_{max}$ is reached (mM), and pH in variable pH solutions when $\Gamma_{max}$ is reached. All data are reported for T = 20˚C ..... 45

4. Table 2.3. Predicted CMCs of PFOA and PFBS from surface tension data of both pH environments and conductivity measurements. All predictions based on measurements performed at 20˚C. ..... 48

5. Table 2.4. PFOA, PFBS, and KPFOS aggregate diameters and estimated number of monomers in aggregate. ..... 50

6. Table 2.5. PFOA, PFBS, and KPFOS aggregate diameter (nm) in 1 mM, pH 8.0 aqueous solution. In all experiments solution temperature was raised from 10˚C to 60˚C and then cooled back to 10˚C in 10˚ increments. Data for PFBS and PFOS equivalent that shown for PFOA in Figure 5 are included in Supporting Information. ..... 56

7. Table 2.6. CMC values reported for PFOA, PFOS, and PFBS using different methods. ..... 58

8. Table 3.1. PFOA concentrations in units of molarity and ppb/ppt (by mass) ..... 70

9. **Table 3.2.** Average enthalpies of DPPC in the PFOA containing solutions. $T_{gel\text{-}LC}$ = 40.4-40.5 ˚C for all PFOA concentrations. $\Delta T$ (FWHM) = 0.2˚C. $\Delta H_{gel\text{-}LC}$ values are the averages of ≥ 9 measurements and uncertainties are reported to one standard deviation. ..... 76

10. Table 3.3. DPPC vesicle diameters (d) from the top panel of Figure 2 and size distributions ($\Delta$) at room temperature. Uncertainties in diameter (d) are ±4 nm and in FWHM ($\Delta$) are ±8 nm except for the pure DPPC vesicle solutions where uncertainties in $d_2$ and $\Delta_2$ are ±2 and ±4 nm, respectively. Uncertainties reflect one standard deviation calculated from 9 measurements. ..... 79

LIST OF TABLES CONTINUED

Table Page

11. Table 3.4. Temperature dependent changes of DPPC vesicles in the absence of PFOA and in 100 nM PFOA solutions, $d_2$ and $\Delta_2$ refer to vesicle sizes. $d_1$ and $\Delta_1$ refer to the niosome-like structures induced by PFOA. ..... 80

12. Table 3.5. Lifetimes and amplitudes data from fitting TCSPC decay traces of C152 in DPPC vesicle solutions at 10, 50 and 70°C. Shown are results from both PFOA-free and 100 nM PFOA solutions. Lifetimes are reported in nanoseconds and the amplitudes are normalized. Lifetime precision is ± 0.1 ns; amplitude precision is ± 0.05. ..... 88

13. Table 4.1. The $r^+/d^+$ ratio for DPPC in the presence of PFOA in the -CH range, 3200 $cm^{-1}$ Integrated $Intensity^{1/2}$, 3450 $cm^{-1}$ Integrated $Intensity^{1/2}$, and Sum of 3200 $cm^{-1}$ and 3450 $cm^{-1}$ in the -OH range. Trials were run in triplicate. ..... 102

14. Table 5.1. The most conservative benchmark for each compound. ..... 126

15. Table A-1. Surface coverages (Γ) for PFAS at variable pH and pH 8 buffer environment. The pH for variable pH experiments is expressed in the parentheses. The terminal surface coverages are noted in bold. ..... 175

16. Table A-2. Particle size (nm) as temperature increases from 10 to 60 degrees before being cooled back down for PFAS of varying pH at 1 mM concentrations. ..... 183

17. Table A-3. Particle size (nm) for SDS and sodium octanoate were subjected to temperature dependent studies from 10°C to 60°C and back down in 10°C increments. ..... 185

18. Table B-1. DSC enthalpy values for DPPC prepared in the presence of octanoic acid. ..... 190

19. Table C-1. PFOA only, No DPPC (OH range)..... 193

20. Table C-2. 40 $Å^2$/molecule DPPC with PFOA (OH range) ..... 193

21. Table C-3. 55 $Å^2$/molecule DPPC with PFOA (OH range) ..... 193

22. Table C-4. 40 $Å^2$/molecule DPPC with PFOA (CH Range) ..... 194

LIST OF TABLES CONTINUED

Table Page

23. Table C-5. 55 Å$^2$/molecule DPPC with PFOA (CH range)..... 194

24. Table C-6. CH Range SDS 55 Å$^2$/molecule DPPC..... 195

25. Table C-7. CH Range SDS 40 Å$^2$/molecule DPPC..... 196

26. Table C-8. 40 Å$^2$/molecule DPPC with SDS (OH range) Single Trial ..... 196

27. Table C-9. 55 Å$^2$/molecule DPPC with SDS (OH range) Single Trial ..... 197

28. Table C-10. SDS Only, No DPPC (OH range) Single Trial..... 198

29. Table C-11. Peak intensities at (A) 3200 cm$^{-1}$, (B) 3450 cm$^{-1}$, (C) sum of both peaks at 3200 cm$^{-1}$ and 3450cm$^{-1}$ showing an increasing trend with increasing concentration of SDS..... 200

30. Table D-1. Method detection limits for individual PFAS measured by two different USGS methods. Method one is USGS 9660 (see Kolpin et al., 2021) for details and method two is USGS 9662. Detection limits are reported as ng/L for both methods. NA means the compound was not analyzed as part of the original method (9660). Six PFAS in red italic font are regulated under the Safe Drinking Water Act (SDWA) National Primary Drinking Water Regulations. ..... 203

31. Table D-2. Summary of PFAS detected and the range of concentrations found in the 59 samples across the three counties. Data was obtained from Method-2..... 205

32. Table D-3. Individual Toxicity Quotients (TQs) and the ΣTQ for each site, based on six of the PFAS detected using the human-health based benchmarks in Table 2. * indicates exceedance of benchmark level (1.0) and ** indicates the exceedance of precautionary screening level of concern (0.1), respectively. ..... 206

# LIST OF FIGURES

Figure Page

1. Figure 1.1. Chemical structures of the three PFAS examined in this work. Perfluorooctanoic acid (PFOA) and perfluorobutane-sulfonic acid (PFBS), and perfluorooctane sulfonic acid (PFOS) was purchased and used as a potassium salt (KPFOS). 3

2. Figure 1.2. 1,2-dipalmitoyl-sn-glycero-3-phosphocholine (DPPC) 8

3. Figure 1.3. DSC endothermic pretransition and gel to liquid-crystalline transition of pure DPPC. 13

4. Figure 1.4. DLS experimental design in which a laser light scatters within a solution. Fluctuations in the Brownian motion are then sent to the detector which then analyzes the diffusion coefficient to determine a hydrodynamic radius. 15

5. Figure 1.5. Determination of CMC of the surfactant sodium dodecyl sulfate (SDS) from surface pressure vs. concentration plot (left). Determination of the limiting surface excess coverage for SDS from surface pressure vs. ln[concentration] plot (right). The dashed line in the plot on the right showing slope of steepest ascent. 17

6. Figure 1.6. Determination of CMC of the surfactant sodium dodecyl sulfate (SDS) from conductivity vs. concentration plot. 19

7. Figure 1.7. Langmuir expansion and compression schematic and stearic acid isotherm. 22

8. Figure 1.8. DPPC Langmuir compression isotherm with phases labeled. 23

9. Figure 1.9. Walker Research Group VSFG schematic and energy level diagram. 25

10. Figure 1.10. (A) Loosely packed Pure 55 $Å^2$/molecule DPPC deposited on a Millipore subphase. (B) Tightly packed Pure 40 $Å^2$/molecule DPPC deposited on a Millipore subphase. 28

11. Figure 2.1. Chemical structures of the three PFAS examined in this work. Perfluorooctanoic acid (PFOA) and perfluorobutane-sulfonic acid (PFBS) were used in their protonated forms. Perfluorooctane sulfonic acid (PFOS) was purchased and used as a potassium salt (KPFOS). 36

LIST OF FIGURES CONTINUED

Figure Page

12. Figure 2.2.(a) Surface pressure as a function of bulk solution concentrations of PFOA, PFBS, and KPFOS (mM) in both low pH and pH 8 environments. (b) Surface pressure plotted against ln[conc] to calculate the terminal surface coverages as described in Equations 1-3. ..... 44

13. Figure 2.3. Conductivities of PFOA, PFBS, and KPFOS solutions in variable pH and pH 8.0 solutions. Concentrations range from 1 nM PFAS up to 4 mM PFAS. Note that the conductivity of the KPFOS, pH 8.0 solution is controlled by small additions of NaOH. The small amount of NaOH required raises the KPFOS pH 8.0 solution conductivity to 69.9 μS/cm in contrast to the ~1000 μS/cm conductivity for the PFOA and PFBS solutions buffered to pH = 8.0. ..... 47

14. Figure 2.4. Dynamic light scattering traces from solutions of PFOA, PFBS, and KPFOS as a function of concentration in pH 8.0 solutions. Sample temperature was held constant at 20 °C. ..... 49

15. Figure 2.5. Cryo-EM images of an 8 mM PFOA sample (pH = 8.0). (A) Survey image of the entire EM grid showing the 2 μm pores. Of interest is the gray area inside of the white dashed box. Scale bar in 5A is 1 μm. (B) An expanded image of part of the area shown in the white dashed box in (A). Objects in panel (B) range in size from ~15 nm to ~110 nm in diameter. The scale bar in 5B is 50 nm. ..... 52

16. Figure 2.6. DLS traces showing the temperature dependent behavior of PFOA aggregates in a 1 mM, pH 8.0 solution. In this experiment solution temperature was raised from 10˚C to 60˚C and then cooled back to 10˚C in 10˚ increments. ..... 54

17. Figure 2.7. Temperature dependent aggregate diameters for PFOA, PFBS, and PFOS in 1 mM, pH 8.0 solutions. In these experiments, solution temperature was raised from 10˚C to 60˚C and then cooled back to 10˚C in 10˚ increments. Error bars represent the 1 sigma standard deviation of 9 measurements. ..... 55

LIST OF FIGURES CONTINUED

Figure Page

18. Figure 3.1. (A) Differential scanning calorimetry isotherms of pure DPPC and DPPC with increasing [PFOA] ranging from 0.1 nM to 10 μM. Isotherms have been offset vertically for clarity. (B) Average enthalpies of the gel-liquid crystalline transition as a function of [PFOA]. The inset shows an expanded view of ΔH for [PFOA] ≤ 100 nM. At a concentration of 10 μM, the peak shows noticeable broadening. Note that the calculated enthalpy for pure DPPC vesicles is assigned an arbitrarily low PFOA concentration of $10^{-5}$ nM to place it on scale. ..... 75

19. Figure 3.2. (top) Dynamic light scattering from DPPC vesicle solutions containing 0 nM, 1 nM, 100 nM, and 1 μM PFOA. (middle) DPPC vesicle size as a function of temperature in the absence of PFOA. (bottom) DPPC/PFOA solutions at 25˚C, heated to 50˚C, and then returned to 25˚C. ..... 78

20. Figure 3.3. Representative cryo-EM images of DPPC vesicles prepared in a 10 mM carbonate buffer solution. A) DPPC vesicle prepared in the absence of PFOA. B and C both show images of DPPC vesicles prepared in the presence of 100 nM PFOA. Representative niosomes are indicated with the short red arrows. Medium white arrows show multilamellar structures in vesicles formed in PFOA solutions. The long black arrows show faceted vesicles. ..... 81

21. Figure 3.4. TCSPC traces of DPPC vesicle solutions containing 6 μM C152 and 100 nM PFOA as a function of temperature. The multiexponential decay visibly changes with temperature. Data are fit to three independent lifetimes as described. ..... 85

22. Figure 3.5. A plot of the 3 lifetimes of C152 as a function of temperature from 10-70-10 ˚C. The dotted lines show the lifetime behavior of C152 in a solution of DPPC vesicles without PFOA. The solid lines show lifetimes of C152 in a solution of DPPC vesicles and 100 nM PFOA. The 2nd lifetime of C152 shows the largest change in lifetime when PFOA is present, an effect attributed to PFOA-enabled hydration of the bilayer below $T_{gel\text{-}LC}$. ..... 86

23. Figure 3.6. A plot of the relative amplitudes of each C152 fluorescence lifetime as a function of temperature. The dotted lines show amplitudes for C152 in pure DPPC vesicle solutions and the symbols show lifetime amplitudes for C152 in DPPC vesicle/100 nM PFOA solutions. ..... 87

LIST OF FIGURES CONTINUED

Figure Page

24. Figure 4.1. DPPC and PFOA structures ..... 96

25. Figure 4.2. (A) 55 $Å^2$/molecule DPPC with increasing concentrations of PFOA in the CH region. A shift of ~ 5 cm-1 is seen. (B) 40 $Å^2$/molecule DPPC with increasing concentrations of PFOA in the CH region. A shift of ~ 5 cm-1 is observed. ..... 101

26. Figure 4.3. The $r^+/d^+$ ratio for DPPC in the presence of PFOA. Error bars represent standard deviations from ≥ 3 independent measurements. ..... 103

27. Figure 4.4. (A) PFOA surface activity in OH stretching region. (B) 55 $Å^2$/molecule DPPC in the presence of PFOA showing interfacial water signal with growing intensity for the disordered $H_2O$. (C) 40 $Å^2$/molecule DPPC in the presence of PFOA showing interfacial water signal with growing intensity for the disordered $H_2O$. ..... 106

28. Figure 4.5. Integrated intensities$^{1/2}$ at (A) 3200 $cm^{-1}$, (B) 3450 $cm^{-1}$, (C) sum of both peaks at 3200 $cm^{-1}$ and 3450 $cm^{-1}$ as functions of PFOA concentration. (D) A comparison between total VSFG intensity$^{1/2}$ vs. PFOA concentration and the interfacial Debye length created by charged surfactant adsorption to the water/air interface. ..... 109

29. Figure 4.6. Langmuir compression isotherm of DPPC on a Millipore subphase and varying concentrations of PFOA with vertical lines indicating the of 40 and 55 $Å^2$/molecule DPPC coverages used in the VSFG measurements. ..... 112

30. Figure 4.7. Compressibility of DPPC isotherms with 0 – 100 μM PFOA subphases. ..... 113

31. Figure 1. Geographic distribution of four Montana towns (Whitehall, Sheridan, Ennis, and Bozeman) within three counties (Jefferson, Madison, and Gallatin), detailing the number of wells tested, the number (and %) of wells with detectable PFAS concentrations, the number (and %) of wells with ∑ TQ > 1.0, and the number of wells with 1-7 PFAS compounds detected. ..... 127

LIST OF FIGURES CONTINUED

Figure Page

32. Figure 5.2. Count of wells by number of PFAS detected across the study area. The X axis is the number of PFAS detected per well (1-7) and the Y axis is the number of wells with that PFAS detections. This figure represents the prevalence of multiple PFAS in wells, for a total of 31 positive detections. 28 wells were found to have zero detected PFAS. ..... 131

33. Figure 5.3. Range, mean and median concentrations for positive detections as a function of concentration (ng/L) using Method-2. The circle represents the mean concentration, the triangle the median, and the line extends to the minimum and maximum concentration of each analyte detected. Detection limits can be found in the Appendix D. ..... 132

34. Figure 5.4. Property size vs. PFAS compounds detected. For the categories along the X axis, n is the number of wells of that property size, and median is the median number of PFAS compounds detected for that size category. ..... 134

35. Figure 5.5. (A) Well depth vs. PFAS detected with high confidence well depth (B) Well depth vs. PFAS detected with at least medium confidence well depth data added. *High confidence indicates that a well log with a depth was identified, was clearly linked to the well, and confirmed by the participant A well depth was categorized as high confidence (A) when a well log was identified with the depth specified, the log was clearly linked to the well and the linkage was confirmed by the participant. A well depth was categorized as medium (B) when a well log was identified that appeared clearly linked to the well, but the participant was not able to be contacted to confirm the linkage OR if the participant provided the well depth and indicated it was not an estimate, but a well log could not be located. ..... 135

36. Figure 5.6. Human-health benchmark cumulative toxicity quotient ($\Sigma_{TQ}$) for six PFAS (PFOA, PFOS, PFHxS, PFBS, PFHxA, and PFBA), for each of 22 wells with PFAS detections. Red triangles (▲) are the sum of individual TQs across sites with PFAS detections. The red line at 1.0 represents the threshold at which risk can be assumed. The orange dashed line at 0.1 indicates a precautionary screening threshold. Nine other sites had detectable PFAS concentrations but negligible $\Sigma_{TQ}$ (i.e., $\Sigma_{TQ}$ <0.00001) and are not included in the plot. ..... 136

LIST OF FIGURES CONTINUED

Figure Page

37. Figure A-1. Surface tension of SDS on left (CMC 8.3 mM) and sodium octanoate on right(CMC 380 mM). Both surfactants have concentrations in the millimolar range while PFAS are found much lower in the micromolar range. ..... 175

38. Figure A-2. Conductivity measurements of SDS showing a drastic change of slope after CMC is reached. ..... 176

39. Figure A-3. Concentration dependence of PFOA, PFBS, and KPFOS on particle size (nm) at variable pH. ..... 176

40. Figure A-4. Average particle size of PFOA, PFBS, and KPFOS nanodroplets as a function of concentration for samples with varying pH (made in Millipore) ..... 177

41. Figure A-5. 1 mM solutions of PFBS at pH 8 subjected to temperature dependent studies from 10°C to 60°C and back down in 10°C increments. The particle size reduces to micellar size before disappearing at 60°C and then returns upon cooling the solution back down. ..... 178

42. Figure A-6. 1 mM solutions of KPFOS at pH 8 subjected to temperature dependent studies from 10°C to 60°C and back down in 10°C increments. ..... 179

43. Figure A-7. 1 mM solutions of PFOA at pH 3.3 subjected to temperature dependent studies from 10°C to 60°C and back down in 10°C increments. ..... 180

44. Figure A-8. 1 mM solutions of PFBS at pH 3.5 subjected to temperature dependent studies from 10°C to 60°C and back down in 10°C increments. ..... 181

45. Figure A-9. 1 mM solutions of KPFOS at pH 5.0 subjected to temperature dependent studies from 10°C to 60°C and back down in 10°C increments. ..... 182

46. Figure A-10. Average particle size as a function of temperature for 1mM PFOA (pH 3.3), 1mM PFBS (3.5), and 1mM KPFOS (pH 5.0) as a function of temperature. Samples are heated from 10 to 60 degrees before being cooled back to 10 degrees. ..... 183

47. Figure A-11. Sodium dodecyl sulfate (SDS) particle size as a function of temperature for a 10 mM SDS solution. Samples are heated from 10 to 60 degrees before being cooled back to 10 degrees. ..... 184

LIST OF FIGURES CONTINUED

Figure Page

48. Figure A-12. Sodium octanoate particle size as a function of temperature in a 380 mM solution. Samples are heated from 10 to 60 degrees before being cooled back to 10 degrees. ..... 184

49. Figure A-13. A Cryo-EM image of a frozen 12 mM SDS solution with the black arrows designating SDS micelles. The micelle images range in size from 5 – 9 nm. The scale bar in the lower right corner of the image is 25 nm. ..... 186

50. Figure B-1. Cryo-EM Images of DPPC vesicles prepared in pure buffer solutions containing no PFOA. These images can be compared directly to those in Figure 4 of the manuscript. These images are provided to demonstrate DPPC vesicle preparation generally leads to large unilamellar vesicles. Scale bars are 50 nm. ..... 188

51. Figure B-2. Cryo-EM Images of DPPC vesicles prepared in solutions containing 100 nM PFOA. These images can be compared directly to those in Figure 5 of the manuscript. These images are provided to demonstrate generally that 100 nM PFOA introduces significant structural changes in DPPC vesicles. Scale bars are 50 nm. ..... 188

52. Figure B-3. Zoomed in image of a DPPC vesicle prepared in pure buffer solution. The scale bar is 6 nm and is chosen to span the bilayer width. ..... 189

53. Figure B-4. DSC traces for DPPC prepared in the presence of octanoic acid. ..... 190

54. Figure A-5. DLS traces for DPPC prepared in the presence of octanoic acid at room temperature, heated to 50°C and then cooled back to room temperature. ..... 191

55. Figure C-1. (A) 55 $Å^2$/molecule DPPC with SDS (B) 40 $Å^2$/molecule DPPC and SDS deposited into the subphase (CH stretching region). ..... 195

56. Figure C-2. The $r^+/d^+$ ratio for DPPC in the presence of SDS ..... 196

57. Figure C-3. 40 and 55 $Å^2$/molecule DPPC with SDS deposited into the subphase (OH stretching region). ..... 197

LIST OF FIGURES CONTINUED

Figure Page

58. Figure C-4. OH region SDS surface activity leads to the formation of interfacial water signal. ..... 198

59. Figure C-5. OH 3200 $cm^{-1}$ ice like water to OH 3450 $cm^{-1}$ water like water ratio with no DPPC in solution, 40 $Å^2$/molecule DPPC, and 55 $Å^2$/molecule DPPC..... 198

60. Figure C-6. Peak intensities at (A) 3200 $cm^{-1}$, (B) 3450 $cm^{-1}$, (C) sum of both peaks at 3200 $cm^{-1}$ and 3450$cm^{-1}$ showing an increasing trend with increasing concentration of SDS. ..... 199

# GLOSSARY or NOMENCLATURE

| | |
|---|---|
| **PFOA:** | Perfluorooctanoic Acid |
| **PFBS:** | Perfluorobutanesulfonic Acid |
| **KPFOS:** | Potassium Perfluorooctanesulfonic Acid |
| **DPPC:** | 1,2-dipalmitoyl-*sn*-glycero-3-phosphocholine |
| **SDS:** | Sodium Dodecyl Sulfate |
| **DSC:** | Differential Scanning Calorimetry |
| **DLS:** | Dynamic Light Scattering |
| **VSFG:** | Vibrational Sum Frequency Generation |

# ABSTRACT

Poly- and perfluoroalkyl substances (PFAS) are synthetic chemicals used in industrial and consumer products for their water, grease, and stain-resistant properties. Despite their widespread use, PFAS persist in the environment for decades and pose significant public health threats. This dissertation investigates the surface and bulk solution behavior of legacy PFAS and PFAS effects on lipid bilayers and monolayers.

Surface tension, conductivity, and dynamic light scattering (DLS) were used to examine the behavior of perfluorooctanoic acid (PFOA), perfluorobutanesulfonic acid (PFBS), and perfluorooctanesulfonic acid (PFOS). Results showed that surface activity is pH-dependent. Furthermore, these surfactants form aggregates in solution rather than micelles. These aggregates continue to grow with increasing solute concentration in contrast to traditional surfactant behavior. Cryo-EM images confirm a broad distribution of aggregates in solution.

Differential scanning calorimetry (DSC) and DLS studies examining the effects of PFOA on DPPC lipid bilayers showed that sub-micromolar PFOA concentrations lowered the gel-liquid crystalline transition enthalpy without affecting transition temperature. DLS measurements also revealed the formation of smaller objects resembling niosomes. Again, cryo-EM images confirmed multilamellar vesicle and niosome formation.

Vibrational sum frequency generation (VSFG) and Langmuir isotherms quantified the effects of PFOA on DPPC monolayers adsorbed to the air-water interface. PFOA had minimal impact on lipid structure in tightly packed monolayers but significantly affected moderately packed films. Furthermore, data from the -OH stretching region demonstrated that PFOA adsorption to moderately and tightly packed films created a charged surface whose electric double layer that oriented interfacial water molecules. Langmuir isotherms showed that PFOA shifted the transition surface area and decreased collapse pressure, indicating PFOA interacts with DPPC monolayers without disrupting the lipid film's integrity.

The final chapter details efforts to identify PFAS concentrations in private wells in rural Montana. Shallow wells and smaller properties had higher PFAS levels, with elevated health risks in a quarter of the tested wells. These findings highlight the importance of using advanced methods to assess PFAS contamination and associated health risks in drinking water.

# INTRODUCTION

Poly and perfluoroalkyl substances (PFAS) are anthropogenic compounds consisting of chains of carbon atoms with fluorine atoms attached. PFAS are found throughout the environment, due to their widespread use and persistence. Legacy and currently produced PFAS pose serious health risks, such as hormone disruption, immune system damage, and increased cancer risks. Because of these dangers, governments and health agencies have set and continue to update drinking water standards to protect public health by limiting PFAS levels in water supplies. Understanding how PFAS interact with biological materials is necessary for identifying their harmful effects, as these interactions influence how these chemicals are absorbed, transported, and retained in living organisms. Work described in this dissertation addresses PFAS behaviors in model biological systems using a variety of independent methods including differential scanning calorimetry, dynamic light scattering, surface tensiometry, conductivity, Langmuir pressure-area isotherms, and vibrational sum frequency generation. Findings from these studies show that legacy PFAS a) form aggregates rather than micelles in aqueous solutions; b) fluidize lipid bilayers and promote secondary solute bioconcentration; and c) cooperatively adsorbs to lipid monolayers at the air-water interface.

This chapter begins by motivating studies of PFAS/lipid interactions by considering the significance of PFAS/lipid interactions. This section addresses key health and environmental concerns. The section then explores how PFAS interact with biological lipid films at the molecular level, influencing structure, dynamics, and function. Understanding these interactions provides insight into PFAS bioaccumulation mechanisms and health risks. After considering the outstanding scientific questions of how PFAS interact with lipids, subsequent sections describe

the methods used in this research. These sections describe the operating principles of techniques such as DSC, DLS, surface tension measurements, and VSFG, incorporating representative model system data where applicable. The section concludes with a summary of key findings from each experimental study presented in Chapters 2–5.

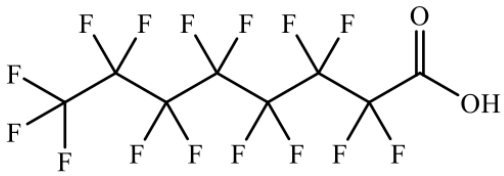
## 1.1 Motivation

### 1.1.1 Poly and Perfluoroalkyl Substances

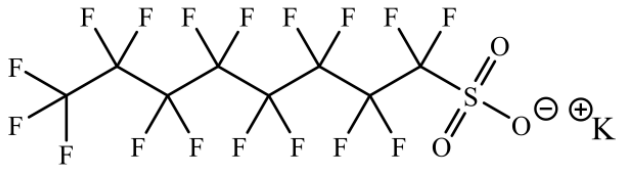
To be considered a member of the PFAS family, only one carbon atom must be fully fluorinated, while one adjacent carbon atom must be at least partially fluorinated. This broad definition encompasses more than ten thousand compounds. Carbon-fluorine bonds are some of the shortest and strongest bonds in nature, and they are resistant to chemical and biological destruction. Called “forever chemicals” because of their environmental persistence and long half-lives,[1] PFAS have been manufactured since the 1940s to be used in oil- and water-resistant non-stick products that are present in almost every household around the world. From non-stick cookware, water-repellent clothing,[2] cleaning products, petroleum firefighting foams,[3] and food packaging,[4] measurable amounts of PFAS can be found in the blood of 99% of all people.[5] Furthermore, PFAS in consumer products leads to PFAS leakage into municipal waste landfills creating another source of transport into the environment. To determine PFAS presence in food products and the environment, methods such as LC-MS/MS have been used, however the development of low-cost and more accessible methods has been of recent focus.

Both perfluorooctanoic Acid (PFOA, $C_8HF_{15}O_2$) and perfluorooctane sulfonic acid (PFOS, $C_8HF_{17}O_3S$) are no longer commercially manufactured in the United States and are deemed “legacy” PFAS. Newer, alternative compounds such as perfluorobutanesulfonic acid

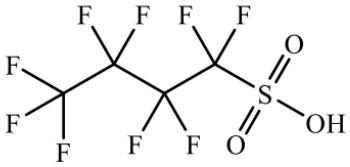
(PFBS, $C_4HF_9O_3S$) and other GenX (example $C_6O_2F_{11}OH$) chemicals have been used as replacements. Despite the United States no longer producing PFOA and PFOS in manufacturing, both are still being used in manufacturing processes in other countries and can be present in imported consumer goods. Moreover, PFOA and PFOS, mass-produced until 2015, will remain in the environment for decades.



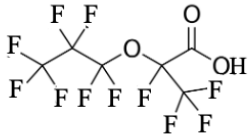
PFOA



KPFOS



PFBS



GenX

Figure 1.1. Chemical structures of the three PFAS examined in this work. Perfluorooctanoic acid (PFOA) and perfluorobutane-sulfonic acid (PFBS), and perfluorooctane sulfonic acid (PFOS) was purchased and used as a potassium salt (KPFOS).

PFAS threaten both ecosystem and human health as they are mobile in soil, groundwater, and surface water.[6-13] Recent reports have even noted risks posed by airborne PFAS transport.[14, 15] PFAS compounds do not break down easily even when subjected to environmental degradation processes, leading to compounds persisting in the environment for decades and causing extensive global environmental contamination. Estimated to be present in nearly 45% of tap water sources, even in rural community drinking water, PFAS have infiltrated waters assumed to be untouched from commercial activity.[8, 9] Because PFAS persist in the air, water, and soil, significant research has focused on PFAS bioaccumulation in humans and wildlife. Watersheds impacted by PFAS contamination have found high PFAS levels in wildlife including freshwater fish across the United States,[16, 17] aquatic food webs,[18-21] and cattle and livestock serum.[22, 23] However, the *mechanisms* responsible for bioaccumulation in both humans and wildlife remain largely unexplored.[24]

### 1.1.2 Health Effects and Bioaccumulation of PFAS

PFAS bioaccumulation is a major concern for individual and community health, as these chemicals do not break down easily and can build up in organisms over time. PFAS enter the food chain through contaminated water, soil, and food, accumulating in fish, wildlife, and humans. Once in the body, PFAS can persist for years, concentrating in organs such as the liver, kidneys, and blood.[6, 25, 26] As a result, growing global concerns have led to stricter regulations aimed at reducing PFAS content in water, food, and consumer products. Virtually all Americans have at least one PFAS compound in blood serum at detectable levels.[27] This statistic has raised concerns about adverse health effects due to PFAS's linkages to various cancers,[28-30] reduced vaccine response,[31, 32] high cholesterol,[33, 34] and thyroid disease.[35] Reduced vaccine response has

been observed for both the tetanus vaccine as well as the diphtheria vaccine in children ages 5-12 years old with elevated PFOA and PFOS concentrations in their blood.[36, 37] Further, studies have correlated elevated PFOS levels with decreased vaccine responses for the Rubella vaccine.[38, 39] High cholesterol linked with PFOA has been observed in adults ages 18-80 years old.[40-42] The increase in serum liver enzymes indicative of liver damage in adults above the age of 18 has been correlated with higher PFOA concentrations.[43, 44]

PFOA has been designated a carcinogen while PFOS has been listed as a potential carcinogen. Children are particularly vulnerable to PFAS exposure. PFAS in children are believed to result in developmental delays, low birth weights, and disruption to growth and behavior.[45, 46] Some long and short chain PFAS have been linked with human developmental effects, reduced antibody counts,[47] and several types of cancers. PFAS are also documented in many human plasma samples showing that contaminants can be transferred to children before and after birth from the mother.[48]

### 1.1.3 PFAS Drinking Water Standards

Health concerns associated with PFAS contamination have spurred efforts to establish stringent drinking water limits. Regulatory agencies and scientific communities are working together to set safer thresholds, improve water treatment technologies, and raise public awareness to protect individuals and communities from the harmful effects of PFAS exposure. Due to PFAS persistence and bioaccumulation potential, governmental officials have attempted to reduce the output of PFAS released including both PFOA and PFOS. Prior to its current standing regulation, the U.S. Environmental Protection Agency (EPA) issued non-enforceable health advisories for PFOA and PFOS in drinking water in 2016, recommending a combined

limit of 70 parts per trillion (ppt). This guideline was not a legal limit but served as a reference for public health protection. As the research for health effects and environmental persistence has grown, the recommended limits have tightened and become enforceable.

In the Spring of 2024 under the Safe Drinking Water Act, the EPA established legally enforceable drinking water limits for six PFAS commonly found in drinking water: PFOA, PFOS, PFHxS, PFNA, HFPO-DA, and PFAS mixtures with PFHxS, PFNA, HFPO-DA, and PFBS. PFOA and PFOS set final maximum contaminant levels (MCLs) of 4.0 ppt or ng/L.[49-51] PFHxS, PFNA, and HFPO-DA have set MCLs of 10 ppt.[9, 52] Mixtures of PFHxS, PFNA, HFPO-DA, and PFBS are set to be under a hazardous index unit of 1. Further, the EPA also set MCLGs which are the maximum contaminant level goals. For PFOA and PFOS, MCLGs are set to 0 ppt. MCLGs are health-based and non-enforceable concentration goals for compounds.[52, 53]

Table 1.1. EPA Maximum Contaminant Levels (MCL) for 6 PFAS and mixtures

| Compound | Final MCL (enforceable) | Final MCLG (health goal) |
|---|---|---|
| PFOA | 4.0 ppt | 0 ppt |
| PFOS | 4.0 ppt | 0 ppt |
| PFHxS | 10 ppt | 10 ppt |
| PFNA | 10 ppt | 10 ppt |
| HFPO-DA | 10 ppt | 10 ppt |
| Mixtures | 1 (unitless) Hazardous Index | 1 (unitless) Hazardous Index |

The parts per trillion (ppt) is in the sub-nanomolar concentration range for PFOA, PFOS, and PFBS.

### 1.1.4 Model Biomembranes and Monolayers

PFAS bioaccumulation is strongly influenced by interactions with cellular components, particularly lipids, biological membranes, and lipid films. Due to their amphiphilic nature, PFAS

can embed themselves in lipid bilayers, disrupting membrane structure and function. Lipids play a critical role in understanding the contaminant partitioning behavior in biological and environmental systems. Understanding these interactions is essential for modeling bioaccumulation mechanisms and predicting the environmental and health impacts of PFAS exposure. Lipid monolayers formed at air-water interfaces, for example, serve as valuable models for studying the effects of PFAS on pulmonary surfactant. Due to their hydrophobic fluorinated tails and hydrophilic functional groups, PFAS molecules can insert themselves into lipid monolayers, disrupting their organization and two-dimensional phase behavior. Specifically, PFAS can alter lipid monolayer packing density, fluidity, and surface pressure and provide insight into how PFAS contaminants affect pulmonary surfactant behavior.

1,2-dipalmitoyl-sn-glycero-3-phosphocholine (DPPC) is a common model biomembrane.[54-56] DPPC is a sixteen-carbon chain lipid with phosphocholine head group and is the primary component of lung surfactant, coating the walls of alveoli and enabling lung expansion and compression. DPPC is also a component of eukaryotic cells. In aqueous solution, DPPC spontaneously forms lipid bilayers. If these solutions are sonicated and extruded through porous filters, these bilayer structures form vesicles. Vesicles can be thought of as model cells. They consist of a spherical lipid bilayer surrounding an aqueous interior. Vesicle bilayers comprised of lipids having saturated acyl chains are characterized by a gel-liquid crystalline phase transition temperature ($T_{gel\text{-}LC}$) that describes the bilayer melting temperature. In the gel state, the saturated acyl chains are rigid and primarily in all-*trans* conformations. Above $T_{gel\text{-}LC}$ the acyl chains are more disordered and decoupled from each other in the bilayer. $T_{gel\text{-}LC}$ for DPPC has been reported to be between 40 and 41˚C.[57-59] Above $T_{gel\text{-}LC,}$ membrane permeability

increases allowing the lipid bilayer to become hydrated and enabling aqueous phase solutes to more easily accumulate in the bilayer.

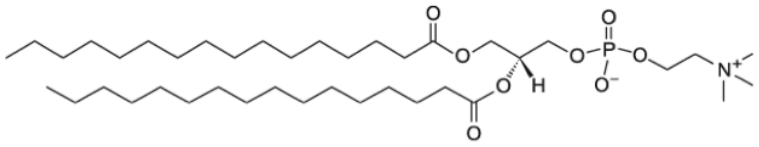


Figure 1.2. 1,2-dipalmitoyl-sn-glycero-3-phosphocholine (DPPC)

One mechanism responsible for PFAS bioaccumulation occurs through partitioning into cellular membranes, although the molecular details of PFAS partitioning remain unclear.[24, 60] Low PFAS concentrations are difficult to quantify, and their effects on biological materials are not well understood. Predictive models of PFAS affinity for biomembranes are limited by uncertainty, particularly with log P and log D values. Here, Log P represents the logarithm of the partition coefficient (P), which describes how a compound distributes itself between two immiscible phases, typically octanol and water. This empirical scale is a measure of a compound's lipophilicity and is defined as $\log P = \left(\frac{[Compound]_{octanol}}{[Compound]_{water}}\right)$. A higher Log P value indicates greater lipophilicity, meaning the compound prefers to dissolve in lipids rather than in water. Log D is the logarithm of the distribution coefficient (D), which considers both the partitioning of a compound between octanol and water and its ionization state at a given pH. The LogD scale accounts for both ionized and non-ionized forms of the compound, making it more relevant for ionizable solutes. Log D is defined similarly to log P however in the denominator ionized species are included with water.

According to publicly available data compiled by ADC/Laboratories, the protonated form of PFOA is predicted to have a log P value of ~7.7.[61] In contrast, when PFOA is deprotonated at

a biologically relevant pH of 7.4, its predicted log D value is 1.8.[61] (*Note: The log D scale takes into account the pH of the solution when modeling solute partitioning.)* Nonetheless, both the log P and log D values suggest that PFOA is inherently lipophilic regardless of its charge state. Despite the uncertainty from prediction models, all models show PFOA is likely to partition into lipid membranes similarly to other alkyl surfactants.

While lipid vesicles serve as model systems to examine cellular function and membrane dynamics, monolayers, composed of a single lipid layer at an air-water interface, are often used to interpret other biological systems including lung surfactant. In the case of monolayers, ordering within the film depends upon surface coverage as well as temperature. Even with expanded surface coverages, DPPC monolayers can attract solutes in bulk solution to the surface through cooperative adsorption mechanisms. Lung surfactant is a heterogeneous mixture comprised mostly of saturated DPPC with small amounts of surfactant associated proteins. DPPC monolayers help reduce the surface tension of the lungs and allow alveoli to expand and contract during breathing. Lung surfactant prevents alveoli from collapse during exhalation and minimizes the amount of work required to expand the alveoli during inhalation.[62] While PFAS compounds are known to induce impaired lung function, inflammation in lung cells, and potential links to asthma,[63] little to no mechanistic information is known about how PFAS inhalation affects lung surfactant expansion and compression. For the studies discussed in this thesis the control of lipid composition and PFAS concentration enable us to study how specific properties of the air-water interface change with the inclusion of PFAS.

1.1.5 Cooperative Adsorption and the Air-Water Interface

The air-water interface is a critical boundary where various physical processes and reactions occur, including adsorption. In the context of this dissertation, cooperative adsorption at the air-water interface describes a phenomenon where the presence of one species at the surface increases the likelihood of a second species adsorbing to the surface from bulk solution, resulting a higher surface coverage than would be predicted in the absence of surface modification. This definition of cooperative adsorption has been used to describe surface concentrations in different liquid interface systems,[64-66] but other fields define cooperative adsorption differently. For example, cooperative adsorption of gas phase particles to solid surface refers to adsorbate-adsorbate and/or adsorbate-substrate interactions enhancing additional particle adsorption to nearby sites.[348-349]

In the case of DPPC, cooperative adsorption occurs when highly soluble solutes in solution adsorb to the air-water interface due to changes in interfacial properties created by the adsorbed lipid monolayer. Our lab has recently examined cooperative adsorption of saccharides and disaccharides to air water interfaces covered with DPPC monolayers.[64-66] Research employed vibrational sum frequency generation (VSFG) spectroscopy and surface tension measurements to investigate how water-soluble saccharides affect the structure and organization of DPPC lipid monolayers at the air-water interface. Complementary differential scanning calorimetry (DSC) experiments were conducted to assess the impact of these saccharides on the phase behavior of DPPC vesicles. The findings revealed that both glucosamine and glucuronic acid enhance the organization of compressed DPPC monolayers, irrespective of the saccharide's charge.

The current work in our lab considers if PFOA monomers in bulk aqueous solution cooperatively adsorb to water-air interfaces modified by insoluble DPPC monolayers adsorbed to the aqueous/air interface. The work is motivated by a need to identify and understand how PFOA specifically, and PFAS in general affect the monolayer properties of this lipid that comprises 90% of human lung surfactant.

### 1.1.6 Hypotheses

Given concerns about PFAS compounds' persistence in the environment, impacts on human health, and the knowledge gaps surrounding PFOA, PFOS, and PFBS behavior in biological materials, work described in this dissertation addresses the following hypotheses:

1. Perfluorooctanoic acid (PFOA) at submicromolar concentrations fluidizes lipid bilayers and promotes secondary solute partitioning.
2. Perfluorinated compounds such as perfluorooctanoic acid (PFOA), perfluorobutanesulfonic acid (PFBS), and the potassium salt of perfluorooctanesulfonic acid (KPFOS) will not form micelles as traditional surfactants do due to their fluorous nature. The highly stable and hydrophobic fluorinated carbon chains in these molecules reduce intermolecular interactions with water, leading to non-conventional aggregation patterns or an absence of micelle formation typical of hydrocarbon-based surfactants.
3. Perfluorooctanoic acid (PFOA) cooperatively adsorbs to DPPC at the air-water interface and induces a charged double water layer observed in the OH stretching region using vibrational sum frequency generation.

A final part of this dissertation describes exploratory research that investigated the presence of PFAS in rural groundwater sources of southern Montana, where contamination from traditional industrial sources should, in principle, be minimal or absent.

## 1.2 Methods and Techniques

This dissertation examines legacy PFAS behavior focusing on their surface and bulk solution interactions, as well as the impact of PFOA on DPPC membrane properties and monolayers at the air-water interface. Techniques employed in this research include differential scanning calorimetry (DSC) to study thermal properties, dynamic light scattering (DLS) to analyze particle size distributions, and surface tensiometry for interfacial properties, and conductivity measurements for CMC determination. Additionally, Langmuir area-pressure isotherms provide insight into monolayer behavior, and vibrational sum frequency generation (VSFG) spectroscopy provides molecular-level information on interfacial interactions.

### 1.2.1 Differential Scanning Calorimetry

Differential Scanning Calorimetry (DSC) is a thermal technique used to study phase transitions a compound undergoes and is commonly used to study biomembranes.[55, 57, 59, 67-69] As a reference and the sample cell are heated simultaneously, the difference in heat flow required to keep the sample and reference cell at the same temperature is measured (Equation 1.1).[68] Thus, DSC enables both crystalline and melting transitions to be measured. Previously mentioned, DPPC has a s main gel to liquid-crystalline transition that occurs shown in Figure 3.[59, 70-72] The transition corresponds to the melting of the acyl chains present in the DPPC structure. The gel-to-liquid crystalline transition of DPPC is an exothermic process.

$$\text{Heat flow} = {}^{q_P}/_{T} \qquad (1.1)$$

$$\Delta H = q_P \qquad (1.2)$$

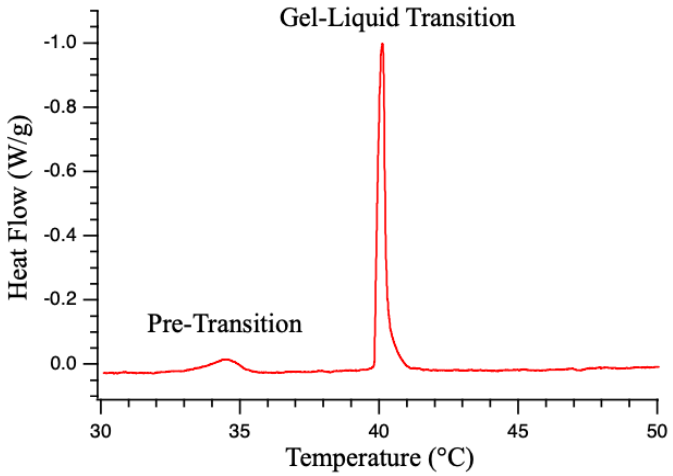



Figure 1.3. DSC endothermic pretransition and gel to liquid-crystalline transition of pure DPPC.

Characterization studies examining the phase transition of DPPC are taken on a TA Instruments Discovery Q2000 DSC with ±0.1 °C precision and accuracy across its operational range. The transition temperature indicates the temperature at which a lipid membrane undergoes a phase transition (from gel to liquid crystalline phase). Changes in $T_m$ suggest alterations in membrane packing and fluidity due to PFAS interactions. Enthalpy values represent the energy required for the phase transition the energy required for the phase transition and can be used to examine membrane permeability and lipid-lipid cohesion forces (Equation 1.2). Upon integrating the transition peak area of pure DPPC, the gel-liquid crystalline transition enthalpy measures 44 J/g, consistent with literature reports.[70, 73, 74] Further examination of how PFAS effect the gel-liquid crystalline transition enthalpy will be examined in Chapter 2.

1.2.2 Dynamic Light Scattering

Dynamic light scattering (DLS), also known as photon correlation spectroscopy, is a powerful technique used for measuring particle size for particles as small as 0.3 nm. In a DLS experiment, a monochromatic beam of light impinges on a solution containing macromolecules that scattering light in all directions. The DLS instrument used for studies described in the following chapters operated with a 633 nm laser. Light scattering depends on particle size and shape. A photon detector records the scattered light at a fixed angle, and the scattered light is analyzed by the time averaged intensity fluctuations to determine the speed at which particles diffuse. The diffusion constant can then be calculated.[75] The size of the particle d(H) (where H refers to the hydrodynamic diameter) is calculated from the translational diffusion coefficient (D) using the Stokes-Einstein equation (Equation 1.3). DLS assumes a spherical particle shape thus giving a hydrodynamic diameter d(H).[76]

$$d(\mathrm{H}) = \frac{kT}{3\pi\eta D} \qquad (1.3)$$

A Malvern Zetasizer Pro Red from Malvern Instruments was used to conduct experiments of PFAS solutions of varying concentration across a temperature gradient. Additional experiments were conducted to investigate the impact of PFOA on DPPC vesicle size. The Zetasizer Pro uses a non-invasive back scattering method with a scattering angle of 173° to measure particle sizes ranging from 0.3 nm to 10 μm of solutions placed in polystyrene cuvettes. The ZS Xplorer software version 1.30 automatically determines the size once parameters including the cell type, refractive index, concentration, temperature, and time for equilibration for each sample are entered.

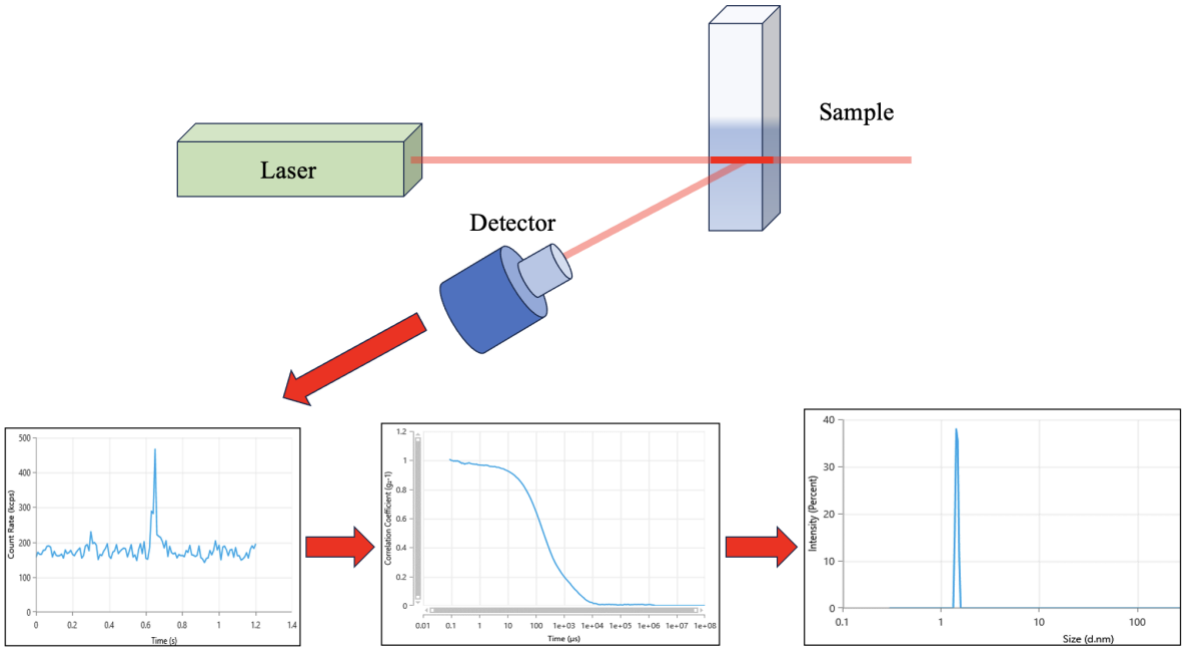



Figure 1.4. DLS experimental design in which a laser light scatters within a solution. Fluctuations in the Brownian motion are then sent to the detector which then analyzes the diffusion coefficient to determine a hydrodynamic radius.

### 1.2.3 Surface Activity and Micelle Formation

Legacy PFAS are surfactants characterized by both hydrophobic and hydrophilic regions, enabling them to reduce a system's overall free energy by adsorbing to interfaces. In aqueous solutions, their surface activity is evident by monomer adsorption to the air-water interface. As the surface becomes saturated limiting further adsorption bulk structures such as micelles or other aggregated phases begin to form in solution.

Surface tension measurements were used to study PFAS surface activity. Pure water has a surface tension ($\gamma_0$) of 72.8 mN/m at 20°C.[77, 78] For compounds that are soluble in water, a decrease in the surface tension of the air-water interface is expected as surfactants form monolayers. At the interface, the hydrophilic heads remain solvated in with the water while the hydrophobic tails extend out of the water into the air. As surfactant molecules accumulate at the

interface, more water molecules are pushed into the bulk solution creating more hydrogen bonding opportunities.

Surface tension measurements described in this dissertation used a Wilhelmy plate and a NIMA PS4 pressure sensor. To test the surface activity of PFOA, the surface tension of PFOA solutions are measured ($\gamma$) as a function of PFOA concentration. Surface tension data are then converted into surface pressure ($\Pi$), where $\Pi$ is defined as the difference between the surface tension of the neat subphase (Millipore water) and the surface tension of the subphase containing PFOA as shown in Equation 1.4 below. As more surfactants adsorb to the interface, $\gamma$ decreases and $\Pi$ increases. Surface pressure vs. concentration data for surfactant solutions are frequently analyzed using a Gibbs isotherm to determine surface excess coverage.[79] When surface pressure is plotted against the natural log of the concentration, the slope of steepest descent can be used to calculate the Gibbs surface excess as it relates to the concentration of surfactant molecules at the air-water interface (Equation 1.5).

$$\Pi = \gamma_0 - \gamma \qquad (1.4)$$

$$\Gamma = \mathrm{n/A} = \text{terminal surface coverage} \qquad (1.5)$$

$$\Gamma = -\frac{1}{\mathrm{RT}}\left(\frac{\partial \gamma}{\partial \mathrm{C}}\right)_{\mathrm{T}} \qquad (1.6)$$

$$\frac{d\Pi}{dln(conc)} = \frac{n}{A} \times kT \qquad (1.7)$$

In Equation 1.6 and 2.7 $\Gamma$ is the surface excess at the air-water interface, R is the universal gas constant (8.314 J/mol K), T is the temperature (K), $\gamma$ is the surface tension (mN/m), and lnC is the natural log of the bulk concentration. This equation can then be rearranged as

shown in Equation 1.7. In Equation 1.7 n is the number of molecules, A is the area each molecule occupies at the surface, k is Boltzmann's constant, T is the temperature (K), and $\frac{d\Pi}{dln(conc)}$ is the slope of steepest ascent from the plot of surface pressure versus the natural log of concentration. For soluble surfactants such as sodium dodecyl sulfate (SDS) or dodecyl trimethyl ammonium chloride (DTAC), limiting surface excess coverages are ~45-50 $Å^2$/molecule or ~2 x $10^{14}$ molecules/cm.[2,79]

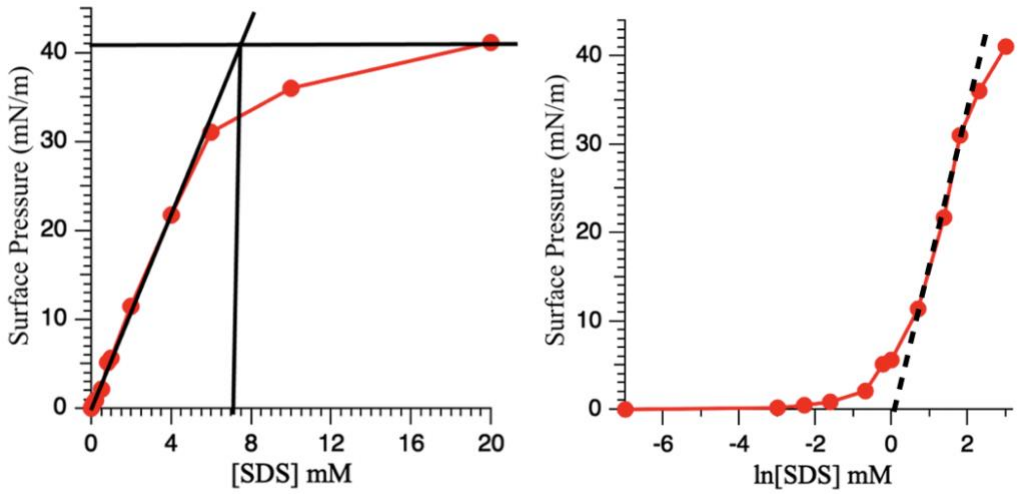



Figure 1.5. Determination of CMC of the surfactant sodium dodecyl sulfate (SDS) from surface pressure vs. concentration plot (left). Determination of the limiting surface excess coverage for SDS from surface pressure vs. ln[concentration] plot (right). The dashed line in the plot on the right showing slope of steepest ascent.

The Critical Micelle Concentration (CMC) is the concentration of a surfactant in a solution at which monomers saturate the interface, and excess surfactant molecules begin to form micelles in the bulk solution. Below the CMC, surfactants exist as individual monomers in solution. Once the CMC is reached and the surface becomes fully saturated, additional surfactant molecules aggregate to minimize free energy, often forming micelles. The CMC is a fundamental

property of surfactants, indicating the transition between monomer-dominated and micelle-dominated behavior in solution. Two common methods used to calculate CMCs are surface pressure and conductivity measurements.[80] Equation 1.7 shows that slope of a graph plotting surface pressure vs. the natural log of surfactant concentration reports surfactant surface excess concentration. The terminal surface coverage is determined by the slope of steepest ascent. A leveling off of the slope is traditionally associated with micelle formation, and the intersection between a line extrapolated from the steepest ascent and the high concentration asymptotic limit is used to denote the surfactant's CMC.

CMCs are also determined independently via conductivity by measuring the electrical conductivity of a surfactant solution as a function of its concentration. Solution phase conductivity arises from the movement of charged species (ions) under the influence of an applied electric field. In surfactant solutions, conductivity is primarily due to dissociated ionic surfactant molecules (such as sodium dodecyl sulfate, SDS) and their counter ions, as well as the mobility of free ions in water, including any added electrolytes. Below the CMC, conductivity increases linearly with increasing surfactant concentration because the ionic surfactant molecules contribute to charge conduction. As the concentration approaches the CMC, the slope of this relationship changes due to the micelle formation. As micelles form, the effective number of free ions in solution decreases. The CMC is identified where the plot of conductivity vs. surfactant concentration shows a discontinuous change in slope.

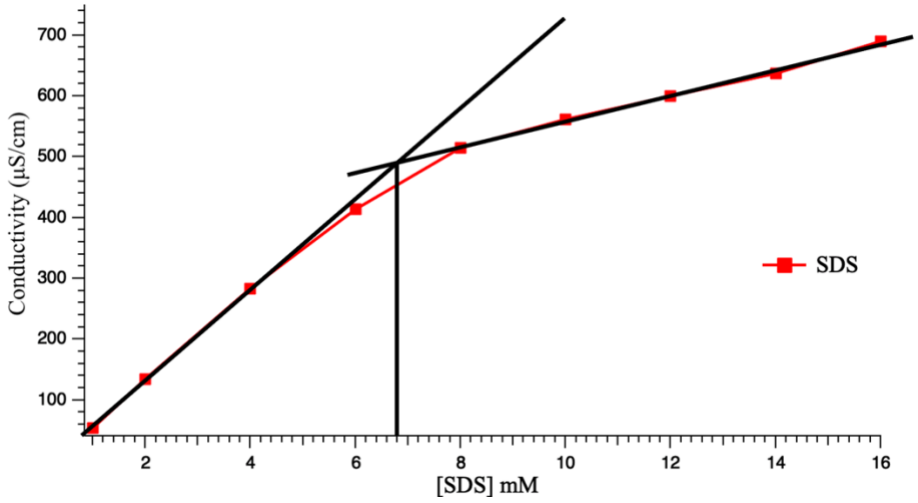



Figure 1.6. Determination of CMC of the surfactant sodium dodecyl sulfate (SDS) from conductivity vs. concentration plot.

Data in Figure 1.6 show that for solutions of the common surfactant sodium dodecyl sulfate (SDS), the surface pressure rises steeply at low concentrations before rising steeply and eventually leveling off. The slope of steepest ascent and the asymptotic limit are determined and report an SDS CMC of 7 mM in slightly lower than literature, although fluctuations in temperature and pH could account for this. For conductivity vs. concentration plots, the CMC is determined from the intersection of the low concentration and high concentration linear regimes. Typical surfactants such as SDS or DTAC form micelles of consistent sizing under 5 nm (Appendix A). Chapter 2 describes the surface tension behavior of PFOA, PFBS, and KPFOS. All three PFAS show behavior consistent with micelle formation, but complementary DLS measurements and Cryo-EM images show clearly that these solutes form aggregates in solution that grow with concentration rather than well-defined micelles.

### 1.2.4 Langmuir Surface Pressure – Area Isotherms

Langmuir monolayers are films comprised of insoluble surfactants constrained to aqueous interfaces. Most lipids – including DPPC – form Langmuir monolayers at the air-water interface, and these systems are commonly used as models of biological films including lung surfactant.[65, 66, 81-83] Surface tension measurements using a Langmuir trough are commonly used to measure the two-dimensional phase behavior of these films as a function of available surface area. In effect, these experiments serve as the two-dimensional analog of three-dimensional pressure-volume measurements.

The Langmuir trough is commonly employed to investigate surface properties, such as surface pressure, molecular packing, and interactions of surfactant molecules, lipids, and other films. The trough consists of a shallow, rectangular reservoir filled with 250 mL of solution and equipped with movable barriers that can compress or expand the film, allowing the user to control the area available for the monolayer. In a typical Langmuir experiment, the trough is filled with Millipore water. An insoluble surfactant is dissolved in a spreading solvent, such as chloroform. This solution is carefully deposited onto the clean water surface, where the solvent evaporates, leaving behind a monolayer of surfactant molecules. Initially, the barriers of the trough are fully expanded, providing ample space for the monolayer. After the solvent has evaporated, the barriers are gradually moved towards each other compressing the monolayer.

Compression speed is a variable in these measurements and must be considered when analyzing results. When barriers are compressed rapidly, the monolayer may be trapped in a metastable state leading to the non-equilibrium configurations and other artifacts. On the other hand, when the barriers are compressed slowly, the system is always in a reversible equilibrium, and the resulting Langmuir isotherm shows well-defined 2-dimensional phase behavior.

As an example of the type of insights that come from Langmuir trough measurements, Figure 1.7 shows an isothermal compression of a stearic acid monolayer adsorbed to the air/water (pH = 6) interface. Stearic acid ($C_{18}H_{36}O_2$) is a saturated fatty acid composed of a long hydrocarbon chain and a carboxyl group. Its structure features a straight alkyl chain with 16 methylene ($CH_2$) units and a terminal methyl ($CH_3$) group, making it non-polar and hydrophobic. At one end, the molecule has a polar, hydrophilic carboxyl group (COOH), capable of forming hydrogen bonds with water. This amphipathic nature allows stearic acid to interact with both polar and non-polar substances functioning as emulsifying agent in various applications.[79, 84]

Stearic acid's adsorption isothermal compression shows 2-dimension phase transitions that are readily identified. At very low surface concentrations, the stearic acid molecules are sparsely distributed across the surface and described as a two-dimensional gas. With further compression, the molecules pack more tightly, and their hydrocarbon chains start to align more vertically while maintaining flexibility. Stronger intermolecular interactions, such as Van der Waals forces, develop. The surface pressure increases more steeply with shrinking area and describes a two-dimensional liquid. When the molecules are packed closely together, surface pressure rises almost vertically with small changes in area and the monolayer is described as a two dimensional solid with the molecules tightly packed. The acyl chains are in all-trans conformations and directed along the surface normal. Further compression leads to monolayer collapse.

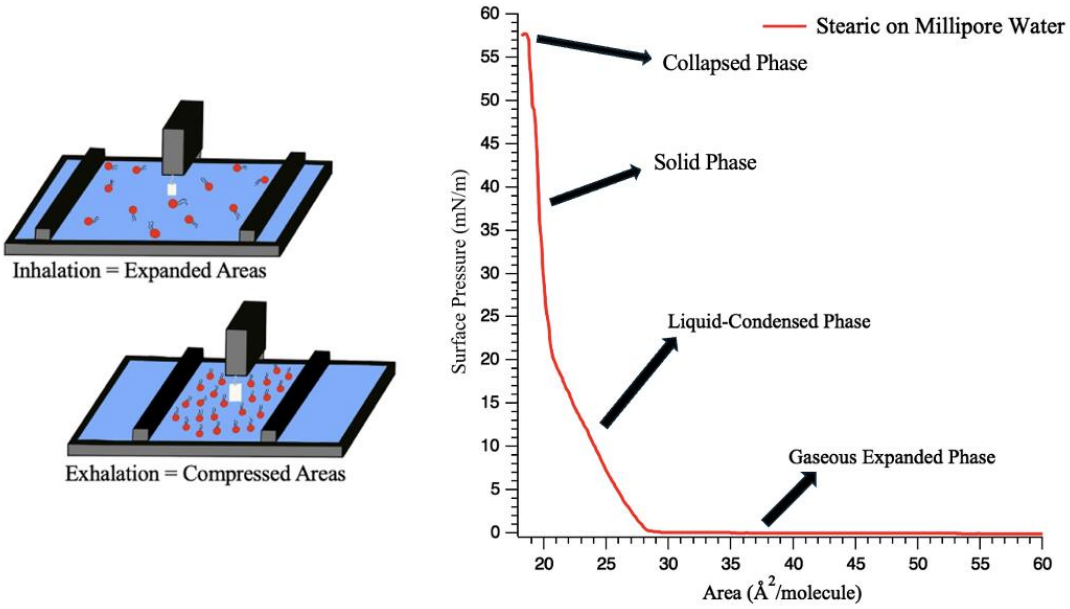



Figure 1.7. Langmuir expansion and compression schematic and stearic acid isotherm.

The two-dimensional surface behavior of DPPC monolayers is slightly more complicated than that of stearic acid. At low surface coverages, molecules are in a two-dimensional gaseous (G) phase where the tails are randomly oriented and are in contact with the surface. Upon compression the monolayer passes through a liquid-expanded (LE) phase where the hydrophobic tails of the lipid begin to adopt upright orientations. Further compression of the monolayer creates a liquid-condensed (LC) phase where the chains become more ordered. There is a liquid expanded-liquid condensed (LC-LE) coexistence phase which is seen as a plateau midway through the isotherm.[85, 86] DPPC collapses as when the surface pressure approaches 72 mN/m (or ~0 mN/m surface tension.).

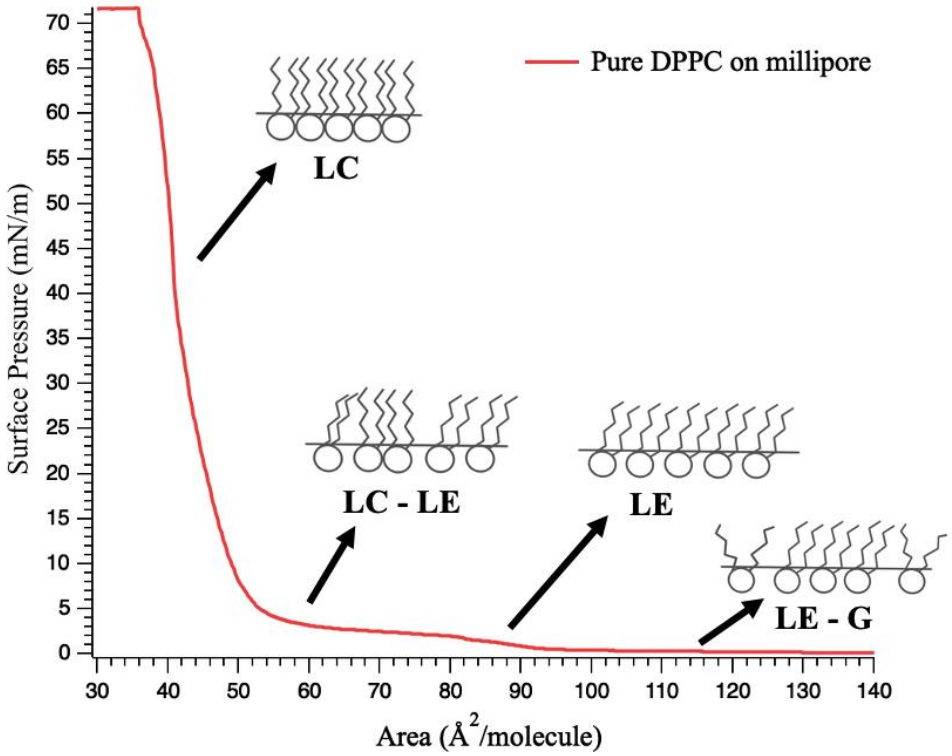



Figure 1.8. DPPC Langmuir compression isotherm with phases labeled.

1.2.5 Vibrational Sum Frequency Generation (VSFG)

VSFG is a surface specific, second order nonlinear optical technique that measures vibrational spectra of molecules at interfaces. While surface tension measurements including those using the Langmuir are useful in identifying thermodynamic behaviors at interfaces, these data do not directly measure properties related to molecular structure and organization. To determine how PFOA changes the structure and organization of DPPC monolayers adsorbed to the air-water interface, vibrational sum frequency generation (VSFG) is used to characterize DPPC chain conformation and organization in Langmuir films. Additionally, VSFG data also reported on water organization in the surface double layer formed when PFOA adsorbs to DPPC monolayers.

In VSFG two light beams at different frequencies (a fixed visible 800 nm and a tunable IR) are aligned spatially and temporally on the surface. The two beams couple through the second order susceptibility tensor and create a nonlinear polarization that has a frequency equal to the sum of the two input frequencies (Equation 1.8). The VSFG set up in our lab is equipped with a Coherent Libra Ti:sapphire laser with an 85-femtosecond pulse width and a 1 kHz repetition rate that produces the 800 nm visible light. A beam splitter reflects 80% of the light into the Coherent OPerA Solo amplifier that generates the IR light while the other 20% of the light is shaped to a resolution in the submicron region. Both the visible and IR light beams change polarization using waveplates.

$$\omega_{sum} = \omega_{IR} + \omega_{Vis} \qquad (1.8)$$

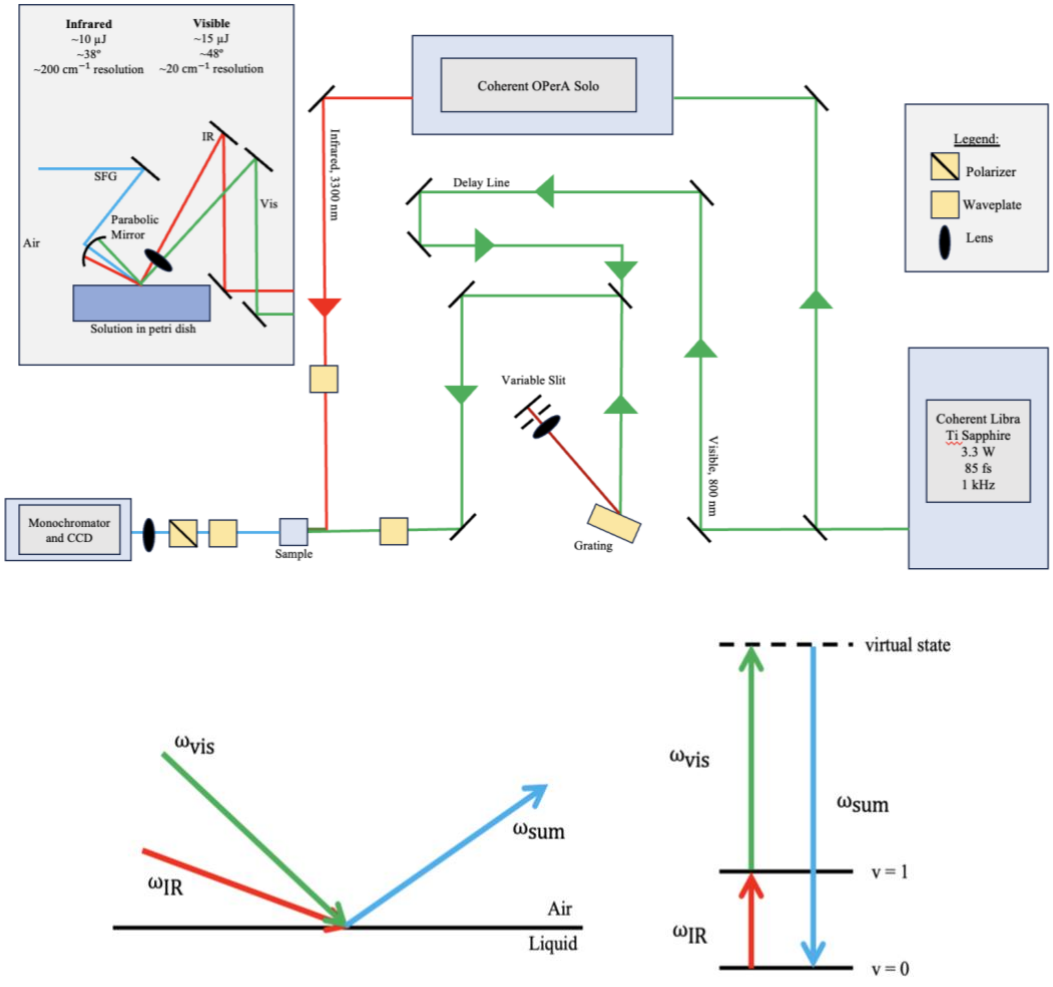



Figure 1.9. Walker Research Group VSFG schematic and energy level diagram.

VSFG is both surface and molecularly specific and can be described semi-quantitatively using Equations 1.9 - 1.12. Light incident on a surface induces a polarization that can be described as a power series expansion (Equation 1.9) in terms of the strengths of the incident fields.

$$P = P^{(0)} + P^{(1)} + P^{(2)} + \cdots \qquad (1.9)$$

The intensity of the sum frequency light is the magnitude squared of the 2nd order polarizability ($P^{(2)}$) or, equivalently, the magnitude squared of the second order susceptibility ($\chi^{(2)}$) and the intensity of both the visible and infrared pulses (Equation 1.10):

$$I_{SFG} = \left|P^{(2)}\right|^2 = \left|\chi^{(2)}\right|^2 I_{vis} I_{IR} \qquad (1.10)$$

$\chi^{(2)}$ is a third rank tensor whose elements must change sign upon inversion (Equation 1.11):

$$\chi^{(2)}(x,y,z) = -\chi^{(2)}(x,y,z) \qquad (1.11)$$

The only way this condition can be met in isotropic media is for all elements of $\chi^{(2)}$ to be zero. Interfaces, however, lack inversion symmetry so $\chi^{(2)}$ can take on nonzero values and VSFG becomes symmetry allowed. This condition makes VSFG surface specific. Each element in the $\chi^{(2)}$ tensor has resonant and nonresonant contributions. The resonant portion results from the vibrational modes, while the nonresonant portion results from the electronic responses. The resonant term of $\chi^{(2)}$ is described by a Lorentzian function and depends on the sum of all contributing vibrational resonances, where $A_q$, the amplitude term, is a product of the IR and Raman transition dipole moments (Equation 1.12).

$$\chi_{res}^{(2)} = \sum_q \frac{A_q}{\omega - \omega_{IR} + i\Gamma_q} \qquad (1.12)$$

By examining the surface of the air-liquid interface with different polarization combinations, the relative orientation of molecules at the surface can be determined. The three polarization combinations most relevant for my proposed research are SSP ($S_{sum}S_{vis}P_{IR}$), SPS

($S_{sum}P_{vis}S_{IR}$), and PPP ($P_{sum}P_{vis}P_{IR}$). The SSP combination selects vibrations having their IR transition moment projected along the surface normal; The SPS combination probes vibrational modes with IR transition moments parallel to the surface; and the PPP combination samples *all* non-zero elements of the $\chi^{(2)}$ tensor. All VSFG experiments will be performed with lipid monolayers having varying surface coverages and compositions. More specifically a loosely packed lipid monolayer of DPPC (55 $Å^2$/molecule) and a tightly packed lipid monolayer of DPPC (40 $Å^2$/molecule). By examining both loosely and tightly packed DPPC in the presence of PFOA, we will be able to examine microscopic changes occurring at the surface effecting the orientation of DPPC.

The Walker Research Group's VSFG set up is optimized to measure spectra in the CH and OH stretching regions of the spectrum (2700-3500 $cm^{-1}$). The DPPC vibrational spectrum is denoted with "r" and "d" where "r" represents the methyl group of DPPC, and "d" represents the methylene groups. The "+" and "-" symbols denote a symmetric and antisymmetric stretch, respectively. When measuring the effects of PFOA on DPPC monolayers, only -CH signals from the DPPC are measured given that PFOA contains only carbon-fluorine bonds. In a VSFG spectrum centered on the -CH stretching region, $d^+$ at ~2850 $cm^{-1}$ corresponds to a $CH_2$ SS, $r^+$ at ~2880 $cm^{-1}$ corresponds to a $CH_3$ SS, and the peak at ~2955 $cm^{-1}$ corresponds to a $CH_3$ AS/Fermi resonant peak as the feature is an overlap of both.

The $r^+/d^+$ ratio of methyl to methylene intensities is a useful qualitative measure of conformational order in the DPPC monolayer because it reflects the arrangement of the lipid molecules within the monolayer. When the monolayer is highly ordered, the acyl chains tend to be more aligned, and the ratio of methyl to methylene intensities ($r^+/d^+$) will show higher methyl

group intensity relative to methylene. In a more disordered state, the conformation of the lipid tails becomes more fluid, which changes the distribution of intensities between the two types of groups. Thus, the $r^+/ d^+$ ratio gives insight into the degree of order or disorder in the lipid tails, providing a qualitative measure of conformational changes in the DPPC monolayer.

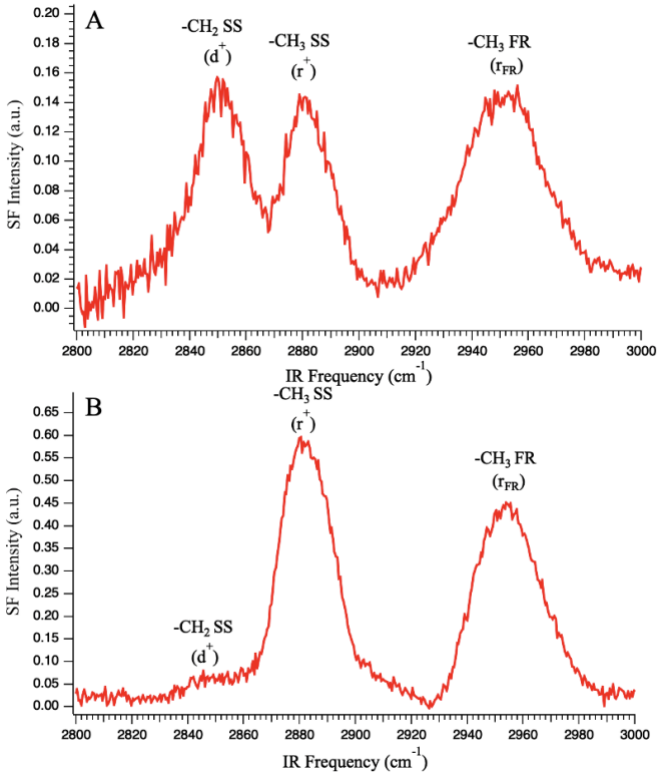



Figure 1.10. (A) Loosely packed Pure 55 Å$^2$/molecule DPPC deposited on a Millipore subphase. (B) Tightly packed Pure 40 Å$^2$/molecule DPPC deposited on a Millipore subphase.

To study changes in structure and orientation distribution of the interface with the addition of PFOA, studies will focus on loosely packed lipid films (55 Å$^2$/molecule) and densely packed lipid films (40 Å$^2$/molecule). In lower surface coverage (55 Å$^2$/molecule) there is more surface area that is unoccupied by the lipid film so PFOA should have a more significant impact on the DPPC monolayer than for higher surface coverage (40 Å$^2$/molecule). The VSFG

vibrational spectra allow us to deduce information about changes in lipid orientation in the monolayer with the addition of PFOA to the aqueous subphase.

## 1.3 Thesis Organization

Chapter 2:

PFOA, PFBS, and KPFOS are shown to form large aggregate structures contrary to previous reports defining PFAS as micellar forming surfactants. DLS studies of PFOA, PFBS, and KPFOS in solutions of varying pH and temperature reveal aggregation behavior, not micelle formation. Surface tension data show surfactant-like properties, with PFOA forming tightly packed monolayers in mildly acidic solutions. Conductivity experiments indicate that micelle formation occurred at concentrations below 1 mM in pH 8.0 solutions, aligning with surface tension findings. Cryo-EM images confirm a broad distribution of aggregates, supporting the DLS results.

Chapter 3:

Nanomolar PFOA concentrations are shown to affect DPPC lipid membrane structures by fluidizing lipid bilayers. DSC findings show that PFOA alters DPPC vesicle bilayer properties by lowering the gel–liquid crystalline transition enthalpy. DLS results reveal that these PFOA concentrations lead to increased vesicle size and aggregation. Cryo-EM images confirm that PFOA changes the vesicle structure, inducing distortions in the bilayer and the formation of larger aggregates. These results highlight potential impacts on bioconcentration mechanisms of PFAS compounds.

Chapter 4:

Studies focus on loosely packed lipid films (55 $Å^2$/molecule) and tightly packed lipid films (40 $Å^2$/molecule) using VSFG and Langmuir isotherms. At lower surface coverages, more interstitial space exists between the DPPC monomers allowing soluble surfactants to adsorb cooperatively to the surface and strongly impact DPPC organization and structure. In contrast, tightly packed DPPC monolayers have little interstitial space between monomers, although soluble surfactants can still adsorb to the lipid film driven by Coulomb interactions with the DPPC headgroups. Langmuir trough isotherms allow for information regarding the thermodynamic and structural properties at the air-water interface to be understood. VSFG and results indicate PFOA adsorbs cooperatively to DPPC monolayers at the air-water interface through the presence of interfacial water in the OH region and an increasing $r^+/d^+$ ratio.

Chapter 5:

Exploratory research on 59 private wells in three developing southern Montana counties reveal 12 PFAS compounds are detected at low concentrations in 31 wells. Samples were tested under Method-1 (method detection limit(s) [MDL] range: 5 – 22.8 ng/L for 6 regulated PFAS) and Method-2 (MDL range: 0.2 – 1.0 ng/L for 6 regulated PFAS). Under the first method with higher detection limits no PFAS were detected in the studied wells; however, when the same samples were run under the second, lower detection limit method, 31 wells had PFAS compounds detected. A greater number of compounds were generally detected in shallower wells and on smaller property sizes, consistent with higher prevalence in younger (shallower) groundwater in areas with higher intensity land use. Potential human exposure risk assessments were analyzed and found to be driven by PFOA and PFOS.

Chapter 6:

Chapters 2-5 includes a summary of research described followed by discussion on further experiments that should be performed to continue this project.

# CHAPTER TWO

# AGGREGATION NOT MICELLIZATION: PERFLUOROOCTANOIC ACID, PERFLUOROBUTANESULFONIC ACID, AND POTASSIUM PERFLUOROOCTANESULFONATE BEHAVIOR IN AQUEOUS SOLUTION

## Contribution of Authors and Co-Authors

Manuscript in Chapter 3:

Author: Tess N. Sobolewski

Contributions: Collected and analyzed experimental data. Assisted in writing and editing manuscript.

Co-Author: J. Luke Findlay

Contributions: Collected cryo-electron microscopy data.

Co-Author: Jackilyn E. Hemphill

Contributions: Collected data in supporting information.

Co-Author: Robert A. Walker

Contributions: Assisted with data analysis, writing, and editing of manuscript.

Manuscript Information

Tess N. Sobolewski, J. Luke Findlay, Jackilyn E. Hemphill, and Robert A. Walker

Langmuir

Status of Manuscript:
☐ Prepared for submission to a peer-reviewed journal
☐ Officially submitted to a peer-reviewed journal
☐ Accepted by a peer-reviewed journal
☒ Published in a peer-reviewed journal

Publisher: American Chemical Society – Langmuir
Date of Submission: July 6, 2024
Date Accepted: October 30, 2024
Volume 40, Issue 47 November 2024, 24820 - 24831
DOI: 10.1021/acs.langmuir.4c02566

## 2.0 Abstract

Surface tension, conductivity, and dynamic light scattering (DLS) measurements were used to examine the surface and bulk solution behaviors of three members of the PFAS family, perfluoro-octanoic acid (PFOA), perfluorobutane sulfonic acid (PFBS), and the potassium salt of perfluorooctane sulfonic acid (PFOS). Measurements were carried out in solutions having variable (acidic) pH and in solutions buffered to pH = 8.0. Surface tension data show traditional soluble surfactant behavior, and results illustrate that PFOA, PFBS, and PFOS surface activity depends sensitively on solution-phase pH. The tightly packed monolayers formed by PFOA in mildly acidic solutions imply that the surface pH of PFOA solutions is several units lower than bulk. Results from conductivity experiments generally show increasing conductivity with increasing bulk solution surfactant concentration. In pH = 8.0 solutions, changes in conductivity slope with surfactant concentration suggest the onset of micelle formation at concentrations $< 1$ mM, markedly lower than reported in literature. In general, apparent critical micelle concentrations (CMCs) determined from conductivity data agree with similar predictions made from surface tension results. DLS measurements show that at concentrations close to the predicted PFAS CMCs, objects with diameters $\leq$ 10nm start to form. However, unlike micelles, these objects continue to grow with increasing bulk solute concentration. These aggregates form structures having diameters of 50-150 nm. Aggregate size shrinks modestly as solution phase temperature increases, and this behavior is reversible. Cryo-EM images of PFOA solutions confirm a broad distribution of particles, supporting the DLS measurements. Findings reported in this work represent the first evidence that these three EPA-regulated PFAS surfactants form aggregates rather than micelles in solution. Findings also begin to reconcile differences in

reported surface behaviors that have led to CMC predictions in the literature varying by more than an order of magnitude.

## 2.1 Introduction

Per- and polyfluoroalkyl substances (PFAS) are a class of anthropogenic contaminants threatening community and ecosystem health.[10, 24, 87-89] Detected PFAS concentrations across surface waters globally and the health implications associated with PFAS exposure speak to the near universal risk posed by these 'forever chemicals' that have long been used in the textile, food-packaging, and firefighting industries.[2, 90-93] Given their widespread use and their environmental persistence, PFAS are estimated to be present in 45% of tap water sources,[9] even in remote rural community drinking water supplies.[94] PFAS have even been detected in watersheds that were assumed to be pristine and not subject to contamination from commercial sources. For example, total combined PFAS levels as high as 12920 ppt have been measured in the Upper Missouri River,[95] and studies assessing bioconcentration in fish from this watershed have reported PFAS concentrations as high as 88 ng/g (or 88000 ppt) with one PFAS molecule in particular, perfluoro-octane sulfonic acid or PFOS, being the primary constituent.[96] Studies from these and other locations have reported PFAS bioconcentration factors ≥1000.[20, 97, 98]

Detecting PFAS in ground and surface water has been a focal point of many recent studies as scientists, regulatory agencies, and policy makers consider environmental PFAS persistence and transport.[9, 10, 87, 99-104] Related efforts have explored strategies for destroying PFAS and remediating contaminated landscapes.[105-109] Despite this extensive research activity, however, surprisingly little is known about PFAS behavior in aqueous solution. PFAS species

such as perfluoro-octanoic acid (PFOA), perfluorobutane sulfonic acid (PFBS), PFOS, and others have surfactant structures (Figure 3.1), but reports of PFAS surface activity and bulk solution properties vary widely in their findings. Reported critical micelle concentrations (CMCs) differ by as much as an order of magnitude in some cases,[110-112] and the community's understanding of PFAS behavior as a function aqueous phase pH and temperature remain incomplete. This knowledge gap must be redressed if proposed transport models and exposure estimates are to be experimentally tested and validated.[113, 114]

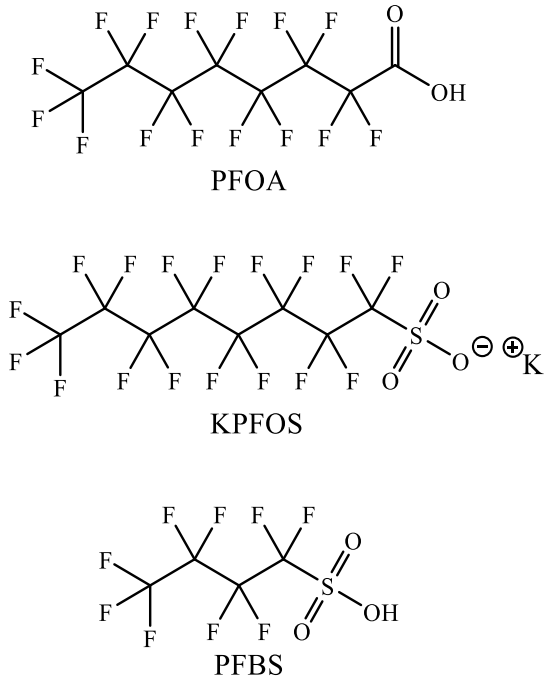



Figure 2.1. Chemical structures of the three PFAS examined in this work. Perfluorooctanoic acid (PFOA) and perfluorobutane-sulfonic acid (PFBS) were used in their protonated forms. Perfluorooctane sulfonic acid (PFOS) was purchased and used as a potassium salt (KPFOS).

Previous work examining PFOA's pH-dependent properties focused primarily on the solute's deprotonated anionic form, with Armitage, et al. maintaining that PFOA exists almost exclusively in the anionic form at environmentally relevant pH and the partitioning and

degradation behavior of this anionic form can be reasonably estimated.[115] This assumption is conditional, however, given that PFOA's $pK_a$ changes as a function of concentration[116] and knowing that surface pH across the air/water interface can vary by 3.0 units or more.[115, 117] Similar concerns are relevant for other PFAS surfactants including PFOS and PFBS.[118-123]

Surface tension and conductivity experiments reported below characterize the amphiphilic and some bulk solution properties of PFOA, PFBS, and PFOS. Data show that behaviors depend on bulk solution pH but generally conform to expectations from typical surfactants. Importantly, however, dynamic light scattering (DLS) data show that neither protonated nor deprotonated forms of these solutes show traditional micellar behavior, contradicting an extensive body of literature citing CMCs for a host of PFAS.[110-112, 119, 124-141] Instead, PFOA, PFBS, and PFOS appear to form aggregates in solution having diameters of ~50-150 nm. Aggregate size depends on both solute concentration and temperature.[142-146,147, 148] Taken together, these findings comprise the most extensive assessment to date of PFOA, PFOS, and PFBS behavior in aqueous solutions, and results have direct consequences for how PFAS persist, spread through, and accumulate in environmental systems.

## 2.2 Experimental Materials and Methods

### 2.2.1 Materials.

Perfluorooctanoic acid (95% purity) was purchased from Sigma Aldrich (St. Louis, MO) and were used as received. Perfluorobutanesulfonic acid (98% purity) was purchased from ALFA Chemistry (Ronkonkoma, NY) and was used as received. The potassium salt of perfluorooctane sulfonic acid (96.4% purity) was purchased from LGC Standards (Manchester, UK) and used as received. For carbonate-based solutions, sodium bicarbonate was purchased

from Sigma-Aldrich (St. Louis, MO). All chemicals were used without further purification. Millipore water (resistivity of 18.2 MW) was used for all aqueous sample preparation.

2.2.2 Sample Preparation.

Samples were prepared under two separate conditions. In the first, the PFAS solute was simply dissolved into solution to create a stock solution having a concentration of 100 μM or 1 mM depending on the concentration range being sampled. Higher concentration solutions were prepared directly. Serial dilutions were made to create PFAS solutions having concentrations as low as 1 nM. Stock solutions were made and diluted multiple times and independently to reduce the uncertainty in reported data.

2.2.2.1 Preparation of Variable pH Solutions: This work examined PFAS behavior under a variety of conditions. This broad-brush survey included PFAS in pure water (low ionic strength, initial pH ~5.8) and in buffered, pH = 8.0 solutions (50 mM carbonate/bicarbonate). The pure water experiments probed PFOA, PFBS, and PFOS behavior in aqueous solution in the absence of competing effects from other ions. The pH = 8.0 experiments were carried out to ensure that the three PFAS surfactants were exclusively negatively charged. We note that the most significant property changes were observed at PFOA, PFBS and PFOS concentrations ≤ 1 mM, meaning that the buffered pH solutions effectively were at constant ionic strength. Work described in this manuscript consider the properties of three different solutes at two different pH and at different temperatures. Given the surprising findings from all three solutes, considerable work remains to characterize how solution phase ionic strength and dissolved ion specificity affect PFAS surfactant behavior. PFOA, PFBS, and PFOS were all prepared in Millipore water and the pH was tested using a Xplorer GLX pH probe. For the concentrations sampled, PFOA

had a pH range of 2-5, PFBS had a pH range of 3-5, and KPFOS had a pH range of 4-5. Given that PFAS concentrations are typically reported in terms of ppt/ppm for regulatory purposes, Table 2.1 notes how these units correspond to more traditional, molarity-based units for the three solutes studied in this work.

Table 2.1. Parts per trillion (ppt) conversion to nanomolar (nM) concentrations

| PPT Concentrations | Concentration (nM) | | |
|---|---|---|---|
| | PFOA | PFBS | KPFOS |
| 1000 ppt | 2.415 | 3.332 | 1.86 |
| 100 ppt | 0.242 | 0.333 | 0.19 |
| 10 ppt | 0.024 | 0.033 | 0.02 |
| 4 ppt | 0.009 | 0.013 | 0.007 |
| 1 ppt | 0.002 | 0.003 | 0.002 |

No effort was made to control solution phase ionic strength in the variable pH solutions beyond controlling the amount of dissolved PFAS solute.

2.2.2.2 Preparation of pH 8 Solutions: PFOA and PFBS samples were made in 50 mM carbonate buffer (pH =8.0) for DLS measurements, while 10 mM carbonate buffer was used for surface tension and conductivity measurements. In general, buffer preparation required adding an appropriate amount of sodium bicarbonate ($NaHCO_3$, ACS Reagent Grade, Sigma Aldrich) – 0.05 moles or 0.01 moles for 50 mM or 10 mM, respectively – and then making small adjustments with a 1M NaOH solution to reach the desired pH. Different buffer concentrations were used to minimize the intrinsic effect of the buffer on the property being measured. Surface tension and conductivity measurements were made mostly with sub-mM PFAS solutions, so a 10 mM carbonate buffer had adequate buffering capacity. DLS measurements were performed with solutions having PFAS concentrations as high as 8 mM thus motivating higher carbonate buffer concentrations.

2.2.3 Experimental Techniques

2.2.3.1 Surface Tensiometry: Surface tension measurements were used to study PFOA, PFBS, and PFOS surface activity at the air-water interface. Surface tension measurements were performed using a NIMA PS4 pressure sensor and paper Wilhelmy plates purchased from Brown Waite Engineering (Oxfordshire, England) using methods previously described.[64, 147, 149] Surface pressure was calculated as the difference between the surface tension of the neat subphase ($\gamma_0$) Millipore water (72.8 mN/m at 20˚C)[150], and the surface tension of the solution containing the surfactant (γ) (Equation 1).

$$\Pi = \gamma_0 - \gamma \qquad (2.1)$$

Data were analyzed using the Gibbs adsorption equation to calculate the PFAS surface excess coverages (Equation 2) as a function of bulk phase solute concentration.[79, 151] In both Equations 2 and 3, n is the number of molecules adsorbed to the surface and A is the sample area.

$$\Pi A = n \times k \times T \times \ln\,(conc) \qquad (2.2)$$

Equation 2 can be rearranged to determine surface excess concentration, Γ:

$$\Gamma = \frac{n}{A} = \frac{d\Pi}{dln(conc)} \times \frac{1}{KT} \qquad (2.3)$$

where $\frac{d\Pi}{dln(conc)}$ is the slope of steepest ascent, k is the Boltzmann constant, and T is the absolute temperature in Kelvin.

2.2.3.2 Conductivity: Conductivity measurements were performed using a Mettler Toledo LE703 Sensor for FiveGO conductivity meter able to measure a range 10 µS/cm to 200 mS/cm. Experiments used a LE703 IP67 probe suitable for aqueous samples having medium to high conductivities. Tests using calibrated standards reported an accuracy of ±0.5%. Conductivity

measurements were used to estimate putative CMCs for PFOA, PFBS, and KPFOS. Predictions based on conductivities were generally consistent with those from surface tension data.[152] All measurements were performed at 20˚C.

2.2.3.3 Dynamic Light Scattering: DLS measurements were performed using a Malvern Zetasizer Pro Red from Malvern Instruments Ltd. (Worcestershire, England). The Zetasizer measurements use a non-invasive back scattering method at a scattering angle of 173° to measure particle sizes ranging from 0.3nm to 10µm. Solutions were contained in polystyrene cuvettes, and measurements were performed in triplicate and then averaged. For temperature dependent experiments, the instrument was calibrated at the desired temperature for 60 seconds. Longer dwell times (up to 10 minutes) did not change results. Data were evaluated using L-curve analyses with automatic attenuation and the average particle size of the three trials is reported.

Measurements were conducted using disposable 10x10 plastic cuvettes (DTS0012), where "10x10" refers to the cuvette's 10 mm path length, which is the standard distance the light travels through the sample. The cuvettes were made of polystyrene, and water was used as the dispersant. Advanced settings parameters were also selected. Parameters included selecting back scatter as the angle of detection, measuring at optimal position, automatic attenuation, and a 1 second pause between repeat scans. Using the method builder tab, the size measurement is selected with scans run in triplicate providing both individual scan results and an average of the three trials. Most scans were run at 25.0 °C and some experiments varied temperature from 0 – 70 °C. All scans were equilibrated for 60 seconds before optimization and were analyzed using L-curve analysis. L-curve analysis optimizes the distribution result to give the highest resolution

while reducing the background noise. This process is ideal for low scattering samples known to have particles of similar sizes rather than a broader distribution.

2.2.3.4 Cryo-EM: Samples were frozen on Quantifoil 200 mesh R2/1 Cu grids. 4 μL of samples were deposited on the grid, blotted for 4 seconds at a blot force of 5. Frozen grids were then imaged on a Talos Arctica transmission electron microscope at 200 kV. Images were taken with a Gatan K3 camera using SerialEM. The overview of the total conglomeration was taken at 1600x mag. Closer images were taken at 36 kx, -2 μm defocus, and 60 e-/a2 dose. SDS images were taken at a full exposure of 55e-/a2 total dose.

## 2.3 Results and Discussion

### 2.3.1 Surface Tension.

Figure 2.2 illustrates the importance of controlling solution phase pH when interpreting surface activity results. Focusing first on PFOA, data in Figure 2.2 show that surface pressure rises steeply with increasing PFOA concentration under both variable pH and pH 8.0 conditions. In the variable pH solutions, the surface pressure requires higher PFOA concentrations before it starts to rise and ultimately reaches a higher terminal surface pressure (51.6 mN/m). In contrast, surface pressure of the pH 8.0 PFOA solution begins rising immediately at the lowest bulk PFOA concentrations tested (≤ 1 nM) before leveling off at 44.5 mN/m at bulk PFOA concentrations of ~1.5-2.0 mM. Analyzing these data using Eq. 3, we calculate terminal surface excess concentrations of 5.4 x $10^{14}$ /$cm^2$ and 2.3 x $10^{14}$ /$cm^2$ in the variable pH and pH 8.0 buffered PFOA solutions, respectively. These concentrations correspond to terminal areas per molecule of 19 $Å^2$/molecule (variable pH) and 44 $Å^2$/molecule (pH 8.0). The former surface excess concentration

matches closely the values measured for tightly packed, neutral alkyl surfactants having similar chain lengths[149] while the latter surface excess is comparable to those of similarly sized charged alkyl surfactants.[153, 154]

PFBS surface activity also shows a strong dependence on solute charge state, with PFBS having a 30% higher terminal surface coverage in the variable pH solution ($6.6 \times 10^{13}$ $cm^{-2}$) compared to the pH 8.0 solutions ($5.0 \times 10^{13}$ $cm^{-2}$). KPFOS is the potassium salt of a weak conjugate base, and the solution pH has little effect on KPFOS surface activity or surface coverage. An important point to note is that KPFOS is much less soluble in aqueous solution (at any pH) and its isotherm does not converge to an asymptotic limit before reaching its solubility limit (approximately 1.0 mM). Despite this comparatively low solubility, KPFOS monolayers have surface excess concentrations comparable to those of PFOA in the pH 8 solutions.

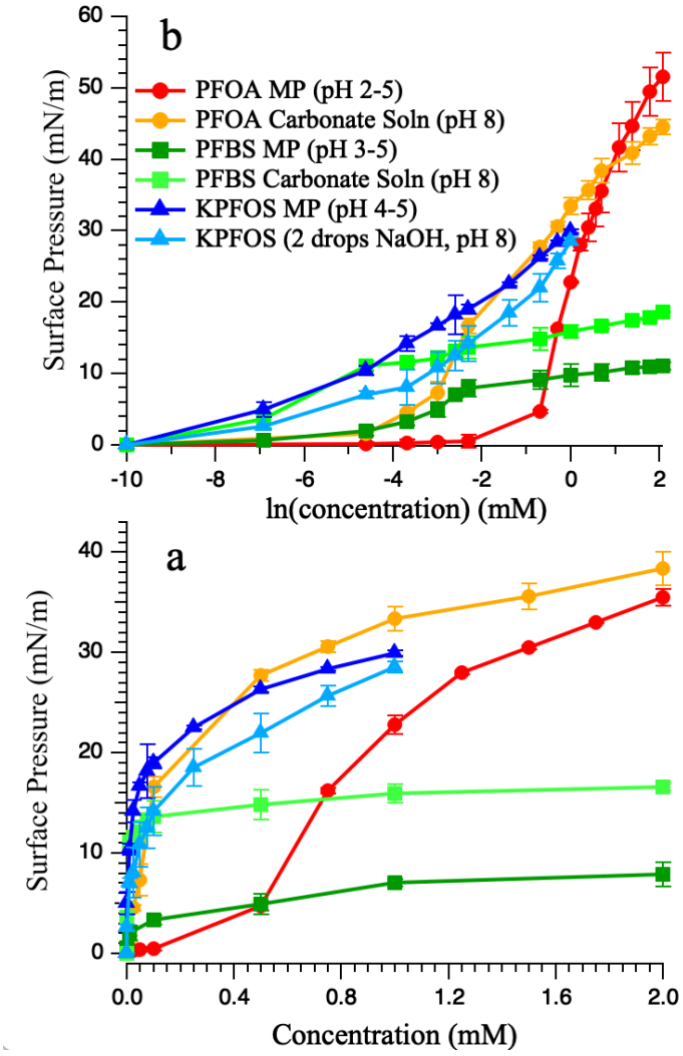



Figure 2.2. (a) Surface pressure as a function of bulk solution PFAS (PFOA, PFBS, and KPFOS) (mM) in both low pH and pH 8 environments. (b) Surface pressure plotted against ln[conc] to calculate the terminal surface coverages as described in Equations 1-3.

The isotherms in Figure 2.2 were analyzed using Equation 3, and surface pressures are plotted vs. the natural log of concentration in Figure 2.2b. Surface excess concentrations were calculated over a bulk concentration range spanning 7 orders of magnitude. Terminal surface coverages for all three surfactants in variable pH and pH = 8.0 solutions are reported in Table 2.2 and surface coverages at all concentrations are reported in Supporting Information. We note that

solutions containing PFOA and KPFOS do not reach their terminal surface coverages until ~0.1 – 1.0 mM. In contrast, PFBS – the least surface active of the three PFAS studied – establishes a terminal surface coverage at much lower concentrations: ~1 μM for the variable pH solutions and ~1 nM in pH 8 solutions.

Table 2.2. Terminal surface excess concentrations, $\Gamma_{max}$ (molecules/cm$^2$), bulk concentration when $\Gamma_{max}$ is reached (mM), and pH in variable pH solutions when $\Gamma_{max}$ is reached. All data are reported for T = 20˚C

| | PFOA | | PFBS | | PFOS | |
|---|---|---|---|---|---|---|
| | Variable pH | pH 8 | Variable pH | pH 8 | Variable pH | pH 8 |
| $\Gamma_{max}$ | 5.4E14 | 2.3E14 | 6.6E13 | 5.0E13 | 1.3E14 | 2.0E14 |
| Bulk conc. at $\Gamma_{max}$ (mM) | 1 | 0.1 | 0.001 | 1E-6 | 1 | 1 |
| pH at $\Gamma_{max}$ | 3.3 | – | 4.5 | – | 5.0 | – |

One additional observation from Figure 2.2 is that all three surfactants under both variable pH and pH 8 conditions show classic isotherm behavior with surface pressure rising steeply at lower surfactant concentrations and then leveling off. In the case of PFOS, data can be fit to extrapolate to a presumed asymptotic limit.

Isotherms such as those presented in Figure 2.2 are often analyzed to predict CMCs. The isotherms in Figure 2.2a predict CMCs for PFOA, PFBS, and PFOS of 200 μM, 10 μM, and 150 μM, respectively, in pH 8 solutions. (Table 2.3) Predicted CMCs for PFOA and PFBS in the variable pH solutions are considerably higher for PFOA (1.5 mM) and PFBS (100 μM). The predicted PFOS CMC in the variable pH solution is comparable to the pH 8 system. We note the ~$10^{-5}$ – $10^{-4}$ M predicted CMC concentrations are much lower than the ~$10^{-3}$ – $10^{-1}$ M CMC

concentrations observed for traditional alkyl surfactants having similar sizes. We believe our reported putative CMC estimates are accurate given control experiments carried out with both sodium dodecyl sulfate (SDS) and with sodium octanoate. (Data from control experiments using both SDS (CMC = 8.3 mM) and sodium octanoate (CMC = 380 mM) are presented in Supporting Information.)

2.3.2 Conductivity.

Given the surprisingly low predicted PFAS CMC concentrations, we sought an independent method for determining putative CMC concentrations for PFOA, PFBS, and PFOS. An alternative approach for determining a surfactant's CMC is to measure solution phase conductivity as a function of solute concentration.[147, 152, 155, 156] Figure 2.3 shows the conductivity of aqueous solutions as a function PFAS concentration. Experiments were again carried out under two different pH conditions: variable pH with the solute simply dissolved in Millipore water and pH 8.0 carbonate buffer solutions. The one exception to these sample preparations was PFOS in pH 8.0 solutions where pH was adjusted with NaOH. Conductivities for the different PFAS solutions are shown in Figure 2.3.

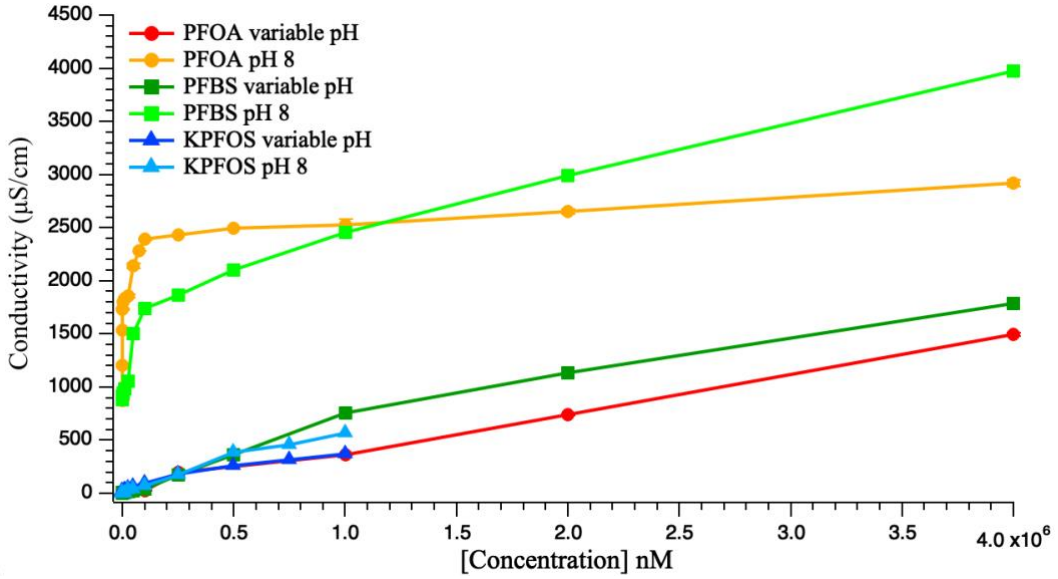



Figure 2.3. Conductivities of PFOA, PFBS, and KPFOS solutions in variable pH and pH 8.0 solutions. Concentrations range from 1 nM PFAS up to 4 mM PFAS. Note that the conductivity of the KPFOS, pH 8.0 solution is controlled by small additions of NaOH. The small amount of NaOH required raises the KPFOS pH 8.0 solution conductivity to 69.9 µS/cm in contrast to the ~1000 µS/cm conductivity for the PFOA and PFBS solutions buffered to pH = 8.0.

Like the surface pressure isotherms in Figure 2.2a, surfactant CMCs inferred from conductivity data require finding the concentration where a steeply rising line defined by low concentration limit intersects the horizontal line defined by the solution's high concentration asymptotic limit. Data in Figure 2.3 suggest that only PFOA and PFBS in the pH = 8 buffer have CMCs, based on the noticeable change in conductivity at ~0.1 mM. The other systems studied – PFOA, PFBS and PFOS with variable pH and PFOS in pH = 8 buffer – show conductivities that rise monotonically up to concentrations ≥ 4 mM. To ensure confidence in these measurements, we also performed conductivity measurements using SDS and determined a room temperature CMC for SDS of 8.3 mM, consistent with both literature and surface tension measurements performed in our own laboratory. (See Supporting Information.)

Table 2.3 summarizes the CMC values for PFOA, PFBS, and PFOS predicted by surface tension and conductivity data in Figures 3.2 and 3.3, respectively.

Table 2.3. Predicted CMCs of PFOA and PFBS from surface tension data of both pH environments and conductivity measurements. All predictions based on measurements performed at 20˚C.

| | Predicted CMC from surface pressure data | | Predicted CMC from conductivity data |
|---|---|---|---|
| | Variable pH | Controlled pH 8 | Controlled pH 8 |
| PFOA | 1.5 mM | 200 μM | 100 μM |
| PFBS | 100 μM | 10 μM | 10 μM |
| PFOS | 100 μM | 150 μM | - |

While we would expect these values to decrease with increasing ionic strength and depend on the identity of salts in solution, these experiments were beyond the scope of these studies and will be investigated further in future work. Previous studies have reported a wide range of CMC values for PFOA and for PFOS, and these findings are examined in the Discussion section below.[110-112, 119, 124-141] Considerably less is known about PFBS surface activity and bulk solution behavior.

2.3.2 Dynamic Light Scattering.

DLS measurements were performed with PFOA, PFBS, and PFOS solutions having concentrations near and above the predicted CMC concentrations for both variable pH and pH 8.0 conditions. Data show that macromolecular structures with diameters ≤10 nm form in PFAS solutions at concentrations close to the predicted PFAS CMCs. However, unlike traditional surfactants whose micelle structure remains largely unchanged as surfactant concentration increases – the surfactants simply make more micelles – structures formed from PFAS continue

to grow in size as concentration increases. In the following section, only results from the pH 8.0 studies are described in detail. When appropriate, comparisons are made with DLS measurements of PFOA, PFBS, and PFOS in the variable pH solutions. All data from DLS measurements from the variable pH solutions appear in Supporting Information.

Figure 2.4 shows DLS traces from PFOA, PFBS and PFOS solutions as a function of bulk PFAS concentration. Numerical results from these traces are reported in Table 2.4.

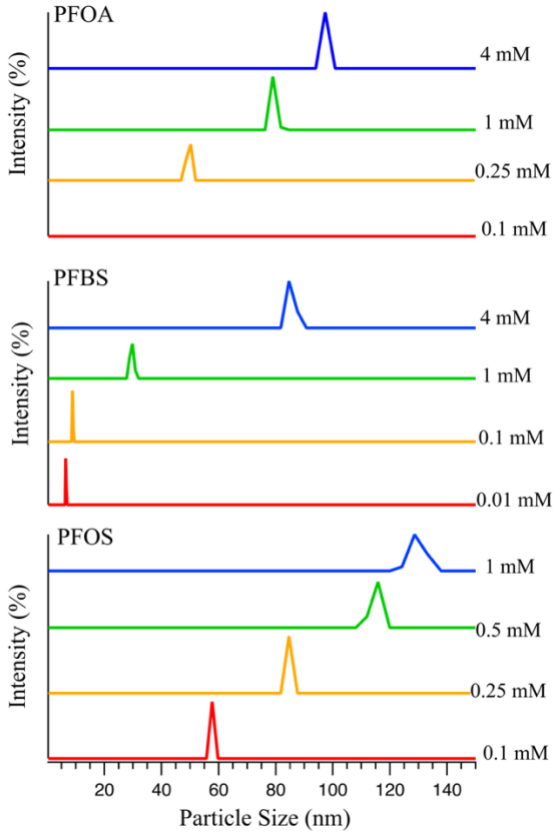



Figure 2.4. Dynamic light scattering traces from solutions of PFOA, PFBS, and KPFOS as a function of concentration in pH 8.0 solutions. Sample temperature was held constant at 20 °C.

Table 2.4. PFOA, PFBS, and KPFOS aggregate diameters and estimated number of monomers in aggregate.

| | PFOA | | PFBS | | PFOS | |
|---|---|---|---|---|---|---|
| Concentration (mM) | Diameter (nm) | # of Molecules | Diameter (nm) | # of Molecules | Diameter (nm) | # of Molecules |
| 0.01 | - | - | $5 \pm 3$ | $3 \times 10^2$ | - | - |
| 0.1 | - | - | $5 \pm 2$ | $3 \times 10^2$ | $58 \pm 5$ | $2 \times 10^5$ |
| 0.25 | $9 \pm 4$ | $1.5 \times 10^4$ | $6 \pm 3$ | $4 \times 10^2$ | $85 \pm 11$ | $6 \times 10^5$ |
| 0.5 | $50 \pm 7$ | $2 \times 10^5$ | $6 \pm 4$ | $4 \times 10^2$ | $116 \pm 8$ | $2 \times 10^6$ |
| 1 | $79 \pm 6$ | $8 \times 10^5$ | $30 \pm 11$ | $5 \times 10^4$ | $129 \pm 4$ | $2 \times 10^6$ |
| 4 | $97 \pm 11$ | $1 \times 10^6$ | $85 \pm 15$ | $1 \times 10^6$ | - | - |
| 8 | $116 \pm 9$ | $2 \times 10^6$ | $91 \pm 19$ | $1 \times 10^6$ | - | - |

Objects formed by PFAS can become very large having diameters >100 nm. Object size depends on concentration with the diameter of PFOA objects increasing by more than an order of magnitude as the concentration rises from 200 μM to 8 mM. This behavior is not typical of traditional surfactants whose micelles have well defined sizes that vary only slightly with concentration. Instead, the observations in Figure 2.4 and Table 2.4 suggest that PFOA, PFBS, and PFOS begin to self-assemble at concentrations approximately equal to CMCs inferred from surface tension and conductivity data, but self-assembly *does not terminate* in a well-defined, micellar structure. Instead, the three PFAS surfactants appear to continue aggregating, forming increasingly larger structures in solution as concentration increases. In addition to PFOA and PFBS showing this behavior, PFOS whose surface tension isotherms suggest a CMC in the ~100 μM range is forming structures with diameters ~50 nm, much larger than the micelles formed by surfactants such as SDS (3.5 nm) and sodium octanoate (2.5 nm). (See Supporting Information.).

Using the solid-state PFAS densities as a zeroth order approximation and assuming a spherical shape for the detected PFAS aggregates, we estimate the number of monomers required to create the larger aggregates having sizes corresponding to the observed objects in solution to be on the order of ~$10^5$ to $10^6$. These values are *much* larger than the estimated ~50-100 monomers that comprise micelles formed by SDS, DTAC and other common alkyl surfactants.[79] [157, 158] Not surprisingly, the number of monomers per object rise significantly (as $r^3$) as bulk solution concentrations increase. While these estimates of monomer per object have large uncertainties, they further illustrate the non-micellar behavior of PFOA, PFBS, and PFOS.

Second, the relevant concentrations where we observe the onset of self assembly are much lower than traditional surfactant CMC concentrations. The CMC for SDS at room temperature is 8.3 mM. Sodium octanoate's CMC is almost 50x higher (380 mM). In the different PFAS solutions, DLS data are showing objects forming in <u>10 – 200 μM</u> solutions, more than an order of magnitude lower than most CMCs and, as concentration increases, these objects behave less and less like micelles.

*Based on the disparities between data in Figure 4 and typical surfactant micelle behavior, we propose that PFOA, PFBS, and PFOS do not form micelles in solution but instead form aggregates lacking well defined, micellar organization.*

<u>2.3.3 Cryo-EM.</u>

We independently confirmed the formation of large structures by recording Cryo-EM images from an 8 mM PFOA solution. As a control, we also acquired Cryo-EM images from a 12 mM SDS solution. Figure 2.5a shows a wide-field image of a Cryo-EM grid. Of note is the gray patch within the white box. Expanding the field of view to focus on that specific region

(Figure 2.5b), we observe a dense collection of roughly circular objects measuring ~40 nm in diameter albeit with a broad distribution in sizes.

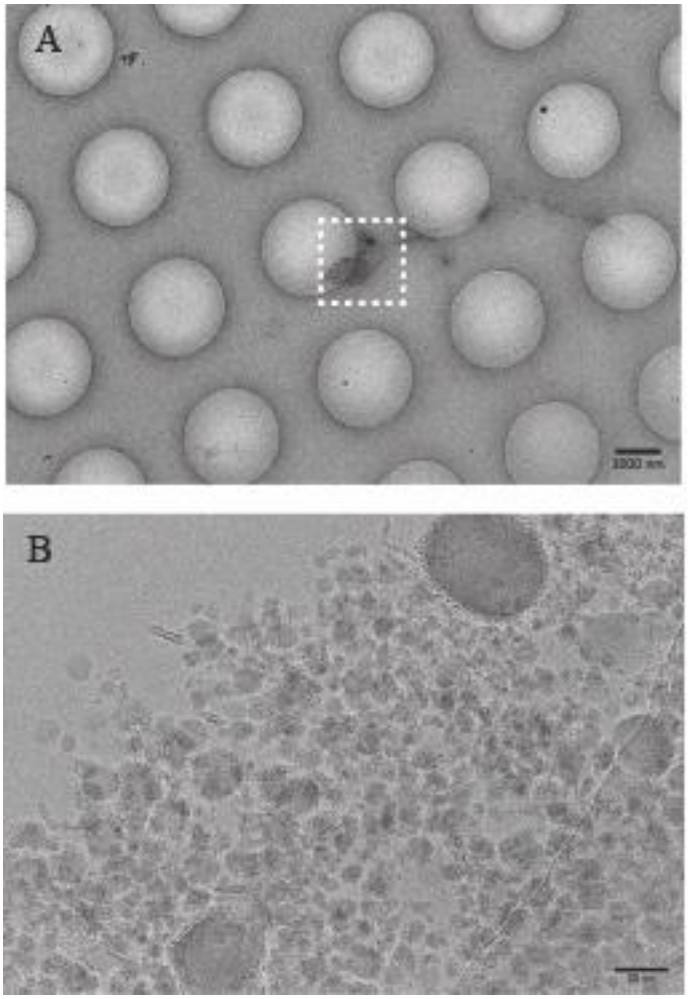



Figure 2.5. Cryo-EM images of an 8 mM PFOA sample (pH = 8.0). (A) Survey image of the entire EM grid showing the 2 μm pores. Of interest is the gray area inside of the white dashed box. Scale bar in 5A is 1 μm. (B) An expanded image of part of the area shown in the white dashed box in (A). Objects in panel (B) range in size from ~15 nm to ~110 nm in diameter. The scale bar in 5B is 50 nm.

The Cryo-EM image in 2.5b shows clearly that PFOA does not form well defined structures in solution. Sample preparation may well perturb the specific sizes and shapes of these

aggregates relative to ambient conditions as the solutions are flash frozen and blotted. The structures and sizes of the PFOA aggregates stand in stark contrast to the Cryo-EM image of SDS that shows very weakly resolved features having diameters between 4 and 9 nm. The Cryo-EM image from the SDS solution is shown in Supporting Information. While the sizes of the PFOA objects in the Cryo-EM images differ from those measured in the DLS measurements, the data show unequivocally that PFOA forms diverse structures in aqueous solutions and these structures do not resemble micelles.

Further evidence of non-micellar behavior is observed when measuring the temperature dependence of aggregates. Figure 2.6 shows DLS traces from a 1 mM, pH 8.0 PFOA solution as the temperature is raised from 10˚C to 60˚C and then cooled back to 10˚C. (Equivalent data for PFBS and PFOS in pH 8.0 solutions are shown in Supporting Information.) Data in Figure 2.6 show that PFOA aggregates shrink as solution temperature is raised. At 60˚C, PFOA aggregates have a diameter (30 nm) that is ~4-fold smaller than at 10˚C. Similar effects are observed for PFBS and PFOS. In contrast, solutions containing SDS micelles show that micelle diameter shrinks only 25% from 3.4 nm to 2.6 nm as solution temperature increases from 10˚C to 60˚C. (See Supporting Information.) Results from all temperature dependent studies of PFAS aggregate behavior are summarized in Figure 2.7 and compiled in Table 2.5.

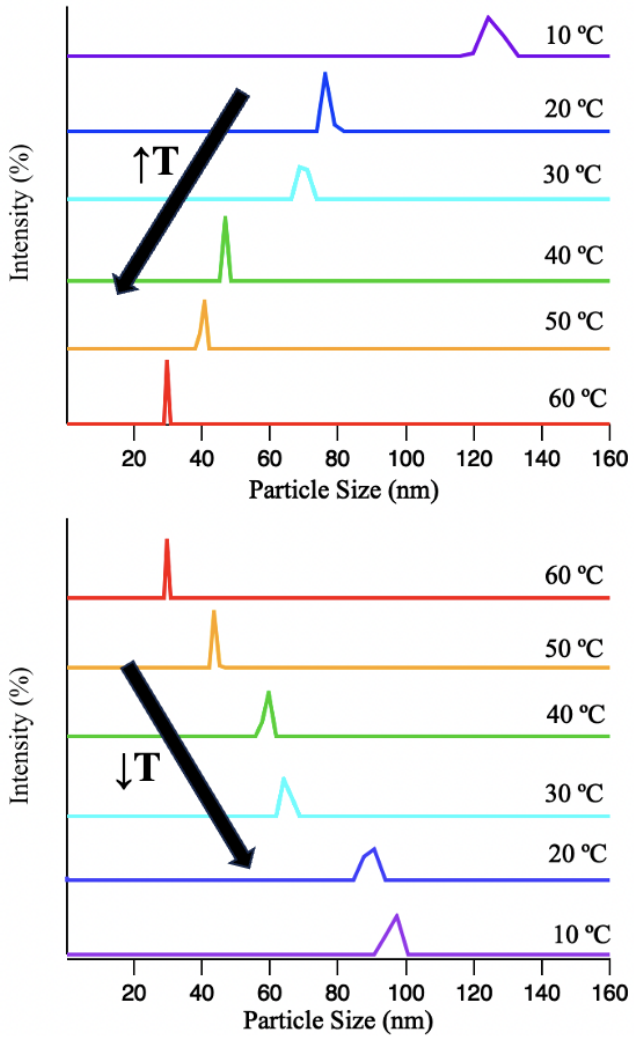



Figure 2.6. DLS traces showing the temperature dependent behavior of PFOA aggregates in a 1 mM, pH 8.0 solution. In this experiment solution temperature was raised from 10˚C to 60˚C and then cooled back to 10˚C in 10˚ increments.

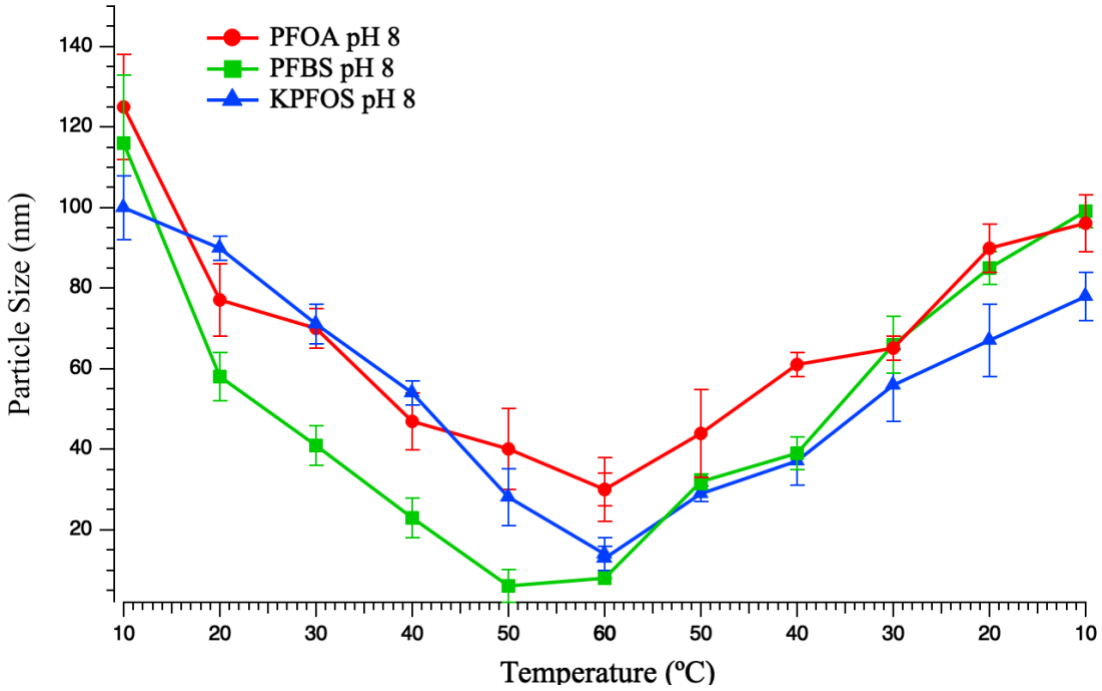



Figure 2.7. Temperature dependent aggregate diameters for PFOA, PFBS, and PFOS in 1 mM, pH 8.0 solutions. In these experiments, solution temperature was raised from 10˚C to 60˚C and then cooled back to 10˚C in 10˚ increments. Error bars represent the 1 sigma standard deviation of 9 measurements.

Table 2.5. PFOA, PFBS, and KPFOS aggregate diameter (nm) in 1 mM, pH 8.0 aqueous solution. In all experiments solution temperature was raised from 10˚C to 60˚C and then cooled back to 10˚C in 10˚ increments. Data for PFBS and PFOS equivalent that shown for PFOA in Figure 5 are included in Supporting Information.

| | | Particle Size (nm) | | |
|---|---|---|---|---|
| | Temperature (ºC) | PFOA | PFBS | KPFOS |
| Heating | 10 | 125 | 116 | 100 |
| | 20 | 77 | 58 | 90 |
| | 30 | 70 | 41 | 71 |
| | 40 | 47 | 23 | 54 |
| | 50 | 40 | 6 | 28 |
| | 60 | 30 | 8 | 14 |
| Cooling | 60 | 30 | 8 | 13 |
| | 50 | 44 | 32 | 29 |
| | 40 | 61 | 39 | 37 |
| | 30 | 65 | 66 | 56 |
| | 20 | 90 | 85 | 67 |
| | 10 | 96 | 99 | 78 |

The general temperature-dependent behaviors of all three PFAS solutes are consistent. At lower temperatures, aggregates are larger than at higher temperatures. However, unlike anionic alkyl surfactants that show reversible temperature-dependent recovery of structure, cooling PFAS solutions leads to smaller aggregates compared to starting conditions. The temperature dependent behavior shown by PFOA aggregates can be rationalized by considering PFOA's presumed increased monomer solubility at higher temperatures.[159] Higher monomer solubility at elevated temperatures necessarily shrinks aggregate size. If the particles are aggregates – as opposed to well defined micellar structures – we would not necessarily expect particle size distributions in the cooled solutions to mirror those in solutions prior to heating.

Equivalent experiments carried out for PFOA, PFBS, and PFOS in variable pH solutions showed qualitatively similar behaviors – large aggregates whose sizes depended on bulk surfactant concentration and temperature – and results are included in Supporting Information.

2.3.4 Impact and Consequences.

Understanding PFAS behavior in relevant environmental settings is critical for modeling PFAS fate and transport. PFAS have a traditional surfactant structure: a hydrophobic chain and a water soluble charged headgroup. Furthermore, methods used to infer the onset of micelle formation such as surface tension and conductivity make clear predictions for PFOA, PFBS, and PFOS CMCs. (Table 2.3). Knowing CMC values allows one to determine the concentration of monomers and micelles in solution, thereby enabling estimates of how solutes migrate through ground and surface water. Predicted PFAS CMCs are significantly lower than one expects for surfactants having 8 carbon chains (in the case of PFOA and PFOS), but this behavior might be justified by postulating that the perfluoro chain's extreme hydrophobic character will lower a surfactant's CMC relative to its related hydrogen alkyl equivalent. Table 2.6 lists literature several reports citing CMC values for PFOA, PFOS, and/or PFBS.

Table 2.6. CMC values reported for PFOA, PFOS, and PFBS using different methods.

| PFAS | Reported CMC | Method | Reference | Notes |
|---|---|---|---|---|
| PFOA | 26.5 mM | Conductivity (23°C) | Dong, D., et. Al.[112] | A |
| | 26.5 mM | Surface tension (23°C) | Kancharla, et. Al.[125] | A |
| | 0.4 mM | Adsorption/LC-MS (25°C) | Lei, et. Al.[110] | G |
| | 14 mM | Surface tension (32°C) | Sorli, et. Al.[127] | A, B |
| | 38 mM | Dye titration | Arrington and Patterson[111] | A |
| | 30 mM | Conductivity (25°C) | De Lisi, et. Al.[128] | C |
| | 36 mM | Solubility (8°C) | Nakayama and Shinoda[130] | C |
| | 27 mM | Solubility (25.6°C) | Nakayama and Shinoda[130] | D |
| | 9 mM | Solubility (20°C) | Nakayama and Shinoda[130] | E |
| PFOS | 7 mM | Surface tension (32°C) | Sorli, et. Al.[127] | B. D |
| | 9 mM | Dye titration | Kissi[131] | C |
| | 2.4 mM | QSPR modeling | Bhhatarai and Gramatica[132] | F |
| PFBS | 22 mM | Surface tension (32°C) | Sorli, et. Al.[127] | B, D |

*Notes: A: ammonium counterion; B: surfactants dissolved in DMSO and then diluted by water; C: sodium counterion; D: potassium counterion; E: hydrogen counterion; F: modeling program; G: no information on preparation of fluoroalkyl substance.

The first observation that stands out in Table 2.6 is the wide range of concentrations reported for PFOA's CMC (and, to a lesser extent, PFOS). Reported PFOA CMCs vary by more than a factor of 50 and PFOS CMCs vary by at least a factor of 3. Even allowing for variability introduced by different methods and different experiment temperatures and pH, these discrepancies are much greater than one would expect to observe for alkyl surfactants. The second observation is that the reported CMCs are higher than those deduced from data presented in Figures 2.2 and 2.3 and summarized in Table 2.3. While we cannot account for this systematic difference, we do note that many of the studies cited in Table 2.6 did not explicitly control solution pH.[111, 112, 125, 128, 130]

In cases where solution phase pH *was* controlled, Lei, *et al*.[110] reported that PFOA adsorption onto graphene oxide (GO) was significantly enhanced by doping the GO with polyethyleneimine (PEI). This enhancement was most pronounced at lower pH (pH < 5) where the PEI functional groups were almost exclusively protonated. By fitting PFOA adsorption data to different isotherm models, Lei, *et al.* concluded that the data were best described by a BET model that accommodates a combination of monolayer and multilayer adsorption leading to a PFOA CMC prediction of 0.4 mM. This result is the closest reported PFOA CMC to the sub-millimolar CMCs predicted by the pH 8.0 surface tension and conductivity measurements presented in Figures 2.2 and 2.3 and summarized in Table 2.3 above.

Sorli, et al.[127] studied PFOA, PFOS and PFBS interactions with lung surfactant using pendant drop surface tension measurements and a controlled pH = 7.0 buffered solution. Assuming that all PFAS were negatively charged, the authors attributed changes in lung surfactant function induced by the different PFAS to differences in PFAS chain length. From their data, the authors reported PFAS CMC values in the ~10-20 mM range.

Bhhatarai and Gramatica[132] carried out quantitative structure-property relationship (QSPR) analyses on a large set of compounds and emphasized the important role played by pH in controlling PFAS surfactant behavior. The authors used existing data to validate their models and predict CMC values for over 200 PFAS compounds. These authors, however, also noted the limited sample size of experimental CMC data available and called for more extensive experimental data that could be used to improve the predictive power of their QSPR models.

An important point to note in all the above reports is that the onset of micellization was inferred from some other measurement, such as surface tension or conductivity. DLS measures

particle size directly, albeit with assumptions related to object shape and diffusivity. DLS data shown in Figures 2.4-2.6 and reported in Tables 2.4 and 2.5 do not support the premise that PFOA, PFBS, and PFOS form micelles in solution. While the DLS measurements show the onset of self-assembly at concentrations approximately equal to the CMCs inferred from surface tension and conductivity data, the objects that form behave less like surfactants and more like aggregates given how the objects depend on both bulk PFAS concentration and system temperature.

We note that several recent literature reports propose that PFAS *might* form aggregates at low concentrations.[160-164] Based on results from solvated electron-driven PFAS reduction in aqueous solutions, Maza, *et al.* suggested that PFOA forms dimers and small aggregates at concentrations well below nominal reported CMCs. These authors based their claim on evidence that SDS dimerizes at concentrations below 1 mM.[160] Bhattacharjee and Kaatze noted that spherically shaped micelles form above the CMC, but proposed that some amphiphile systems are also susceptible to 'pre-CMC' micelle formation, offering a second pathway to lowering the overall free energy of the system in addition to surfactant adsorption to surfaces.[161] Hadgivanova and Diamant proposed that premicellar aggregation into metastable structures is possible below the CMC,[162] but these authors, as well as Cui, *et al.*, predict that the premicellar aggregate size should depend only weakly on concentration below CMC values.[163] Cui, *et al.* also concluded that pre-micelles (or aggregates) exist above and below a surfactant's CMC but the aggregates are smaller than micelles and will grow until they and micelles share approximately the same size. These predicted behaviors are inconsistent with the DLS data presented in Figure 2.4.

Only recently has the micelle/aggregate size distribution as a function of solute concentration been examined explicitly. Using Raman multivariate curve resolution (Raman-MCR) spectroscopy and multi-aggregation chemical potential surface modeling, Ben-Amotz and de Oliveira identified low-order aggregates forming at concentrations below the CMC for surfactants including SDS, sodium octanoate and 1,2-hexane diol. Based on the Raman-MCR data and modeling, the authors calculated aggregation numbers on the order of 40-60 and determined the fraction of unbound and aggregated monomers as a function of solute concentration. The authors noted that they did not account for temperature dependence in their analyses, but anticipated that temperature will likely be a significant factor in the size and structure of surfactant micelles.[164] One important outcome from the Ben-Amotz and de Oliveira findings is that surfactant aggregates are always *smaller* than the micelles themselves. Again, these findings are inconsistent with the DLS data reported in Figures 2.4 and 2.5 where the object size is much, much larger than any reported micelle structure formed by linear, alkyl surfactants.

## 2.4 Conclusions

With increasing attention focused on PFAS transport and fate in the environment, regulatory policy and remediation strategies must be based on accurate data describing PFAS behavior. The most important overall discovery presented in this manuscript is that three of the most common PFAS found in ground and surface water – PFOA, PFBS, and PFOS – appear to form aggregates in solution rather than traditional micellar structures that would be predicted from their surfactant structures. Surface tension and bulk solution conductivity measurements imply that these PFAS have CMCs ≤ 1mM, considerably lower than what has been reported in

previous accounts. Some of this discrepancy may be traced to a failure to control solution phase pH. Surface tension and bulk solution conductivity data, however, can only be used to *infer* CMC. DLS measurements measure micelle (or particulate) size in solution directly. DLS measurements performed with all three PFAS showed that these surfactants do, in fact, form structures in aqueous solution, but the structures are much larger than traditional micellar structures formed by surfactants such as SDS or sodium octanoate. PFAS structures observed using DLS are, for the most part, ≥50 nm in diameter, and structure size depends sensitively on bulk surfactant concentration. (PFBS structures at ≤1 mM concentrations are smaller, 6 – 30 nm in dimeter.) Supporting these results are cryo-EM images of PFOA samples that show an array of shapes and sizes in solution. These structures also depend sensitively on solution phase temperature, with structures becoming smaller as sample temperatures are raised from ambient to 70˚C. These behaviors stand in stark contrast to those of surfactants that form traditional micelles, leading us to propose that PFOA, PFBS and PFOS form unstructured aggregates in solution, although the origin for this tendency remains uncertain. Further studies exploring these behaviors as a function solution phase ionic strength as well as aggregate zeta potential promise to further clarify PFAS behavior across a wide range of environmentally relevant conditions. Taken in their entirety, results reported in this manuscript present a new paradigm for assessing the bulk solution behavior of this increasingly important class of regulated contaminants.

# CHAPTER THREE

# NANOMOLAR PFOA CONCENTRATIONS AFFECT LIPID MEMBRANE STRUCTURE: CONSEQUENCES FOR BIOCONCENTRATION MECHANISMS

## Contribution of Authors and Co-Authors

Manuscript in Chapter 3:

Author: Tess N. Sobolewski

Contributions: A coauthor with equal contributions with Rhys Trousdale. Collected and analyzed experimental data for DLS and DSC. Assisted in writing and editing manuscript.

Author: Rhys C. Trousdale

Contributions: A coauthor with equal contributions. Collected and analyzed experimental data, specifically TCSPC. Assisted in writing and editing manuscript.

Co-Author: Colin L. Gauvin

Contributions: Collected cryo-electron microscopy data.

Co-Author: C. Martin  Lawrence

Contributions: Assisted in cryo-electron microscopy data analysis.

Co-Author: Robert A. Walker

Contributions: Assisted with data analysis, writing, and editing of manuscript.

Manuscript Information

Tess N. Sobolewski, Rhys C. Trousdale, Colin L. Gauvin, C. Martin Lawrence, and Robert A. Walker

Environmental Science & Technology

Status of Manuscript:
☐ Prepared for submission to a peer-reviewed journal
☐ Officially submitted to a peer-reviewed journal
☐ Accepted by a peer-reviewed journal
☒ Published in a peer-reviewed journal

Publisher: American Chemical Society – Environmental Science & Technology
Date of Submission: April 19, 2024
Date Accepted: December 10, 2024
Volume 59, Issue 1, December 2024, 709 - 718
DOI: 10.1021/acs.est.4c03652

## 3.0 Abstract

Independent methods show that sub-microMolar concentrations of perfluorooctanoic acid (PFOA), a member of the PFAS family of 'forever chemicals', change the properties of DPPC vesicle bilayers. Specifically, calorimetry measurements show that PFOA at concentrations as low as 0.1 nM lowers DPPC's gel-liquid crystalline transition enthalpy by several J/g without changing the transition temperature ($T_{gel\text{-}LC}$), and dynamic light scattering (DLS) data illustrate that PFOA markedly broadens the size distribution of DPPC vesicles. Furthermore, DLS results from PFOA-containing, DPPC vesicle solutions also contain smaller objects having diameters of 30-50 nm. Close inspection of cryo-EM images reveals that DPPC vesicles formed in the presence of PFOA are multi-lamellar and the smaller objects have a clear bilayer structure making them resemble niosomes. A consequence of these PFOA-induced changes to DPPC bilayer structure is that the bilayers themselves are more susceptible to secondary solute accumulation. Time resolved emission measurements of Coumarin 152 (C152) report that C152 is 3-fold more likely to partition into the bilayer's acyl chain, hydrophobic interior when PFOA is present, and fluorescence lifetimes from C152 partitioned into the polar region of the lipid bilayer show evidence of PFOA-induced membrane hydration below $T_{gel\text{-}LC}$.

## 3.1 Introduction

Per- and polyfluorinated alkyl substances, or PFAS, are a class of molecules that threatens community and ecosystem health. PFAS are often called 'forever chemicals' because of their environmental persistence, and PFAS have been linked to reduced vaccine response, high cholesterol, compromised immune system function, and certain types of cancer.[20, 49, 165-167]

Despite the hazards they pose, PFAS have only recently been federally regulated as environmental contaminants under the U. S. Clean Water Act, although previously at the state level, more than 20 jurisdictions had imposed maximum allowable PFAS limits in drinking water. These local regulatory limits ranged from 5 ppt (CA) to over 650 ppt (NV).[49, 50] New federal limits released in 2024 by the U. S. Environmental Protection Agency (EPA) mandate a maximum allowable drinking water concentration of 4 ppt for several PFAS species.[49, 50, 168, 169] Such low concentrations can be challenging to quantify reliably, and the effects of these low concentrations on biological materials are not well characterized. Findings presented below show how one of the most common PFAS species – perfluorooctanoic acid (PFOA) – affects model lipid membrane properties at concentrations approaching regulatory limits. Additional experiments illustrate how sub-micromolar PFOA concentrations render model membranes more susceptible to bioconcentration of secondary solutes, with implications for how pollutant bioconcentration factors change in the presence of PFAS contaminants.

PFOA is a legacy member of the PFAS family, having long been used as an aqueous film foaming fire (AFFF) suppression agent as well a means of waterproofing products including cookware, textiles, and food packaging material.[49] While no longer produced for commercial use, PFOA is expected to remain an environmental and human health hazard for decades.[170, 171] PFOA is a per-fluorinated, linear, eight carbon carboxylic acid. Considerable uncertainty surrounds PFOA's membrane affinity. Publicly available data compiled by ADC/Labs and made available from the Royal Society of Chemistry ChemSpider site[172] report that PFOA in its protonated form has a predicted logP value on the order of 7.7, and a predicted logD value of 1.8 at a biologically relevant pH (7.4), when it is deprotonated.[61] (The logD scale considers solution

phase pH as a part of the partitioning scale.) We note that reports predicting octanol partitioning behavior (log P) should be viewed with caution. Many algorithms do not differentiate behavior between PFOA's neutral and deprotonated forms. Nevertheless, both the logP and logD scales predict that PFOA should be lipophilic regardless of charged state, although one expects PFOA's neutral protonated form should show much stronger lipophilicity than the deprotonated PFOA anion.[173] Despite early controversy concerning an anomalously large apparent $pK_a$ (of 3.8),[174-176] calculations and experiments now agree that PFOA's $pK_a$ is in the vicinity of -0.1 - +0.7[116, 176-178] although this value is expected to rise if monomers aggregate.[179-181] A consequence of this behavior is that PFOA should be exclusively in its anionic form under physiological conditions.

To our knowledge, PFOA's membrane partitioning coeffiecient, $K_{mem-w}$ has not yet been directly measured, although the logP scale has been reported as an adequate surrogate for $K_{mem}$ for solutes having log P values $\leq 5$.[182] Several studies using independent methods have examined deprotonated PFOA's membrane affinity for synthetic lipid bilayers, and results all show deprotonated PFOA to be lipophilic. Ebert, *et al.* used dialysis measurements to quantify PFAS partitioning behavior into POPC liposomes and noted that experimental results generally agreed well with predicted log $K_{mem/w}$. Specific to PFOA, the authors reported experimental and predicted partition values of $3.52 \pm 0.08$ and 3.93, respectively.[183] PFOA affinity for lipid bilayers has also been noted by Droge who measured PFOA sorption to supported lipid bilayers using liquid chromatography.[184] Fluorescence anisotropy and calorimetry measurements have noted that deprotonated PFOA partitioning into phosphatidylcholine bilayers is independent of lipid chain length.[185, 186]

With its elevated partitioning tendencies, even at a biological pH, PFOA is a strong candidate to bioconcentrate in lipid membranes, although PFOA's effects on membrane properties remain largely uncharacterized. By analogy, alkyl surfactants have long been used to solubilize lipid membranes, and surfactants have also been shown to induce structural transitions in membranes and micelles.[187] Mechanisms describing surfactant-lipid bilayer interactions begin by assuming that the surfactant partitions into the bilayer up to a membrane solubility limit. Surfactant accumulation leads to bilayer expansion, shape changes, and an increase in membrane permeability.[187-189] Typically, these effects become pronounced for surfactant concentrations $\geq$ 0.5 mM.[188, 190] Even in studies focused on low surfactant:lipid ratios, surfactant concentrations are rarely less than 100 μM. For PFOA and other PFAS species, these concentrations are close to five orders of magnitude higher than the sub-nM PFOA regulatory limits. (For reference, a the 4 ppt regulatory limit for PFOA corresponds to an aqueous concentration of ~10 pM.)

PFAS are distributed widely throughout the environment given their high solubility in ground and surface water[13, 191, 192] as well as their ability to be transported through air.[193-195] This pervasive presence, coupled with PFAS tendency to bioconcentrate in wildlife has been well documented.[196] Long chain PFAS ($C \geq 6$) accumulation has been measured in species including striped dolphins,[197] carp,[17, 198] and other members in aquatic food webs.[18, 19, 21, 175, 199, 200] Individual PFAS concentrations (including PFOA) vary widely ranging from $\leq$10 ppt (by mass) to $\geq$ 7 ppm, with higher concentrations found in organs known to be susceptible to bioaccumulation.[201] While numbers vary from study to study, a growing body of literature cites PFAS bioconcentration factors in excess of 100 and as high as 23,000.[7, 167, 170, 202, 203]

From a human health perspective, PFAS exposure has been correlated with liver disease,[204] reduced birth weights,[48] compromised immune response,[47] impaired platelet aggregation,[205] and a host of other conditions. Given PFOA's ability to bioconcentrate, lipid membranes become effective storage media, even when ambient environmental PFOA concentrations are low.[206] The effects of PFOA on membrane properties, however, remain largely unexplored especially at low PFOA concentrations. Recently reported surface pressure measurements and Brewster Angle Microscopy experiments demonstrated that PFOA and related PFAS fluidize lipid monolayers formed from both synthetic and bacterial lipid mixtures.[207] These studies, however, considered PFAS concentrations on the order of 10-100 μM, considerably higher than concentrations relevant to current regulatory limits.

Studies described in this work are motivated by the hypothesis that PFOA concentrations approaching regulatory limits will affect lipid membrane structure and function. While such an assumption is implicit in many of the reports cited above, never before have the effects of such low PFAS concentrations on biological macrostructures been evaluated quantitatively. Data presented below show that sub-μM PFOA concentrations lower DPPC bilayer transition enthalpies and preferentially promote secondary solute accumulation in the bilayer's hydrophobic interior. Furthermore, these low PFOA concentrations interfere with lipid vesicle formation and promote niosome creation at surfactant:lipid ratios that are orders of magnitude smaller than previously reported. This concerted investigation into PFOA affinity for lipid membranes and the resulting consequences demonstrate sub-μM PFOA concentrations change lipid bilayer properties, and these changes disrupt chain-chain interactions within the membrane making the lipid bilayer intrinsically less cohesive. As scientists and public health officials continue to focus on the

physiological effects of PFOA and other PFAS on human and ecosystem health, findings reported in this work will provide the insight necessary to anticipate how PFOA and other members of the PFAS family affect membrane stability and bioconcentration in the low PFAS concentration limit.

## 3.2 Experimental Materials and Methods.

### 3.2.1 Materials.

Perfluorooctanoic acid (95% purity) was purchased from Sigma Aldrich (St. Louis, MO) and used as received. For carbonate buffer solutions, sodium bicarbonate was purchased from Sigma-Aldrich (St. Louis, MO), dissolved in Millipore water, and set to a pH of 7.2 using 1 M NaOH. PFOA was dissolved in either 10- or 50-mM carbonate buffer (pH 8) to make PFOA solutions. Solutions having low PFOA concentrations were prepared by serial dilutions from 0.1 mM stock solutions. To aid in converting between concentrations expressed in Molar units and in parts per billion and parts per trillion (ppb and ppt, by mass), Table 3.1 presents conversions relevant for the concentrations used in these studies.

Table 3.1. PFOA concentrations in units of molarity and ppb/ppt (by mass)

| PFOA Concentration | |
|---|---|
| nM | ppb/ppt |
| 1000 | 400 ppb |
| 100 | 40 ppb |
| 10 | 4 ppb |
| 1 | 400 ppt |
| 0.1 | 40 ppt[a] |
| 0.01 | 4 ppt[b] |

[a]The following states had previously set jurisdictional regulatory limits ≤40 ppt PFOA in drinking water: California, Michigan, New York, New Hampshire, New Jersey, Massachusetts, Vermont, Minnesota

[b]EPA PFOA regulatory limit for drinking water.

1,2-Dipalmitoyl-*sn*-glycero-3-phosphocholine (DPPC, powder, >99%) was purchased from Avanti Polar Lipids (Birmingham, Alabama). All chemicals were used without further purification. Millipore water (resistivity of 18.2 MΩ·cm) was used for all aqueous sample preparations. Coumarin 152 (C152) was purchased from Exciton (Edmonton, Canada) and used as received. The bulk buffered C152 solution had a concentration of 6 μM.

### 3.2.2 Processing

3.2.2.1 Vesicle Preparation. Lipid vesicles were prepared by dissolving 16:0 PC (DPPC) 1,2-dipalmitoyl-sn-glycero-3-phosphocholine in chloroform. Chloroform was then evaporated off using a rotary evaporator at 45°C. A thin film results and was then rehydrated using 10mM carbonate buffer (pH = 7.2) for a pure DPPC vesicle solution. The solution was sonicated for 30 minutes at 45°C. The solution temperature was held constant as the solution was filtered ten times through an Avanti Mini Extruder from Avanti Polar Lipids with a membrane pore size of 200 nm. For most studies (DLS, Cryo-EM and TCSPC) DPPC vesicles were generated from solutions having 1.5 mM DPPC concentration; for calorimetry studies the lipid concentration was increased to 20 mM to ensure high S/N.

### 3.2.3 Methods.

3.2.3.1 Differential Scanning Calorimetry. DSC measurements were performed using a TA Instruments Discovery Q2000 DSC (Hüllhorst, Germany) that can measure transition temperatures with +/- 0.1 °C accuracy. Vesicle solutions were made of 20mM DPPC vesicles rehydrated with 10 mM carbonate buffer (pH 7.2). For DPPC vesicle solutions with PFOA, the 20mM DPPC samples were rehydrated with PFOA solutions prepared in 50mM carbonate buffer (pH 7.2). Tzero pans and hermetic lids were purchased from DSC Consumables Inc. (Austin, MN) and were used

to hold the sample as it was heated from 10 °C at a ramp rate of 1 °C/min to 55 °C to quantify the gel to liquid-crystalline transition temperature. Samples for DSC experiments were not extruded unlike the DLS and TSCPC experiments that were filtered to create a more uniform distribution of vesicle sizes (< 200 nm). DSC data are reported as the averages of five runs completed on separate days. 3.2.3.2 Dynamic Light Scattering. DLS measurements measuring DPPC vesicle size distributions were performed using a Malvern Zetasizer Pro Red from Malvern Instruments Ltd. (Worcestershire, England) which utilizes a non-invasive back scattering method at a measurement angle of 173° to measure particle sizes ranging from 0.3 nm to 10 μm. Samples are loaded into disposable polystyrene cuvettes (Malvern Instruments Ltd.) and were run in triplicate after calibrating at the desired temperature for 60 seconds. The average of each run is reported. Samples were analyzed using L-curve analysis with automatic attenuation. DLS experiments used 633 nm light for all scattering instruments.

3.2.3.3 Cryo-Electron Microscopy. Samples were plunge frozen on Quantifoil 200 mesh R2/1 Cu grids using a Vitrobot Mark IV plunge freezer set at 4° C and 95% humidity with cellulose blotting paper on both sides. Sample sizes were 4 μL, blot times were 4 seconds at blot force 5. Frozen grids were then imaged on a Talos Arctica transmission electron microscope operating at 200 kV. Images were recorded with a Gatan K3 camera using SerialEM at magnification of 44,700x and defocus value of -3.0 μm. Exposure times were 5 sec at approximately 15 electrons per pixel per second. Magnified pixel size was 1.104 e-/Å$^2$ and total dose was 45 e-/Å$^2$.

3.2.3.4 Time-Correlated Single Photon Counting. TCSPC is used to determine a solute's excited state lifetimes in the sample. The TCSPC assembly used in these experiments has been described previously.[208-210] Briefly, the assembly consists of a Ti:sapphire oscillator (Coherent Chameleon, 80 MHz, 85 fs pulse length) with a fundamental output range of 690-1040 nm. Doubling and tripling harmonic assemblies enable output ranges of 345-520 nm and 230-346 nm respectively. A modulator (Conoptics Model 350-10) is used to reduce the repetition rate of the laser to 4 MHz before entering the sample chamber. Samples are excited using vertically polarized light, and fluorescence emission is collected at the magic angle (57°). To reduce background scattering from the sample, a long pass filter is used between the sample and the monochromator. Picoquant PicoHarp 300 and FluoTime 200 packages are used for data acquisition and analysis. The time-resolved emission data are fit to a linear combination of lifetime decays alongside the relative amplitudes. By correlating solute lifetimes measured in vesicle containing solutions with solute lifetimes in different bulk solvents, we can approximate a solute's local solvation environment and quantify where within a lipid bilayer the solutes have accumulated. TCSPC has been used in our group previously to quantify how solute partitioning depends on temperature and, more importantly, determine *where* in a membrane the solutes accumulate.[55, 56, 67, 211]

For Coumarin 152 fluorescence lifetimes measurements, the samples were excited at 400 nm and emission was collected at 500 nm. A 455 nm long pass filter was used before the PMT to limit noise from scattering. Temperature dependent studies were performed using a Quantum Northwest TC125 temperature control sample chamber. Samples were held at temperature for 7 minutes before performing each scan to allow for equilibration.

## 3.3 Results

### 3.3.1 Differential Scanning Calorimetry.

Surfactants have long been used to solubilize lipid membranes and isolate membrane proteins.[212, 213] Membrane solubilization requires that the lipid bilayer become saturated by the surfactant before the membrane/surfactant system begins to form micelles having mixed composition. Typically, this transformation occurs when surfactant:lipid molar ratios approach unity.[213-215] At lower surfactant concentrations (surfactant:lipid ratios $\leq 0.1$), surfactants will partition into the membrane and increase membrane permeability. All these phenomena reduce lipid-lipid interactions resulting in a more fluid bilayer structure.[190, 216] Figure 3.1 shows DSC results from DPPC vesicle solutions having different PFOA concentrations. In the absence of PFOA, the DSC trace is characterized by a sharp endothermic feature at 40.5˚C corresponding to the DPPC bilayer's gel to liquid crystalline transition. As PFOA is added to solution, the transition temperature does not change, but the amount of heat required for this melting transition diminishes.

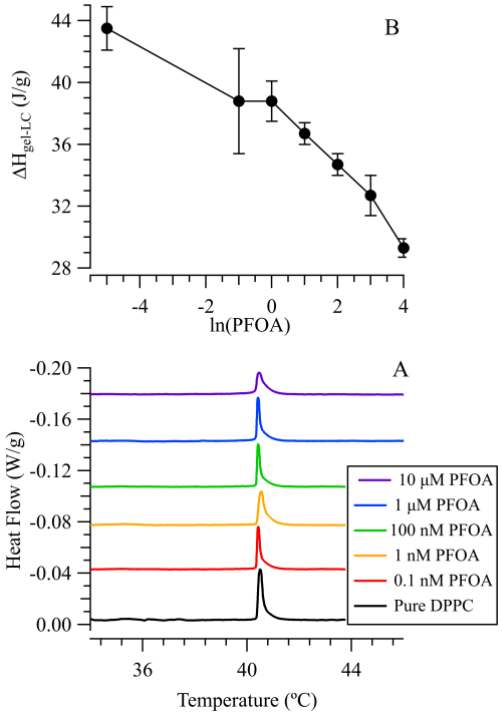



Figure 3.1. (A) Differential scanning calorimetry isotherms of pure DPPC and DPPC with increasing [PFOA] ranging from 0.1 nM to 10 μM. Isotherms have been offset vertically for clarity. (B) Average enthalpies of the gel-liquid crystalline transition as a function of [PFOA]. The inset shows an expanded view of ΔH for [PFOA] ≤ 100 nM. At a concentration of 10 μM, the peak shows noticeable broadening. Note that the calculated enthalpy for pure DPPC vesicles is assigned an arbitrarily low PFOA concentration of $10^{-5}$ nM to place it on scale.

Integrating the peak area results in a calculated gel-liquid crystalline transition enthalpy, $\Delta H_{gel-LC}$. (Figure 3.1b) The 44 ± 1 J/g transition enthalpy measured for pure DPPC vesicles is consistent with values reported in the literature.[70, 73, 74] As expected, higher PFOA concentrations (≥ 1 μm) lower the transition enthalpy. (Figure 3.1 and Table 3.2) Surprisingly, nM and even sub-nM PFOA concentrations also lower DPPC bilayer transition enthalpies. Neither the transition temperature nor the width of the endotherm changes significantly for PFOA concentrations ≤ 1 μM. The diminished enthalpy coupled with a sharp and invariant $T_{gel-LC}$

implies that PFOA penetrates the bilayer and reduces the extent but not the nature of lipid-lipid interactions.

Table 3.2. Average enthalpies of DPPC in the PFOA containing solutions. $T_{gel\text{-}LC}$ = 40.4-40.5 ˚C for all PFOA concentrations. ΔT (FWHM) = 0.2˚C. $\Delta H_{gel\text{-}LC}$ values are the averages of ≥ 9 measurements and uncertainties are reported to one standard deviation.

| [PFOA] nM | $\Delta H_{gel\text{-}LC}$ (J/g) |
|---|---|
| 0 | 44 ± 1 |
| 0.1 | 39 ± 3 |
| 1 | 39 ± 1 |
| 10 | 37 ± 1 |
| 100 | 35 ± 1 |
| 1000 | 33 ± 1 |
| 10000 | 29 ± 1 |

We note that the constant lipid gel-liquid-crystalline transition temperature coupled with decreasing transition enthalpy is relatively common in solutions containing low concentrations (≤ 1μM) of simple surfactants such as SDS or octanoic acid.[217] Lung surfactant proteins have been known to modestly increase DPPC's $T_{gel\text{-}LC}$ by up to 2˚C, an effect assigned to enhanced interactions between the negatively charged DPPC phosphate and positively charged residues within the proteins.[218] In contrast, Maiti *et al.* studied the effects of cationic gemini lipids on DPPC bilayer stability and discovered that these surfactants *lowered* $T_{gel\text{-}LC}$ implying that these linked, charged, lipids (present at a 5-10 mole% concentration) *disrupted* DPPC monomer-monomer interactions destabilizing bilayer structure.[219] Even PFOA has been reported to lower DPPC's $T_{gel\text{-}LC}$ by 1˚C but not until PFOA concentrations reaches ~200 μM.[186] From these and other reports, we conclude that while the low PFOA concentrations are sufficient to lessen the

heat required to melt the lipid bilayer, the intermolecular forces between DPPC monomers remain unchanged within detection limits.

3.3.2 Dynamic Light Scattering

As described in the Methods section, DPPC vesicle solutions were prepared by extrusion above $T_{gel\text{-}LC}$. DLS measurements from samples created in the absence of PFOA show a narrow distribution of vesicles with a diameter centered at 115 nm and a 6 nm FWHM. (Figure 3.2) Creating DPPC vesicles in solutions containing PFOA changes the distribution in several ways. First, while the distribution center does not change systematically with PFOA concentration, the distribution does become much broader. (Table 3.3) Second, addition of PFOA creates to a second population of smaller bodies in solution having diameters between 35 and 40 nm. (Figure 3.2, Table 3.3)

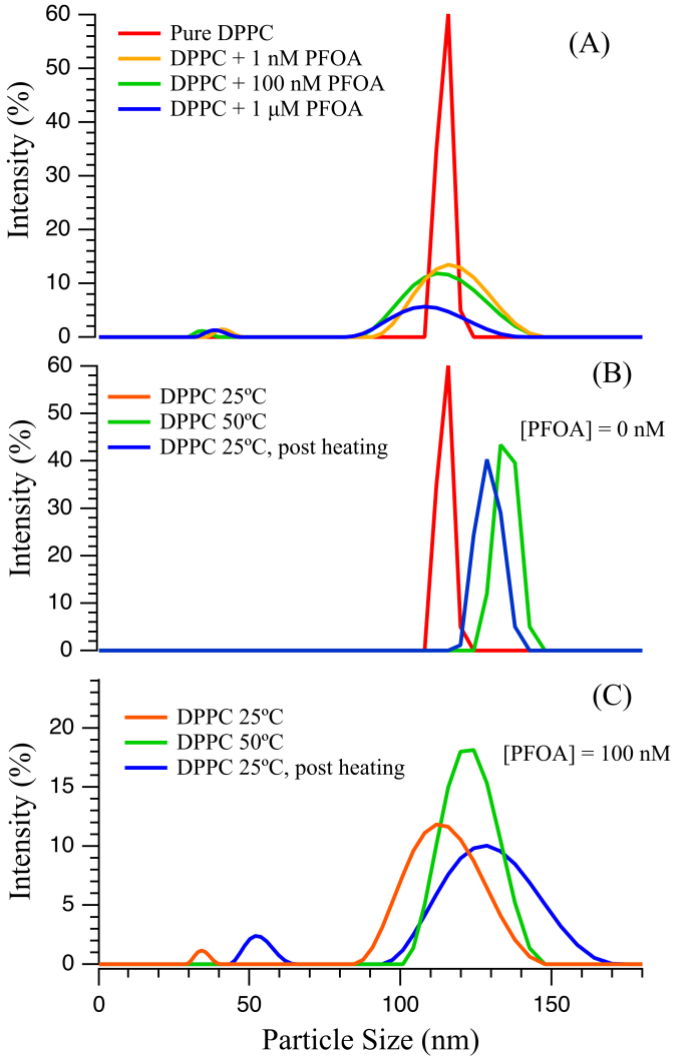



Figure 3.2. (top) Dynamic light scattering from DPPC vesicle solutions containing 0 nM, 1 nM, 100 nM, and 1 µM PFOA. (middle) DPPC vesicle size as a function of temperature in the absence of PFOA. (bottom) DPPC/PFOA solutions at 25˚C, heated to 50˚C, and then returned to 25˚C.

Heating the pure DPPC vesicle solutions above $T_{gel\text{-}LC}$ increases vesicle size by ~15%. The process is not reversible as cooling the sample results in a broader distribution having a larger average diameter than the original sample. (Figure 3.2b, Table 3.3). This result is consistent with literature reports and has been attributed to thermally induced deformation of the

bilayer and a changing bilayer compression modulus.[220] Interestingly, heating the DPPC vesicle/PFOA solutions show the same increase in vesicle size, but the smaller 35 nm objects disappear from the DLS traces, only to reappear when the solution is returned to temperatures below $T_{gel\text{-}LC}$.

Table 3.3. DPPC vesicle diameters (d) from the top panel of Figure 2 and size distributions (Δ) at room temperature. Uncertainties in diameter (d) are ±4 nm and in FWHM (Δ) are ±8 nm except for the pure DPPC vesicle solutions where uncertainties in $d_2$ and $\Delta_2$ are ±2 and ±4 nm, respectively. Uncertainties reflect one standard deviation calculated from 9 measurements.

| [PFOA] (nM) | $d_1$ (nm) | $\Delta_1$ (nm) | $d_2$ (nm) | $\Delta_2$ (nm) |
|---|---|---|---|---|
| 0 | — | — | 115 | 6 |
| 1.0 | 40 | 7 | 116 | 28 |
| 100 | 35 | 5 | 112 | 32 |
| 1000 | 38 | 8 | 108 | 31 |

We note that the smaller objects are >10-fold larger than traditional micelle structures. For reference, sodium dodecyl sulfate and sodium octanoate solutions above their CMCs form micelles having diameters of 2.7 nm and 2.1 nm, respectively. Furthermore, the CMC for these surfactants (8.3mM for SDS and 347 mM for sodium octanoate) are much higher than the PFOA concentrations used in the current studies. The following section presents cryo-EM images that show the smaller objects observed in the DLS traces have distinct, bilayer structures with an aqueous buffer interior, suggesting that they are neither micelles nor disordered aggregates. Instead, the smaller structures share many features in common with niosomes, small bilayer objects composed of nonionic surfactants and other amphiphilic constituents including cholesterol.[221] Niosomes have attracted considerable interest as drug delivery vehicles (Table 3.4).[222, 223]

Table 3.4. Temperature dependent changes of DPPC vesicles in the absence of PFOA and in 100 nM PFOA solutions, $d_2$ and $\Delta_2$ refer to vesicle sizes. $d_1$ and $\Delta_1$ refer to the niosome-like structures induced by PFOA.

| | Temperature (°C) | $d_1$ (nm) | $\Delta_1$ (nm) | $d_2$ (nm) | $\Delta_2$ (nm) |
|---|---|---|---|---|---|
| Pure DPPC | 25 | - | - | 115 | 6 |
| | 50 | - | - | 133 | 12 |
| | 25, post heat | - | - | 129 | 11 |
| DPPC + 100 nM PFOA | 25 | 35 | 5 | 112 | 32 |
| | 50 | - | - | 124 | 25 |
| | 25, post heat | 52 | 9 | 127 | 38 |

3.3.3 Cryo-EM

Figure 3.3 shows representative cryo-EM images of DPPC vesicles created from PFOA-free solutions and solutions containing 100 nM PFOA. Additional images are included in Supporting Information. Figure 3.3a (pure DPPC, no PFOA) shows a representative single unilamellar vesicle having a 121 nm diameter. Across 8 separate images, the average vesicle diameter measured 117 ± 20 nm, consistent with the DLS measurements reported in Figure 3.3 and Table 3.4. Careful measurements of bilayer dimensions results in an average thickness of 7.3 ± 0.4 nm. Experimental and MD simulations report DPPC vesicles with bilayer thickness ranging from 6.7 – 7.7 nm.[224, 225]

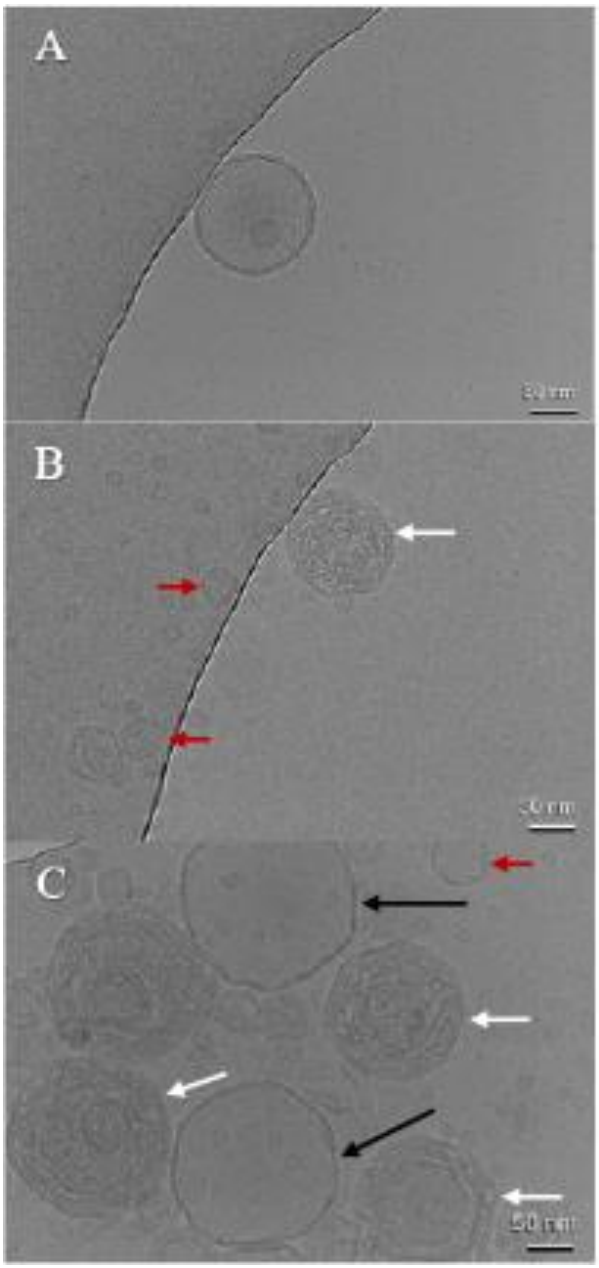



Figure 3.3. Representative cryo-EM images of DPPC vesicles prepared in a 10 mM carbonate buffer solution. A) DPPC vesicle prepared in the absence of PFOA. B and C both show images of DPPC vesicles prepared in the presence of 100 nM PFOA. Representative niosomes are indicated with the short red arrows. Medium white arrows show multilamellar structures in vesicles formed in PFOA solutions. The long black arrows show faceted vesicles.

PFOA-induced structural changes in the lipid bilayer are self-evident in Figures 3.3b and 3.3c. First, the vesicles in the PFOA solution are less round and appear faceted. This phenomenon is ascribed to curvature strain caused by PFOA being integrated into the bilayer during vesicle preparation.[190] Bilayer strain will cause the membranes to become thinner and more flexible due to the bilayer being unable to accommodate for the difference in sizes of the DPPC and PFOA polar head groups and non-polar tails. Membrane thickness was again measured. Results showed that vesicles created in 100 nM PFOA solutions had an average size slightly larger than pure DPPC vesicles (124 nm vs. 117 nm) and with a broader size distribution (±36 nm vs. ±20 nm). Again, these observations are qualitatively consistent with results from DLS measurements reported in Figure 3.2 and Table 3.3. In addition, vesicles containing PFOA had more narrow bilayers (6.2 ± 0.5 nm).

Vesicles created in the presence of PFOA frequently contained dense, nested multi-lamellar structures. We note that in instances where multilamellar structures, the images do not allow us to assess *a priori* if the different objects are nested or simply show a 2-dimensional projection of objects separated in three dimensions. We expect that conformal, multilamellar structures are nested but proof of this assertion will require 3-dimensional, tomographic imaging of structures such as those shown in Figure 3.3. The mechanism responsible for creating these complex structures remains unknown but the interior lamellae having smaller radii are consistent with the notion of bilayer strain described above.

Another effect of PFOA on vesicle formation is the appearance of objects having smaller diameters but retaining a bilayer structure. The appearance of smaller structures is consistent with niosome formation. Niosomes are vesicle-like structures typically generated from nonionic

surfactants and cholesterol for drug delivery purposes.[221] A surprising observation in the results presented here is that while most niosomes are made with ratios of 1:1 surfactant: cholesterol, the DPPC/PFOA solutions used to create the cryo-EM images shown in Figure 3.3 have a DPPC:PFOA ratio of 15,000:1. These findings emphasize PFOA's distinctive properties that fall outside of what one expects for traditional (non-fluorinated) surfactants.[181] Again, when the niosome-like structures are superimposed on larger vesicles, we cannot determine if the niosomes are inside of or external to the larger vesicles, but we expect that the niosomes are outside of the uni- and mutilamellar structures. Overall, sub-nM PFOA concentrations have several effects on DPPC liposomes: i) PFOA induces a more heterogeneous distribution of liposomes including many having multilamellar structures, ii) vesicles formed when PFOA is present appear less faceted, and iii) PFOA enables the creation of bilayer structures resembling niosomes that have diameters ~3-4 times smaller than the uni- or multilamellar DPPC vesicles.

### 3.3.4 PFOA Effects on Secondary Solute Partitioning

Results from DSC, DLS, and cryo-EM measurements shown in Figures 3.1-3.3 illustrate that sub-μM PFOA concentrations affect DPPC bilayer structure and properties. From these data we have inferred that PFOA disrupts domain formation within the lipid bilayer's gel phase and creates smaller structures adjacent to the vesicles. We expect these changes to impact lipid membrane function including the ability of membranes to accommodate secondary solutes from bulk solution. Such secondary solute partitioning is foundational to bioconcentration mechanisms.[226-229]

To understand the effects of PFOA on secondary solute partitioning into DPPC bilayers, we measured the time resolved fluorescence emission from a coumarin dye, Coumarin 152

(C152), in solutions containing DPPC vesicles as well as solutions containing both DPPC vesicles and 100 nM PFOA. C152 is a useful probe of membrane partitioning given that its time resolved emission is largely single exponential and lifetimes depend on solvent polarity and proticity. Previous studies have shown that C152 (LogP =2.7) is particularly sensitive to changes in solvation environment in lipid vesicle solutions and that C152 emission can serve as a sensitive measure of lipid membrane hydration.[56]

Figure 3.4 shows the time resolved emission from C152 in a DPPC vesicle solution containing 100 nM PFOA as a function of temperature. The decay traces are multi-exponential, and a minimum of three lifetimes are required to fit the time resolved data. The lifetimes include a sub-ns contribution that coincides with C152 in bulk aqueous buffer. The other two lifetimes are 1.5 ns and 4.5 ns at 10˚C. Both lifetimes are sensitive to temperature, falling to 0.7 ns and 3.9 ns, respectively at 70˚C. Previous studies have assigned these short, intermediate, and long C152 lifetimes to C152 solvated in aqueous buffer, C152 that has partitioned into the lipid bilayer's polar, glycerol backbone region, and C152 solvated in the lipid bilayer's hydrophobic core, respectively.[56, 230, 231]

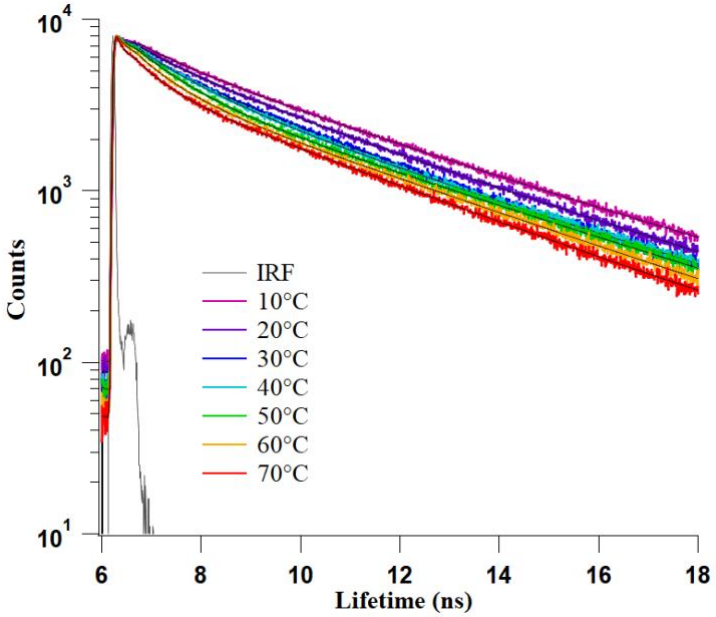



Figure 3.4. TCSPC traces of DPPC vesicle solutions containing 6 μM C152 and 100 nM PFOA as a function of temperature. The multiexponential decay visibly changes with temperature. Data are fit to three independent lifetimes as described.

Figures 3.5 and 3.6 show how the lifetimes and the corresponding amplitudes change with temperature. Also included on these figures (as dashed lines) are C152 lifetimes and amplitudes in DPPC vesicle solutions with no PFOA present. Several observations stand out. First, C152's intermediate lifetime ($\tau_2$) at low temperatures (10˚C) in the DPPC-PFOA solutions lies between a polar aprotic limit (2.4 ns in acetonitrile) and a polar protic limit (1.1 ns in methanol). We interpret this result as evidence that PFOA disrupts lipid packing, enabling water to penetrate the bilayer and promote protic solvation within the bilayer below $T_{gel\text{-}LC}$. Above $T_{gel\text{-}LC}$, $\tau_2$ converges the polar protic limit indicating complete bilayer hydration in the polar backbone region.[56, 230, 231]

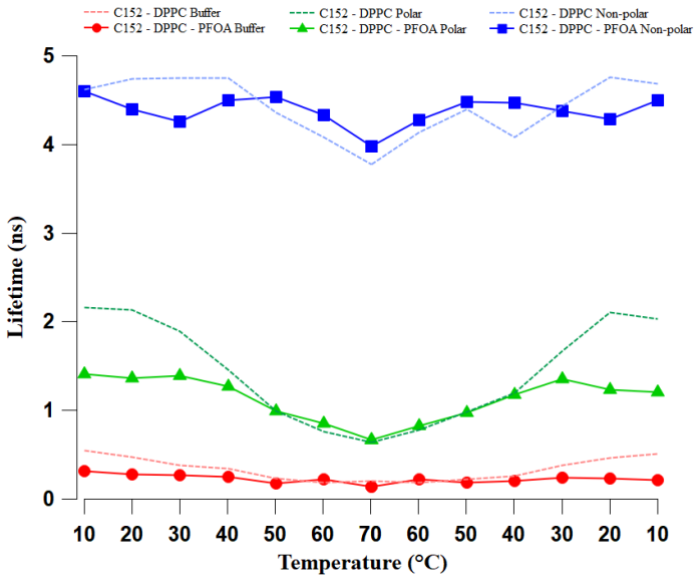



Figure 3.5. A plot of the 3 lifetimes of C152 as a function of temperature from 10-70-10 ˚C. The dotted lines show the lifetime behavior of C152 in a solution of DPPC vesicles without PFOA. The solid lines show lifetimes of C152 in a solution of DPPC vesicles and 100 nM PFOA. The 2$^{nd}$ lifetime of C152 shows the largest change in lifetime when PFOA is present, an effect attributed to PFOA-enabled hydration of the bilayer below $T_{gel\text{-}LC}$.

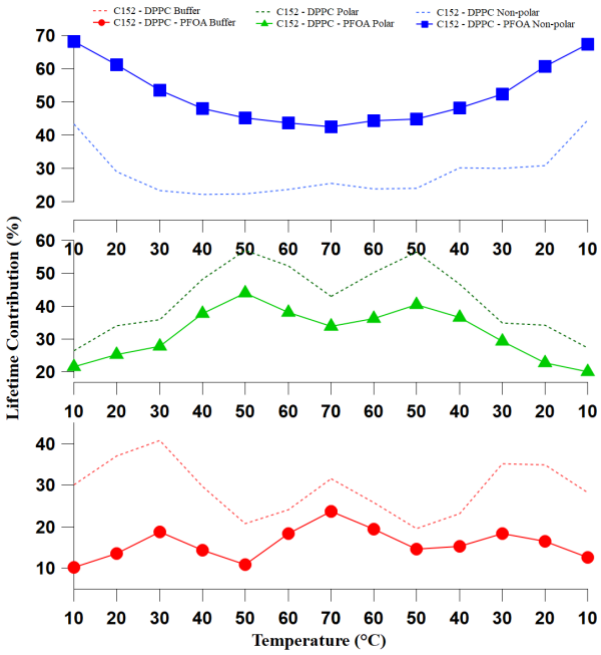



Figure 3.6. A plot of the relative amplitudes of each C152 fluorescence lifetime as a function of temperature. The dotted lines show amplitudes for C152 in pure DPPC vesicle solutions and the symbols show lifetime amplitudes for C152 in DPPC vesicle/100 nM PFOA solutions.

The second observation is that the amount of C152 in the hydrophobic part of the membrane ($A_3$) is 67% higher in the PFOA containing solution ($A_3 = 0.70$) relative to the PFOA-free solution ($A_3 = 0.42$). This increased partitioning into the hydrophobic region of the bilayer comes at the expense of C152 in aqueous solution ($A_1 = 0.1$ with PFOA; $A_1 = 0.3$ without PFOA). This result is also consistent with PFOA disrupting lipid-lipid interactions within the bilayer and making the nonpolar region more accessible to the hydrophobic C152. We note that PFOA enhances C152 accumulation in the membrane's hydrophobic region regardless of bilayer state. The amplitude of the hydrophobic population remains approximately 2-fold greater when PFOA is present in both the DPPC gel and liquid crystalline states.

Table 3.5. Lifetimes and amplitudes data from fitting TCSPC decay traces of C152 in DPPC vesicle solutions at 10, 50 and 70°C. Shown are results from both PFOA-free and 100 nM PFOA solutions. Lifetimes are reported in nanoseconds and the amplitudes are normalized. Lifetime precision is ± 0.1 ns; amplitude precision is ± 0.05.

| Temperature | Sample | $\tau_1$ ($A_1$) | $\tau_2$ ($A_2$) | $\tau_3$ ($A_3$) |
|---|---|---|---|---|
| 10°C | Pure DPPC | 0.55 (0.30) | 2.16 (0.27) | 4.62 (0.43) |
| | DPPC PFOA | 0.32 (0.10) | 1.41 (0.22) | 4.6 (0.68) |
| 50°C | Pure DPPC | 0.23 (0.21) | 0.99 (0.57) | 4.36 (0.22) |
| | DPPC PFOA | 0.18 (0.11) | 0.99 (0.44) | 4.54 (0.45) |
| 70°C | Pure DPPC | 0.2 (0.32) | 0.64 (0.43) | 3.78 (0.25) |
| | DPPC PFOA | 0.14 (0.24) | 0.67 (0.34) | 3.98 (0.42) |

The temperature dependent lifetime and amplitude data in Figures 2.5 and 2.6 show that C152 partitioning is reversible with temperature. Furthermore, the data show a similar functional dependence with changing temperature with and without PFOA present. This behavior again suggests that PFOA in the bilayer disrupts chain-chain interactions enabling C152 to access the bilayer's hydrophobic interior more easily. Additional studies examined changes in C152 partitioning behavior at lower PFOA concentrations to discover if similar behaviors were observed. Equivalent experiments indicate that 1 nM PFOA concentrations did enhance lipid membrane hydration below $T_{gel\text{-}LC}$ relative to PFOA-free samples, although the fraction of C152 that partitioned into the membrane did not change measurably. Taken together, the DSC, DLS, Cryo-EM, and TCSPC data support a mechanism whereby PFOA partitions into biomembranes and fluidizes the membrane hydrophobic interior, enabling access to secondary solutes and lowering collective cohesion within the bilayer. While most studies examining PFOA-lipid

interactions have focused on PFOA concentrations of 100 μM and higher, results presented in this work show that even at the extremely low concentrations currently being considered by regulatory agencies, PFOA effects on lipid membrane structure are profound.

# CHAPTER FOUR

## PFOA COOPERATIVE ADSORPTION TO DPPC MONOLAYERS AND ORDERING OF INTERFACIAL WATER

### Contribution of Authors and Co-Authors

Manuscript in Chapter 4:

Author: Tess N. Sobolewski

Contributions: Collected and analyzed experimental data. Assisted in writing and editing manuscript.

Co-Author: Robert A. Walker

Contributions: Assisted with data analysis, writing, and editing of manuscript.

Manuscript Information

Tess N. Sobolewski and Robert A. Walker

Journal of Physical Chemistry B

Status of Manuscript:
☐Prepared for submission to a peer-reviewed journal
☒ Officially submitted to a peer-reviewed journal
☐ Accepted by a peer-reviewed journal
☐ Published in a peer-reviewed journal

Date of Submission: April 8, 2025

## 4.0 Abstract

Vibrational sum frequency generation (VSFG) and Langmuir trough surface pressure measurements were used to investigate how the soluble surfactant perfluorooctanoic acid (PFOA) affects dipalmitoyl-phosphatidylcholine (DPPC) monolayers adsorbed to the air-water interface. Studies were performed as a function of PFOA concentration for DPPC surface coverages of 40 $Å^2$/monomer and 55 $Å^2$/monomer corresponding to tightly packed and moderately packed monolayers, respectively. VSFG data showed that PFOA does not affect the structure of tightly packed DPPC monolayers, but cooperative adsorption of PFOA to moderately packed DPPC monolayers forces lipid compression creating highly ordered acyl chains. PFOA adsorption to moderately packed DPPC monolayers also creates a charged interface evidenced by significant intensity growth in the -OH stretching region as interfacial water is oriented by the resulting electric double layer. Interestingly, this effect is also observed for the tightly packed DPPC monolayers implying that the surfactant adsorbs to the solvated lipid headgroups without affecting lipid chain conformation. PFOA-DPPC interactions at *all* DPPC surface coverages are apparent in Langmuir isotherms where PFOA concentrations as low as 10 μM induce DPPC monolayer liftoff at 130 $Å^2$/monomer rather than ~90 $Å^2$/monomer observed in the absence of PFOA and a monolayer collapse pressure that is ~6 mN/m lower than that for a pure DPPC monolayer.

## 4.1 Introduction

Perfluorooctanoic acid (PFOA) is a synthetic material mass produced for decades for consumer products. PFOA falls into the PFAS (per and poly-fluorinated alkyl substances) family and these ‘forever chemicals’ have been tied to a host of health threats including different

cancers, reduced vaccine response, liver damage, hormone disruption, and developmental issues.[25, 26, 35, 37, 166, 232] Although most PFAS are nonvolatile and airborne exposure is not considered a threat to the general public, those who live near or work in facilities that incinerate PFAS and PFAS-containing products can be exposed to high concentrations of these toxins through inhalation. PFAS have been recorded in outdoor air near manufacturing plants at concentrations ranging from 1 $pg/m^3$ [233] to 2000 $pg/m^3$.[234] The EPA has established air quality standards under the Clean Air Act for six common pollutants, including particulate matter, with levels ranging from 9 to 150 $\mu g/m^3$.[235] While these standards are significantly higher than typical levels observed for PFAS, the EPA still advises individuals to minimize exposure to air contaminants. PFAS can travel through the air as vapors or as fine particles stuck to other particulate matter.

The release of PFAS into the air near industrial plants is thought to occur both during thermal treatments (such as incineration or chemical manufacturing)[236, 237] and through the use of PFAS-containing fire foams.[87] In thermal treatments, high temperatures can cause PFAS compounds to volatilize, releasing them into the atmosphere. Additionally, PFAS-containing fire foams, which are commonly used in firefighting and training exercises, can also contribute to airborne PFAS contamination when they are applied or disposed of improperly. PFAS have also been used as mist suppressants added to metal plating and finishing baths to prevent air emissions of toxic metal fumes. Half of the chromium electroplating facilities in the United States are thought to use PFAS mists and fume suppressants.[238] Finally, PFAS can also be released into the air from landfills[239] and from heating nonstick cookware.[15]

A previous study showed that wearing PFAS-treated masks during the COVID-19 pandemic may have increased human dermal absorption, inhalation of gaseous PFAS, and ingestion of PFAS particulates.[240] Other studies have examined the risks of PFAS inhalation in households, occupational exposure, and environmental exposure. Sorli, et. al. notes PFAS may increase the risk of acute lung toxicity and cause airway infections.[127] Jabeen, et. al. have correlated PFAS exposure with lung carcinogenesis in patients with pre-existing lung conditions.[241] Despite evidence supporting adverse health effects of PFAS in general and PFOA in particular on pulmonary health, mechanisms describing *how* PFAS affect pulmonary function are lacking. In particular, understanding how PFAS affect pulmonary surfactant properties remains an important knowledge gap.

The alveolar lining of lungs consists of an air-water interface coated by a surfactant mixture comprised primarily of lipids, with smaller contributions from cholesterol and proteins.[242] 1,2-Dipalmitoyl-sn- glycero-3-phosphocholine (DPPC) is a major component of pulmonary lung surfactant and serves as the alveolar lining's last line of defense against environmental toxins and irritants.[243, 244] DPPC reduces the surface tension at the alveoli air-water interface and helps maintain alveolar volume during respiration.[245] These circumstances have led researchers to consider DPPC monolayers adsorbed to the air-water interface as surrogates to study lung surfactant surface behavior.[64, 246, 247] When soluble surfactants adsorb to the air-water surface in the presence of a DPPC film, surfactants can cooperatively adsorb to the surface generating a significant surface charge and creating an electrostatic field across the interfacial double-layer.[248, 249] These interactions affect monolayer properties including compressibility and phase behavior.

Work described below uses both surface specific vibrational spectroscopy and surface tension measurements in a Langmuir trough to examine the effects of PFOA on moderately packed 55 $Å^2$/molecule and tightly packed 40 $Å^2$/molecule DPPC monolayers adsorbed to the air-water interface. While PFOA did not affect lipid structure in tightly packed DPPC monolayers, changes in -CH stretching vibrational band intensities demonstrated that PFOA did force acyl chains in moderately packed DPPC monolayers to adopt highly ordered conformations with the chains aligned predominantly along the surface normal. Interestingly, vibrational intensity in the -OH stretching region suggests that PFOA adsorbs to both moderately packed *and* tightly packed monolayers to form an electric double layer. From these findings, we infer that PFOA adsorption to the lipid covered water-air interface is driven as much by headgroup-headgroup interactions as by the need to solubilize PFOA's hydrophobic tails. Further supporting these discoveries are findings from Langmuir Trough experiments where low PFOA concentrations induce measurable change DPPC's 2-dimensional phase behavior and isothermal compressibility.

## 4.2 Experimental Materials and Methods

### 4.2.1 Materials and Sample Preparation

Perfluorooctanoic acid (95% purity) was purchased from Sigma Aldrich (St. Louis, MO) and used as received. 1,2-Dipalmitoyl-sn- glycero-3-phosphocholine was purchased from Avanti Polar Lipids Inc. (powder, >99% purity, Alabaster, AL). Chloroform (99.8% purity) was purchased from Sigma Aldrich. All chemicals were used without further purification. Millipore water (resistivity of 18.2 MΩ·cm) was used for all aqueous sample preparations.

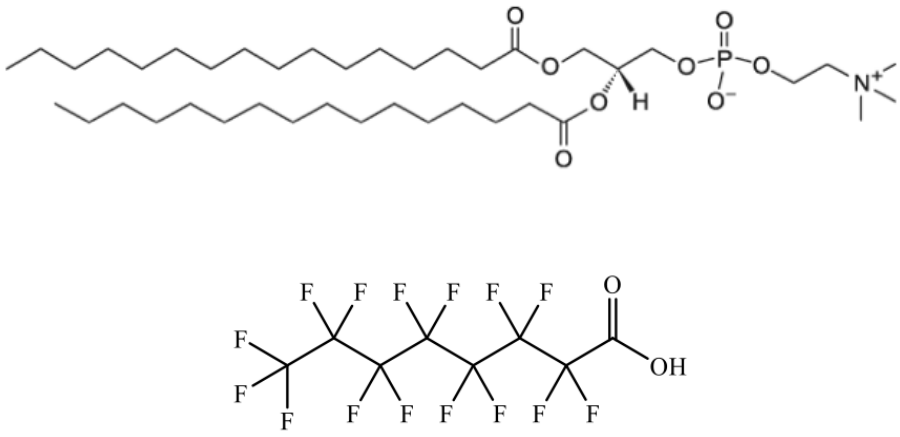


Figure 4.1. DPPC and PFOA structures

PFOA solutions were prepared in Millipore water and sonicated for 20 minutes to ensure complete dissolution. DPPC stock solutions (~1 mg/mL) were prepared in chloroform and sonicated for 10 minutes. Aqueous PFOA samples for VSFG measurements were prepared in Petri dishes. The Petri dishes were soaked in an acid wash (50/50 volume nitric/sulfuric) and then rinsed with Millipore water several times before use. For all Langmuir trough and VSFG experiments, a Hamilton glass microsyringe was used to apply the appropriate volume of the DPPC/chloroform stock solution to the water surface to achieve the intended surface coverage of 55 or 40 $Å^2$/molecule. After the DPPC was deposited at the water–air interface, the sample was allowed to sit for 5 minutes to allow chloroform to evaporate.

4.2.2 Vibrational Sum Frequency Generation (VSFG)

VSFG is a second-order nonlinear optical technique that measures molecular vibrational structure at interfaces. A VSFG experiment requires temporal and spatial overlap between a visible (or near IR) field ($\omega_{vis}$) and an infrared field ($\omega_{IR}$) at the surface being studied. When $\omega_{IR}$ is resonant with a symmetry allowed vibrational transition, $\omega_{IR}$ and $\omega_{vis}$ can couple producing a

third field ($\omega_{sum}$) equal in energy to $\omega_{IR} + \omega_{sum}$. Signal in a VSFG experiment arises from the second order polarization, $P^{(2)}$ created by the incident IR and visible fields:

$$P^{(2)} = \chi^{(2)}\, E(\omega_{IR})E(\omega_{VIS}) \qquad (4.1)$$

The intensity of the sum frequency light is proportional to the magnitude squared of $P^{(2)}$, or equivalently, the magnitude squared of the second-order susceptibility ($\chi^{(2)}$) multiplied by the intensities of both the visible and infrared pulses.

$$I_{SFG} = \left|P^{(2)}\right|^2 \propto \left|\chi^{(2)}\right|^2 I_{vis} I_{IR} \qquad (4.2)$$

$\chi^{(2)}$ is a third-rank tensor whose elements must change sign upon inversion:

$$\chi^{(2)}(x,y,z) = -\chi^{(2)}(x,y,z) \qquad (4.3)$$

This condition renders all elements of the $\chi^{(2)}$ tensor zero in isotropic media. At interfaces, however, inversion symmetry is broken, meaning that elements of the $\chi^{(2)}$ tensor can assume nonzero values and the two incident fields can generate a $P^{(2)}$ response. The $\chi^{(2)}$ tensor is simply the orientationally averaged molecular hyperpolarizability ($\beta_{\alpha\beta\chi}$) where i, j, and k refer to the laboratory frame of reference and α, β, and γ refer to the molecular frame of reference[250]:

$$\chi^{(2)}_{i,j,k} = N \sum_{\nu} < \beta_{\alpha\beta\gamma} > \qquad (4.4)$$

The molecular hyperpolarizability, in turn, can be expressed as the product of a vibration's IR and Raman transition matrix elements, $A_\gamma$ and $M_{\alpha\beta}$, respectively:

$$\beta_{\alpha\beta\gamma} = \frac{1}{2\hbar}\frac{M_{\alpha\beta}A_\gamma}{(\omega_{VIS}-\omega_{IR}-i\Gamma)} \qquad (4.5)$$

Equation 5 shows that the vibration of a molecule at a surface cannot be VSFG active unless it is both IR and Raman allowed. Equations 3 and 5 are responsible for VSFG's surface and molecular specificity.

Assuming that the surface normal defines the z axis and a rotationally invariant surface (x and y are indistinguishable), the nonzero elements of the $\chi^{(2)}$ tensor are $\chi^{(2)}_{xxz}$, $\chi^{(2)}_{xzx}$, $\chi^{(2)}_{zxx}$, and $\chi^{(2)}_{zzz}$. These elements can be accessed by selecting different polarization combinations for the IR, visible, and sum frequency fields. $S_{sum}S_{vis}P_{IR}$ polarization samples $\chi^{(2)}_{xxz}$, $S_{sum}P_{vis}S_{IR}$ samples $\chi^{(2)}_{xzx}$, $P_{sum}S_{vis}S_{IR}$ samples $\chi^{(2)}_{zxx}$, and $P_{sum}P_{vis}P_{IR}$ samples all combinations ($\chi^{(2)}_{zzz}$, $\chi^{(2)}_{xxz}$, $\chi^{(2)}_{xzx}$, and $\chi^{(2)}_{zxx}$).[251, 252] Spectra shown in these studies were acquired using the $S_{sum}S_{vis}P_{IR}$ combination meaning that features are due to vibrational motions having their IR transition moments aligned along the surface normal.

The laser system used for VSFG studies has been described elsewhere in detail.[64, 65, 253] The system consists of a regeneratively amplified Ti: sapphire laser (Coherent Libra HE, 3.4 W, 85 fs pulse duration, 1 KHz repetition rate). Laser output produces a 800 nm light split 80/20 with a beam splitter where 80% is directed into the Coherent OPerA Solo which produces a tunable broadband IR frequency centered in the CH and OH region. The 20% portion remaining is spectrally narrowed with a 4f pulse shaper providing spectral resolution of approximately 15 $cm^{-1}$ used for the visible up-conversion. The 800 nm visible light and the IR light are both spatially and temporally aligned at the surface of the air-water interface at 48° and 38° respectively. The sum frequency is then focused into a monochromator (SpectraPro-300i, Action Research Corp.) and then dispersed into a 1340 x 100-pixel CCD (PIXIS100B, Princeton Instruments). All spectra presented were obtained in the $S_{sum}S_{vis}P_{IR}$ polarization (SFG, VIS, IR) which samples vibrations with transition moments aligned along the surface normal.

### 4.2.3 Langmuir Area-Pressure Isotherms

Langmuir isotherms were obtained using methods previously described.[65, 66, 83] Either a 250 mL neat Millipore subphase or a set concentration of PFOA was poured into the Nima Langmuir Trough (model 302LL) equipped with a Nima PS4 pressure sensor and a platinum plate. The instrument's PTFE trough and barriers were wiped with methanol and chloroform on KimWipes followed by multiple Millipore water rinses. Following this cleaning procedure, the surface tension of water consistently measured 72.0 ± 0.9 mN/m at 22˚C. DPPC was deposited onto the surface and equilibrated before the platinum plate was lowered to the surface of solution. The pressure sensor was then allowed five minutes to stabilize and zeroed before the barriers were closed at a rate of 15 $cm^2/min$. Surface pressure (Π) was measured as a function of surface area. Pressure-area isotherms for DPPC are well characterized in literature.[81, 85, 254] The DPPC isotherm is characterized with a liftoff pressure ~90 $Å^2$/molecule before the isotherm rises steeply and collapses at 32 $Å^2$/molecule.

## 4.3 Results

### 4.3.1 VSFG CH Region Results

Representative VSFG spectra from DPPC monolayers having surface coverages of 55 and 40 $Å^2$/molecule are shown as the top traces in Figures 4.2A and 4.2B, respectively. Following traditional notation, "r" denotes vibrations associated with the DPPC methyl groups and "d" describes vibrations associated with the DPPC's methylene groups.[255, 256] The "+" indicates a symmetric stretch (SS) and a "–" indicates an antisymmetric stretch (AS). As a perfluorinated alkyl surfactant, PFOA's VSFG active features are observed at much lower frequencies than those examined here.[257]

The $r^+$ to $d^+$ intensity ratio often serves as a sensitive indicator of chain conformational order in surfactant films.[65, 149, 258] Under SSP conditions, the disordered 55 Å$^2$/molecule DPPC monolayer has readily apparent $d^+$ signal and a correspondingly small $r^+/d^+$ ratio of ~1.0 indicating significant conformational disorder (Figure 4.2A, top spectrum). In contrast, the tightly packed DPPC monolayer has a large $r^+/d^+$ ratio of ~15 (Figure 4.2B, top spectrum), consistent with previous reports.[64, 65, 83, 251] The weak $d^+$ signal in Figure 4.2B is the result of DPPC's acyl chains adopting an all-trans conformation creating local inversion symmetry about the center of each carbon-carbon bond. Further, if the chains are all trans and aligned with the surface normal (z-axis) the methylene groups will have their IR transition moments aligned in the surface plane and not be accessible with an SSP polarization combination which measures transitions along the surface normal. Peaks were fit using the multipeak fitting option in Igor 8 to determine the amplitude, position, FWHM, and area of each feature in the -CH and -OH regions. We note that these experiments do not probe PFOA behavior directly, given that PFOA's perfluorinated alkyl -CF stretches have frequencies much lower than the frequency ranges covered in this work.[257]

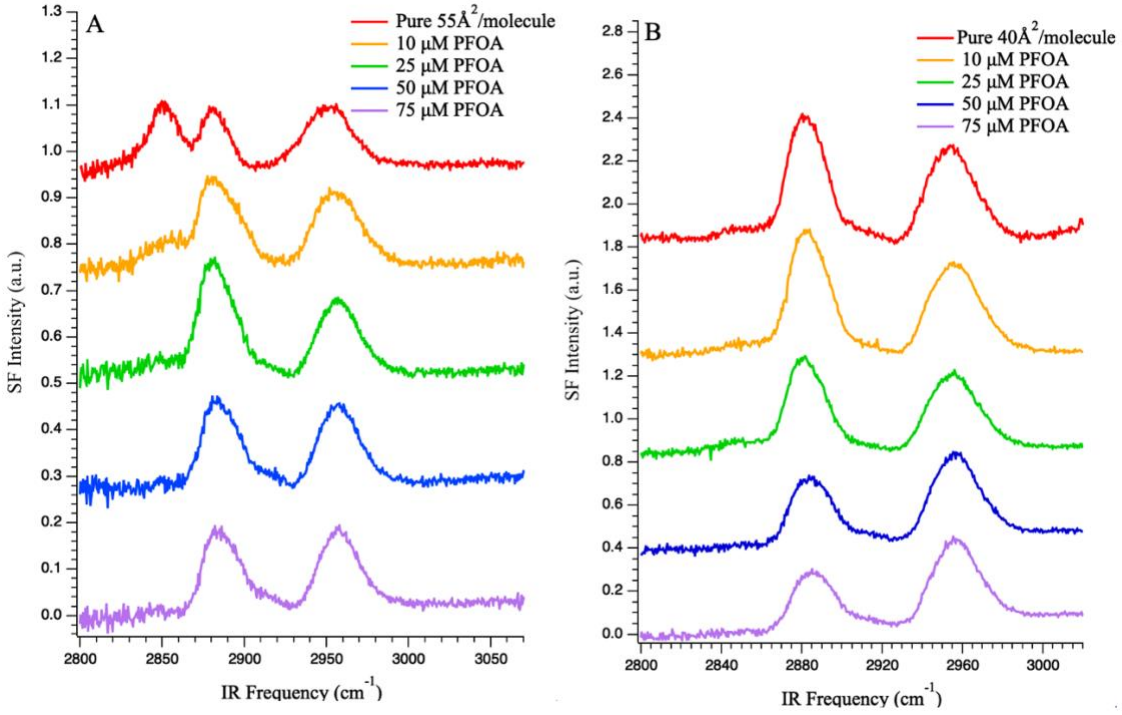



Figure 4.2. (A) 55 Å$^2$/molecule DPPC with increasing concentrations of PFOA in the CH region. A shift of ~ 5 cm$^{-1}$ is seen. (B) 40 Å$^2$/molecule DPPC with increasing concentrations of PFOA in the CH region. A shift of ~ 5 cm$^{-1}$ is observed.

Figure 4.3 shows a plot of $r^+/d^+$ vs. PFOA concentration calculated from peak areas observed in Figure 4.2 and reported in Table 4.1. Standard deviations are shown using error bars determined from a minimum of three independent trials. Figure 4.3 shows that in the absence of PFOA, the $r^+/d^+$ ratio is large for 40 Å$^2$/molecule DPPC and smaller for 55 Å$^2$/molecule DPPC. Ratio data for the tightly packed monolayer do not change as PFOA concentration increases. Intuitively, these results seem sensible given that the tightly packed DPPC monolayer does not contain any interstitial area between monomers that could accommodate adsorbing PFOA perfluoro-alkyl chains. In contrast, DPPC conformational order in the moderately packed DPPC monolayer is very sensitive PFOA concentration in the subphase. As PFOA is added to the

subphase of a 55 Å$^2$/molecule DPPC monolayer, the $r^+/d^+$ ratio increases markedly from approximately 1.0 in the absence of PFOA to values well above 10 when the PFOA concentration climbs to ≥25 μM (Figure 4.3, Table 4.1). Again, these results are intuitively appealing as the more loosely packed DPPC monolayer will have interstitial space between lipid monomers. Given its strongly hydrophobic character, PFOA is expected to adsorb to the water-air interface occupying these spaces and forcing the lipid monomers closer together so that the lipid acyl chains adopt more ordered conformations aligned along the surface normal. Similar results have been observed for the soluble surfactant SDS interacting with DPPC acyl chains, but at considerably higher surfactant concentrations.[249] (See Appendix C.)

Table 4.1. The $r^+/d^+$ ratio for DPPC in the presence of PFOA in the -CH range, 3200 cm$^{-1}$ Integrated Intensity$^{1/2}$, 3450 cm$^{-1}$ Integrated Intensity$^{1/2}$, and Sum of 3200 cm$^{-1}$ and 3450 cm$^{-1}$ in the -OH range. Trials were run in triplicate.

| [PFOA] mM | $r^+/d^+$ | $I_{3200}^{1/2}$ | $I_{3450}^{1/2}$ | $I_{3200}^{1/2} + I_{3450}^{1/2}$ |
|---|---|---|---|---|
| 40 Å$^2$/molecule DPPC (0 PFOA) | 16 ± 4 | 5.46 | 2.43 | 7.89 |
| 10 μM PFOA | 18 ± 2 | 8.27 | 2.57 | 10.84 |
| 25 μM PFOA | 17 ± 1 | 9.25 | 4.21 | 13.46 |
| 50 μM PFOA | 16 ± 2 | 11.14 | 5.89 | 17.03 |
| 75 μM PFOA | 15 ± 4 | 13.54 | 6.45 | 19.99 |
| 100 μM PFOA | - | 12.88 | 5.67 | 18.55 |
| 55 Å$^2$/molecule DPPC (0 PFOA) | 1 ± 0.4 | 2.58 | 1.57 | 4.33 |
| 10 μM PFOA | 4 ± 0.4 | 5.68 | 2.55 | 8.23 |
| 25 μM PFOA | 15 ± 2 | 9.82 | 3.16 | 12.98 |
| 50 μM PFOA | 15 ± 4 | 13.57 | 4.67 | 18.24 |
| 75 μM PFOA | 27 ± 9 | 10.72 | 3.08 | 13.80 |
| 100 μM PFOA | - | 10.55 | 4.29 | 14.84 |
| PFOA Only, 0 μM PFOA | - | 6.30 | 3.51 | 9.81 |
| 10 μM PFOA | - | 3.97 | 3.22 | 10.16 |
| 100 μM PFOA | - | 8.78 | 3.97 | 12.75 |

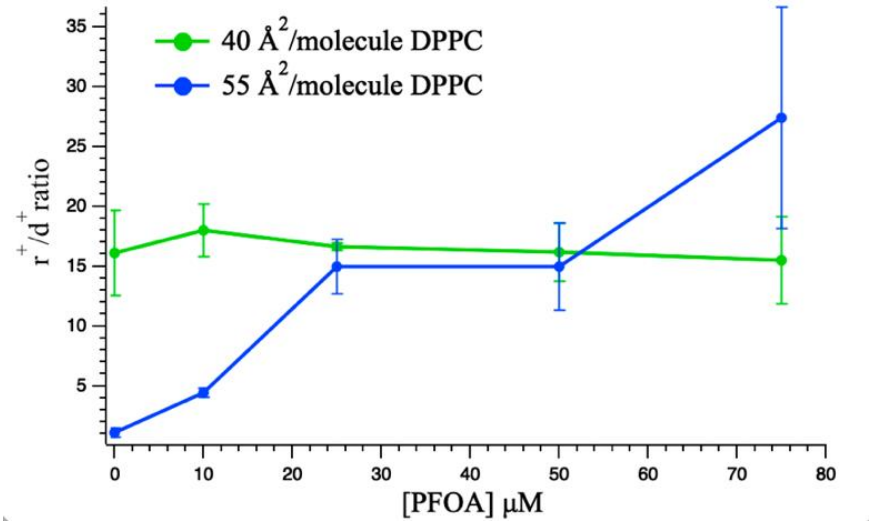



Figure 4.3. The $r^+/d^+$ ratio for DPPC in the presence of PFOA. Error bars represent standard deviations from ≥ 3 independent measurements.

4.3.2 VSFG OH Region Results

VSFG data in Figure 4.2 show that PFOA in the aqueous subphase has no measurable effect on DPPC structure and organization in tightly packed monolayers. In contrast, when DPPC monolayers are more loosely packed – 55 $Å^2$/molecule – PFOA readily adsorbs to the water/air interface forcing DPPC into a more tightly packed, more organized structure. Despite these different – and explainable – outcomes, interfacial water structure in *both* systems is similarly impacted by PFOA in the subphase, implying that PFOA adsorbs to *both* interfaces.

Figure 4.4 shows SSP spectra across the -OH stretching region for three separate systems as a function of PFOA concentration. Due to instrument limitations, spectra do not extend past ~3500 $cm^{-1}$. Figure 4.4A presents spectra from the water-air interface as a function of PFOA concentration in the absence of any DPPC. Figure 4.4B presents spectra from the water air interface as a function of PFOA concentration with a moderately packed (55$Å^2$/molecule) DPPC monolayer and 4.4C shows equivalent data acquired with a tightly packed (40$Å^2$/molecule)

DPPC monolayer. We note that the PFOA concentrations responsible for spectra in Figure 4A range from 0 – 8 mM, while the spectra in Figures 4.4B and 4.4C only show spectra for PFOA concentrations up to 100 μM.

All spectra are dominated by two broad features, one centered at ~3200 $cm^{-1}$ and one centered at 3450 $cm^{-1}$. While the origins of these vibrational transitions have been discussed extensively for more than 30 years,[248, 251, 252, 259-263] a general interpretation is that the lower frequency feature arises from interfacial water molecules that are more strongly hydrogen bonded while the higher frequency feature is due to interfacial water molecules that are more weakly hydrogen bonded. In some reports, the lower frequency feature is said to describe 'ice-like' water in reference to ice's vibrational spectrum.[251, 264] In these same reports, the higher frequency feature is said to refer to more disordered or 'water-like' interfacial water.

In Figure 4.4A show that the interfacial water becomes increasingly ordered as PFOA is added to solution (without any DPPC present), based on the steady growth in peak intensity for the 3200 $cm^{-1}$ and 3450 $cm^{-1}$ features. Growth in the water VSFG spectrum is expected as the charged monolayer forms an electrical double layer with a field that aligns the interfacial solvent. Findings similar to those shown in Figure 4.4A are similar to those from earlier studies using simple anionic surfactants.[248, 252, 259] Previous work from has shown that PFOA on unbuffered, Millipore water will form tightly packed monolayers at bulk PFOA concentrations of 1 mM.[181]

Figure 4.4B shows how water structure is impacted by increasing PFOA concentration *in the presence of* a moderately packed (55 $Å^2$/molecule) DPPC monolayer, PFOA adsorption to the Langmuir film again results in growing intensity of both -OH features. The observed behavior is expected as PFOA adsorption to the interstitial areas creates a charged interface. Furthermore,

PFOA adsorption to the interface covered with the moderately packed DPPC monolayer is also consistent with the VSFG data from the -CH stretching region. As more PFOA adsorb, the DPPC monomers will be forced together leading the acyl chains to become more ordered. (Earlier VSFG studies of DPPC monolayers did not report significant intensity in the -OH stretching region, implying that the charged lipid headgroups align predominantly parallel to the surface and do not create an electric field along the surface normal.)[247, 249, 265, 266]

Curiously, similar behavior is also observed in in the -OH stretching region for the tightly packed, 40 $Å^2$/molecule DPPC monolayer (Figure 4.4C). Even at low PFOA concentrations (10 - 25 μM) when there is no 'space' for the PFOA to adsorb, both water features begin to grow in intensity with the strongly hydrogen bonded water at 3200 $cm^{-1}$ slightly higher in intensity than the 3450 $cm^{-1}$ band. The relative band intensities change slightly at higher PFOA concentrations, but the overall intensity in the -OH stretching region continues to increase with increasing PFOA.

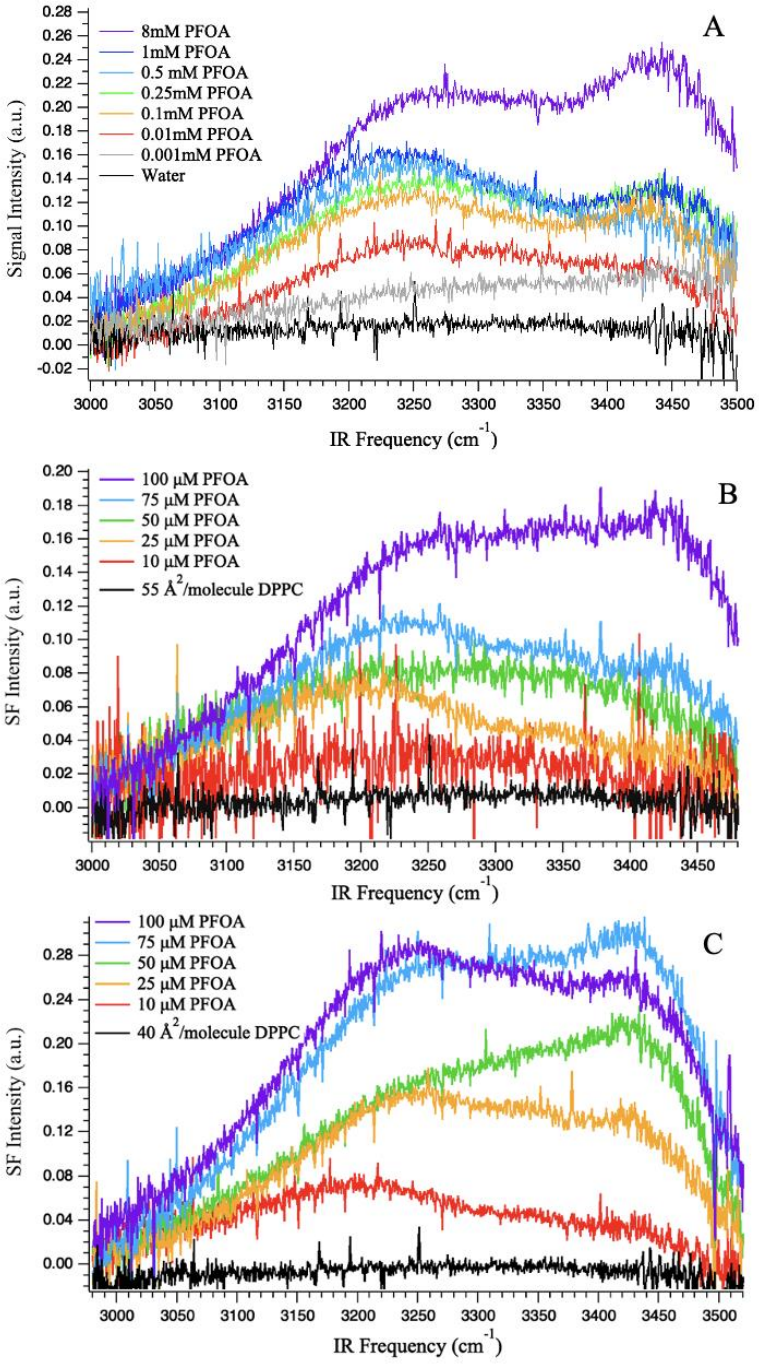



Figure 4.4. (A) PFOA surface activity in OH stretching region. (B) 55 Å$^2$/molecule DPPC in the presence of PFOA showing interfacial water signal with growing intensity for the disordered $H_2O$. (C) 40 Å$^2$/molecule DPPC in the presence of PFOA showing interfacial water signal with growing intensity for the disordered $H_2O$.

The behavior observed in Figures 4A-4C has been widely reported for charged surfactants adsorbing to the water/air interface and has been interpreted in terms of the electrical double layer created by the surfactants and their counterions providing a strong interfacial electric field that aligns water molecules with their $C_2$ axes aligned predominantly along the surface normal.[248, 252, 267-269] Phase dependent VSFG measurements have identified the absolute orientation of aligned water molecules (up or down).[269-271] Not surprisingly, water orientation flips 180˚ when the charges on the surfactant and counterion are reversed and the double layer field reverses direction.[248, 251, 259]

Figures 4.5A – 4.5C show the square root of the intensities of the 3250 $cm^{-1}$ and 3400 $cm^{-1}$ features and the sum of these two square-root intensities. The numerical values are reported in Table 4.1. Given the quadratic dependence of VSFG intensity on surface concentration (Equation 4), the square root of the measured intensity should reflect the relative amount of highly ordered and more disordered water contributing to the spectra shown in Figures 4A-C assuming that the orientationally averaged hyperpolarizabilities do not change significantly. Figures 5A and 5B show -OH stretching data for 40 $Å^2$ and 55 $Å^2$ DPPC monolayers as a function of PFOA concentration. Also included are data for solutions up to 0.1 μM PFOA with no DPPC.

The data lead to several conclusions. First, increasing PFOA increases -OH intensity in the VSFG spectra regardless of whether the water surface supports a DPPC monolayer. Second, all three systems show stronger intensity in the 3200 $cm^{-1}$ highly ordered water feature. Third, the behavior of the total water signal as a function of PFOA concentration is virtually identical for both the 55 $Å^2$ DPPC monolayer and the solutions that contain only soluble PFOA with no DPPC at all. For the 40 $Å^2$ DPPC monolayer, the rise in -OH signal is similar to that in the

55 $Å^2$ DPPC and neat-PFOA systems, but at higher PFOA concentrations, the -OH signal is measurably larger. This difference traces to large differences in the 3450 $cm^{-1}$ feature corresponding to weakly ordered interfacial $H_2O$. We propose that this effect is due to accumulation of the perfluoro chains at the DPPC covered water/air interface disrupting strong interfacial hydrogen bonding (e.g., 3200 $cm^{-1}$ band). At the moderately packed DPPC interface, PFOA monomers adsorbed to the surface can place their chains out of the water causing less disruption to the interfacial solvent hydrogen bonding. We assume that PFOA adsorption to all of the surfaces is self-limiting as Coulomb repulsion will eventually prevent further PFOA accumulation.

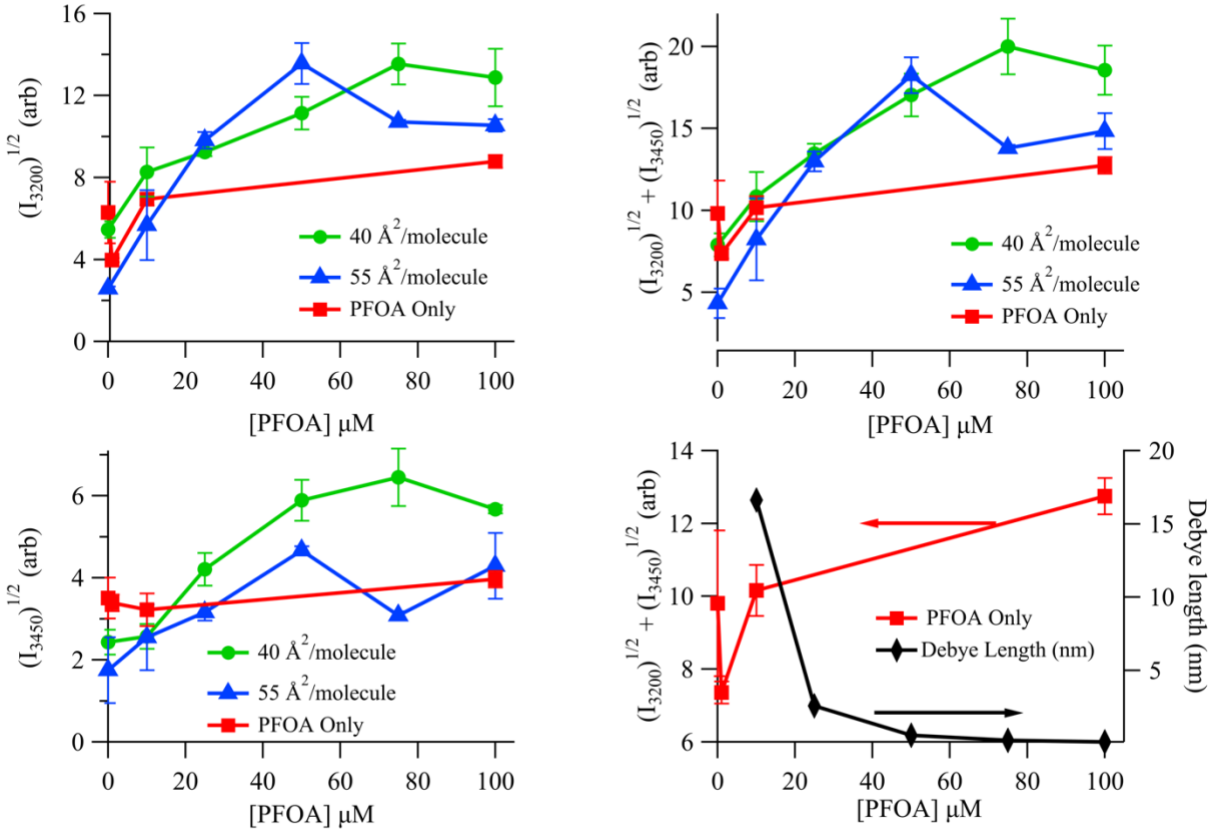



Figure 4.5. Integrated intensities$^{1/2}$ at (A) 3200 cm$^{-1}$, (B) 3450 cm$^{-1}$, (C) sum of both peaks at 3200 cm$^{-1}$ and 3450 cm$^{-1}$ as functions of PFOA concentration. (D) A comparison between total VSFG intensity$^{1/2}$ vs. PFOA concentration and the interfacial Debye length created by charged surfactant adsorption to the water/air interface.

The width of the electrical double layer responsible for these changes in water structure changes with increasing PFOA concentration. At a simple charged interface, the width of the double layer can be described using Gouy-Chapman theory where the Debye length is given by Equation [248, 251, 252]:

$$\lambda = \left(\frac{1000DRT}{8\pi N^2 \epsilon_0^2 I}\right)^{1/2} \qquad (6)$$

Here, the Debye length, λ, is distance required for the surface potential to drop by 1/e. D is the solution dielectric constant, N is the surface charge density, $\varepsilon_0$ is permittivity in a vacuum, and *I* is the solution phase ionic strength. For the data shown in Figure 4, both solution phase ionic strength (*I*) *and* surface charge density (*N*) are changing. In the case of Figure 4A, Equation 6 can be readily solved with data acquired from surface tension measurements. Results from calculating λ vs. PFOA concentration in the absence of DPPC are shown in Figure 5D. PFOA is exceptionally hydrophobic and measurable changes in water/air surface tension have been observed for PFOA concentrations as low as 1 nM. Figure 5D shows that for PFOA ≥ 25 μM the Debye length is less than the diameter of a single water molecules (~3Å).

In principle, limiting cases for *N* can also be determined for the loosely packed DPPC monolayer assuming a) that the DPPC zwitterionic headgroups do not contribute to overall surface charge density and b) that PFOA adsorbs to the surface to force the DPPC monomers into tightly packed structures (40 $Å^2$/molecule). In this case the total area available for PFOA adsorbing to the surface from bulk solution would simply be the number of DPPC monomers multiplied by the difference in monomer area when loosely packed (55 $Å^2$/molecule) and tightly packed (40 $Å^2$/molecule). Determining N for PFOA adsorption to tightly packed DPPC monolayers is not feasible given that the data provide no way of assessing how many PFOA are present as a function of bulk PFOA concentration.

### 4.3.3 Langmuir Area-Pressure Isotherms

Figure 4.6 shows DPPC compression isotherms obtained using a Langmuir trough and solutions with different PFOA concentrations in the subphase. The pure DPPC isotherm lifts off at ~90 Å2/molecule and passes through a liquid expanded-liquid condensed (LE-LC)

coexistence region between 85 and 55 Å2/molecule. The monolayer then collapses at ~40 Å2/molecule. These results compare favorably to the many reports of DPPC P-Area in the literature.[64, 66, 83, 85, 247, 249, 254]

Several observations stand out in the DPPC isotherms on PFOA-containing subphases. First, PFOA concentrations as low as 10 μM cause liftoff to occur at areas ~ 130 $Å^2$/molecule. This result does not change substantively with increasing PFOA concentrations. Second, while the LE/LC coexistence region persists in the DPPC monolayers on a PFOA-containing subphase, the coexistence regions have surface pressures of 5 ± 2 mN/m rather than the 3 ± 1 mN/m for DPPC on pure Millipore water. Like the isotherm liftoff area, this elevated LE/LC coexistence pressure does not change with increasing PFOA concentration. Third, monolayer collapse occurs at larger lipid area *and* at lower surface pressures when PFOA is present in the subphase. These last two results – larger lipid area at collapse and lower surface pressure at collapse –depend on PFOA concentration in the subphase and imply that PFOA monomers embedded within the DPPC monolayer at larger areas do not get 'squeezed out' as the DPPC monolayer compresses. This behavior stands in contrast to DPPC behavior with more typical, alkyl surfactants such as SDS. (Appendix C contains equivalent measurements performed with SDS in the subphase.)

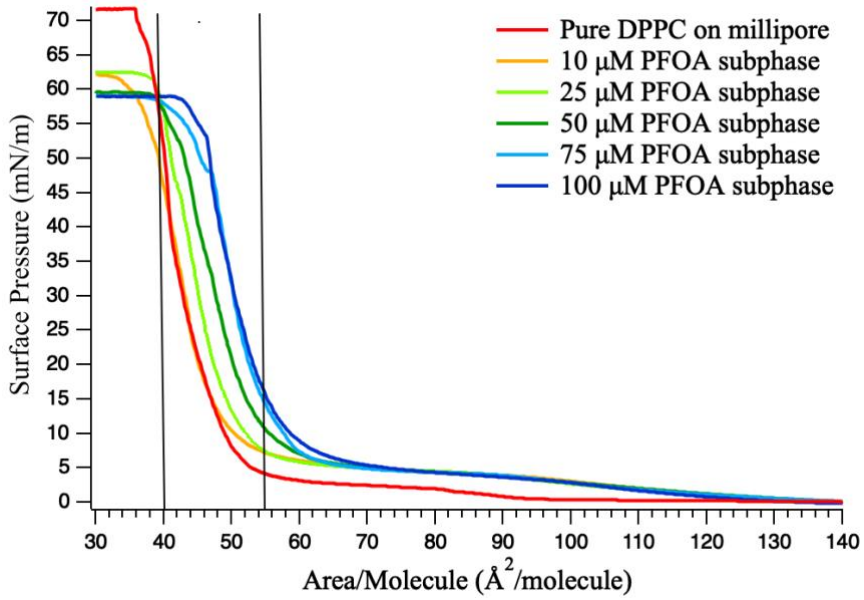



Figure 4.6. Langmuir compression isotherm of DPPC on a Millipore subphase and varying concentrations of PFOA with vertical lines indicating the of 40 and 55 Å$^2$/molecule DPPC coverages used in the VSFG measurements.

A common way to analyze the effects of soluble surfactants on DPPC monolayer behavior is to calculate the lipid monolayer's isothermal compressibility, κ.[272, 273]

$$\text{Equation 7: } \kappa = -A\left[\frac{d\pi}{dA}\right]_T$$

The isothermal compressibility reports how much pressure is needed to change a Langmuir monolayer's surface coverage and can be considered an indicator of monolayer 'stiffness'. Figure 4.7 shows the isothermal compressibility calculated from the isotherms shown in Figure 4.6. Not surprisingly, data for all systems get large and noisy close to monolayer collapse. Importantly, however, the data show that PFOA effects on monolayer compressibility become more pronounced at less compressed DPPC monolayers as PFOA concentration increases.

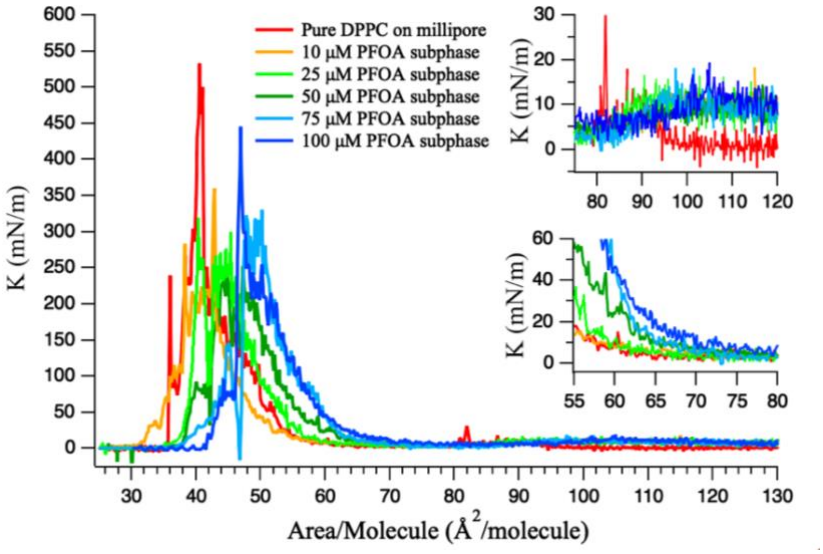



Figure 4.7. Compressibility of DPPC isotherms with 0 – 100 μM PFOA subphases.

Again, these results demonstrate that PFOA is adsorbing cooperatively and irreversibly to the DPPC monolayer (Lower inset.) In addition, the earlier isotherm liftoff for all PFOA concentrations is observed clearly at large areas (upper inset).[274, 275]

## 4.4 Conclusion

**I**n summary, the effects of PFOA on the structural and organizational properties of DPPC monolayers were explored using VSFG spectroscopy and Langmuir isotherms surface pressure measurements. For tightly packed 40 Å²/molecule DPPC monolayers, PFOA did not significantly alter lipid acyl chain conformational order as evidenced by unchanging VSFG spectra in the -CH stretching region. In contrast, lipid chain conformation in the moderately packed 55 Å²/molecule DPPC monolayer demonstrated a strong dependence on PFOA concentration, with the $r^+/d^+$ ratio increasing markedly as PFOA concentration increased and more PFOA monomers adsorbed to the interface. VSFG data from the -OH region show clearly

that PFOA adsorbs to *both* the moderately packed *and* tightly packed DPPC monolayers. Notably, PFOA adsorption to the interface led to a stronger hydrogen bonding environment for interfacial water, as evidenced by the increased intensity of the 3200 $cm^{-1}$ band. This behavior is consistent with the formation of an electric double layer that interfacial water molecules along the surface normal. Given how the total intensity in the water region increases with increasing PFOA concentration, the impact of PFOA adsorption to DPPC monolayers on interfacial water structure appears more pronounced for the tightly packed DPPC monolayer than for the moderately packed DPPC monolayer.

Langmuir isotherms calculated isothermal compressibility data provide additional insights, showing that PFOA substantially alters the compressibility and collapse behavior of DPPC monolayers, particularly at lower PFOA concentrations. PFOA increased the liftoff area and shifted the LE/LC coexistence region to higher surface pressures. PFOA that adsorbed to the DPPC monolayer increased monolayer stiffness and remained irreversibly retained in the lipid film even as the film was compressed to collapse pressures. Overall, these findings demonstrate that the packing density of DPPC monolayers plays a critical role in determining the interactions with PFOA, with more loosely packed monolayers being more susceptible to structural changes upon PFOA adsorption. The cooperative adsorption behavior and the creation of a charged interface upon PFOA incorporation emphasize the complex interfacial dynamics between DPPC and PFOA, providing new insights into the molecular interactions at the air-water interface.

# CHAPTER FIVE

## CUMULATIVE RISK ASSESSMENT: PER- AND POLYFLUOROALKYL SUBSTANCES (PFAS) IN MONTANA RURAL AND DEVELOPING PRIVATE WELLS

### Contribution of Authors and Co-Authors

Manuscript in Chapter 5:
Author: Tess N. Sobolewski

Contributions: Collected participant samples, analyzed data for results, and writing - original draft preparation, review and editing

Co-Author: Paul M. Bradley

Contributions: Conceptualization, data curation, formal analysis, investigation, methodology, project administration, funding acquisition, visualization, writing – review & editing.

Co-Author: Kelly L. Smalling

Contributions: Conceptualization, investigation, funding acquisition, writing – review & editing.

Co-Author: Margaret J. Eggers

Contributions: conceptualization, investigation, writing – original draft preparation, review & editing.

Co-Author: Kristin M. Romanok

Contributions: Data curation, formal analysis, investigation, methodology, visualization, writing – review & editing.

Co-Author: Molly L. Schreiner

Contributions: Conceptualization, data curation, formal analysis, investigation, methodology, project administration, funding acquisition, visualization, writing – review & editing.

Co-Author: James L. Gray

Contributions: Tested samples obtained from the 59 participants under both methodologies.

Co-Author: W. Adam Sigler

Contributions: Collected participant samples, analyzed data for results, and writing - original draft preparation, review and editing.

Co-Author: Robert A. Walker

Contributions: Assisted with result analysis, conceptualization, writing, and editing of manuscript.

Manuscript Information

Tess N. Sobolewski, Margaret J. Eggers, Paul M. Bradley, Kelly L. Smalling, Kristin M. Romanok, Molly L. Schreiner, James L. Gray, W. Adam Sigler, and Robert A. Walker

Environmental Science & Technology: Water

Status of Manuscript:
☒ Prepared for submission to a peer-reviewed journal
☐ Officially submitted to a peer-reviewed journal
☐ Accepted by a peer-reviewed journal
☐ Published in a peer-reviewed journal

## 5.0 Abstract

Exposure to per-polyfluoroalkyl substances (PFAS) through drinking water is a global concern, but information on drinking-water PFAS exposures in private-well-dependent communities like rural and developing areas of Montana remains limited. PFAS tap-water sampling was conducted in three southwestern Montana counties from 59 private-well-dependent residences. Initial sample analysis using analytical Method 1 (MDL range: 5 – 22.8 ng/L for 6 regulated PFAS) detected no PFAS. Reanalysis employing a recently developed, more sensitive (approximately 10X) and analytically extensive protocol, research Method 2 (MDL range: 0.2 – 1.0 ng/L for 6 regulated PFAS), detected at least one PFAS in 53% (31/59) of wells. Twelve PFAS were observed at least once with PFOS, PFOA, PFBS, PFHxS, FOSA, PFHpA, and PFHxA observed most frequently and in 10% - 25% of the samples. The number of individual PFAS observed in a single well ranged from 0 to 7 with cumulative concentrations (sum of PFAS detected) ranging from 0 to 22.2 ng/L. A greater number of compounds were generally detected in shallower wells and on smaller property sizes, consistent with higher prevalence in younger (shallower) groundwater in areas with higher intensity land use. Human health risks were driven by PFOA and PFOS. Cumulative toxicity quotients ($\Sigma_{TQ}$) ranged from 0.03 to >1 in wells with PFAS detections, with elevated risk ($\sum_{TQ} \geq 1$) predicted in 25% of these wells. Individual results were returned to participants, with an explanation of risks and links to additional resources. These findings document the presence of PFAS in private-well drinking water in rural and minimally-developed areas and demonstrate the critical importance of employing newer PFAS analytical methods with below-MCL detection limits to more accurately assess corresponding drinking-water human health risk.

## 5.1 Introduction

Across the United States, private wells supply drinking water for more than 40 million people, or approximately 13% of the population.[276, 277] However, private wells (i.e., <25 people served, <15 service connections) are not regulated under the federal Safe Drinking Water Act,[278] and also are not regulated under state laws in most states.[279] Hence, well owners are responsible for the testing and safety of their drinking water.[280, 281]

Synthetic poly- and perfluorinated compounds (PFAS) contaminate groundwater drinking water sources globally,[282] yet there is minimal information about PFAS contamination of private drinking water supplies; most of the data released is for public water supplies.[9] Private well owner responsibility to test and treat their drinking water is even more onerous for PFAS contamination, as these "forever chemicals" are a class of over ten-thousand compounds of growing environmental concern due to their environmental persistence and presence,[283] health effects linked to even low level exposures,[25, 26, 166, 232] environmental recalcitrance due to strong carbon-fluorine bonds,[284] high analytical costs, and filtration system requirements.

The health risks associated with exposure to PFAS include reduced vaccine response,[31, 32, 36-38] birth defects,[38, 285] increased cholesterol,[26, 33, 41, 166, 286] and certain types of cancer.[29, 165, 287] For example, PFAS in drinking water has been associated with increased rates of cancer in the oral cavity/pharynx, respiratory, endocrine and digestive systems, and soft tissues.[287] Additionally, males are at higher risk for cancers of the brain and urinary system as well as leukemia, and females are at higher risk for thyroid cancers.[287] Perfluorooctanoic acid (PFOA) has been classified as a human carcinogen, while perfluorooctanesulfonic acid (PFOS) has been classified as a possible carcinogen.[288]

Exposure routes can be occupational, environmental, from consumer products, via food and drinking water, and from mother to fetus.[289] Among the many household products known to contain PFAS are non-stick cookware, water resistant clothing, personal care products, cleaning products, and grease resistant food packaging.[290] Drinking-water resources can be contaminated via industrial discharges, biosolids application to land, landfill leachate, stormwater, wastewater effluent, septage, firefighting foam, rain, snowfall, and more.[291-300] The same properties that allow PFAS to be so diverse and effective in consumer products also promote bioaccumulation in humans and wildlife and broad distribution in soil, air, and water.[20, 24, 26, 113] While 99% of humans are estimated to have measurable levels of PFAS in their bloodstreams,[285] much is still unknown about the prevalence of exposure through drinking water from private wells, as private well testing is generally not required despite new regulatory standards for PFAS in public drinking water supplies. The USGS identified "systematic evaluation of human exposure to PFAS in water for human consumption or ingestion," including via private well water, as one of their key "Science Opportunities" in their 2021 Strategic Science Vision for the study of PFAS in the environment.[301] A recent USGS nationwide study detected PFAS in 20% (55/269) of private wells tested,[9] and recent USGS modeling indicated that 27–45% of private well users in the conterminous US potentially rely on PFAS-impacted groundwater.[302]

Risk assessment is a key public policy tool, combining health effects and exposure data to estimate health risks to populations. It plays a crucial role in supporting the mission of the U.S. Environmental Protection Agency (EPA) and other federal agencies by evaluating health risks from environmental exposures, guiding regulatory and technological choices, and setting research priorities and funding allocations. In the 1970s and 1980s, traditional human health risk

assessments primarily focused on single-chemical exposures, with agencies like the EPA and the National Research Council (NRC) developing frameworks that assessed risks in isolation.[303] However, as scientific understanding advanced, building evidence demonstrated that real-world exposure scenarios often involve multiple pollutants interacting in complex ways, requiring a more comprehensive, cumulative assessment approach.[304] The EPA's Superfund program, for instance, began conducting cumulative risk assessments (CRAs) at hazardous waste sites as early as the 1980s;[305] the USGS and other national and international agencies also now employ similar approaches.[202, 306-308]

In 2011, the EPA advanced its approach to cumulative risk assessment (CRA) by incorporating it into the National-Scale Air Toxics Assessment (NATA),[309] which evaluated the combined risks of multiple air pollutants. This tool allowed for a more comprehensive understanding of potential health effects by considering the cumulative exposures people might face across different environmental sources. The approach uses a hazard quotient (HQ) to gauge risk, where HQ is the ratio of the chemical concentration to its health standard, with an HQ greater than 1 suggesting potential for harmful health impacts, and values under 0.1 indicating minimal risk.[14] The sum of HQs represents the cumulative risk from exposure to multiple contaminants.[303, 310-312] In short, cumulative risk assessments (CRA) are "an analysis, characterization, and possible quantification of the combined risks to human health or the environment from multiple agents or stressors."[313] The recent EPA PFAS rulemaking established a HI approach for drinking-water regulation of four PFAS (perfluorobutanesulfonate [PFBS], perfluorohexanesulfonate [PFHxS], perfluorononanoic acid [PFNA], hexafluoropropylene oxide

dimer acid [HFPO-DA or GenX]).[61, 62] If two or more compounds are detected and HQ > 1, the drinking water treatment plant (DWTP) must treat the water to comply.

The goal of this study is to assess the prevalence and levels of PFAS contamination in private well water across southwestern rural and developing Montana communities and better understand the potential for health risks associated with cumulative exposure to these chemicals through drinking water. This study compares the results from a previously employed analytical method developed to detect PFAS in water[314] above the new EPA MCLs,[53, 315] with a new method capable of measuring concentrations below MCL detection limits for all EPA-regulated PFAS. This new method provides a more accurate assessment of human health risks from consuming private well water.

## 5.2 Experimental Materials and Methods

### 5.2.1 Sample Collection and Participant Instructions

The assessment of PFAS in private drinking wells across southwestern Montana was conducted in three counties: Jefferson, Madison, and Gallatin, which were selected because the Montana State University Extension Water Quality (MSUEWQ) program[316] had broad community participation and well water sampling data from these counties. Altogether, 59 test kits were distributed to residents to collect tap water samples from their private wells. Each participant was given a packet containing instructions for testing, gloves, and six 2 mL polypropylene centrifuge tubes. Instructions for collection at the kitchen faucet detailed that centrifuge tubes be rinsed three times, filled halfway, capped, and immediately stored in the freezer until retrieval of each kit. Twenty-eight participants from Gallatin County, seven from Jefferson County, and 24 from Madison County contributed samples during the period October

23, 2023 through November 4, 2023. The samples were then shipped on ice to the U.S. Geological Survey (USGS) National Water Quality Laboratory (NWQL) in Denver, Colorado.

Prior to receiving a test kit, participants were required to fill out a short registration form to gather information about their well, water treatment and plumbing materials. Information collected from participants was limited to attributes of the property, water system, and water uses, which the Montana State University Institutional Review Board determined was not Human Subjects Research.

Property size and well depth information were collected to facilitate a qualitative assessment of PFAS detection compared to land use intensity and depth to groundwater. Property size was determined from a question on the registration sheet. Well depth was determined with a combination of participant questions and cross check with a well log where available. Well logs were queried from the Montana Bureau of Mines and Geology, Ground Water Information Center (GWIC).[317]

Following sample analysis, participants received letters detailing the test results, including identities and concentrations of any PFAS detected, respective health thresholds, and whether concentrations measured were above or below thresholds. The letters also included instructions on how to access additional online information and resources related to water quality, PFAS, and human health from the Montana Well Educated Program.[318]

### 5.2.2 Analytical Methods and Quality Assurance

The well water samples were analyzed for up to 54 different PFAS compounds using two different methods: Method-1 (USGS 9660) and Method-2 (USGS 9662). All samples were first analyzed using Method-1 (Kolpin et al., 2021; Gray et al., 2024)[314, 319]

, which included the analysis of 34 individual PFAS (including PFOS and PFHxS reported separately as branched and linear) in matrix-modified samples by direct aqueous injection-liquid chromatography/tandem mass spectrometry (DAI-LC/MS/MS) with isotope-dilution quantification. Data were acquired in dynamic multiple reaction monitoring (dMRM) mode with two transitions per analyte for confirmation (except for PFBA and PFPeA that only had one confirming ion). Detection limits ranged from 2.0-162 ng/L for all analytes and from 5.2-22.8 ng/L for the six newly regulated PFAS (SI Table 1). Method-2 included the analysis of 56 individual PFAS in matrix-modified samples, with an initial preconcentration using solid phase extraction (SPE) followed by DAI- LC-MS/MS. Preconcentration of the samples by SPE prior to analysis resulted in substantially lower detection limits ranging 0.1-22.3 ng/L (SI Table 1) for all analytes and 0.2-1.0 ng/L for the six newly regulated PFAS. Importantly, Method-2, detection limits for the six regulated PFAS were below their newly established maximum contaminant level(s) (MCL).

Quality-assurance/ quality-control included analyses of field blanks and stable isotope surrogates. The median surrogate recovery for PFAS using Method-1 and Method-2 was 102% (interquartile range (IQR): 93–112%) and 90% (IQR: 74-108%), respectively. Due to logistical constraints, field blanks were not collected as part of this study, however, 2 field blanks collected during the same timeframe from other studies were submitted for analysis using Method-2 and no PFAS were detected. For Method-1, field blanks were collected previously by 47 volunteers selected at random from 37 states in 2021; only PFBA was detected and only in one field blank.[9]

5.2.3 Cumulative Risk Assessments

Cumulative risk assessments were conducted to evaluate the potential health risks associated with drinking-water PFAS exposure from each private well. For each well water sample, the Toxicity Quotient (TQ, aka HQ), was calculated for each PFAS by dividing the measured concentration of that chemical by its available benchmark concentration (Table 1). A precautionary screening–level approach was employed based on the most protective human-health benchmark (i.e., lowest benchmark concentration) available. $\Sigma_{TQ}$ stands for sum **toxicity quotient.** It is used to assess the toxicity of a substance by comparing its concentration to a reference concentration known to cause a specific level of harm. An STQ assumes **additivity**, meaning that when multiple substances are present, their combined toxic effects are simply the sum of their individual toxicities. This assumes that each substance contributes independently to the overall toxicity, without any synergistic or antagonistic interactions between them. For the $\Sigma_{TQ}$ assessment, MCLG values of zero (i.e., no identified safe-exposure level for sensitive sub-populations, including infants, children, the elderly, and those with compromised immune systems and chronic diseases[320]) were set to 0.1 ng/L for PFOA and PFOS.

Table 5.1. The most conservative benchmark for each compound.

| Compound | Benchmark | Benchmark concentration ppt (ng/L) | Reference |
|---|---|---|---|
| **6:2FTS** | Health Canada | 200 | Health Canada, 2023[321] |
| **8:2FTS** | CO WQCC TL [a] | 70 | COWQCC, 2020[322] |
| **FOSA** | HI DOH EAL[71] | 46 | HIDOH, 2024[323] |
| **N-MeFOSAA (linear)** | CO WQCC TL [a] | 70 | COWQCC, 2020[322] |
| **PFBA** | MN DOH HRL 2018 | 7000 | MNDOH, 2018[324] |
| **PFBS** | MN DOH HRL 2023 | 100 | MNDOH, 2023[325] |
| **PFDS** | HI DOH EAL | 38 | HIDOH, 2024[323] |
| **PFHpA** | VT DEC PAL [b] | 2 | VTDEC, 2019[326] |
| **PFHxA** | RI DEM AL [c] | 70 | RIDEM, 2023[327] |
| **PFHxS** | EPA MCL and HI [d] | 10 | USEPA, 2024[328] |
| **PFOA** | EPA MCLG | Zero* | USEPA, 2024[328] |
| **PFOS** | EPA MCLG | Zero* | USEPA, 2024[328] |

CO WQCC, Colorado Water Quality Control Commission; HI DOH, Hawai'i Department of Health, MN DOH, Minnesota Department of Health, VT DEC, Vermont Department of Environmental Conservation, RI DEM, Rhode Island Department of Environmental Management; TL, translation levels; EAL environmental action level, HRL, health risk limit; EPA, Environmental Protection Agency; AL, action level; PAL protective action level; MCL, maximum contaminant level; HI, hazard index; MCLG; maximum contaminant level goal
a Applies to the sum of PFOA, 8:2 FTS, PFOS, NEtFOSAA, NMeFOSAA, and PFOSA
b Applies to the sym of any combination of PFOA, PFOS, PFHxS, PFHpA, and PFNA
c Applies to the sum of PFOA, PFOS, PFHxS, PFNA, PFHpA, PFDA, PFHxA, and PFPeA
d EPA Hazard Index > 1, Applies to the concentrations of mixtures of two of more PFNA, PFHxA, HFPO-Da (GenX), and PFBS.
* value set to 0.1 ng/L for TQ calculation

## 5.3 Results and Discussion

### 5.3.1 PFAS Detected in Private Well Samples

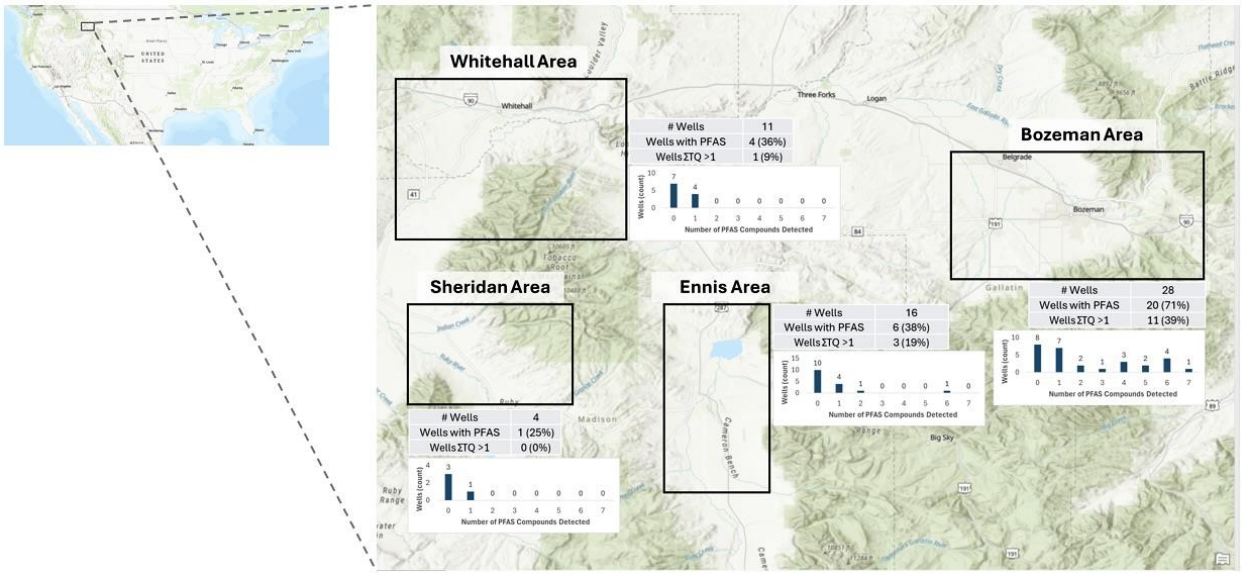



Figure 1. Geographic distribution of four Montana towns (Whitehall, Sheridan, Ennis, and Bozeman) within three counties (Jefferson, Madison, and Gallatin), detailing the number of wells tested, the number (and %) of wells with detectable PFAS concentrations, the number (and %) of wells with ∑ TQ > 1.0, and the number of wells with 1-7 PFAS compounds detected.

Well samples were analyzed by two different methods described above and discussed further in the SI. The first method (Method-1) was characterized by MDLs greater than newly established MCLs for some PFAS. The second method (Method-2) incorporated a pre-concentration step to achieve detection limits at or below newly established MCLs for regulated PFAS and below 1 ng/L for most PFAS. Using Method-1, no PFAS were detected in any of the private wells. However, when the same samples were reanalyzed using Method-2, PFAS were detected in 31 of the 59 (52%) private wells assessed. Using Method-2, 12 PFAS were detected.[329] Gallatin County samples had the highest PFAS detection frequency at 69% of wells, followed by Jefferson County (57%), and Madison County (29%). The maximum number

of PFAS found in a single well was seven (Figure 2). Among the 12 detected PFAS, PFOS exhibited the highest individual PFAS detection frequency in 25% of the 59 wells tested (Figure 3, SI Table 2). Two wells tested positive for PFOS above its EPA MCL of 4 ng/L and one of those two wells also tested above the EPA MCL of 4 ng/L for PFOA (SI Table 2). Other detected PFAS included perfluorooctane sulfonamide (FOSA), 6:2 fluorotelomer sulfonic acid (6:2 FTS), 8:2 fluorotelomer sulfonic acid (8:2 FTS), N-methyl perfluorooctane sulfonamidoacetic acid (N-MeFOSAA), perfluorobutanoic acid (PFBA), perfluorobutane sulfonic acid (PFBS), perfluorodecanesulfonic acid (PFDS), perfluoroheptanoic acid (PFHpA), perfluorohexanoic acid (PFHxA), and perfluorohexane sulfonic acid (PFHxS). However, none of these compounds exceeded their respective MCLs. In wells that tested positive for any single PFAS, cumulative PFAS concentrations ranged from 0.205 ng/L to 22.2 ng/L (Figure 3). These results highlight the importance of utilizing the most sensitive detection methods available to accurately assess the presence of PFAS and other contaminants in groundwater sources.

The findings of this study align with those of Smalling et al. (2023) regarding PFAS detection in drinking water sources. In both studies, PFOS was among the most frequently detected PFAS, reinforcing its prevalence in groundwater and tap water systems. While this study found PFOS in 25% of tested private wells, with two exceeding the EPA's MCL of 4 ng/L, Smalling et al. (2023) also reported PFOS and PFOA detections above regulatory limits in both private wells and public supply systems, highlighting widespread contamination concerns. Additionally, both studies detected multiple PFAS compounds in individual samples, including short-chain and long-chain PFAS. However, in both cases, most detected compounds did not exceed their respective MCLs. The similarities between these findings emphasize the ongoing

need for monitoring and intervention efforts to address PFAS contamination across different water sources, particularly in private wells that may lack regulatory oversight.

The drastic difference in rates of PFAS detection between the two methods employed in this study – 0% vs. 51% of home wells - has important public health implications. Method-2, with its ability to detect much lower concentrations of PFAS below all respective MCLs, represents a significant advance in the PFAS analysis of drinking water sources. The 2023 nationwide study which screened 716 diverse drinking water sources for PFAS utilizing Method-1 found PFAS in about 45% of samples, with public and private sources presenting roughly comparable risk.[9] Based on the results of the current study, drinking water PFAS exposures, including at levels relevant for human-health concerns (e.g., MCLG for PFOS/PFOA is "zero"), may be higher than previously estimated[9] and consistent with recent USGS model estimating 50% to 66% of the US population potentially relying on groundwater with detectable PFAS for drinking water.[302]

Predictive modeling carried out by Tokranov et al.[302] emphasize the widespread nature of PFAS contamination in groundwater sources at drinking water supply depths. The authors highlight areas where PFAS levels are likely to be significantly higher due to industrial, military, and urban activities. Based on the result of the national groundwater model, occurrence can be estimated across grid cells[330] and can be used to estimate the probability of PFAS occurrence. For the Montana municipal areas of Bozeman, Ennis, Sheridan, and Whitehall sampled as part of the current study, estimated PFAS occurrence from the groundwater model was compared to the occurrence in tap water measured across our three counties. In the Bozeman and Belgrade region of Gallatin County, prediction models show that almost the entire city is covered in grids with a

probability of detecting PFAS ranging between 0.316 – 1 and exhibit the highest predicted probability of PFAS detection compared to the other cities discussed. As expected, the highest probabilities of occurrence are concentrated in the most populated areas of both towns. Ennis, located in Madison County, has one grid with a probability of PFAS detection between 0.501 and 0.75, with other grids showing no probability of detecting PFAS. Sheridan, also in Madison County, has multiple grids with probabilities in the ranges of 0.316 – 0.5 and 0.501 – 0.75. Lastly, in Whitehall, located in Jefferson County, several grids fall within the probability ranges of 0.316 – 0.5 and 0.501 – 0.75, with the highest probabilities occurring in the central downtown area. These data suggest a strong likelihood of PFAS contamination across these regions, particularly in more populated areas. Further, PFAS are predicted to occur even in rural developing communities across Montana. In Gallatin county (specifically Belgrade and Bozeman) where the predicted model showed a high probability of detecting PFAS, detection of PFAS were highest.The Tokranov et al. findings underscore the risk of PFAS contamination in groundwater, a primary source of drinking water for many regions, especially in areas with known contamination sources. This aligns with the hypothesis that PFAS exposures could be much higher than previously realized, due to the limitations of prior detection methods and the expansive distribution of PFAS in groundwater sources, as demonstrated by the modeling efforts in their study.

In this study, PFAS were detected in groundwater even in rural areas located upgradient of any industrial activity. These findings highlight how contaminants can enter groundwater through various sources unrelated to recognized industrial contamination. Landfill leachate is a known source of PFAS, as these chemicals are often found in consumer products buried in

landfills.[299] Septage from septic systems and agricultural application of biosolids (treated sewage sludge) can also be sources of PFAS contamination, as these materials may contain PFAS originating in household products.[298] Additionally, PFAS can be atmospherically transported from distant sources, deposited via rainfall and snowfall, and subsequently infiltrate into the ground.[294] Rural areas that rely on public wastewater treatment systems may be at risk for PFAS exposure in drinking water, as these systems may not be equipped to remove PFAS, allowing the contaminated effluent to be discharged and seep into the groundwater. These diverse pathways highlight the potential for and complexity of PFAS contamination of groundwater, even in areas without significant industrial presence.

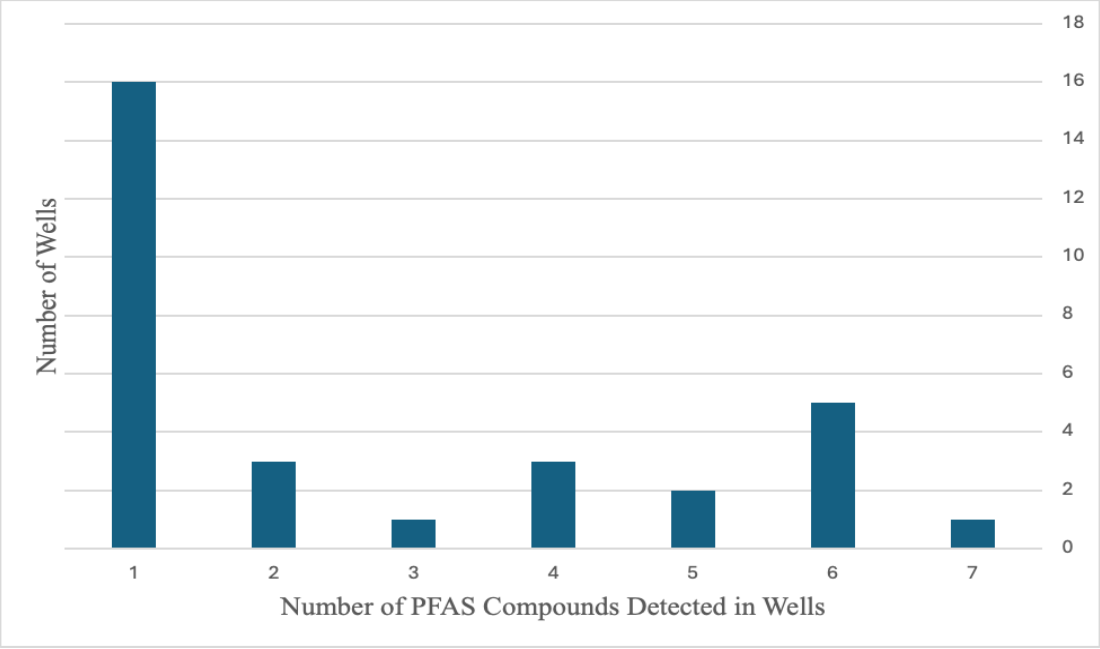



Figure 5.2. Count of wells by number of PFAS detected across the study area. The X axis is the number of PFAS detected per well (1-7) and the Y axis is the number of wells with that PFAS detections. This figure represents the prevalence of multiple PFAS in wells, for a total of 31 positive detections. 28 wells were found to have zero detected PFAS.

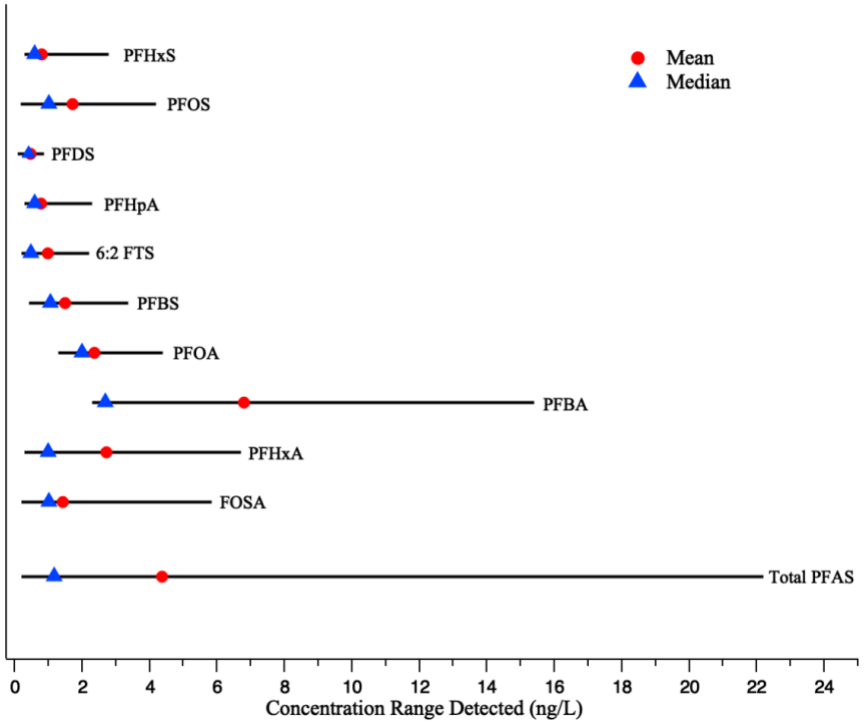



Figure 5.3. Range, mean and median concentrations for positive detections as a function of concentration (ng/L) using Method-2. The circle represents the mean concentration, the triangle the median, and the line extends to the minimum and maximum concentration of each analyte detected. Detection limits can be found in the Appendix D.

### 5.3.2 PFAS Detection by Property Size

Most detections of PFAS in well water were for properties less than 4 hectares (10 acres) in size (Figure 5.4). Furthermore, properties under 4 hectares had higher numbers of PFAS in groundwater. Qualitatively, our finding of higher PFAS detection counts from wells on smaller property sizes agrees with previous studies that found higher likelihood of PFAS presence in areas with concentrated human activity, such as urbanized regions that typically feature smaller properties.[9, 331] Ninety-eight percent of wells tested in this study were on properties that also had a septic tank and in subdivisions where all properties rely on individual septic systems, property size serves as a direct indicator of the density of septic drain fields discharging wastewater to

groundwater.[332, 333] Higher-density developments with smaller lots contribute to greater localized PFAS loading due to greater per-area wastewater discharge, as seen with other contaminants such as nitrogen and phosphorus.[333]

Larger properties, by contrast, exhibit a lower probability of PFAS detections in groundwater. This result may simply be due to the reduced density of contaminant sources. However, specific land uses—such as historical industrial activity, landfills, firefighting training areas, and certain agricultural practices—can still lead to elevated PFAS concentrations even on large land parcels.[11, 12] While property size is a coarse metric, it functions as a surrogate for land use intensity, particularly in areas dependent on septic systems, where wastewater discharge patterns directly influence groundwater PFAS contamination.

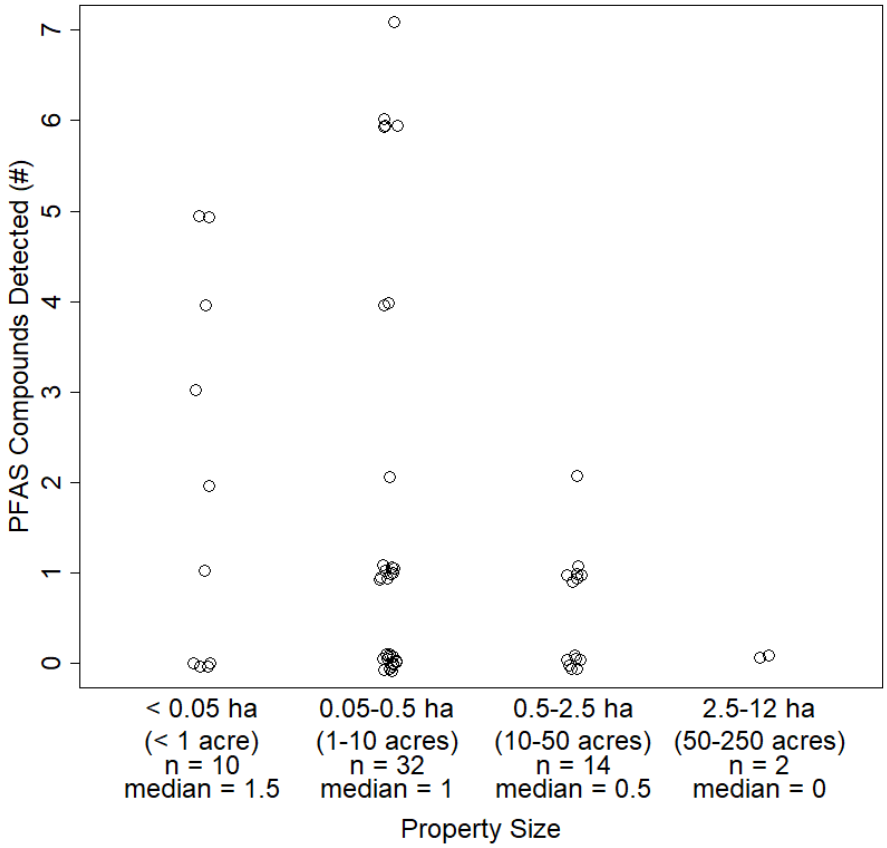



Figure 5.4. Property size vs. PFAS compounds detected. For the categories along the X axis, n is the number of wells of that property size, and median is the median number of PFAS compounds detected for that size category.

5.3.3 PFAS Detection by Well Depth

Private wells are often much shallower than public wells,[334] and hence are more vulnerable to PFAS contamination. Two primary factors likely drive this pattern. First, deeper groundwater is generally older, meaning it was recharged before widespread PFAS use and contamination.[335] As a result, older water is less likely to contain anthropogenic PFAS inputs. Second, deeper groundwater follows a longer flow path through the subsurface, increasing the likelihood of PFAS sorption by soil and sediment particles and resultant removal from the mobile, dissolved phase.[335] In contrast, shallow groundwater commonly has shorter residence

times and can be more directly affected by recent surface contamination sources, such as septic system discharge, industrial runoff, and atmospheric deposition.[333] [333] Figure 5.5 illustrates that shallower wells in our study exhibited higher levels of PFAS compared to deeper wells. This pattern suggests that PFAS contamination may be more concentrated in shallow, often unconfined groundwater.

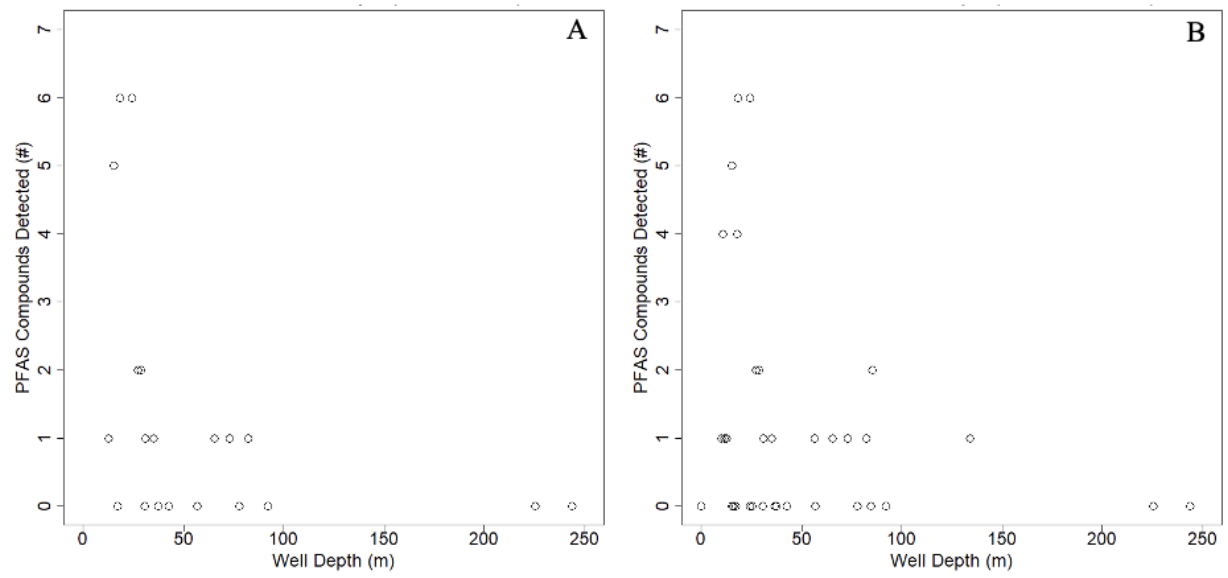



Figure 5.5. (A) Well depth vs. PFAS detected with high confidence well depth (B) Well depth vs. PFAS detected with at least medium confidence well depth data added.
*High confidence indicates that a well log with a depth was identified, was clearly linked to the well, and confirmed by the participant A well depth was categorized as high confidence (A) when a well log was identified with the depth specified, the log was clearly linked to the well and the linkage was confirmed by the participant. A well depth was categorized as medium (B) when a well log was identified that appeared clearly linked to the well, but the participant was not able to be contacted to confirm the linkage OR if the participant provided the well depth and indicated it was not an estimate, but a well log could not be located.

### 5.3.4 Cumulative Risk Assessment

Assessing the cumulative health risk from multiple PFAS exposures is particularly appropriate because of the large number of different PFAS that may coexist in the environment. Studies have shown that exposure to PFAS mixtures can lead to additive or synergistic adverse

health effects, making cumulative risks assessments a critical contributor to public health awareness.[336] The EPA has increasingly adopted CRA methodologies to assess PFAS risks, using these frameworks to inform the development of regulatory limits, such MCLs,[310] and to guide public health strategies to reduce PFAS exposure in affected populations.[313, 337]

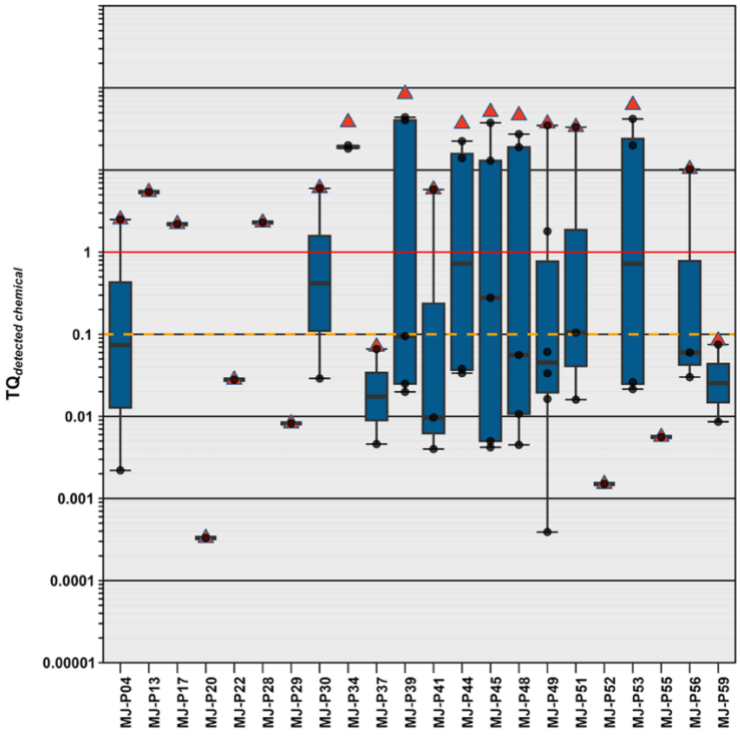



Figure 5.6. Human-health benchmark cumulative toxicity quotient ($\Sigma_{TQ}$) for six PFAS (PFOA, PFOS, PFHxS, PFBS, PFHxA, and PFBA), for each of 22 wells with PFAS detections. Red triangles (▲) are the sum of individual TQs across sites with PFAS detections. The red line at 1.0 represents the threshold at which risk can be assumed. The orange dashed line at 0.1 indicates a precautionary screening threshold. Nine other sites had detectable PFAS concentrations but negligible $\Sigma_{TQ}$ (i.e., $\Sigma_{TQ}$ <0.00001) and are not included in the plot.

Of the 31 wells assessed for cumulative risk (CRA), 15 were found to have a $\Sigma_{TQ}$ exceeding 1.0, indicating risks for adverse health effects from lifetime consumption of PFAS-contaminated water (Figure 5.6, Appendix Table D-3). Note, nine wells with detectable PFAS but $\Sigma_{TQ}$ less than 0.00001 are not included in Appendix Table D-3 or in Figure 5.6. in Appendix

Table D-3 highlights that PFOA and PFOS (MCLGs of "zero") are the primary contributors to the cumulative risk in the studied wells, accounting for most of the total risk (Table 5.1 and in Appendix Table D-3). The presence of PFAS at levels that constitute chronic health risk underscores the importance of addressing contamination in private wells, particularly in developing areas where the density of septic systems increases groundwater contamination levels.[338] These findings emphasize the need for targeted interventions in private-well-dependent communities, including more groundwater quality monitoring for complex mixtures of PFAS and implementation of affordable and accessible home well water testing, education and dissemination of in-home treatment systems to protect public health.

The findings of this study align closely with those of Smalling et al. (2023), both demonstrating that PFAS contamination in drinking water poses a significant cumulative risk. In this study, 15 of 31 assessed wells had a ΣTQ exceeding 1.0, indicating potential adverse health effects from long-term PFAS exposure, a pattern also observed in Smalling et al., where both private well and tap water samples exceeded this risk threshold. In both studies, PFOA and PFOS were the primary contributors to cumulative risk due to their proposed MCLGs of zero. Additionally, the frequent detection of multiple PFAS compounds in single samples was consistent across studies, reinforcing concerns about widespread contamination. The presence of PFAS at levels constituting chronic health risks highlights the urgent need to address contamination in private wells, particularly in developing areas where increasing septic system density may exacerbate groundwater pollution.

Community partnerships, such as those with Well Educated, play a vital role in advancing research on PFAS contamination in private wells. These collaborations provide access to crucial

well water data that would otherwise be difficult to obtain, given the decentralized and private nature of these water sources. However, the success of such partnerships depends on building and maintaining trust with well owners and local communities. Transparency, education, and open communication are essential to fostering this trust, ensuring that residents feel empowered to participate in data collection efforts. By strengthening these relationships, we can enhance our ability to monitor and address PFAS contamination, ultimately leading to more effective public health interventions.

## 5.4 Conclusions

Given the growing concerns over the presence of PFAS, especially the recent epidemiology study which found associations between PFAS in drinking water and increased incidence of multiple types of cancer (incidence ratios from 1.02 to 1.33), application of more sensitive PFAS methods are essential. The results of the current study indicate that widely-employed less-sensitive PFAS methods may substantially underestimate the true occurrence and associated health risks of PFAS exposure from groundwater-based drinking water sources, as the application of a more sensitive PFAS analytical method revealed the previously-unrecognized presence of PFAS in private-well drinking water in rural to minimally-developed areas of Montana. Community partnerships like Well Educated are crucial for accessing private well data and understanding PFAS contamination. These collaborations rely on trust, built through transparency, education, and engagement. Strengthening these relationships will improve data collection and support more effective public health interventions.

# CHAPTER 6

# CONCLUSION AND FUTURE DIRECTIONS

## 6.1 Summary of Research

This thesis investigates the surface and bulk solution behavior of PFAS, the impact of PFOA on biomembranes, the cooperative adsorption of PFOA to lipid monolayers, and the presence of PFAS in private wells across rural southern Montana counties.

Initial research focused on the behavior of three PFAS compounds—PFOA, PFOS, and PFBS—in both surface and bulk solutions. Chapter 2 specifically examined the reported critical micelle concentration (CMC) values in the literature, revealing that all three PFAS compounds have significantly lower CMCs than previously stated. Additionally, instead of forming small micelles (<10 nm) as commonly believed, all three PFAS were found to aggregate at the air-water interface. Surface tension and conductivity data confirmed that PFOA, PFBS, and PFOS exhibit surface-active properties, behaving like traditional soluble surfactants. Further investigations into the effects of pH on surface activity revealed that the behavior of these compounds is highly pH dependent. Both surface tension and conductivity measurements showed consistent CMC values in the micromolar concentration range. Dynamic Light Scattering (DLS) measurements indicated that at concentrations near the predicted CMC, particles smaller than 10 nm form. However, unlike typical micelles, these particles continuously grow with increasing concentration, reaching sizes between 50 to 150 nm. Cryo-EM images of PFOA corroborated these findings, showing a wide distribution of particle sizes that supports the DLS results.

Chapter 3 explores the impact of nanomolar concentrations of PFOA on the properties of DPPC vesicle bilayers. Differential Scanning Calorimetry (DSC) measurements revealed that PFOA concentrations just above regulatory limits (~1 nM) reduce the enthalpy of the gel-to-liquid crystalline transition of DPPC without altering the transition temperature. Dynamic Light Scattering (DLS) measurements indicated that the addition of PFOA to DPPC vesicle solutions broadens the size distribution of the vesicles, with a new peak emerging for smaller particles in the 30–50 nm range. Cryo-EM images further confirmed that DPPC vesicles formed in the presence of PFOA develop multilamellar structures, along with niosome-like formations. Niosomes are composed of lamellar structures formed from nonionic surfactants and biological materials. Additional research by co-author Rhys Trousdale using Time-Correlated Single Photon Counting (TCSPC) measurements showed that, in the presence of PFOA, the compound C152 is more likely to partition into the hydrophobic interior of the bilayer.

Chapter 4 examined PFOA's cooperative adsorption to loosely and tightly packed DPPC monolayers. Vibrational sum frequency generation (VSFG) measurements of the CH stretching region, PFOA was shown to decrease the $CH_2$ stretching in loosely packed 55 $Å^2$/molecule DPPC monolayers, suggesting that PFOA makes the monolayer more ordered by pushing DPPC groups together at the air-water interface. In contrast, PFOA had little effect on tightly packed 40 $Å^2$/molecule DPPC monolayers, as there was no space for PFOA to interact with the DPPC groups. VSFG OH data shows interfacial water is present with both PFOA in solution and in samples with DPPC at the surface. Despite different outcomes in the CH region, PFOA impacts interfacial water structure similarly in both systems. The spectra display two broad features around 3200 $cm^{-1}$ (ordered "ice-like" water) and 3450 $cm^{-1}$ (disordered "water-like" water). This

behavior, commonly observed for charged surfactants, is explained by the double layer formed by surfactants and their counterions, creating a strong interfacial electric field that aligns water molecules with their $C_2$ axes along the surface normal. DPPC compression isotherms obtained on a Langmuir trough with varying PFOA concentrations in the subphase showed that PFOA shifts the behavior of the DPPC monolayer. In the presence of PFOA, the liftoff occurs at higher surface areas, and the liquid expanded-liquid condensed coexistence region shifts to higher surface pressures. As PFOA concentration increases, the surface pressure rises significantly, and the monolayer collapses at a lower pressure compared to pure DPPC. These results indicate that PFOA remains at the surface with DPPC throughout compression.

Chapter 5 explores private wells in Montana counties to understand if PFAS compounds are observed in rural and developing areas. Results show PFAS were detected in private wells in rural Montana, where no industrial use of these chemicals occurs. Initial testing under Method-1, with a higher detection limit, found no PFAS, but more sensitive reanalysis, Method-2 (with lower detection capabilities) revealed PFAS in 53% of wells, with common compounds including PFOS and PFOA. Shallow wells and smaller properties had higher PFAS concentrations, and health risks were elevated in 25% of wells. These findings highlight the need for advanced analytical methods to better assess PFAS contamination and associated health risks in drinking water.

## 6.2 Future Directions

The experiments presented have provided new and significant insights into the behavior of legacy PFAS and their impact on biological membranes and monolayers. However, there are still unresolved questions within these systems that require further revision and exploration. The

remaining questions arising from this research can be grouped into two main areas: developing a more accurate model of cell membranes and lung surfactant and exploring the coexistence of PFAS within a single system.

### 6.2.1 Accurate Modeling of Membranes and Surfactant

#### 6.2.1.1 Cell Membranes.

The work described in this dissertation examined PFOA's impact on lipid vesicle bilayers. Phospholipids are a major component of cell membranes, with DPPC being a significant contributor to the phospholipid composition.[56, 339, 340] To more accurately understand the effects of PFOA and other legacy PFAS on cell membranes, developing a more comprehensive model that includes other lipids, proteins, and carbohydrates could provide a clearer representation of the interactions and behaviors within the membrane system. This approach would allow for a more holistic understanding of how PFAS molecules interact with various components of the membrane, affecting its stability, fluidity, and functionality. Additionally, incorporating proteins and carbohydrates, which play vital roles in membrane signaling, transport, and cellular communication, would provide insights into how PFAS may disrupt these processes.[341] By advancing the model to reflect the complexity of biological membranes, we can better assess the potential cellular impacts of PFAS exposure and develop more accurate predictions for their effects on health and membrane integrity.

#### 6.2.1.2 Lung Surfactant.

The work described in this dissertation examined DPPC as a model monolayer due to its prominence as the primary lipid component of lung surfactant. Lung surfactant, which is essential for reducing surface tension in the lungs and preventing alveolar collapse, is composed of approximately 90% lipids and 10% proteins.[245] The lipid content consists predominantly of DPPC (dipalmitoylphosphatidylcholine), with smaller amounts of

other lipids, including phosphatidylserine, phosphatidylethanolamine, and sphingomyelin. In addition to the lipids, lung surfactant also contains several surfactant-associated proteins: SP-A, SP-B, SP-C, and SP-D.[245, 342] These proteins are integral to the function and regulation of surfactant. SP-A and SP-D, which are surfactant collectins, play roles in the immune defense of the lungs by facilitating pathogen recognition and clearance, as well as modulating inflammation.[343] SP-B and SP-C are hydrophobic proteins that are critical for the proper formation and stability of the surfactant film at the alveolar surface.[344] SP-B, in particular, is essential for reducing surface tension and ensuring the proper spreading and retraction of the surfactant film during the respiratory cycle.

While DPPC is a well-established model for studying lung surfactant, the inclusion of the other lipids and proteins found in natural surfactant is essential for developing a more accurate model. The interactions between lipids and surfactant proteins are complex and dynamic, and their role in lung surfactant function can be better understood by considering both lipid-lipid and lipid-protein interactions within the monolayer. Because inhalation of PFAS such as PFOA can cause acute lung toxicity and cause airway infections, using a more accurate model of lung surfactant should be an important mission of future research.

### 6.2.2 Coexistence of PFAS

This dissertation primarily examined the individual behaviors of PFOA, PFOS, and PFBS. However, these PFAS compounds often coexist in the environment and within the human body. When multiple PFAS are present together in a system, they have the potential to interact, resulting in synergistic, antagonistic, or additive effects, depending on the compounds and the

biological environment.[336, 345] While research into the synergistic effects of PFAS interactions is ongoing, much remains to be understood about how these substances behave when combined.

Different PFAS molecules may interact with lipid membranes in distinct ways, altering fluidity, permeability, and protein function. The presence of multiple PFAS could amplify these changes, leading to greater disruption of cellular membranes or increased bioaccumulation. On the other hand, some PFAS may have antagonistic effects, potentially counteracting each other's toxicity. However, antagonistic effects are less commonly observed or discussed. Synergistic effects have been noted in endocrine disruption, immune system suppression, and liver toxicity, where multiple PFAS chemicals may work together to exacerbate these issues.[345-347] Environmental and biological factors, such as pH, temperature, and exposure duration, can further influence these effects. As the research into PFAS mixtures is still in its early stages, more studies are needed to fully understand the broader implications for human health and ecosystems.

# CUMULATIVE REFERENCES CITED

(1) Fu, J.; Gao, Y.; Cui, L.; Wang, T.; Liang, Y.; Qu, G.; Yuan, B.; Wang, Y.; Zhang, A.; Jiang, G. Occurrence, temporal trends, and half-lives of perfluoroalkyl acids (PFAAs) in occupational workers in China. *Sci Rep* **2016**, *6*, 38039. DOI: 10.1038/srep38039.

(2) Schellenberger, S.; Liagkouridis, I.; Awad, R.; Khan, S.; Plassmann, M.; Peters, G.; Benskin, J. P.; Cousins, I. T. An Outdoor Aging Study to Investigate the Release of Per- And Polyfluoroalkyl Substances (PFAS) from Functional Textiles. *Environ Sci Technol* **2022**, *56* (6), 3471-3479. DOI: 10.1021/acs.est.1c06812.

(3) Li, M.; Hu, J.; Cao, X.; Chen, H.; Lyu, Y.; Sun, W. Nontarget Analysis Combined with TOP Assay Reveals a Significant Portion of Unknown PFAS Precursors in Firefighting Foams Currently Used in China. *Environ Sci Technol* **2024**. DOI: 10.1021/acs.est.4c07879.

(4) Eze, C. G.; Okeke, E. S.; Nwankwo, C. E.; Nyaruaba, R.; Anand, U.; Okoro, O. J.; Bontempi, E. Emerging contaminants in food matrices: An overview of the occurrence, pathways, impacts and detection techniques of per- and polyfluoroalkyl substances. *Toxicol Rep* **2024**, *12*, 436-447. DOI: 10.1016/j.toxrep.2024.03.012.

(5) Dewapriya, P.; Chadwick, L.; Gorji, S. G.; Schulze, B.; Valsecchi, S.; Samanipour, S.; Thomas, K. V.; Kaserzon, S. L. Per- and polyfluoroalkyl substances (PFAS) in consumer products: Current knowledge and research gaps. *Journal of Hazardous Materials Letters* **2023**, *4*. DOI: 10.1016/j.hazl.2023.100086.

(6) US Environmental Protection Agency. *Our Current Understanding of the Human Health and Environmental Risks of PFAS*. 2024. https://www.epa.gov/pfas/our-current-understanding-human-health-and-environmental-risks-pfas?utm_source=chatgpt.com

(7) Fujii, S.; Polprasert, C.; Tanaka, S.; Hong Lien, N. P.; Qiu, Y. New POPs in the water environment: distribution, bioaccumulation and treatment of perfluorinated compounds – a review paper. *J. Water Supply: Rese.Technol.-Aqua* **2007**, *56* (5), 313-326. DOI: 10.2166/aqua.2007.005.

(8) Von Behren, J.; Reynolds, P.; Bradley, P. M.; Gray, J. L.; Kolpin, D. W.; Romanok, K. M.; Smalling, K. L.; Carpenter, C.; Avila, W.; Ventura, A.; et al. Per- and polyfluoroalkyl substances (PFAS) in drinking water in Southeast Los Angeles: Industrial legacy and environmental justice. *Sci Total Environ* **2024**, *953*, 176067. DOI: 10.1016/j.scitotenv.2024.176067.

(9) Smalling, K. L.; Romanok, K. M.; Bradley, P. M.; Morriss, M. C.; Gray, J. L.; Kanagy, L. K.; Gordon, S. E.; Williams, B. M.; Breitmeyer, S. E.; Jones, D. K.; et al. Per- and polyfluoroalkyl substances (PFAS) in United States tapwater: Comparison of underserved private-well and public-supply exposures and associated health implications. *Environ Int* **2023**, *178*, 108033. DOI: 10.1016/j.envint.2023.108033.

(10) McMahon, P. B.; Tokranov, A. K.; Bexfield, L. M.; Lindsey, B. D.; Johnson, T. D.; Lombard, M. A.; Watson, E. Perfluoroalkyl and Polyfluoroalkyl Substances in Groundwater Used as a Source of Drinking Water in the Eastern United States. *Environ Sci Technol* **2022**, *56* (4), 2279-2288. DOI: 10.1021/acs.est.1c04795.

(11) Wang, Y.; Munir, U.; Huang, Q. Occurrence of per- and polyfluoroalkyl substances (PFAS) in soil: Sources, fate, and remediation. *Soil & Environmental Health* **2023**, *1* (1). DOI: 10.1016/j.seh.2023.100004.

(12) Brusseau, M. L.; Anderson, R. H.; Guo, B. PFAS concentrations in soils: Background levels versus contaminated sites. *Sci Total Environ* **2020**, *740*, 140017. DOI: 10.1016/j.scitotenv.2020.140017.

(13) Borthakur, A.; Cranmer, B. K.; Dooley, G. P.; Blotevogel, J.; Mahendra, S.; Mohanty, S. K. Release of soil colloids during flow interruption increases the pore-water PFAS concentration in saturated soil. *Environ Pollut* **2021**, *286*, 117297. DOI: 10.1016/j.envpol.2021.117297.

(14) US Environmental Protection Agency. National-Scale Air Toxics Assessment. US Environmental Protection Agency, Ed.; 2011.

(15) Morales-McDevitt, M. E.; Becanova, J.; Blum, A.; Bruton, T. A.; Vojta, S.; Woodward, M.; Lohmann, R. The Air that we Breathe: Neutral and volatile PFAS in Indoor Air. *Environ Sci Technol Lett* **2021**, *8* (10), 897-902. DOI: 10.1021/acs.estlett.1c00481.

(16) Barbo, N.; Stoiber, T.; Naidenko, O. V.; Andrews, D. Q. Locally caught freshwater fish across the United States are likely a significant source of exposure to PFOS and other perfluorinated compounds. *Environ Res* **2023**, *220*, 115165. DOI: 10.1016/j.envres.2022.115165.

(17) Manera, M.; Castaldelli, G.; Giari, L. Perfluorooctanoic Acid Promotes Recruitment and Exocytosis of Rodlet Cells in the Renal Hematopoietic Tissue of Common Carp. *Toxics* **2023**, *11* (10). DOI: 10.3390/toxics11100831.

(18) Ren, J. D.; Point, A. D.; Baygi, S. F.; Fernando, S.; Hopke, P. K.; Holsen, T. M.; Crimmins, B. S. Bioaccumulation of polyfluoroalkyl substances in the Lake Huron aquatic food web. *Sci. Total Environ.* **2022**, *819*. DOI: 10.1016/j.scitotenv.2022.152974.

(19) Munoz, G.; Mercier, L.; Duy, S. V.; Liu, J. X.; Sauve, S.; Houde, M. Bioaccumulation and trophic magnification of emerging and legacy per-and polyfluoroalkyl substances (PFAS) in a St. Lawrence River food web. *Environ. Pollut.* **2022**, *309*. DOI: 10.1016/j.envpol.2022.119739.

(20) Brase, R. A.; Schwab, H. E.; Li, L.; Spink, D. C. Elevated levels of per- and polyfluoroalkyl substances (PFAS) in freshwater benthic macroinvertebrates from the Hudson River Watershed. *Chemosphere* **2022**, *291* (Pt 2), 132830. DOI: 10.1016/j.chemosphere.2021.132830.

(21) Kannan, K.; Hansen, K. J.; Wade, T. L.; Giesy, J. P. Perfluorooctane sulfonate in oysters, Crassostrea virginica, from the Gulf of Mexico and the Chesapeake Bay, USA. *rch. Environ. Contam. Toxicol.* **2002**, *42* (3), 313-318. DOI: 10.1007/s00244-001-0003-8.

(22) Drew, R.; Hagen, T. G.; Champness, D.; Sellier, A. Half-lives of several polyfluoroalkyl substances (PFAS) in cattle serum and tissues. *Food Addit Contam Part A Chem Anal Control Expo Risk Assess* **2022**, *39* (2), 320-340. DOI: 10.1080/19440049.2021.1991004.

(23) Drew, R.; Hagen, T. G.; Champness, D. Accumulation of PFAS by livestock - determination of transfer factors from water to serum for cattle and sheep in Australia. *Food Addit Contam Part A Chem Anal Control Expo Risk Assess* **2021**, *38* (11), 1897-1913. DOI: 10.1080/19440049.2021.1942562.

(24) De Silva, A. O.; Armitage, J. M.; Bruton, T. A.; Dassuncao, C.; Heiger-Bernays, W.; Hu, X. C.; Karrman, A.; Kelly, B.; Ng, C.; Robuck, A.; et al. PFAS Exposure Pathways for Humans and Wildlife: A Synthesis

of Current Knowledge and Key Gaps in Understanding. *Environ Toxicol Chem* **2021**, *40* (3), 631-657. DOI: 10.1002/etc.4935.

(25) Woolf, A. D.; Zajac, L. Report outlines health effects of PFAS chemicals in children, provides recommendations for testing. *AAP News* **2022**.

(26) Wee, S. Y.; Aris, A. Z. Environmental impacts, exposure pathways, and health effects of PFOA and PFOS. *Ecotoxicol Environ Saf* **2023**, *267*, 115663. DOI: 10.1016/j.ecoenv.2023.115663.

(27) National Center for Environmental Health (U.S.). Division of Laboratory Sciences.;; National Center for Health Statistics (U.S.);National Health and Nutrition Examination Survey (U.S.). Fourth national report on human exposure to environmental chemicals. Updated tables, March 2021 : volume three: Analysis of Pooled Serum Samples for Select Chemicals, NHANES 2005-2016. **2021**, *3*.

(28) Winquist, A.; Hodge, J. M.; Diver, W. R.; Rodriguez, J. L.; Troeschel, A. N.; Daniel, J.; Teras, L. R. Case-Cohort Study of the Association between PFAS and Selected Cancers among Participants in the American Cancer Society's Cancer Prevention Study II LifeLink Cohort. *Environ Health Perspect* **2023**, *131* (12), 127007. DOI: 10.1289/EHP13174.

(29) Shearer, J. J.; Callahan, C. L.; Calafat, A. M.; Huang, W. Y.; Jones, R. R.; Sabbisetti, V. S.; Freedman, N. D.; Sampson, J. N.; Silverman, D. T.; Purdue, M. P.; et al. Serum Concentrations of Per- and Polyfluoroalkyl Substances and Risk of Renal Cell Carcinoma. *J Natl Cancer Inst* **2021**, *113* (5), 580-587. DOI: 10.1093/jnci/djaa143.

(30) Purdue, M. P.; Rhee, J.; Denic-Roberts, H.; McGlynn, K. A.; Byrne, C.; Sampson, J.; Botelho, J. C.; Calafat, A. M.; Rusiecki, J. A Nested Case-Control Study of Serum Per- and Polyfluoroalkyl Substances and Testicular Germ Cell Tumors among U.S. Air Force Servicemen. *Environ Health Perspect* **2023**, *131* (7), 77007. DOI: 10.1289/EHP12603.

(31) Bailey, J. M.; Wang, L.; McDonald, J. M.; Gray, J. S.; Petrie, J. G.; Martin, E. T.; Savitz, D. A.; Karrer, T. A.; Fisher, K. A.; Geiger, M. J.; et al. Immune response to COVID-19 vaccination in a population with a history of elevated exposure to per- and polyfluoroalkyl substances (PFAS) through drinking water. *J Expo Sci Environ Epidemiol* **2023**, *33* (5), 725-736. DOI: 10.1038/s41370-023-00564-8.

(32) Crawford, L.; Halperin, S. A.; Dzierlenga, M. W.; Skidmore, B.; Linakis, M. W.; Nakagawa, S.; Longnecker, M. P. Systematic review and meta-analysis of epidemiologic data on vaccine response in relation to exposure to five principal perfluoroalkyl substances. *Environ Int* **2023**, *172*, 107734. DOI: 10.1016/j.envint.2023.107734.

(33) Andersen, M. E.; Hagenbuch, B.; Apte, U.; Corton, J. C.; Fletcher, T.; Lau, C.; Roth, W. L.; Staels, B.; Vega, G. L.; Clewell, H. J., 3rd; et al. Why is elevation of serum cholesterol associated with exposure to perfluoroalkyl substances (PFAS) in humans? A workshop report on potential mechanisms. *Toxicology* **2021**, *459*, 152845. DOI: 10.1016/j.tox.2021.152845.

(34) Haug, M.; Dunder, L.; Lind, P. M.; Lind, L.; Salihovic, S. Associations of perfluoroalkyl substances (PFAS) with lipid and lipoprotein profiles. *J Expo Sci Environ Epidemiol* **2023**, *33* (5), 757-765. DOI: 10.1038/s41370-023-00545-x.

(35) Coperchini, F.; Croce, L.; Ricci, G.; Magri, F.; Rotondi, M.; Imbriani, M.; Chiovato, L. Thyroid Disrupting Effects of Old and New Generation PFAS. *Front Endocrinol (Lausanne)* **2020**, *11*, 612320. DOI: 10.3389/fendo.2020.612320.

(36) Budtz-Jorgensen, E.; Grandjean, P. Application of benchmark analysis for mixed contaminant exposures: Mutual adjustment of perfluoroalkylate substances associated with immunotoxicity. *PLoS One* **2018**, *13* (10), e0205388. DOI: 10.1371/journal.pone.0205388.

(37) Timmermann, C. A. G.; Pedersen, H. S.; Weihe, P.; Bjerregaard, P.; Nielsen, F.; Heilmann, C.; Grandjean, P. Concentrations of tetanus and diphtheria antibodies in vaccinated Greenlandic children aged 7-12 years exposed to marine pollutants, a cross sectional study. *Environ Res* **2022**, *203*, 111712. DOI: 10.1016/j.envres.2021.111712.

(38) Granum, B.; Haug, L. S.; Namork, E.; Stolevik, S. B.; Thomsen, C.; Aaberge, I. S.; van Loveren, H.; Lovik, M.; Nygaard, U. C. Pre-natal exposure to perfluoroalkyl substances may be associated with altered vaccine antibody levels and immune-related health outcomes in early childhood. *J Immunotoxicol* **2013**, *10* (4), 373-379. DOI: 10.3109/1547691X.2012.755580.

(39) Zhang, Y.; Mustieles, V.; Wang, Y. X.; Sun, Q.; Coull, B.; Sun, Y.; Slitt, A.; Messerlian, C. Red Blood Cell Folate Modifies the Association between Serum Per- and Polyfluoroalkyl Substances and Antibody Concentrations in U.S. Adolescents. *Environ Sci Technol* **2023**, *57* (6), 2445-2456. DOI: 10.1021/acs.est.2c07152.

(40) Dong, Z.; Wang, H.; Yu, Y. Y.; Li, Y. B.; Naidu, R.; Liu, Y. Using 2003–2014 U.S. NHANES data to determine the associations between per- and polyfluoroalkyl substances and cholesterol: Trend and implications. *Ecotoxicol. Environ. Saf.* **2019**, *173*, 461-468. DOI: 10.1016/j.ecoenv.2019.02.061.

(41) Steenland, K.; Tinker, S.; Frisbee, S.; Ducatman, A.; Vaccarino, V. Association of perfluorooctanoic acid and perfluorooctane sulfonate with serum lipids among adults living near a chemical plant. *Am J Epidemiol* **2009**, *170* (10), 1268-1278. DOI: 10.1093/aje/kwp279.

(42) Lin, P. D.; Cardenas, A.; Hauser, R.; Gold, D. R.; Kleinman, K. P.; Hivert, M. F.; Fleisch, A. F.; Calafat, A. M.; Webster, T. F.; Horton, E. S.; et al. Per- and polyfluoroalkyl substances and blood lipid levels in pre-diabetic adults-longitudinal analysis of the diabetes prevention program outcomes study. *Environ Int* **2019**, *129*, 343-353. DOI: 10.1016/j.envint.2019.05.027.

(43) Gallo, V.; Leonardi, G.; Genser, B.; Lopez-Espinosa, M. J.; Frisbee, S. J.; Karlsson, L.; Ducatman, A. M.; Fletcher, T. Serum perfluorooctanoate (PFOA) and perfluorooctane sulfonate (PFOS) concentrations and liver function biomarkers in a population with elevated PFOA exposure. *Environ Health Perspect* **2012**, *120* (5), 655-660. DOI: 10.1289/ehp.1104436.

(44) Darrow, L. A.; Groth, A. C.; Winquist, A.; Shin, H. M.; Bartell, S. M.; Steenland, K. Modeled Perfluorooctanoic Acid (PFOA) Exposure and Liver Function in a Mid-Ohio Valley Community. *Environ Health Perspect* **2016**, *124* (8), 1227-1233. DOI: 10.1289/ehp.1510391.

(45) Coprario, A. What a pediatrician wants parents to know about PFAS, the ‘forever chemicals.’. Novant Health: 2023.

(46) Anderko, L.; Pennea, E. Exposures to per-and polyfluoroalkyl substances (PFAS): Potential risks to reproductive and children's health. *Current Problems in Pediatric and Adolescent Health Care* **2020**, *50* (2), 100760. DOI: 10.1016/j.cppeds.2020.100760.

(47) Phelps, D. W.; Palekar, A. I.; Conley, H. E.; Ferrero, G.; Driggers, J. H.; Linder, K. E.; Kullman, S. W.; Reif, D. M.; Sheats, M. K.; DeWitt, J. C.; et al. Legacy and emerging per- and polyfluoroalkyl substances suppress the neutrophil respiratory burst. *J. Immunotoxicol.* **2023**, *20* (1). DOI: 10.1080/1547691x.2023.2176953.

(48) Zheng, T.; Kelsey, K.; Zhu, C.; Pennell, K. D.; Yao, Q.; Manz, K. E.; Zheng, Y. F.; Braun, J. M.; Liu, Y.; Papandonatos, G.; et al. Adverse birth outcomes related to concentrations of per- and polyfluoroalkyl substances (PFAS) in maternal blood collected from pregnant women in 1960-1966. *Environ Res* **2024**, *241*, 117010. DOI: 10.1016/j.envres.2023.117010.

(49) Key EPA Actions to Address PFAS. https://www.epa.gov/newsreleases/biden-harris-administration-announces-new-steps-protect-communities-pfas-and-other (accessed February 2024).

(50) Brennan, N. M.; Evans, A. T.; Fritz, M. K.; Peak, S. A.; von Holst, H. E. Trends in the Regulation of Per- and Polyfluoroalkyl Substances (PFAS): A Scoping Review. *Int J Environ Res Public Health* **2021**, *18* (20). DOI: 10.3390/ijerph182010900.

(51) Gatz, L. Regulating PFAS Under the Clean Water Act. Service, C. R., Ed.; 2022.

(52) U.S. Environmental Protection Agency. *Per- and Polyfluoroalkyl Substances (PFAS) Proposed PFAS National Primary Drinking Water Regulation*. 2023. https://www.epa.gov/sdwa/and-polyfluoroalkyl-substances-pfas.

(53) U.S. Environmental Protection Agency. *National Primary Drinking Water Regulations*. 2024. https://www.epa.gov/ground-water-and-drinking-water/national-primary-drinking-water-regulations (accessed 2024 December).

(54) Piosik, E.; Zaryczniak, A.; Mylkie, K.; Ziegler-Borowska, M. Probing of Interactions of Magnetite Nanoparticles Coated with Native and Aminated Starch with a DPPC Model Membrane. *Int J Mol Sci* **2021**, *22* (11). DOI: 10.3390/ijms22115939.

(55) Duncan, K. M.; Trousdale, R. C.; Gonzales, C. N.; Steel, W. H.; Walker, R. A. l-Phenylalanine Partitioning Mechanisms in Model Biological Membranes. *J. Phys. Chem. B* **2023**, *127* (25), 5633-5644. DOI: 10.1021/acs.jpcb.2c08582.

(56) Duncan, K. M.; Casey, A.; Gobrogge, C. A.; Trousdale, R. C.; Piontek, S. M.; Cook, M. J.; Steel, W. H.; Walker, R. A. Coumarin Partitioning in Model Biological Membranes: Limitations of log P as a Predictor. *J Phys Chem B* **2020**, *124* (38), 8299-8308. DOI: 10.1021/acs.jpcb.0c06109.

(57) Biltonen, R. L.; Lichtenberg, D. The use of differential scanning calorimetry as a tool to characterize liposome preparations. *Chemistry and Physics of Lipids* **1993**, *64*, 129-142. DOI: 10.1016/0009-3084(93)90062-8.

(58) Chen, W.; Dusa, F.; Witos, J.; Ruokonen, S. K.; Wiedmer, S. K. Determination of the Main Phase Transition Temperature of Phospholipids by Nanoplasmonic Sensing. *Sci Rep* **2018**, *8* (1), 14815. DOI: 10.1038/s41598-018-33107-5.

(59) Rieth, M. D.; Lozano, A. Preparation of DPPC liposomes using probe-tip sonication: Investigating intrinsic factors affecting temperature phase transitions. *Biochem Biophys Rep* **2020**, *22*, 100764. DOI: 10.1016/j.bbrep.2020.100764.

(60) Greaves, A. K.; Letcher, R. J.; Sonne, C.; Dietz, R.; Born, E. W. Tissue-specific concentrations and patterns of perfluoroalkyl carboxylates and sulfonates in East Greenland polar bears. *Environ Sci Technol* **2012**, *46* (21), 11575-11583. DOI: 10.1021/es303400f.

(61) ChemSpider. *CSID:9180 Perfluorooctanoic Acid*. Royal Society of Chemistry, https://www.chemspider.com/Chemical-Structure.9180.html, (accessed Nov 12, 2024).

(62) Zuo, Y. Y.; Veldhuizen, R. A.; Neumann, A. W.; Petersen, N. O.; Possmayer, F. Current perspectives in pulmonary surfactant--inhibition, enhancement and evaluation. *Biochim Biophys Acta* **2008**, *1778* (10), 1947-1977. DOI: 10.1016/j.bbamem.2008.03.021.

(63) Dragon, J.; Hoaglund, M.; Badireddy, A. R.; Nielsen, G.; Schlezinger, J.; Shukla, A. Perfluoroalkyl Substances (PFAS) Affect Inflammation in Lung Cells and Tissues. *Int J Mol Sci* **2023**, *24* (10). DOI: 10.3390/ijms24108539.

(64) Link, K. A.; Hsieh, C.-Y.; Tuladhar, A.; Chase, Z.; Wang, Z.; Wang, H.; Walker, R. A. Vibrational studies of saccharide-induced lipid film reorganization at aqueous/air interfaces. *Chem. Phys.* **2018**, *512*, 104-110. DOI: 10.1016/j.chemphys.2018.02.011.

(65) Link, K. A.; Spurzem, G. N.; Tuladhar, A.; Chase, Z.; Wang, Z.; Wang, H.; Walker, R. A. Organic Enrichment at Aqueous Interfaces: Cooperative Adsorption of Glucuronic Acid to DPPC Monolayers Studied with Vibrational Sum Frequency Generation. *J Phys Chem A* **2019**, *123* (26), 5621-5632. DOI: 10.1021/acs.jpca.9b02255.

(66) Link, K. A.; Spurzem, G. N.; Tuladhar, A.; Chase, Z.; Wang, Z.; Wang, H.; Walker, R. A. Cooperative Adsorption of Trehalose to DPPC Monolayers at the Water-Air Interface Studied with Vibrational Sum Frequency Generation. *J Phys Chem B* **2019**, *123* (42), 8931-8938. DOI: 10.1021/acs.jpcb.9b07770.

(67) Gobrogge, C. A.; Kong, V. A.; Walker, R. A. Temperature-Dependent Partitioning of C152 in Binary Phosphatidylcholine Membranes and Mixed Phosphatidylcholine/Phosphatidylethanolamine Membranes. *J Phys Chem B* **2017**, *121* (33), 7889-7898. DOI: 10.1021/acs.jpcb.7b04831.

(68) McElhaney, R. N. The use of differential scanning calorimetry and differential thermal analysis in studies of model and biological membranes. *Chemistry and Physics of Lipids* **1982**, *30*, 229-259.

(69) Repakova, J.; Holopainen, J. M.; Morrow, M. R.; McDonald, M. C.; Capkova, P.; Vattulainen, I. Influence of DPH on the structure and dynamics of a DPPC bilayer. *Biophys J* **2005**, *88* (5), 3398-3410. DOI: 10.1529/biophysj.104.055533.

(70) Almeida, P. F. A simple thermodynamic model of the liquid-ordered state and the interactions between phospholipids and cholesterol. *Biophys J* **2011**, *100* (2), 420-429. DOI: 10.1016/j.bpj.2010.12.3694.

(71) Drabik, D.; Chodaczek, G.; Kraszewski, S.; Langner, M. Mechanical Properties Determination of DMPC, DPPC, DSPC, and HSPC Solid-Ordered Bilayers. *Langmuir* **2020**, *36* (14), 3826-3835. DOI: 10.1021/acs.langmuir.0c00475.

(72) Grażyna Neunert, J. T.-G., Aneta Baj, Marlena Gauza-Włodarczyk, Stanislaw Witkowski, and Krzysztof Polewski. Phase Transitions and Structural Changes in DPPC Liposomes Induced by a 1-Carba-Alpha-Tocopherol Analogue. *Molecules* **2021**, *26(10)*, 2851. DOI: 10.3390/molecules26102851.

(73) Morandi, M. I.; Sommer, M.; Kluzek, M.; Thalmann, F.; Schroder, A. P.; Marques, C. M. DPPC Bilayers in Solutions of High Sucrose Content. *Biophys J* **2018**, *114* (9), 2165-2173. DOI: 10.1016/j.bpj.2018.04.003.

(74) Sabín, J.; Prieto, G.; Sennato, S.; Blanco, E.; Messina, P. V.; Ruso, J. M.; Angelini, R.; Bordi, F.; Sarmiento, F. Examination of the influence of F6H10 fluorinated diblocks on DPPC liposomes. *Journal of Thermal Analysis and Calorimetry* **2007**, *87* (1), 301-304. DOI: 10.1007/s10973-006-7846-1.

(75) Stetefeld, J.; McKenna, S. A.; Patel, T. R. Dynamic light scattering: a practical guide and applications in biomedical sciences. *Biophys Rev* **2016**, *8* (4), 409-427. DOI: 10.1007/s12551-016-0218-6.

(76) Hassan, P. A.; Rana, S.; Verma, G. Making sense of Brownian motion: colloid characterization by dynamic light scattering. *Langmuir* **2015**, *31* (1), 3-12. DOI: 10.1021/la501789z.

(77) Soderlund, T.; Alakoskela, J. M.; Pakkanen, A. L.; Kinnunen, P. K. Comparison of the effects of surface tension and osmotic pressure on the interfacial hydration of a fluid phospholipid bilayer. *Biophys J* **2003**, *85* (4), 2333-2341. DOI: 10.1016/S0006-3495(03)74657-8.

(78) Kontogeorgis, G. M.; Holster, A.; Kottaki, N.; Tsochantaris, E.; Topsøe, F.; Poulsen, J.; Bache, M.; Liang, X.; Blom, N. S.; Kronholm, J. Water structure, properties and some applications – A review. *Chemical Thermodynamics and Thermal Analysis* **2022**, *6*. DOI: 10.1016/j.ctta.2022.100053.

(79) Rosen, M. J. *Surfactants and interfacial phenomena*; John Wiley & Sons, Inc., 2004.

(80) Hammouda, B. Temperature Effect on the Nanostructure of SDS Micelles in Water. *J Res Natl Inst Stand Technol* **2013**, *118*, 151-167. DOI: 10.6028/jres.118.008.

(81) Tatur, S.; Badia, A. Influence of hydrophobic alkylated gold nanoparticles on the phase behavior of monolayers of DPPC and clinical lung surfactant. *Langmuir* **2012**, *28* (1), 628-639. DOI: 10.1021/la203439u.

(82) Harishchandra, R. K.; Saleem, M.; Galla, H. J. Nanoparticle interaction with model lung surfactant monolayers. *J R Soc Interface* **2010**, *7 Suppl 1* (Suppl 1), S15-26. DOI: 10.1098/rsif.2009.0329.focus.

(83) Shaikh, N.; Andriolo, J. M.; Skinner, J. L.; Walker, R. A. Carbon Nanoparticle-Induced Changes to Lipid Monolayer Structure at Water-Air Interfaces. *J Phys Chem B* **2022**, *126* (30), 5667-5677. DOI: 10.1021/acs.jpcb.2c02526.

(84) McClements, D. J. *Food Emulsions: Principles, Practices, and Techniques*; CRC Press, 2004. DOI: 10.1201/9781420039436.

(85) Duncan, S. L.; Larson, R. G. Comparing experimental and simulated pressure-area isotherms for DPPC. *Biophys J* **2008**, *94* (8), 2965-2986. DOI: 10.1529/biophysj.107.114215.

(86) Siebert, T. A.; Rugonyi, S. Influence of liquid-layer thickness on pulmonary surfactant spreading and collapse. *Biophys J* **2008**, *95* (10), 4549-4559. DOI: 10.1529/biophysj.107.127654.

(87) Hu, X. C.; Andrews, D. Q.; Lindstrom, A. B.; Bruton, T. A.; Schaider, L. A.; Grandjean, P.; Lohmann, R.; Carignan, C. C.; Blum, A.; Balan, S. A.; et al. Detection of Poly- and Perfluoroalkyl Substances (PFASs) in U.S. Drinking Water Linked to Industrial Sites, Military Fire Training Areas, and Wastewater Treatment Plants. *Environ Sci Technol Lett* **2016**, *3* (10), 344-350. DOI: 10.1021/acs.estlett.6b00260.

(88) Chohan, A.; Petaway, H.; Rivera-Diaz, V.; Day, A.; Colaianni, O.; Keramati, M. Per and polyfluoroalkyl substances scientific literature review: water exposure, impact on human health, and implications for regulatory reform. *Rev. Environ. Health* **2021**, *36* (2), 235-259. DOI: 10.1515/reveh-2020-0049.

(89) Andrews, D. Q.; Naidenko, O. V. Population-Wide Exposure to Per- and Polyfluoroalkyl Substances from Drinking Water in the United States. *Environmental Science & Technology Letters* **2020**, *7* (12), 931-936. DOI: 10.1021/acs.estlett.0c00713.

(90) Garg, S.; Kumar, P.; Mishra, V.; Guijt, R.; Singh, P.; Dumée, L. F.; Sharma, R. S. A review on the sources, occurrence and health risks of per-/poly-fluoroalkyl substances (PFAS) arising from the manufacture and disposal of electric and electronic products. *JWPE* **2020**, *38*. DOI: 10.1016/j.jwpe.2020.101683.

(91) Ruyle, B. J.; Thackray, C. P.; Butt, C. M.; LeBlanc, D. R.; Tokranov, A. K.; Vecitis, C. D.; Sunderland, E. M. Centurial Persistence of Forever Chemicals at Military Fire Training Sites. *Environ Sci Technol* **2023**, *57* (21), 8096-8106. DOI: 10.1021/acs.est.3c00675.

(92) Phelps, D. W.; Parkinson, L. V.; Boucher, J. M.; Muncke, J.; Geueke, B. Per- and Polyfluoroalkyl Substances in Food Packaging: Migration, Toxicity, and Management Strategies. *Environ Sci Technol* **2024**, *58* (13), 5670-5684. DOI: 10.1021/acs.est.3c03702.

(93) Gluge, J.; Scheringer, M.; Cousins, I. T.; DeWitt, J. C.; Goldenman, G.; Herzke, D.; Lohmann, R.; Ng, C. A.; Trier, X.; Wang, Z. An overview of the uses of per- and polyfluoroalkyl substances (PFAS). *Environ Sci Process Impacts* **2020**, *22* (12), 2345-2373. DOI: 10.1039/d0em00291g.

(94) US Environmental Protection Agency. *Biden-Harris Administration Finalizes First-Ever National Drinking Water Standard to Protect 100M People from PFAS Pollution*. U.S. Environmental Protection Agency. 2024. https://www.epa.gov/newsreleases/biden-harris-administration-finalizes-first-ever-national-drinking-water-standard (accessed July 2024).

(95) Montana DEQ. *Per- and Polyfluoroalkyl Substances Water Monitoring Project 2021 Fact Sheets*; 2022. https://deq.mt.gov/cleanupandrec/Programs/pfas (accessed July 2024).

(96) Ye, X.; Strynar, M. J.; Nakayama, S. F.; Varns, J.; Helfant, L.; Lazorchak, J.; Lindstrom, A. B. Perfluorinated compounds in whole fish homogenates from the Ohio, Missouri, and Upper Mississippi Rivers, USA. *Environ Pollut* **2008**, *156* (3), 1227-1232. DOI: 10.1016/j.envpol.2008.03.014.

(97) Kannan, K.; Tao, L.; Sinclair, E.; Pastva, S. D.; Jude, D. J.; Giesy, J. P. Perfluorinated compounds in aquatic organisms at various trophic levels in a Great Lakes food chain. *Arch Environ Contam Toxicol* **2005**, *48* (4), 559-566. DOI: 10.1007/s00244-004-0133-x.

(98) Lam, N. H.; Cho, C. R.; Lee, J. S.; Soh, H. Y.; Lee, B. C.; Lee, J. A.; Tatarozako, N.; Sasaki, K.; Saito, N.; Iwabuchi, K.; et al. Perfluorinated alkyl substances in water, sediment, plankton and fish from Korean rivers and lakes: a nationwide survey. *Sci Total Environ* **2014**, *491-492*, 154-162. DOI: 10.1016/j.scitotenv.2014.01.045.

(99) da Silva, B. F.; Aristizabal-Henao, J. J.; Aufmuth, J.; Awkerman, J.; Bowden, J. A. Survey of per- and polyfluoroalkyl substances (PFAS) in surface water collected in Pensacola, FL. *Heliyon* **2022**, *8* (8), e10239. DOI: 10.1016/j.heliyon.2022.e10239.

(100) Menger, R. F.; Funk, E.; Henry, C. S.; Borch, T. Sensors for detecting per- and polyfluoroalkyl substances (PFAS): A critical review of development challenges, current sensors, and commercialization obstacles. *Chem Eng J* **2021**, *417*, 129133. DOI: 10.1016/j.cej.2021.129133.

(101) Bai, X.; Son, Y. Perfluoroalkyl substances (PFAS) in surface water and sediments from two urban watersheds in Nevada, USA. *Sci Total Environ* **2021**, *751*, 141622. DOI: 10.1016/j.scitotenv.2020.141622.

(102) Viticoski, R. L.; Wang, D.; Feltman, M. A.; Mulabagal, V.; Rogers, S. R.; Blersch, D. M.; Hayworth, J. S. Spatial distribution and mass transport of Perfluoroalkyl Substances (PFAS) in surface water: A statewide evaluation of PFAS occurrence and fate in Alabama. *Sci Total Environ* **2022**, *836*, 155524. DOI: 10.1016/j.scitotenv.2022.155524.

(103) Ahrens, L.; Rakovic, J.; Ekdahl, S.; Kallenborn, R. Environmental distribution of per- and polyfluoroalkyl substances (PFAS) on Svalbard: Local sources and long-range transport to the Arctic. *Chemosphere* **2023**, *345*, 140463. DOI: 10.1016/j.chemosphere.2023.140463.

(104) Guelfo, J. L.; Korzeniowski, S.; Mills, M. A.; Anderson, J.; Anderson, R. H.; Arblaster, J. A.; Conder, J. M.; Cousins, I. T.; Dasu, K.; Henry, B. J.; et al. Environmental Sources, Chemistry, Fate, and Transport of Per- and Polyfluoroalkyl Substances: State of the Science, Key Knowledge Gaps, and Recommendations Presented at the August 2019 SETAC Focus Topic Meeting. *Environ Toxicol Chem* **2021**, *40* (12), 3234-3260. DOI: 10.1002/etc.5182.

(105) Bolan, N.; Sarkar, B.; Yan, Y.; Li, Q.; Wijesekara, H.; Kannan, K.; Tsang, D. C. W.; Schauerte, M.; Bosch, J.; Noll, H.; et al. Remediation of poly- and perfluoroalkyl substances (PFAS) contaminated soils - To mobilize or to immobilize or to degrade? *J Hazard Mater* **2021**, *401*, 123892. DOI: 10.1016/j.jhazmat.2020.123892.

(106) Verma, S.; Lee, T.; Sahle-Demessie, E.; Ateia, M.; Nadagouda, M. N. Recent advances on PFAS degradation via thermal and nonthermal methods. *Chem Eng J Adv* **2022**, *13*, 1-11. DOI: 10.1016/j.ceja.2022.100421.

(107) Yang, N.; Yang, S.; Ma, Q.; Beltran, C.; Guan, Y.; Morsey, M.; Brown, E.; Fernando, S.; Holsen, T. M.; Zhang, W.; et al. Solvent-Free Nonthermal Destruction of PFAS Chemicals and PFAS in Sediment by Piezoelectric Ball Milling. *Environ Sci Technol Lett* **2023**, *10* (2), 198-203. DOI: 10.1021/acs.estlett.2c00902.

(108) Das, S.; Ronen, A. A Review on Removal and Destruction of Per- and Polyfluoroalkyl Substances (PFAS) by Novel Membranes. *Membranes (Basel)* **2022**, *12* (7). DOI: 10.3390/membranes12070662.

(109) Cui, J.; Gao, P.; Deng, Y. Destruction of Per- and Polyfluoroalkyl Substances (PFAS) with Advanced Reduction Processes (ARPs): A Critical Review. *Environ Sci Technol* **2020**, *54* (7), 3752-3766. DOI: 10.1021/acs.est.9b05565.

(110) Lei, X.; Lian, Q.; Zhang, X.; Wang, T.; Gee, M.; Holmes, W.; Jin, S.; Ponnusamy, S. K.; Gang, D. D.; Zappi, M. E. Removal of perfluorooctanoic acid via polyethyleneimine modified graphene oxide: Effects of water matrices and understanding mechanisms. *Chemosphere* **2022**, *308* (Pt 2), 136379. DOI: 10.1016/j.chemosphere.2022.136379.

(111) Arrington, C. H., Patterson, G. D. Colloidal Properties of Highly Fluorinated Alkanoic Acids. *J. Phys. Chem.* **1953**, *57*, 247-250.

(112) Dong, D.; Kancharla, S.; Hooper, J.; Tsianou, M.; Bedrov, D.; Alexandridis, P. Controlling the self-assembly of perfluorinated surfactants in aqueous environments. *Phys Chem Chem Phys* **2021**, *23* (16), 10029-10039. DOI: 10.1039/d1cp00049g.

(113) Sims, J. L.; Stroski, K. M.; Kim, S.; Killeen, G.; Ehalt, R.; Simcik, M. F.; Brooks, B. W. Global occurrence and probabilistic environmental health hazard assessment of per- and polyfluoroalkyl substances (PFASs) in groundwater and surface waters. *Sci Total Environ* **2022**, *816*, 151535. DOI: 10.1016/j.scitotenv.2021.151535.

(114) Arshadi, M.; Garza-Rubalcava, U.; Guedes, A.; Capiro, N. L.; Pennell, K. D.; Christ, J.; Abriola, L. M. Modeling 1-D aqueous film forming foam transport through the vadose zone under realistic site and release conditions. *Sci Total Environ* **2024**, *919*, 170566. DOI: 10.1016/j.scitotenv.2024.170566.

(115) Armitage, J., Cousins, I. T., Buck, R. C., Prevedouros, K., Russel, M. H., MacLeod, M., Korzeniowski, S. H. Modeling Global-Scale Fate and Transport of Perfluorooctanoate Emitted from Direct Sources. *Environ. Sci. Tech.* **2006**, *40* (22), 6969-6975. DOI: 10.1021/es0614870.

(116) Brace, N. O. Long Chain Alkanoic and Alkenoic Acids with Perfluoroalkyl Terminal Segments. *J. Org. Chem* **1962**, *27* (12), 4491-4498. DOI: 10.1021/jo01059a090.

(117) Musegades, L. J.; Curtin, O. P.; Cyran, J. D. Determining the surface pKa of perfluorooctanoic acid. *Journal of Physical Chemistry C* **2024**, *128* (5), 1946-1951. DOI: DOI: 10.1021/acs.jpcc.3c07235.

(118) Chen, J., A. Adegbule, J. Huang, And M. Brooks. . Surface Tension, pH, and Specific Conductance of Select PFAS and their Mixtures. American Geophysical Union Fall Meeting, 2021.

(119) Costanza, J.; Arshadi, M.; Abriola, L. M.; Pennell, K. D. Accumulation of PFOA and PFOS at the Air–Water Interface. *Environ Sci Technol Letters* **2019**, *6* (8), 487-491. DOI: 10.1021/acs.estlett.9b00355.

(120) Lunkenheimer, K.; Prescher, D.; Hirte, R.; Geggel, K. Adsorption properties of surface chemically pure sodium perfluoro-n-alkanoates at the air/water interface: counterion effects within homologous series of 1:1 ionic surfactants. *Langmuir* **2015**, *31* (3), 970-981. DOI: 10.1021/la503450k.

(121) Lunkenheimer, K.; Geggel, K.; Prescher, D. Role of Counterion in the Adsorption Behavior of 1:1 Ionic Surfactants at Fluid Interfaces-Adsorption Properties of Alkali Perfluoro-n-octanoates at the Air/Water Interface. *Langmuir* **2017**, *33* (39), 10216-10224. DOI: 10.1021/acs.langmuir.7b00786.

(122) López-Fontán, J. L.; Sarmiento, F.; Schulz, P. C. The aggregation of sodium perfluorooctanoate in water. *Colloid Polym. Sci.* **2004**, *283* (8), 862-871. DOI: 10.1007/s00396-004-1228-7.

(123) Brusseau, M. L.; Van Glubt, S. The influence of surfactant and solution composition on PFAS adsorption at fluid-fluid interfaces. *Water Res* **2019**, *161*, 17-26. DOI: 10.1016/j.watres.2019.05.095 From NLM Medline.

(124) Gil, P. S.; Lacks, D. J. Geometric Origins of Surfactant Effectiveness in Mixed Solvent Systems. *J Phys Chem C* **2015**, *119* (50), 28061-28067. DOI: 10.1021/acs.jpcc.5b09603.

(125) Kancharla, S.; Dong, D.; Bedrov, D.; Alexandridis, P.; Tsianou, M. Binding of Perfluorooctanoate to Poly(ethylene oxide). *Macromol.* **2022**, *55* (11), 4624-4636. DOI: 10.1021/acs.macromol.2c00371.

(126) Ma, W.; Lopez, G.; Ameduri, B.; Takahara, A. Fluoropolymer Nanoparticles Prepared Using Trifluoropropene Telomer Based Fluorosurfactants. *Langmuir* **2020**, *36* (7), 1754-1760. DOI: 10.1021/acs.langmuir.9b03914.

(127) Sorli, J. B.; Lag, M.; Ekeren, L.; Perez-Gil, J.; Haug, L. S.; Da Silva, E.; Matrod, M. N.; Gutzkow, K. B.; Lindeman, B. Per- and polyfluoroalkyl substances (PFASs) modify lung surfactant function and pro-inflammatory responses in human bronchial epithelial cells. *Toxicol In Vitro* **2020**, *62*, 104656. DOI: 10.1016/j.tiv.2019.104656.

(128) De Lisi, R., Inglese, A., Milioto, S., and Pellerito A. Demixing of Mixed Micelles. Thermodynamics of Sodium Perfluorooctanoate-Sodium Dodecanoate Mixtures in Water. *Langmuir* **1997**, *13*, 192-202. DOI: 10.1021/la960636x.

(129) Lin, I. J. Hydrophile-lipophile balance (hlb) of fluorocarbon surfactants and its relation to the critical micelle concentration (cmc). *J. Phys. Chem.* **1972**, *76* (14), 2019-2023. DOI: 10.1021/j100658a020.

(130) Nakayama, H., Shinoda, K. . The Effect of Added Salts on the Solubilities and Krafft Points of Sodium Dodecyl Sulfate and Potassium Perfluoro-octanoate. *BCSJ* **1967**, *40* (8), 1797-1799.

(131) Kissi, E. *Fluorinated surfactants and repellents*; Marcel Dekker, Inc., 1994.

(132) Bhhatarai, B.; Gramatica, P. Prediction of aqueous solubility, vapor pressure and critical micelle concentration for aquatic partitioning of perfluorinated chemicals. *Environ Sci Technol* **2011**, *45* (19), 8120-8128. DOI: 10.1021/es101181g.

(133) Kancharla, S.; Choudhary, A.; Davis, R. T.; Dong, D.; Bedrov, D.; Tsianou, M.; Alexandridis, P. GenX in water: Interactions and self-assembly. *J Hazard Mater* **2022**, *428*, 128137. DOI: 10.1016/j.jhazmat.2021.128137.

(134) Fedorenko, M.; Alesio, J.; Fedorenko, A.; Slitt, A.; Bothun, G. D. Dominant entropic binding of perfluoroalkyl substances (PFASs) to albumin protein revealed by (19)F NMR. *Chemosphere* **2021**, *263*, 128083. DOI: 10.1016/j.chemosphere.2020.128083.

(135) Steffens, S. D.; Sedlak, D. L.; Alvarez-Cohen, L. Enhanced aggregation and interfacial adsorption of an aqueous film forming foam (AFFF) in high salinity matrices. *Environ Sci Process Impacts* **2023**, *25* (12), 2181-2188. DOI: 10.1039/d3em00247k.

(136) Wanzek, T. A.; Field, J. A.; Kostarelos, K. Repeated Aqueous Film-Forming Foams Applications: Impacts on Polyfluoroalkyl Substances Retention in Saturated Soil. *Environ Sci Technol* **2024**, *58* (3), 1659-1668. DOI: 10.1021/acs.est.3c04595.

(137) Sahara, T.; Wongsawaeng, D.; Ngaosuwan, K.; Kiatkittipong, W.; Hosemann, P.; Assabumrungrat, S. Highly effective removal of perfluorooctanoic acid (PFOA) in water with DBD-plasma-enhanced rice husks. *Sci Rep* **2023**, *13* (1), 13210. DOI: 10.1038/s41598-023-40197-3.

(138) Kunieda , H., Shinoda, K. . Krafft Points, Critical Micelle Concentrations, Surface Tension, and Solubilizing Power of Aqueous Solutions of Fluorinated Surfactants. *J Phys Chem* **1976**, *80* (22), 2468-2470.

(139) MacManus-Spencer, L. A., Tse, M. L., Hebert, P. C., Bischel, H. N., Luthy, R. G. . Binding of Perfluorocarboxylates to Serum Albumin: A Comparison of Analytical Methods. *Anal. Chem* **2010**, *82* (3), 974-981.

(140) Yu, Q.; Zhang, R.; Deng, S.; Huang, J.; Yu, G. Sorption of perfluorooctane sulfonate and perfluorooctanoate on activated carbons and resin: Kinetic and isotherm study. *Water Res* **2009**, *43* (4), 1150-1158. DOI: 10.1016/j.watres.2008.12.001.

(141) Shinoda, K.; Hato, M.; Hayashi, T. The Physicochemical Properties of Aqueous Solutions of Fluorinated Surfactants. *J Phys Chem* **1971**, *76* (6), 909-914.

(142) Molero, M., Andreu, R., González, D., Calvente, J. J., López-Pérez, G. . An Isotropic Model for Micellar Systems: Application to Sodium Dodecyl Sulfate Solutions. *Langmuir* **2001**, *17* (2), 314-322.

(143) Kumar, D.; Khan, J. M.; Posa, M.; Pulikkal, A. K.; Saha, B.; Bhattarai, A. Effect of Quaternary Ammonium Gemini Surfactant Solution on the Rate Constant of the Ninhydrin–Lysine Reaction. *Industrial & Engineering Chemistry Research* **2023**, *62* (39), 15897-15906. DOI: 10.1021/acs.iecr.3c02499.

(144) Abdul Rub, M.; Kumar, D. Micellization Behavior of Antidepressant Imipramine Hydrochloride Drug and Hydrotrope (Sodium Tosylate) Mixtures at Different Compositions and Temperatures in Different Media. *Journal of Chemical & Engineering Data* **2020**, *65* (5), 2659-2672. DOI: 10.1021/acs.jced.0c00038.

(145) Bhuiyan, H. A.; Anis-Ul-Haque, K.; Joy, M. T. R.; Rana, S.; Khan, J. M.; Kumar, D.; Rehman, M. T.; Goni, M. A.; Hoque, M. A.; Kabir, S. E. Aggregation phenomena and physico-chemical properties of tetradecyltrimethylammonium bromide and protein (bovine serum albumin) mixture: Influence of electrolytes and temperature. *Int. J. Biol. Macromol.* **2023**, *253*. DOI: 10.1016/j.ijbiomac.2023.127101.

(146) Prasad Niraula, T.; Narayan Sah, S.; Bhattarai, A.; Dominguez, H.; Beatriz Salazar-Arriaga, A.; Kumar, D. The physicochemical properties and contact angle of sodium dodecyl sulfate in water–acetone with and without sodium nitrate (NaNO3). *J. Mol. Liq.* **2022**, *367*. DOI: 10.1016/j.molliq.2022.120339.

(147) Perinelli, D. R.; Cespi, M.; Lorusso, N.; Palmieri, G. F.; Bonacucina, G.; Blasi, P. Surfactant Self-Assembling and Critical Micelle Concentration: One Approach Fits All? *Langmuir* **2020**, *36* (21), 5745-5753. DOI: 10.1021/acs.langmuir.0c00420.

(148) Kumar, D.; Farkaš Agatić, Z.; Popović, K.; Poša, M. Binary Mixed Micelles of Hexadecyltrimethylammonium Bromide–Sodium Deoxycholate and Dodecyltrimethylammonium Bromide–Sodium Deoxycholate: Thermodynamic Stabilization and Mixed Micelle Solubilization Capacity of Daidzein (Isoflavonoid). *Industrial & Engineering Chemistry Research* **2024**, *63* (7), 3336-3348. DOI: 10.1021/acs.iecr.3c04484.

(149) Can, S. Z.; Mago, D. D.; Walker, R. A. Structure and Organization of Hexadecanol Isomers Adsorbed to the Air/Water Interface. *Langmuir* **2006**, *22*, 8049.

(150) Kanthe, A. D.; Carnovale, M. R.; Katz, J. S.; Jordan, S.; Krause, M. E.; Zheng, S.; Ilott, A.; Ying, W.; Bu, W.; Bera, M. K.; et al. Differential Surface Adsorption Phenomena for Conventional and Novel Surfactants Correlates with Changes in Interfacial mAb Stabilization. *Mol Pharm* **2022**, *19* (9), 3100-3113. DOI: 10.1021/acs.molpharmaceut.2c00152.

(151) Can, S. Z.; Mago, D. D.; Esenturk, O.; Walker, R. A. Balancing hydrophobic and hydrophilic forces at the water/vapor interface: surface structure of soluble alcohol monolayers. *Journal of Physical Chemistry C* **2007**, *111* (25), 8739-8748. DOI: 10.1021/jp066896x.

(152) Herrington, K. L.; Kaler, E. W.; Miller, D. D.; Zasadzinski, J. A.; Chiruvolu, S. Phase Behavior of Aqueous Mixtures of Dodecyltrimethylammonium Bromide (DTAB) and Sodium Dodecyl Sulfate (SDS). *J. Phys. Chem.* **1993**, *97*, 13792-13802. DOI: 10.1021/j100153a058.

(153) Steel, W. H.; Damkaci, F.; Nolan, R.; Walker, R. A. Molecular rulers: new families of molecules for measuring interfacial widths. *Journal of the American Chemical Society* **2002**, *124* (17), 4824-4831. DOI: 10.1021/ja012457u.

(154) Beildeck, C. L.; Steel, W. H.; Walker, R. A. Cationic molecular rulers: synthesis, characterization, and intramolecular complications. *Langmuir* **2003**, *19* (12), 4933-4939. DOI: 10.1021/la0343122.

(155) Azam, M. R.; Tan, I. M.; Ismail, L.; Mushtaq, M.; Nadeem, M.; Sagir, M. Static adsorption of anionic surfactant onto crushed Berea sandstone. *Journal of Petroleum Exploration and Production Technology* **2013**, *3* (3), 195-201. DOI: 10.1007/s13202-013-0057-y.

(156) Perez-Rodriguez, M.; Prieto, G.; Rega, C.; Varela, L. M.; Sarmiento, F.; Mosquera, V. A Comparative Study of the Determination of the CriticalMicelle Concentration by Conductivity and DielectricConstant Measurements. *Langmuir* **1998**, *14*, 4422-4426. DOI: 10.1021/la980296a.

(157) Tartar, H. V., Lelong, A. L. M. Micellar Molecular Weights of Some Paraffin Chain Salts by Light Scattering. *J. Phys. Chem.* **1955**, *59* (12), 1185-1190. DOI: 10.1021/j150534a001.

(158) Sowada, R. The effect of electrolytes on the critical micelle concentration of tonic surfactants: the Corrin-Harkins equatin. *Tenside Surfactant Detergents* **1994**, *31* (3), 195-199. DOI: 10.1515/tsd-1994-310323.

(159) Bober, K.; Garus, M. RP-HPTLC Application in the Investigation of Solubility in Water of Long-Chain Fatty Acids. *J. Liq. Chromatogr.* **2006**, *29* (19), 2787-2794. DOI: 10.1080/10826070601001476.

(160) Maza, W. A.; Etz, B. D.; Schutt, T. C.; Chaloux, B. L.; Breslin, V. M.; Pate, B. B.; Shukla, M. K.; Owrutsky, J. C.; Epshteyn, A. Impact of Submicellar Aggregation on Reduction Kinetics of Perfluorooctanoate by the Hydrated Electron. *Environmental Science & Technology Letters* **2022**, *9* (3), 226-232. DOI: 10.1021/acs.estlett.1c01020.

(161) Bhattacharjee, J. K.; Kaatze, U. Fluctuations near the critical micelle concentration. I. Premicellar aggregation, relaxation rate, and isentropic compressibility. *J Phys Chem B* **2013**, *117* (14), 3790-3797. DOI: 10.1021/jp4011185.

(162) Hadgiivanova, R., Diamant, H. Premicellar Aggregation of Amphiphilic Molecules. *J. Phys. Chem.* **2007**, *111*, 8854−8859.

(163) Cui, X.; Mao, S.; Liu, M.; Yuan, H.; Du, Y. Mechanism of Surfactant Micelle Formation. *Langmuir* **2008**, *24*, 10771-10775.

(164) Ben-Amotz, D.; Mendes de Oliveira, D. Surfactant aggregate size distributions above and below the critical micelle concentration. *J Chem Phys* **2021**, *155* (22), 224902. DOI: 10.1063/5.0071246.

(165) Sunderland, E. M.; Hu, X. C.; Dassuncao, C.; Tokranov, A. K.; Wagner, C. C.; Allen, J. G. A review of the pathways of human exposure to poly- and perfluoroalkyl substances (PFASs) and present understanding of health effects. *J Expo Sci Environ Epidemiol* **2019**, *29* (2), 131-147. DOI: 10.1038/s41370-018-0094-1.

(166) Fenton, S. E.; Ducatman, A.; Boobis, A.; DeWitt, J. C.; Lau, C.; Ng, C.; Smith, J. S.; Roberts, S. M. Per- and Polyfluoroalkyl Substance Toxicity and Human Health Review: Current State of Knowledge and Strategies for Informing Future Research. *Environ Toxicol Chem* **2021**, *40* (3), 606-630. DOI: 10.1002/etc.4890.

(167) Pandelides, Z.; Conder, J.; Choi, Y.; Allmon, E.; Hoskins, T.; Lee, L.; Hoverman, J.; Sepulveda, M. A Critical Review of Amphibian Per- and Polyfluoroalkyl Substance Ecotoxicity Research Studies: Identification of Screening Levels in Water and Other Useful Resources for Site-Specific Ecological Risk Assessments. *Environ Toxicol Chem* **2023**, *42* (10), 2078-2090. DOI: 10.1002/etc.5695.

(168) Gatz, L. Regulating PFAS Under the Clean Water Act. Service, C. R., Ed.; 2022.

(169) US Environmental Protection Agency. Biden-Harris Administration Finalizes First-Ever National Drinking Water Standard to Protext 100M People from PFAS Pollution. EPA Press Office 2024.

(170) Ahrens, L.; Bundschuh, M. Fate and effects of poly- and perfluoroalkyl substances in the aquatic environment: a review. *Environmental Toxicology and Chemistry* **2014**, *33* (9), 1921-1929. DOI: 10.1002/etc.2663.

(171) Wee, S. Y.; Aris, A. Z. Revisiting the “forever chemicals”, PFOA and PFOS exposure in drinking water. *npj Clean Water* **2023**, *6* (1). DOI: 10.1038/s41545-023-00274-6.

(172) Daina, A.; Michielin, O.; Zoete, V. SwissADME: a free web tool to evaluate pharmacokinetics, drug-likeness and medicinal chemistry friendliness of small molecules. *Sci. Rep.* **2017**, *7*, 42717. DOI: 10.1038/srep42717.

(173) Daina, A. M., O.; Zoete, V. SwissADME: a free web tool to evaluate pharmacokinetics, drug-likeness and medicinal chemistry friendliness of small molecules. *Sci. Rep.* **2017**, *7*. DOI: 10.1038/srep42717.

(174) Burns, D. C. E., D.A.; Li, H.; McMurdo, C.J.; Webster, E. . Experimental pKa Determination for Perfluorooctanoic Acid (PFOA) and the Potential Impact of pKa Concentration Dependence on Laboratory-Measured Patitioning Phenomena and Environmental Modeling. *Environ. Sci. Technol.* **2008**, *42*, 9238-9288.

(175) Li, F.; Duan, J.; Tian, S.; Ji, H.; Zhu, Y.; Wei, Z.; Zhao, D. Short-chain per- and polyfluoroalkyl substances in aquatic systems: Occurrence, impacts and treatment. *Chemical Engineering Journal* **2020**, *380*. DOI: 10.1016/j.cej.2019.122506.

(176) Goss, K. U. The pKa Values of PFOA and Other Highly Fluorinated Carboxylic Acids. *Environ. Sci. Technol.* **2008**, *42* (13), 456-458.

(177) Goss, K. U. The pKa values of PFOA and other highly fluorinated carboxylic acids. *Environ. Sci. Tech.* **2008**, *42*, 5032. DOI: 10.1021/es8011904.

(178) Goss, K. U.; Arp, H. P. H. Comment on ″Experimental pKa Determination for Perfluorooctanoic Acid (PFOA) and the Potential Impact of pKa Concentration Dependence on Laboratory-Measured Partitioning Phenomena and Envrionmental Modeling. *Environ. Sci. Tech.* **2009**, *43* (13), 5150-5151. DOI: 10.1021/es900451s.

(179) Blanco, E.; González-Pérez, A.; Ruso, J. M.; Pedrido, R.; Prieto, G.; Sarmiento, F. A comparative study of the physicochemical properties of perfluorinated and hydrogenated amphiphiles. *J. Colloid Interface Sci* **2005**, *288* (1), 247-260. DOI: 10.1016/j.jcis.2005.02.085.

(180) Burns, D. C.; Ellis, D. A.; Webster, E.; McMurdo, C. J. Response to Comment on "Experimental pKa Determination for Ferfluorooctanoic Acid (PFOA) and the Potental Impact of pKa Concentration Dependence on Laboratory-Measured Partitioning Phenomena and Environmental Modeling. *Environ. Sci. Tech.* **2009**, *43*, 5152-5154. DOI: 10.1021/es900815a.

(181) Sobolewski, T. N.; Findlay, J. L.; Hemphill, J. E.; Walker, R. A. Aggregation, Not Micellization: Perfluorooctanoic Acid, Perfluorobutanesulfonic Acid, and Potassium Perfluorooctanesulfonate Behavior in Aqueous Solution. *Langmuir* **2024**, *40* (47), 24820-24831. DOI: 10.1021/acs.langmuir.4c02566.

(182) Gobas, F. A.; Lahittete, J. M.; Garofalo, G.; Wan, Y. S.; Mackay, D. A Novel Method for Measuring Membrane-Water Partition-Coefficients of Hydrophobic Organic Chemicals - Comparison with 1-Octanol-Water Partitioning. *J. Pharm. Sci.* **1988**, *77* (3), 265-272. DOI: 10.1002/jps.2600770317.

(183) Ebert, A.; Allendorf, F.; Berger, U.; Goss, K. U.; Ulrich, N. Membrane/Water Partitioning and Permeabilities of Perfluoroalkyl Acids and Four of their Alternatives and the Effects on Toxicokinetic Behavior. *Environ Sci Technol* **2020**, *54* (8), 5051-5061. DOI: 10.1021/acs.est.0c00175.

(184) Droge, S. T. J. Membrane-Water Partition Coefficients to Aid Risk Assessment of Perfluoroalkyl Anions and Alkyl Sulfates. *Environ Sci Technol* **2019**, *53* (2), 760-770. DOI: 10.1021/acs.est.8b05052.

(185) Xie, W.; Bothun, G. D.; Lehmler, H. J. Partitioning of perfluorooctanoate. into phsphatidylcholine bilayers is chain length-independent. *Chem. Phys. Lipids* **2010**, *163* (3), 300-308. DOI: 10.1016/j.chemphyslip.2010.01.003.

(186) Xie, W.; Kania-Korwel, I.; Bummer, P. M.; Lehmler, H. J. Effect of potassium perfluorooetanesulfonate, perfluorooctanoate and octanesulfonate on the phase transition of dipalmitoylphosphatidylcholine (DPPC) bilayers. *Biochim. Biophys. Acta, Biomembr.* **2007**, *1768* (5), 1299-1308. DOI: 10.1016/j.bbamem.2007.02.003.

(187) Bnyan, R. K., I; Ehtezazi, T; Saleem, I; Gordon, S; Neill, FO; Roberts, M. Surfactant effects on lipid based vesicle properties. *Journal of Pharmaceutical Sciences* **2018**, *107* (5), 1237-1246. DOI: 10.1016/j.xphs.2018.01.005.

(188) Deo, N.; Somasundaran, P. Effects of Sodium Dodecyl Sulfate on Mixed Liposome Solubilization. *Langmuir* **2003**, *19*, 7271-7275. DOI: 10.1021/la020962e 31.

(189) Fessler, M. B.; Summer, R. S. Surfactant Lipids at the Host-Environment Interface. Metabolic Sensors, Suppressors, and Effectors of Inflammatory Lung Disease. *Am J Respir Cell Mol Biol* **2016**, *54* (5), 624-635. DOI: 10.1165/rcmb.2016-0011PS.

(190) Heerklotz, H. Interactions of surfactants with lipid membranes. *Q Rev Biophys* **2008**, *41* (3-4), 205-264. DOI: 10.1017/S0033583508004721.

(191) Silva, J. A. K.; Simunek, J.; McCray, J. E. A Modified HYDRUS Model for Simulating PFAS Transport in the Vadose Zone. *Water* **2020**, *12* (10). DOI: 10.3390/w12102758.

(192) Lyu, X. Y.; Xiao, F.; Shen, C. Y.; Chen, J. J.; Park, C. M.; Sun, Y. Y.; Flury, M.; Wang, D. J. Per- and Polyfluoroalkyl Substances (PFAS) in Subsurface Environments: Occurrence, Fate, Transport, and Research Prospect. *Rev. Geophys.* **2022**, *60* (3). DOI: 10.1029/2021rg000765.

(193) Radi, A. B.; Noll, K. E.; Oskouie, A. K. Per- and Polyfluoroalkyl Substances: Background Information with Focus on Modeling of Fate and Transport of Per- and Polyfluroalkyl Substances in Air Media. *Journal of Environmental Engineering* **2022**, *148* (6). DOI: 10.1061/(asce)ee.1943-7870.0001989.

(194) Mahmoudnia, A.; Mehrdadi, N.; Baghdadi, M.; Moussavi, G. Change in global PFAS cycling as a response of permafrost degradation to climate change. *J. Hazard.Mater. Adv.* **2022**, *5*. DOI: 10.1016/j.hazadv.2021.100039.

(195) Faust, J. A. PFAS on atmospheric aerosol particles: a review. *Environ. Sci.:Processes Impacts* **2023**, *25* (2), 133-150. DOI: 10.1039/d2em00002d.

(196) Dassuncao, C.; Pickard, H.; Pfohl, M.; Tokranov, A. K.; Li, M. L.; Mikkelsen, B.; Slitt, A.; Sunderland, E. M. Phospholipid Levels Predict the Tissue Distribution of Poly- and Perfluoroalkyl Substances in a Marine Mammal. *Environ. Sci. Technol. Lett.* **2019**, *6* (3), 119-125. DOI: 10.1021/acs.estlett.9b00031.

(197) Garcia-Garin, O.; Borrell, A.; Colomer-Vidal, P.; Vighi, M.; Trilla-Prieto, N.; Aguilar, A.; Gazo, M.; Jiménez, B. Biomagnification and temporal trends (1990-2021) of perfluoroalkyl substances in striped dolphins (Stenella coeruleoalba) from the NW Mediterranean sea. *Environ. Pollut.* **2023**, *339*. DOI: 10.1016/j.envpol.2023.122738.

(198) Dong, H. K.; Lu, G. H.; Yan, Z. H.; Liu, J. C.; Ji, Y. Molecular and phenotypic responses of male crucian carp exposed to perfluorooctanoic acid. *Sci. Total Environ.* **2019**, *653*, 1395-1406. DOI: 10.1016/j.scitotenv.2018.11.017.

(199) Kannan, J. P.; Kannan, K. Global Distribution of Perfluorooctane Sulfonate in Wildlife. *Environ. Sci. Technol.* **2001**, *35*, 1339-1342.

(200) Corsolin, K. K. S.; Corsolini, S.; Falandysz, J.; Oehme, G.; Focardi, S.; Giesy, J. P. Perfluorooctanesulfonate and related fluorinated hydrocarbons in marine mammals, fishes, and birds from coats of the Baltic and the Mediterranean seas. *Environ. Sci. Technol.* **2002**, *36*, 3210-3216.

(201) Perez, F.; Nadal, M.; Navarro-Ortega, A.; Fabrega, F.; Domingo, J. L.; Barcelo, D.; Farre, M. Accumulation of perfluoroalkyl substances in human tissues. *Environ. Int.* **2013**, *59*, 354-362. DOI: 10.1016/j.envint.2013.06.004.

(202) European Food Safety Authority. Perfluorooctane sulfonate (PFOS), perfluorooctanoic acid (PFOA) and their salts Scientific Opinion of the Panel on Contaminants in the Food chain. *EFSA J* **2008**, *6* (7), 653. DOI: 10.2903/j.efsa.2008.653.

(203) Martin, J. W.; Mabury, S. A.; Solomon, K. R.; Muir, D. C. G. Bioconcentration and tissue distribution of perfluorinated acids in rainbow trout (Oncorhynchus mykiss). *Environ. Toxicol. Chem.* **2003**, *22* (1), 196-204. DOI: 10.1002/etc.5620220126.

(204) Dai, C.; Peng, L.; Li, Y. J.; Li, Z. D.; Chen, D.; Wang, F.; Lin, N. Distribution of per- and polyfluoroalkyl substances in blood, serum, and urine of patients with liver cancer and associations with liver function biomarkers. *Journal of Environmental Sciences* **2024**, *139*, 418-427. DOI: 10.1016/j.jes.2023.05.026.

(205) De Toni, L.; Radu, C. M.; Sabovic, I.; Di Nisio, A.; Dall'Acqua, S.; Guidolin, D.; Spampinato, S.; Campello, E.; Simioni, P.; Foresta, C. Increased Cardiovascular Risk Associated with Chemical Sensitivity to Perfluoro-Octanoic Acid: Role of Impaired Platelet Aggregation. *Int. J. Mol. Sci.* **2020**, *21* (2). DOI: 10.3390/ijms21020399.

(206) McLachlan, M. S.; Ebert, A.; Armitage, J. M.; Arnot, J. A.; Droge, S. T. J. A framework for understanding the bioconcentration of surfactants in fish. *Environ. Sci. Process Impacts* **2023**, *25* (7), 1238-1251. DOI: 10.1039/d3em00070b.

(207) Naumann, A.; Alesio, J.; Poonia, M.; Bothun, G. D. D. PFAS fluidize synthetic and bacterial lipid monolayers based on hydrophobicity and lipid charge. *J. Environ. Chem. Eng.* **2022**, *10* (2). DOI: 10.1016/j.jece.2022.107351.

(208) Roy, D.; Liu, S.; Woods, B. L.; Siler, A. R.; Fourkas, J. T.; Weeks, J. D.; Walker, R. A. Nonpolar Adsorption at the Silica/Methanol Interface: Surface Mediated Polarity and Solvent Density across a Strongly Associating Solid/Liquid Boundary. *The Journal of Physical Chemistry C* **2013**, *117* (51), 27052-27061. DOI: 10.1021/jp410756g.

(209) Gobrogge, C. A.; Blanchard, H. S.; Walker, R. A. Temperature-Dependent Partitioning of Coumarin 152 in Phosphatidylcholine Lipid Bilayers. *J Phys Chem B* **2017**, *121* (16), 4061-4070. DOI: 10.1021/acs.jpcb.6b10893.

(210) Purnell, G. E.; McNally, M. T.; Callis, P. R.; Walker, R. A. Buried Liquid Interfaces as a Form of Chemistry in Confinement: The Case of 4-Dimethylaminobenzonitrile at the Silica-Aqueous Interface. *J Am Chem Soc* **2020**, *142* (5), 2375-2385. DOI: 10.1021/jacs.9b11662.

(211) Gobrogge, C. A.; Walker, R. A. Quantifying Solute Partitioning in Phosphatidylcholine Membranes. *Anal. Chem.* **2017**, *89* (22), 12587-12595. DOI: 10.1021/acs.analchem.7b03964.

(212) le Maire, M.; Champeil, P.; Møller, J. V. Interaction of membrane proteins and lipids with solubilizing detergents. *Biochim. Biophys. Acta, Biomembr.* **2000**, *1508*, 86-111. DOI: 10.1016/S0304-4157(00)00010-1.

(213) Lichtenberg, D. Characterization of the solubilization of lipid bilayers by surfactants. *Biochim. Biophys. Acta, Biomembr.* **1985**, *821*, 470-478. DOI: 10.1016/0005-2736(85)90052-5.

(214) Lichtenberg, D.; Robson, R. J.; Dennis, E. A. Solubilization of Phospholipids by Detergents Structural and Kinetic Aspects. *Biochimica et Biophysica Acta* **1983**, *737* (2), 285-304. DOI: 10.1016/0304-4157(83)90004-7.

(215) Bjornestad, V. A.; Lund, R. Pathways of Membrane Solubilization: A Structural Study of Model Lipid Vesicles Exposed to Classical Detergents. *Langmuir* **2023**, *39* (11), 3914-3933. DOI: 10.1021/acs.langmuir.2c03207.

(216) Csiszár, Á., Bóta, A., Novák, C. et al. Calorimetric study of the effects of 2,4-dichlorophenol on the thermotropic phase behavior of DPPC liposomes. *Journal of Thermal Analysis and Calorimetry* **2002**, *69*, 53-63. DOI: 10.1023/A:1019977404803.

(217) Ortona, O.; Vitagliano, V.; Fessas, D.; Del Vecchio, P.; D'Errico, G. Inhomogeneities in sodium decylsulfate doped 1,2-dipalmitoylphosphatidylcholine bilayer. *J. Colloid Interface Sci.* **2010**, *343* (2), 401-407. DOI: 10.1016/j.jcis.2009.11.054.

(218) Shiffer, K.; Hawgood, S.; Haagsman, H. P.; Benson, B.; Clements, J. A.; Goerke, J. Lung Surfactant Proteins, SP-B and SP-C, Alter the Thermodynamic Properties of Phospholipid Membranes: A Differential Calorimetry Study. *Biochemistry* **1993**, *32* (2), 590-597. DOI: 10.1021/bi00053a026.

(219) Maiti, B.; Kumar, K.; Datta, S.; Bhattacharya, S. Physical-Chemical Characterization of Bilayer Membranes Derived from (±) α-Tocopherol-Based Gemini Lipids and Their Interaction with Phosphatidylcholine Bilayers and Lipoplex Formation with Plasmid DNA. *Langmuir* **2022**, *38* (1), 36-49. DOI: 10.1021/acs.langmuir.1c01039.

(220) Kudella, P. W.; Preissinger, K.; Morasch, M.; Dirscherl, C. F.; Braun, D.; Wixforth, A.; Westerhausen, C. Fission of Lipid-Vesicles by Membrane Phase Transitions in Thermal Convection. *Sci Rep* **2019**, *9* (1), 18808. DOI: 10.1038/s41598-019-55110-0.

(221) Uchegbu, I. F.; Vyas, S. P. Non-ionic surfactant based vesicles (niosomes) in drug delivery. *J. Pharm.* **1998**, *172*, 33-70. DOI: 10.1016/S0378-5173(98)00169-0.

(222) Bhardwaj, P.; Tripathi, P.; Gupta, R.; Pandey, S. Niosomes: A review on niosomal research in the last decade. *J. Drug Delivery Sci. Technol.* **2020**, *56*, 101581. DOI: 10.1016/j.jddst.2020.101581.

(223) Gharbavi, M.; Amani, J.; Kheiri-Manjili, H.; Danafar, H.; Sharafi, A. Niosome: A Promising Nanocarrier for Natural Drug Delivery through Blood-Brain Barrier. *Adv. Pharmacol. Sci.* **2018**, *2018*, 6847971. DOI: 10.1155/2018/6847971.

(224) Åkesson, A.; Lind, T.; Ehrlich, N.; Stamou, D.; Wacklin, H.; Cárdenas, M. Composition and structure of mixed phospholipid supported bilayers formed by POPC and DPPC. *Soft Matter* **2012**, *8* (20), 5658-5665. DOI: 10.1039/c2sm00013.

(225) Exerowa, D.; Todorov, R.; Nikolov, L. Amphiphile bilayer films from DPPC: bilayer lipid membranes and Newton black films. *Colloids and Surfaces A: Physicochemical and Engineering Aspects* **2004**, *250* (1-3), 195-201. DOI: 10.1016/j.colsurfa.2004.04.089.

(226) Maherani, B.; Arab-Tehrany, E.; Kheirolomoom, A.; Geny, D.; Linder, M. Calcein release behavior from liposomal bilayer; influence of physicochemical/mechanical/structural properties of lipids. *Biochimie* **2013**, *95* (11), 2018-2033. DOI: 10.1016/j.biochi.2013.07.006.

(227) Mason, R. P.; Gonye, G. E.; Chester, D. W.; Herbette, L. G. Partitioning and location of BAY-K-8644, 1,4-Dihydropyridine calcium-channel agonist, in model and biological membranes. *Biophys. J.* **1989**, *55* (4), 769-778. DOI: 10.1016/S0006-3495(89)82875-9.

(228) Robinson, M.; Turnbull, S.; Lee, B. Y.; Leonenko, Z. The effects of melatonin, serotonin, tryptophan and NAS on the biophysical properties of DPPC monolayers. *Biochim. Biophys. Acta, Biomembr.* **2020**, *1862* (9), 183363. DOI: 10.1016/j.bbamem.2020.183363.

(229) Yuan, S. D.; Zhang, H.; Yuan, S. L. Theoretical insights into the uptake of sulfonamides onto phospholipid bilayers: Mechanisms, interaction and toxicity evaluation. *J. Hazard. Mater.* **2022**, *435*, 129033. DOI: 10.1016/j.jhazmat.2022.129033.

(230) Perkins, R.; Vaida, V. Phenylalanine Increases Membrane Permeability. *J Am Chem Soc* **2017**, *139* (41), 14388-14391. DOI: 10.1021/jacs.7b09219.

(231) Ng, C. A.; Hungerbuhler, K. Bioaccumulation of perfluorinated alkyl acids: observations and models. *Environ Sci Technol* **2014**, *48* (9), 4637-4648. DOI: 10.1021/es404008g.

(232) Bell, E. M.; De Guise, S.; McCutcheon, J. R.; Lei, Y.; Levin, M.; Li, B.; Rusling, J. F.; Lawrence, D. A.; Cavallari, J. M.; O'Connell, C.; et al. Exposure, health effects, sensing, and remediation of the emerging PFAS contaminants - Scientific challenges and potential research directions. *Sci Total Environ* **2021**, *780*, 146399. DOI: 10.1016/j.scitotenv.2021.146399.

(233) Zhou, J.; Baumann, K.; Surratt, J. D.; Turpin, B. J. Legacy and emerging airborne per- and polyfluoroalkyl substances (PFAS) collected on PM(2.5) filters in close proximity to a fluoropolymer manufacturing facility. *Environ Sci Process Impacts* **2022**, *24* (12), 2272-2283. DOI: 10.1039/d2em00358a.

(234) Interstate Technology & Regulatory Council: Per- and Polyfluoroalkyl Substances Team. PFAS Technical and Regulatory Guidance Document. 2023.

(235) U.S. Environmental Protection Agency. *NAAQS Table*. 2024. https://www.epa.gov/criteria-air-pollutants/naaqs-table (accessed 2024 March 25).

(236) Wang, Y.; Good, K. D. Microplastics and PFAS air-water interaction and deposition. *Sci Total Environ* **2024**, *954*, 176247. DOI: 10.1016/j.scitotenv.2024.176247.

(237) Wickersham, L. C.; Mattila, J. M.; Krug, J. D.; Jackson, S. R.; Wallace, M. A. G.; Shields, E. P.; Halliday, H.; Li, E. Y.; Liberatore, H. K.; Farrior, S. M.; et al. Characterization of PFAS air emissions from thermal application of fluoropolymer dispersions on fabrics. *J Air Waste Manag Assoc* **2023**, *73* (7), 533-552. DOI: 10.1080/10962247.2023.2192009.

(238) US Environmental Protection Agency. Multi-Industry Per- and Polyfluoroalkyl Substances (PFAS) Study – 2021 Preliminary Report. US Environmental Protection Agency, Ed.; 2021; Vol. EPA-821-R-21-004.

(239) Ahrens, L.; Shoeib, M.; Harner, T.; Lane, D. A.; Guo, R.; Reiner, E. J. Comparison of annular diffusion denuder and high volume air samplers for measuring per- and polyfluoroalkyl substances in the atmosphere. *Anal Chem* **2011**, *83* (24), 9622-9628. DOI: 10.1021/ac202414w.

(240) Muensterman, D. J.; Cahuas, L.; Titaley, I. A.; Schmokel, C.; De la Cruz, F. B.; Barlaz, M. A.; Carignan, C. C.; Peaslee, G. F.; Field, J. A. Per- and Polyfluoroalkyl Substances (PFAS) in Facemasks: Potential Source of Human Exposure to PFAS with Implications for Disposal to Landfills. *Environ Sci Technol Lett* **2022**, *9* (4), 320-326. DOI: 10.1021/acs.estlett.2c00019.

(241) Jabeen, M.; Fayyaz, M.; Irudayaraj, J. Epigenetic Modifications, and Alterations in Cell Cycle and Apoptosis Pathway in A549 Lung Carcinoma Cell Line upon Exposure to Perfluoroalkyl Substances. *Toxics* **2020**, *8* (4). DOI: 10.3390/toxics8040112.

(242) Seifert, M.; Breitenstein, D.; Klenz, U.; Meyer, M. C.; Galla, H. J. Solubility versus electrostatics: what determines lipid/protein interaction in lung surfactant. *Biophys J* **2007**, *93* (4), 1192-1203. DOI: 10.1529/biophysj.107.106765.

(243) Frerking, I.; Gunther, A.; Seeger, W.; Pison, U. Pulmonary surfactant: functions, abnormalities and therapeutic options. *Intensive Care Med* **2001**, *27* (11), 1699-1717. DOI: 10.1007/s00134-001-1121-5.

(244) Can, S. Z.; Chang, C. F.; Walker, R. A. Spontaneous formation of DPPC monolayers at aqueous/vapor interfaces and the impact of charged surfactants. *Biochim Biophys Acta* **2008**, *1778* (10), 2368-2377. DOI: 10.1016/j.bbamem.2008.06.002.

(245) Han, S.; Mallampalli, R. K. The Role of Surfactant in Lung Disease and Host Defense against Pulmonary Infections. *Ann Am Thorac Soc* **2015**, *12* (5), 765-774. DOI: 10.1513/AnnalsATS.201411-507FR.

(246) Kozak, M.; Domka, L.; Jurga, S. Interactions of Cationic Surfactants with DPPC. *J. Therm. Anal. Calorim.* **2007**, *88* (2), 395-399. DOI: 0.1007/s10973-006-8061-9.

(247) Ma, G.; Allen, H. C. DPPC Langmuir Monolayer at the Air-Water Interface: Probing the Tail and Head Groups by Vibrational Sum Frequency Generation Spectroscopy. *Langmuir* **2006**, *22* (12), 5341-5349. DOI: 10.1021/la0535227.

(248) Gragson, D. E.; Richmond, G. L. Potential Dependent Alignment and Hydrogen Bonding of Water Molecules at Charged Air/Water and $CCl_4$ /Water Interfaces. *J. Am. Chem. Soc.* **1998**, *120* (2), 366-375. DOI: 10.1021/ja972570d.

(249) Harper, K. L.; Allen, H. C. Competition between DPPC and SDS at the Air−Aqueous Interface. *Langmuir* **2007**, *23* (17), 8925-8931. DOI: 10.1021/la7006974.

(250) Oh-e, M.; Lvovsky, A. I.; Wei, X.; Shen, Y. R. Sum-frequency generation (SFG) vibrational spectroscopy of side alkyl chain structures of polyimide surfaces. *The Journal of Chemical Physics* **2000**, *113* (19), 8827-8832. DOI: 10.1063/1.1318199.

(251) Gragson, D. E.; Richmond, G. L. Investigations of the Structure and Hydrogen Bonding of Water Molecules at Liquid Surfaces by Vibrational Sum Frequency Spectroscopy. *J Phys. Chem. B* **1998**, *102* (20), 3847-3861. DOI: 10.1021/jp9806011.

(252) Gragson, D. E.; McCarty, B. M.; Richmond, G. L. Ordering of Interfacial Water Molecules at the Charged Air/Water Interface Observed by Vibrational Sum Frequency Generation. *J. Am. Chem. Soc.* **1997**, *119* (26), 6144-6152. DOI: 10.1021/ja962277y.

(253) Yiyen, G.; Sobolewski, T. N.; Walker, R. A. Nonlinear Optical Studies of Water at Gypsum–Air and Gypsum–Aqueous Interfaces. *The Journal of Physical Chemistry C* **2024**, *128* (5), 2076-2085. DOI: 10.1021/acs.jpcc.3c04844.

(254) Pereira-Leite, C.; Lopes-de-Campos, D.; Fontaine, P.; Cuccovia, I. M.; Nunes, C.; Reis, S. Licofelone-DPPC Interactions: Putting Membrane Lipids on the Radar of Drug Development. *Molecules* **2019**, *24* (3). DOI: 10.3390/molecules24030516.

(255) Snyder, R. G.; Strauss, H. L.; Elliger, C. A. C-H Stretching Modes and the Structure of n-Alkyl Chains. 1. Long Disordered Chains. *J. Phys. Chem.* **1982**, 5145-5150. DOI: 10.1021/j100223a018.

(256) MacPhail, R. A.; Strauss, H. L.; Snyder, R. G.; Elliger, C. A. Carbon-hydrogen stretching modes and the structure of n-alkyl chains. 2. Long, all-trans chains. *J. Phys. Chem.* **1984**, *88* (3), 334-341. DOI: 10.1021/j150647a002.

(257) Musegades, L. J.; Curtin, O. P.; Cyran, J. D. Determining the Surface pK(a) of Perfluorooctanoic Acid. *J Phys Chem C Nanomater Interfaces* **2024**, *128* (5), 1946-1951. DOI: 10.1021/acs.jpcc.3c07235.

(258) Walker, R. A.; Gruetzmacher, J. A.; Richmond, G. L. Phosphatidylcholine Monolayer Structure at a Liquid-Liquid Interface. *J. Am. Chem. Soc.* **1998**, *120*, 6991-7003.

(259) Smiley, B. L.; Walker, R. A.; Gragson, D. E.; Hannon, T. E.; Richmond, G. L. Vibrational sum frequency spectroscopy of surfactants and phospholipid monolayers at liquid-liquid interfaces. *Proc. SPIE 3273, Laser Techniques for Condensed-Phase and Biological Systems* **1988**. DOI: 10.1117/12.306122.

(260) Shen, C. Y.; Ostroverkhov, V. Sum-Frequency Vibrational Spectroscopy on Water Interfaces: Polar Orientation of Water Molecules at Interfaces. *Chem. Rev.* **2006**, *106*, 1140-1154. DOI: 10.1021/cr040377d.

(261) Bonn, M.; Nagata, Y.; Backus, E. H. Molecular structure and dynamics of water at the water-air interface studied with surface-specific vibrational spectroscopy. *Angew Chem Int Ed Engl* **2015**, *54* (19), 5560-5576. DOI: 10.1002/anie.201411188.

(262) Nguyen, K. T.; Nguyen, A. V.; Evans, G. M. Interfacial Water Structure at Surfactant Concentrations below and above the Critical Micelle Concentration as Revealed by Sum Frequency Generation Vibrational Spectroscopy. *The Journal of Physical Chemistry C* **2015**, *119* (27), 15477-15481. DOI: 10.1021/acs.jpcc.5b04416.

(263) Shultz, M. J.; Schnitzer, C.; Simonelli, D.; Baldelli, S. Sum frequency generation spectroscopy of the aqueous interface: Ionic and soluble molecular solutions. *International Reviews in Physical Chemistry* **2000**, *19* (1), 123-153. DOI: 10.1080/014423500229882.

(264) Gragson, D. E.; Richmond, G. L. Comparisons of the Structure of Water at Neat Oil/Water and Air-Water Interfaces As Determined by Vibrational Sum Frequency Generation. *Langmuir* **1997**, *13*, 4804-4806. DOI: 10.1021/la970497z.

(265) Okuno, M.; Mezger, M.; Stangenberg, R.; Baumgarten, M.; Mullen, K.; Bonn, M.; Backus, E. H. Interaction of a patterned amphiphilic polyphenylene dendrimer with a lipid monolayer: electrostatic interactions dominate. *Langmuir* **2015**, *31* (6), 1980-1987. DOI: 10.1021/la504252s.

(266) Bonn, M.; Bakker, H. J.; Tong, Y.; Backus, E. H. No Ice-Like Water at Aqueous Biological Interfaces. *Biointerphases* **2012**, *7* (20). DOI: 10.1007/s13758-012-0020-3.

(267) Nguyen, T. T. P.; Raji, F.; Nguyen, C. V.; Nguyen, N. N.; Nguyen, A. V. Effects of Charged Surfactants on Interfacial Water Structure and Macroscopic Properties of the Air-Water Interface. *Chemphyschem* **2023**, *24* (23), e202300062. DOI: 10.1002/cphc.202300062.

(268) Truong, V. N. T.; Wang, X.; Dang, L. X.; Miller, J. D. Interfacial Water Features at Air-Water Interfaces as Influenced by Charged Surfactants. *J Phys Chem B* **2019**, *123* (10), 2397-2404. DOI: 10.1021/acs.jpcb.9b01246.

(269) Dogangun, M.; Ohno, P. E.; Liang, D.; McGeachy, A. C.; Be, A. G.; Dalchand, N.; Li, T.; Cui, Q.; Geiger, F. M. Hydrogen-Bond Networks near Supported Lipid Bilayers from Vibrational Sum Frequency Generation Experiments and Atomistic Simulations. *J Phys Chem B* **2018**, *122* (18), 4870-4879. DOI: 10.1021/acs.jpcb.8b02138.

(270) Gan, W.; Wu, D.; Zhang, Z.; Feng, R.; Wang, H. Polarization and experimental configuration analyses of sum frequency generation vibrational spectra, structure, and orientational motion of the air/water interface. *J. Chem. Phys.* **2006**, *124*. DOI: 10.1063/1.2179794

(271) Feng, R. R.; Guo, Y.; Wang, H. F. Reorientation of the "free OH" group in the top-most layer of air/water interface of sodium fluoride aqueous solution probed with sum-frequency generation vibrational spectroscopy. *J Chem Phys* **2014**, *141* (18), 18C507. DOI: 10.1063/1.4895561.

(272) Sheridan, A. J.; Slater, J. M.; Arnold, T.; Campbell, R. A.; Thompson, K. C. Changes to DPPC Domain Structure in the Presence of Carbon Nanoparticles. *Langmuir* **2017**, *33* (39), 10374-10384. DOI: 10.1021/acs.langmuir.7b01077.

(273) Liekkinen, J.; de Santos Moreno, B.; Paananen, R. O.; Vattulainen, I.; Monticelli, L.; Bernardino de la Serna, J.; Javanainen, M. Understanding the Functional Properties of Lipid Heterogeneity in Pulmonary Surfactant Monolayers at the Atomistic Level. *Front Cell Dev Biol* **2020**, *8*, 581016. DOI: 10.3389/fcell.2020.581016.

(274) Matyszewska, D.; Bilewicz, R. DPPC monolayers as simple models of biological membranes for studies of interactions with perfluorinated compounds. *Anneles* **2008**, *16*. DOI: 10.2478/v10063-009-0009-z.

(275) Matyszewska, D.; Tappura, K.; Oradd, G.; Bilewicz, R. Influence of perfluorinated compounds on the properties of model lipid membranes. *J Phys Chem B* **2007**, *111* (33), 9908-9918. DOI: 10.1021/jp068874g.

(276) Johnson, T. D.; Belitz, K.; Lombard, M. A. Estimating domestic well locations and populations served in the contiguous U.S. for years 2000 and 2010. *Science of The Total Environment* **2019**, *687*, 1261-1273. DOI: 10.1016/j.scitotenv.2019.06.036.

(277) Dieter, C. A.; Maupin, M., A.; Caldwell, R. R.; Harris, M. A.; Ivahnenko, T. I.; Lovelace, J. K.; Barber, N. L.; Linsey, K. S. Estimated use of water in the United States in 2015. U. S. Geological Survey. *Circular* **2018**, *1441* (76). DOI: 10.3133/cir1441.

(278) U.S. Environmental Protection Agency (EPA). *Private Drinking Water Wells*. 2025. https://www.epa.gov/privatewells (accessed 2025 March 16).

(279) Schmitt, K.; Minovi, D.; Loeb, S.; Ward, M. H. A state-by-state comparison of policies that protect private well users. *J Expo Sci Environ Epidemiol* **2024**, *34* (1), 155-160. DOI: 10.1038/s41370-024-00645-2.

(280) *Private Drinking Water Well Programs in Your State*. Environmental Protection Agency 2024. https://www.epa.gov/privatewells/private-drinking-water-well-programs-your-state#:~:text=While%20most%20states%20have%20zero,links%20include%20non%2Dfederal%20site.

(281) Montana DEQ. *Water Resources: Private Wells & Septic Systems*. MONTANA.GOV, 2024. https://deq.mt.gov/water/resources .

(282) Evich, M. G.; Davis, M. J. B.; McCord, J. P.; Acrey, B.; Awkerman, J. A.; Knappe, D. R. U.; Lindstrom, A. B.; Speth, T. F.; Tebes-Stevens, C.; Strynar, M. J.; et al. Per- and polyfluoroalkyl substances in the environment. *Science* **2022**, *375* (6580). DOI: 10.1126/science.abg9065.

(283) Brunn, H.; Arnold, G.; Körner, W.; Rippen, G.; Steinhäuser, K. G.; Valentin, I. PFAS: forever chemicals—persistent, bioaccumulative and mobile. Reviewing the status and the need for their phase out and remediation of contaminated sites. *Environmental Sciences Europe* **2023**, *35* (1). DOI: 10.1186/s12302-023-00721-8.

(284) Cousins, I. T.; DeWitt, J. C.; Gluge, J.; Goldenman, G.; Herzke, D.; Lohmann, R.; Ng, C. A.; Scheringer, M.; Wang, Z. The high persistence of PFAS is sufficient for their management as a chemical class. *Environ Sci Process Impacts* **2020**, *22* (12), 2307-2312. DOI: 10.1039/d0em00355g.

(285) Zheng, T.; Kelsey, K.; Zhu, C.; Pennell, K. D.; Yao, Q.; Manz, K. E.; Zheng, Y. F.; Braun, J. M.; Liu, Y.; Papandonatos, G.; et al. Adverse birth outcomes related to concentrations of per- and polyfluoroalkyl substances (PFAS) in maternal blood collected from pregnant women in 1960–1966. *Environ. Res.* **2024**, *241*, 117010. DOI: 10.1016/j.envres.2023.117010.

(286) Ritscher, A.; Wang, Z.; Scheringer, M.; Boucher, J. M.; Ahrens, L.; Berger, U.; Bintein, S.; Bopp, S. K.; Borg, D.; Buser, A. M.; et al. Zurich Statement on Future Actions on Per- and Polyfluoroalkyl Substances (PFASs). *Environ Health Perspect* **2018**, *126* (8), 84502. DOI: 10.1289/EHP4158.

(287) Li, S.; Oliva, P.; Zhang, L.; Goodrich, J. A.; McConnell, R.; Conti, D. V.; Chatzi, L.; Aung, M. Associations between per-and polyfluoroalkyl substances (PFAS) and county-level cancer incidence between 2016 and 2021 and incident cancer burden attributable to PFAS in drinking water in the United States. *J Expo Sci Environ Epidemiol* **2025**. DOI: 10.1038/s41370-024-00742-2.

(288) Zheng, J.; Liu, S.; Yang, J.; Zheng, S.; Sun, B. Per- and polyfluoroalkyl substances (PFAS) and cancer: Detection methodologies, epidemiological insights, potential carcinogenic mechanisms, and future perspectives. *Sci Total Environ* **2024**, *953*, 176158. DOI: 10.1016/j.scitotenv.2024.176158.

(289) Beesoon, S.; Webster, G. M.; Shoeib, M.; Harner, T.; Benskin, J. P.; Martin, J. W. Isomer Profiles of Perfluorochemicals in Matched Maternal, Cord, and House Dust Samples: Manufacturing Sources and Transplacental Transfer. *Environmental Health Perspectives* **2011**, *119* (11), 1659-1664. DOI: 10.1289/ehp.1003265.

(290) Wisconsin Department of Health Services. *Chemicals: Perfluoroalkyl and Polyfluoroalkyl (PFAS) Substances What are PFAS?* 2024. https://www.dhs.wisconsin.gov/chemical/pfas.htm.

(291) Breitmeyer, S. E.; Williams, A. M.; Conlon, M. D.; Wertz, T. A.; Heflin, B. C.; Shull, D. R.; Duris, J. W. Predicted Potential for Aquatic Exposure Effects of Per- and Polyfluorinated Alkyl Substances (PFAS) in Pennsylvania's Statewide Network of Streams. *Toxics* **2024**, *12* (12). DOI: 10.3390/toxics12120921.

(292) Kurwadkar, S.; Dane, J.; Kanel, S. R.; Nadagouda, M. N.; Cawdrey, R. W.; Ambade, B.; Struckhoff, G. C.; Wilkin, R. Per- and polyfluoroalkyl substances in water and wastewater: A critical review of their global occurrence and distribution. *Sci Total Environ* **2022**, *809*, 151003. DOI: 10.1016/j.scitotenv.2021.151003.

(293) Cousins, I. T.; Johansson, J. H.; Salter, M. E.; Sha, B.; Scheringer, M. Outside the Safe Operating Space of a New Planetary Boundary for Per- and Polyfluoroalkyl Substances (PFAS). *Environ Sci Technol* **2022**, *56* (16), 11172-11179. DOI: 10.1021/acs.est.2c02765.

(294) Kim, S. K.; Kannan, K. Perfluorinated acids in air, rain, snow, surface runoff, and lakes: relative importance of pathways to contamination of urban lakes. *Environ. Sci. Tech.* **2007**, *41* (24). DOI: 10.1021/es072107t.

(295) Kim, Y.; Pike, K. A.; Gray, R.; Sprankle, J. W.; Faust, J. A.; Edmiston, P. L. Non-targeted identification and semi-quantitation of emerging per- and polyfluoroalkyl substances (PFAS) in US rainwater. *Environ Sci Process Impacts* **2023**, *25* (11), 1771-1787. DOI: 10.1039/d2em00349j.

(296) Coates, K. A.; Harrington, P. B. Contamination levels of per- and polyfluoroalkyl substances (PFAS) in recent North American precipitation events. A review. *Water Res* **2024**, *266*, 122390. DOI: 10.1016/j.watres.2024.122390.

(297) Houtz, E. F.; Higgins, C. P.; Field, J. A.; Sedlak, D. L. Persistence of perfluoroalkyl acid precursors in AFFF-impacted groundwater and soil. *Environ Sci Technol* **2013**, *47* (15), 8187-8195. DOI: 10.1021/es4018877.

(298) Gyimah, R.; Lebu, S.; Owusu-Frimpong, I.; Semiyaga, S.; Salzberg, A.; Manga, M. Effluents from septic systems and impact on groundwater contamination: a systematic review. *Environ Sci Pollut Res Int* **2024**, *31* (54), 62655-62675. DOI: 10.1007/s11356-024-35385-1.

(299) Masoner, J. R.; Kolpin, D. W.; Cozzarelli, I. M.; Smalling, K. L.; Bolyard, S. C.; Field, J. A.; Furlong, E. T.; Gray, J. L.; Lozinski, D.; Reinhart, D.; et al. Landfill leachate contributes per-/poly-fluoroalkyl substances (PFAS) and pharmaceuticals to municipal wastewater. *Environmental Science: Water Research & Technology* **2020**, *6* (5), 1300-1311. DOI: 10.1039/d0ew00045k.

(300) Salvatore, D.; Mok, K.; Garrett, K. K.; Poudrier, G.; Brown, P.; Birnbaum, L. S.; Goldenman, G.; Miller, M. F.; Patton, S.; Poehlein, M.; et al. Presumptive Contamination: A New Approach to PFAS Contamination Based on Likely Sources. *Environ Sci Technol Lett* **2022**, *9* (11), 983-990. DOI: 10.1021/acs.estlett.2c00502.

(301) Tokranov, A. K.; Bradley, P. M.; Focazio, M. J.; Kent, D. B.; LeBlanc, D. R.; McCoy, J. W.; Smalling, K. L.; Steevens, J. A.; Toccalino, P. L. Integrated science for the study of perfluoroalkyl and polyfluoroalkyl substances (PFAS) in the environment—A strategic science vision for the U.S. Geological Survey: U.S. Geological Survey. *Circular* **2021**, *1490*. DOI: 10.3133/cir1490.

(302) Tokranov, A. K.; Ransom, K. M.; Bexfield, L. M.; Lindsey, B. D.; Watson, E.; Dupuy, D. I.; Stackelberg, P. E.; Fram, M. S.; Voss, S. A.; Kingsbury, J. A.; et al. Predictions of groundwater PFAS occurrence at drinking water supply depths in the United States. *Science* **2024**, *386* (6723), 748-755. DOI: 10.1126/science.ado6638.

(303) National Research Council (NRC). *Science and Decisions: Advancing Risk Assessment*; National Academies Press, 2009.

(304) Sexton, K.; Hattis, D. Assessing cumulative health risks from exposure to environmental mixtures - three fundamental questions. *Environ Health Perspect* **2007**, *115* (5), 825-832. DOI: 10.1289/ehp.9333.

(305) U.S. Environmental Protection Agency (EPA). Risk Assessment Guidance for Superfund Volume III Human Health Evaluation Manual (Part A), Process for Conducting Probabilistic Risk Assessment. U.S. Environmental Protection Agency., Ed.; Washington, D.C., 1989.

(306) Eggers, M. J.; Sigler, W. A.; Kiekover, N.; Bradley, P. M.; Smalling, K. L.; Parker, A.; Peterson, R. K. D.; LaFave, J. I. Statewide cumulative human health risk assessment of inorganics-contaminated groundwater wells, Montana, USA. *Environ Pollut* **2025**, *369*, 125810. DOI: 10.1016/j.envpol.2025.125810.

(307) Meek, M. E.; Boobis, A. R.; Crofton, K. M.; Heinemeyer, G.; Raaij, M. V.; Vickers, C. Risk assessment of combined exposure to multiple chemicals: A WHO/IPCS framework. *Regul Toxicol Pharmacol* **2011**. DOI: 10.1016/j.yrtph.2011.03.010.

(308) Bradley, P. M.; Romanok, K. M.; Smalling, K. L.; Gordon, S. E.; Huffman, B. J.; Paul Friedman, K.; Villeneuve, D. L.; Blackwell, B. R.; Fitzpatrick, S. C.; Focazio, M. J.; et al. Private, public, and bottled drinking water: Shared contaminant-mixture exposures and effects challenge. *Environ Int* **2025**, *195*, 109220. DOI: 10.1016/j.envint.2024.109220.

(309) U.S. Environmental Protection Agency (EPA). Summary of Results for the 2011 National-Scale Assessment. U.S. Environmental Protection Agency, Ed.; Wahsington, D.C. , 2015.

(310) U.S. Environmental Protection Agency (EPA). Per- and Polyfluoroalkyl Substances (PFAS) Hazard Index for Drinking Water. U.S. Environmental Protection Agency, Ed.

(311) European Food Safety Authority (EFSA). Chemical Mixtures. European Food Safety Authority, Ed.

(312) Borg, D.; Lund, B. O.; Lindquist, N. G.; Hakansson, H. Cumulative health risk assessment of 17 perfluoroalkylated and polyfluoroalkylated substances (PFASs) in the Swedish population. *Environ Int* **2013**, *59*, 112-123. DOI: 10.1016/j.envint.2013.05.009.

(313) US Environmental Protection Agency. Framework for Cumulative Risk Assessment. US Environmental Protection Agency, Ed.; 2003.

(314) Kolpin, D. W.; Hubbard, L. E.; Cwiertny, D. M.; Meppelink, S. M.; Thompson, D. A.; Gray, J. L. A Comprehensive Statewide Spatiotemporal Stream Assessment of Per- and Polyfluoroalkyl Substances (PFAS) in an Agricultural Region of the United States. *Environmental Science & Technology Letters* **2021**, *8* (11), 981-988. DOI: 10.1021/acs.estlett.1c00750.

(315) U.S. Environmental Protection Agency (EPA). *Per- and Polyfluoroalkyl Substances (PFAS): Final PFAS National Primary Drinking Water Regulation*. 2025. https://www.epa.gov/sdwa/and-polyfluoroalkyl-substances-pfas (accessed 2024 December).

(316) MSU Extension Water Quality: Department of Land Resources and Environmental Sciences. *MSU Extension Water Quality*. https://waterquality.montana.edu/#:~:text=The%20Montana%20State%20University%20Extension,research%2C%20education%2C%20and%20outreach. (accessed 2025 March 7).

(317) Montana Bureau of Mines and Geology (MBMG). *Groundwater Information Center.* https://mbmggwic.mtech.edu. (accessed 2025 March 3).

(318) MSU Extension Water Quality. *PFAS*. 2025. https://waterquality.montana.edu/well-ed/pfas/index.html (accessed 2025 March 10).

(319) Gray, J. L.; Kanagy, L. K.; Kanagy, C. J.; Anderson, C. A. Concentrations of per- and polyfluoroalkyl substances (PFAS) from validation experiments and custom sample analysis by U.S. Geological Survey (USGS) National Water Quality Laboratory (NWQL) Laboratory Code 9660, December 2020 to March 2022: U.S. Geological Survey data release. **2024**. DOI: 10.5066/P9P3YPXG.

(320) US Environmental Protection Agency. *Safe Drinking Water Act (SDWA)*. 2025. https://www.epa.gov/sdwa.

(321) Health Canada. *Water talk: Per-and polyfluoroalkyl substances (PFAS) in drinking water*. 2025. https://www.canada.ca/en/health-canada/services/environmental-workplace-health/reports-publications/water-quality/water-talk-per-polyfluoroalkyl-substances-drinking-water.html.

(322) Colorado Department of Public Health & Environment. Policy 20-1: Policy for Interpreting the Narrative Water Quality Standards for Per- and Polyfluoroalkyl Substances (PFAS). Colorado Department of Public Health & Environment, Ed.; 2020.

(323) State of Hawaii Department of Health. Interim Soil and Water Environmental Action Levels (EALs) for Perfluoroalkyl and Polyfluoroalkyl Substances (PFASs) State of Hawaii Department of Health, Ed.; Honolulu, HI, 2024.

(324) Minnesota Department of Health. Perfluorobutyrate (PFBA) Toxicological Summary Sheet. Minnesota Department of Health, Ed.; Saint Paul, MN, 2018.

(325) Minnesota Department of Health. Perfluorobutane Sulfonate (PFBS) Toxicological Summary. Minnesota Department of Health, Ed.; Saint Paul, MN, 2023.

(326) Vermont Agency of Natural Resources, D. o. E. C. Groundwater Protection Rule and Strategy (GWPRS). Vermont Agency of Natural Resources, Ed.; Montpelier, VT, 2019.

(327) Rhode Island Department of Environmental Management. Regulation 13028: Water Quality Standards. Rhode Island Department of Environmental Management, Ed.; Providence, RI, 2023.

(328) U.S. Environmental Protection Agency. PFAS National Primary Drinking Water Regulation (NPDWR) Fact Sheet. U.S. Environmental Protection Agency, Ed.; Washington, D.C., 2024.

(329) Schreiner, M. L.; Romanok, K. M.; Bradley, P. M.; Smalling, K. L.; Gray, J. L.; Kanagy, L. K. Per- and polyfluoroalkyl substances (PFAS) results in tapwater samples, in selected areas within the United States, beginning 2023: U.S. Geological Survey data release. 2025.

(330) PFAS in US Groundwater Interactive Dashboard. U.S. Geological Survey. https://geonarrative.usgs.gov/pfasinusgroundwater/.

(331) Paige, T.; De Silva, T.; Buddhadasa, S.; Prasad, S.; Nugegoda, D.; Pettigrove, V. Background concentrations and spatial distribution of PFAS in surface waters and sediments of the greater Melbourne area, Australia. *Chemosphere* **2024**, *349*, 140791. DOI: 10.1016/j.chemosphere.2023.140791.

(332) Yates, M. V. Septic Tank Density and Ground-Water Contamination. *Groundwater* **2006**, *23* (5), 586-591. DOI: 10.1111/j.1745-6584.1985.tb01506.x.

(333) Tooele County Health Department. *Septic System Density Study*; Tooele County, UT, 2016. https://tooelehealth.org/wp-content/uploads/2016/05/Tooele-County-Septic-Density-Study-FINAL-00000002-5.pdf.

(334) USGS: Water Resources Mission Area. *Domestic (Private) Supply Wells*. 2019. https://www.usgs.gov/mission-areas/water-resources/science/domestic-private-supply-wells#overview.

(335) Ferguson, G.; McIntosh, J. C.; Jasechko, S.; Kim, J.-H.; Famiglietti, J. S.; McDonnell, J. J. Groundwater deeper than 500 m contributes less than 0.1% of global river discharge. *Communications Earth & Environment* **2023**, *4* (1). DOI: 10.1038/s43247-023-00697-6.

(336) Addicks, G. C.; Rowan-Carroll, A.; Reardon, A. J. F.; Leingartner, K.; Williams, A.; Meier, M. J.; Moffat, I.; Carrier, R.; Lorusso, L.; Wetmore, B. A.; et al. Per- and polyfluoroalkyl substances (PFAS) in mixtures show additive effects on transcriptomic points of departure in human liver spheroids. *Toxicological Sciences* **2023**, *194* (1), 38-52. DOI: 10.1093/toxsci/kfad044.

(337) Kwiatkowski, C. F.; Andrews, D. Q.; Birnbaum, L. S.; Bruton, T. A.; DeWitt, J. C.; Knappe, D. R. U.; Maffini, M. V.; Miller, M. F.; Pelch, K. E.; Reade, A.; et al. Scientific Basis for Managing PFAS as a Chemical Class. *Environ Sci Technol Lett* **2020**, *7* (8), 532-543. DOI: 10.1021/acs.estlett.0c00255.

(338) U.S. Environmental Protection Agency. Onsite Wastewater Treatment Systems Manual. U.S. Environmental Protection Agency., Ed.; 2002.

(339) Wang, B.; Tontonoz, P. Phospholipid Remodeling in Physiology and Disease. *Annu Rev Physiol* **2019**, *81*, 165-188. DOI: 10.1146/annurev-physiol-020518-114444.

(340) Andrade, S.; Ramalho, M. J.; Loureiro, J. A.; Pereira, M. C. Liposomes as Biomembrane Models: Biophysical Techniques for Drug-Membrane Interaction Studies. *Journal of Molecular Lipids* **2021**, *334*. DOI: 10.1016/j.molliq.2021.116141.

(341) Cooper, G. M. *The Cell: A Molecular Approach*; 2000.

(342) Weaver, T. E.; Whitsett, J. A. Function and Regulation of Expression of Pulmonary Surfactant-Associated Proteins. *Biochem. J.* **1991**, *273*, 249-264. DOI: 10.1042/bj2730249.

(343) Crouch, E.; Wright, J. R. Surfactant Proteins A and D and Pulmonary Host Defense. *Annual Review of Physiology* **2001**, *63*, 521-554. DOI: 10.1146/annurev.physiol.63.1.521.

(344) Schurch, D.; Ospina, O. L.; Cruz, A.; Perez-Gil, J. Combined and independent action of proteins SP-B and SP-C in the surface behavior and mechanical stability of pulmonary surfactant films. *Biophys J* **2010**, *99* (10), 3290-3299. DOI: 10.1016/j.bpj.2010.09.039.

(345) Ojo, A. F.; Peng, C.; Ng, J. C. Combined effects and toxicological interactions of perfluoroalkyl and polyfluoroalkyl substances mixtures in human liver cells (HepG2). *Environ Pollut* **2020**, *263* (Pt B), 114182. DOI: 10.1016/j.envpol.2020.114182.

(346) Pierozan, P.; Kosnik, M.; Karlsson, O. High-content analysis shows synergistic effects of low perfluorooctanoic acid (PFOS) and perfluorooctane sulfonic acid (PFOA) mixture concentrations on human breast epithelial cell carcinogenesis. *Environ Int* **2023**, *172*, 107746. DOI: 10.1016/j.envint.2023.107746.

(347) Mahoney, H.; da Silva, F.; Brinkmann, M.; Giesy, J. P. Mixtures of legacy and replacement perfluorosulphonic acids (PFSAs) demonstrate ratio-, concentration- and endpoint-dependent synergistic interactions in vitro. *Chemosphere* **2024**, *361*, 142446. DOI: 10.1016/j.chemosphere.2024.142446.

(348) Rabe, M.; Verdes, D.; Seeger, S. Understanding protein adsorption phenomena at solid surfaces. *Adv Colloid Interface Sci.* **2011**, *162* (1-2), 87-106. DOI: 10.1016/j.cis.2010.12.007.

(349) Murialdo, M.; Stadie, N. P.; Ahn, C. C.; Fultz, B. A generalized law of corresponding states for the physisorption of classical gases with cooperative adsorbate-adsorbate interactions. *J. Phys. Chem. C.* **2016**, *120* (22), 11847-11853. DOI: 10.1021/acs.jpcc.6b00289

# APPENDICES

# APPENDIX A

## A. SUPPORTING INFORMATION FOR CHAPTER 2

Table A-1. Surface coverages (Γ) for PFAS at variable pH and pH 8 buffer environment. The pH for variable pH experiments is expressed in the parentheses. The terminal surface coverages are noted in bold.

| | Γ (molecule/$cm^2$) | | | | | |
|---|---|---|---|---|---|---|
| | PFOA | | PFBS | | KPFOS | |
| Concentration (mM) | Variable pH | pH 8 | Variable pH | pH 8 | Variable pH | pH 8 |
| $10^{-7}$ | 6.9$E$9 (4.7) | 1.1$E$13 | 4.2$E$12 (4.7) | 4.8 $E$13 | 5.1$E$13 (4.2) | 2.7$E$13 |
| $10^{-6}$ | 4.0$E$10 (4.7) | 2.3$E$13 | 1.2$E$13 (4.7) | **5.0*E*13** | 6.0$E$13 (4.3) | 3.6$E$13 |
| $10^{-5}$ | 2.3$E$10 (4.6) | 4.6$E$13 | 2.7$E$13 (4.6) | 5.0$E$13 | 7.0$E$13 (4.4) | 4.9$E$13 |
| $10^{-4}$ | 1.4$E$12 (4.5) | 8.8$E$13 | 5.2$E$13 (4.6) | 5.0$E$13 | 8.1$E$13 (4.4) | 6.7$E$13 |
| $10^{-3}$ | 7.7$E$13 (4.3) | 1.5$E$14 | **6.6*E*13** (4.5) | 5.0$E$13 | 9.2$E$13 (4.5) | 9.0$E$13 |
| $10^{-2}$ | 4.6$E$13 (3.9) | 2.1$E$14 | 6.6$E$13 (4.3) | 5.0$E$13 | 1.0$E$14 (4.6) | 1.2$E$14 |
| $10^{-1}$ | 2.1$E$14 ( 3.7) | **2.3*E*14** | 6.6$E$13 (4.2) | 5.0$E$13 | 1.2$E$14 (4.7) | 1.6$E$14 |
| $10^{0}$ | **5.4*E*14**(3.3) | 2.3$E$14 | 6.6$E$13 (3.5) | 5.0$E$13 | 1.3**$E$14** (5.0) | 2.0**$E$14** |

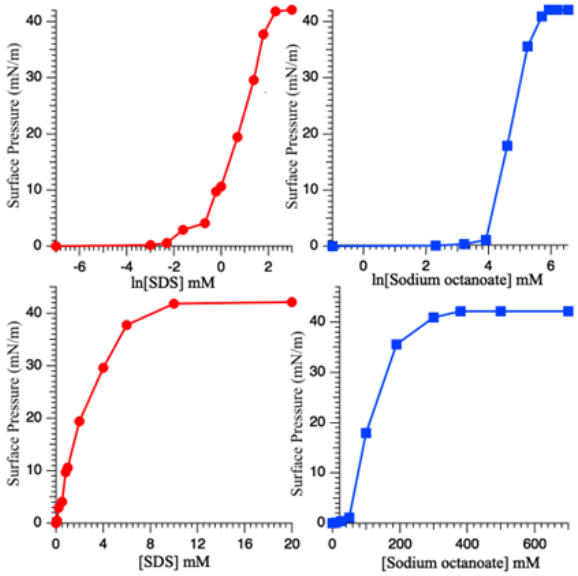



Figure A-1. Surface tension of SDS on left (CMC 8.3 mM) and sodium octanoate on right(CMC 380 mM). Both surfactants have concentrations in the millimolar range while PFAS are found much lower in the micromolar range.

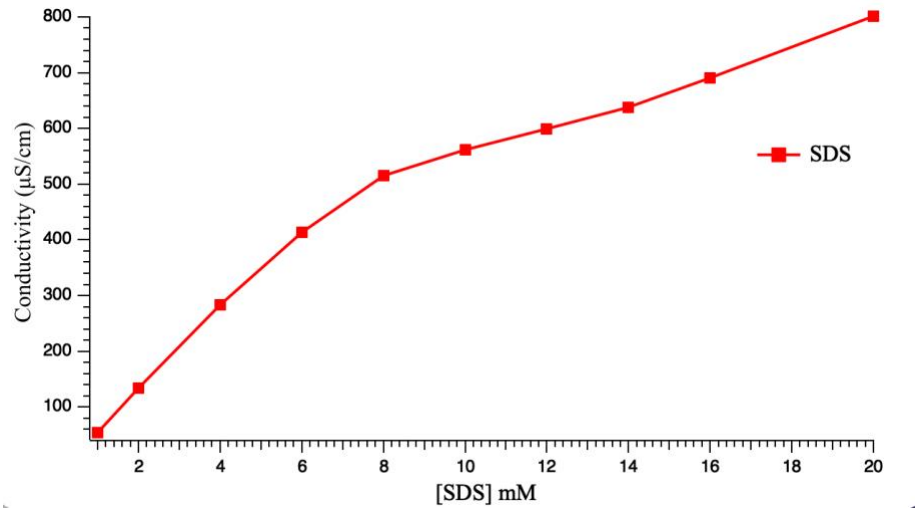



Figure A-2. Conductivity measurements of SDS showing a drastic change of slope after CMC is reached.

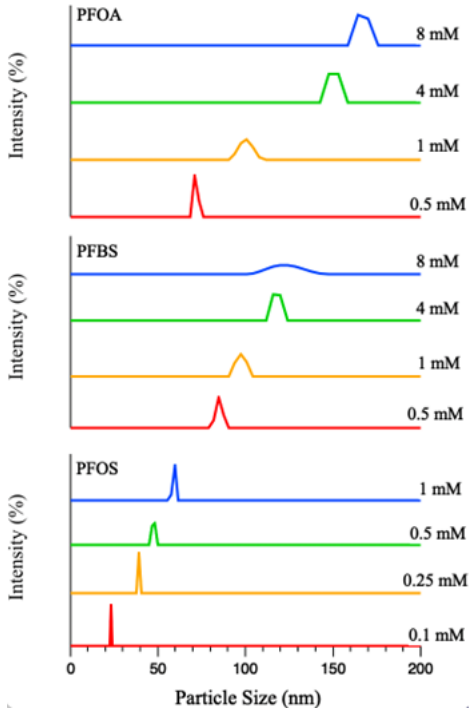



Figure A-3. Concentration dependence of PFOA, PFBS, and KPFOS on particle size (nm) at variable pH.

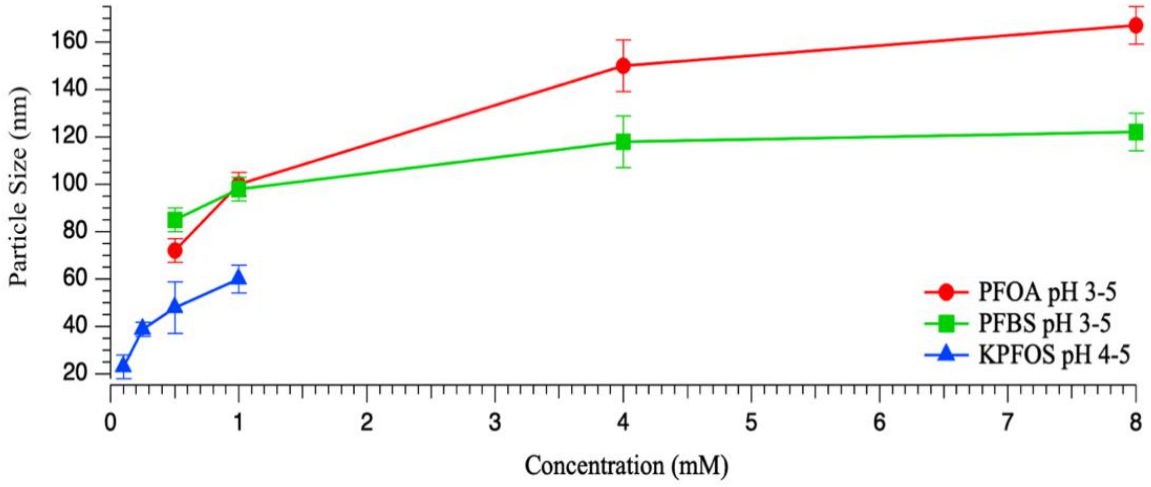



Figure A-4. Average particle size of PFOA, PFBS, and KPFOS nanodroplets as a function of concentration for samples with varying pH (made in Millipore)

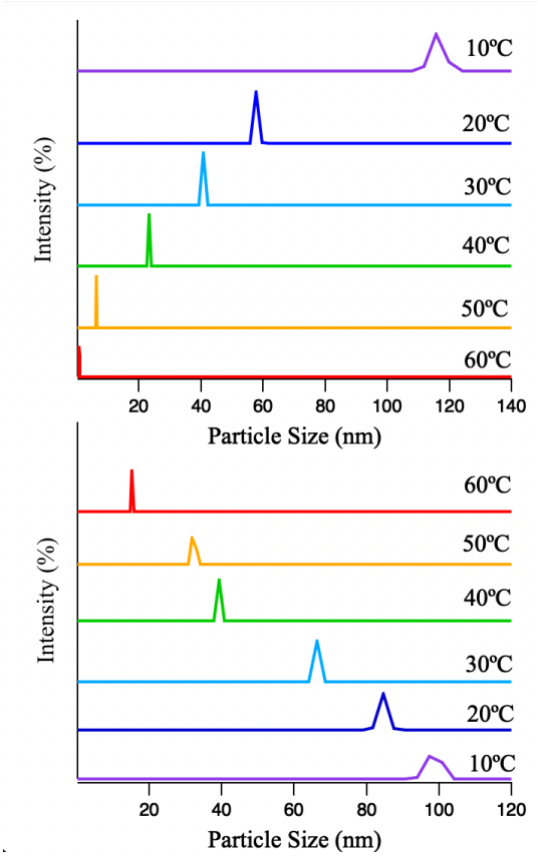



Figure A-5. 1 mM solutions of PFBS at pH 8 subjected to temperature dependent studies from 10°C to 60°C and back down in 10°C increments. The particle size reduces to micellar size before disappearing at 60°C and then returns upon cooling the solution back down.

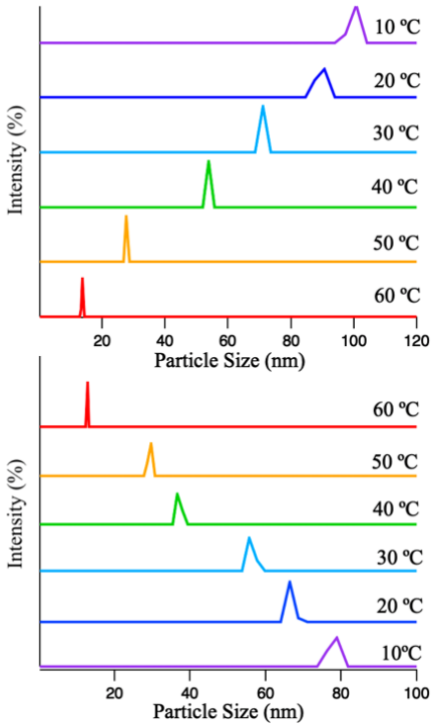



Figure A-6. 1 mM solutions of KPFOS at pH 8 subjected to temperature dependent studies from 10°C to 60°C and back down in 10°C increments.

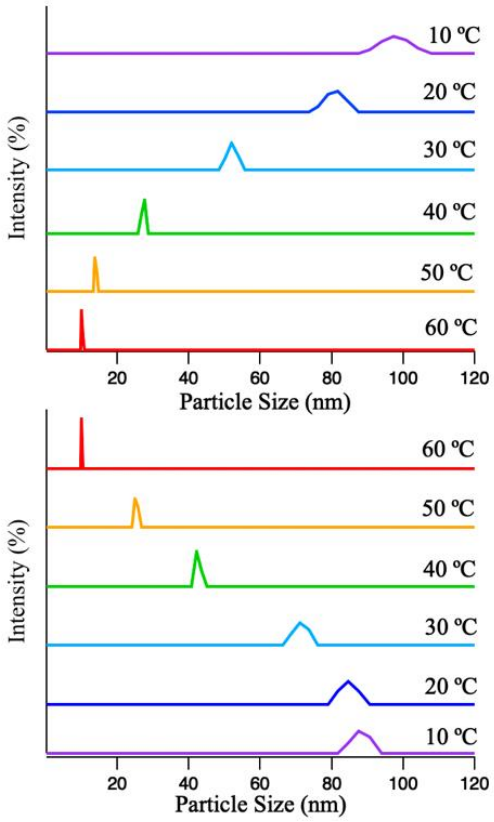



Figure A-7. 1 mM solutions of PFOA at pH 3.3 subjected to temperature dependent studies from 10°C to 60°C and back down in 10°C increments.

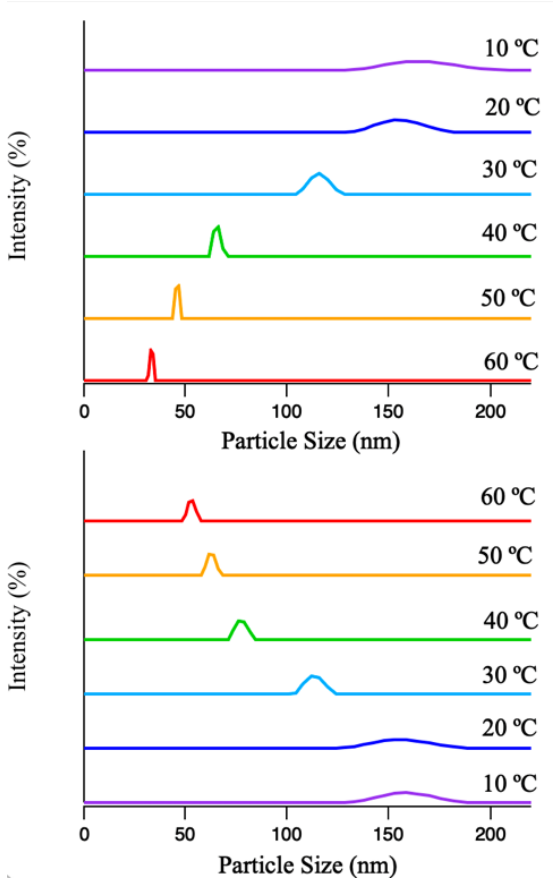



Figure A-8. 1 mM solutions of PFBS at pH 3.5 subjected to temperature dependent studies from 10°C to 60°C and back down in 10°C increments.

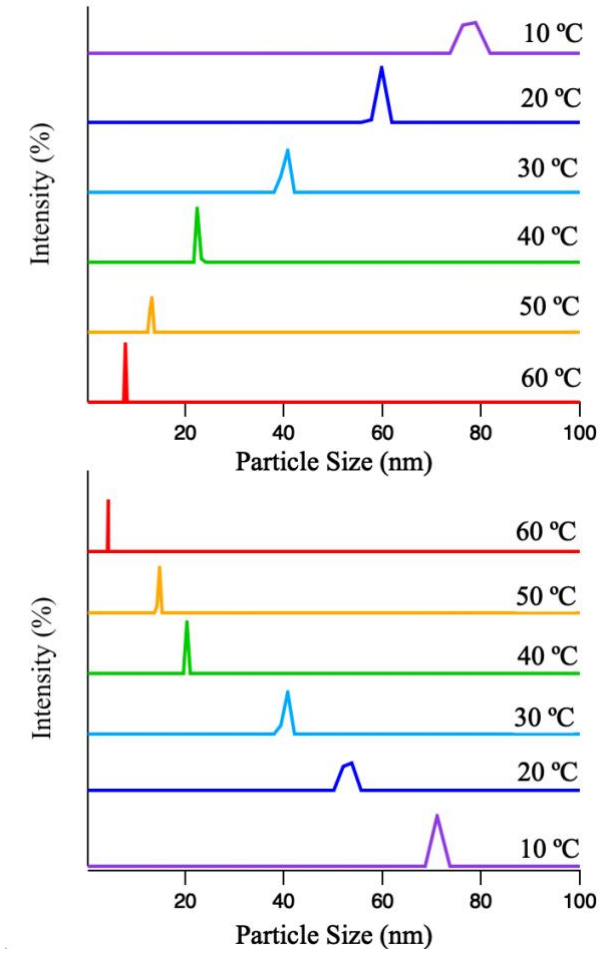



Figure A-9. 1 mM solutions of KPFOS at pH 5.0 subjected to temperature dependent studies from 10°C to 60°C and back down in 10°C increments.

Table A-2. Particle size (nm) as temperature increases from 10 to 60 degrees before being cooled back down for PFAS of varying pH at 1 mM concentrations.

| | | Particle Size (nm) | | |
|---|---|---|---|---|
| | Temperature (ºC) | PFOA (pH 3.3) | PFBS (pH 3.5) | KPFOS (pH 5.0) |
| Heating | 10 | 98 | 165 | 78 |
| | 20 | 81 | 155 | 60 |
| | 30 | 52 | 116 | 40 |
| | 40 | 27 | 66 | 23 |
| | 50 | 14 | 46 | 13 |
| | 60 | 10 | 33 | 8 |
| Cooling | 60 | 10 | 53 | 4 |
| | 50 | 25 | 63 | 15 |
| | 40 | 43 | 78 | 20 |
| | 30 | 71 | 137 | 40 |
| | 20 | 85 | 156 | 53 |
| | 10 | 88 | 158 | 71 |

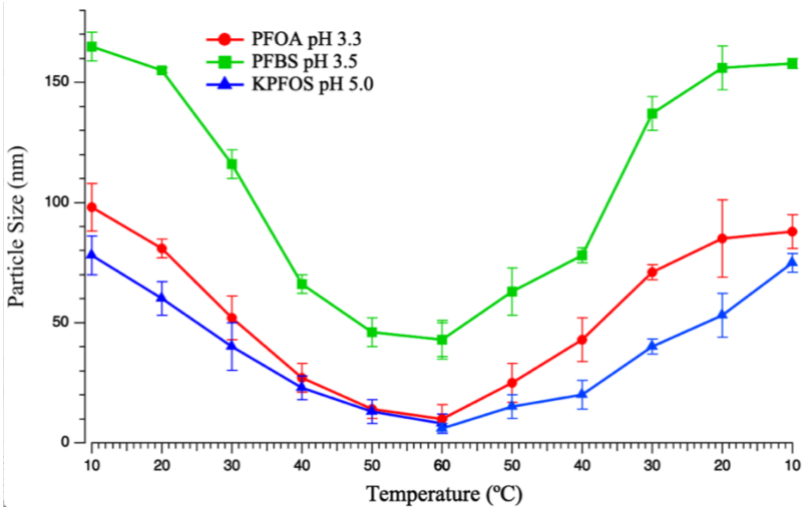



Figure A-10. Average particle size as a function of temperature for 1mM PFOA (pH 3.3), 1mM PFBS (3.5), and 1mM KPFOS (pH 5.0) as a function of temperature. Samples are heated from 10 to 60 degrees before being cooled back to 10 degrees.

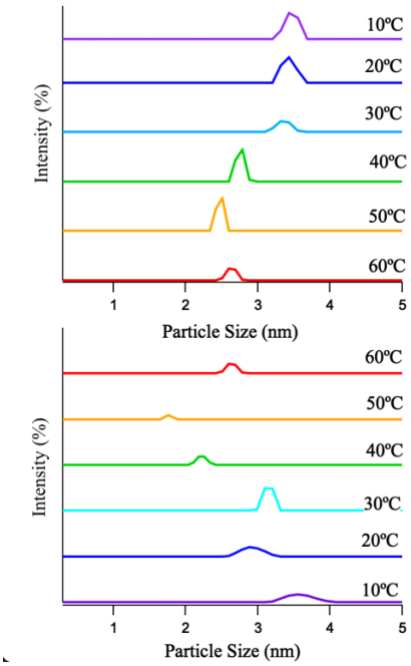



Figure A-11. Sodium dodecyl sulfate (SDS) particle size as a function of temperature for a 10 mM SDS solution. Samples are heated from 10 to 60 degrees before being cooled back to 10 degrees.

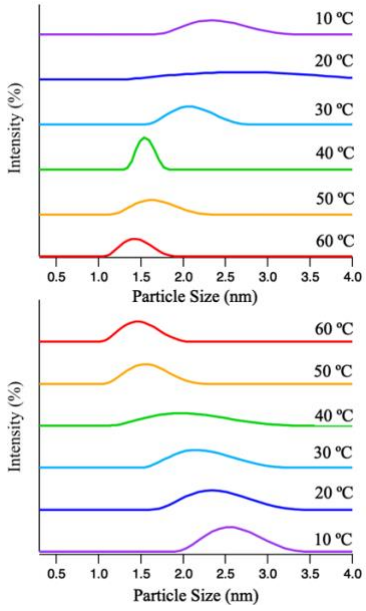



Figure A-12. Sodium octanoate particle size as a function of temperature in a 380 mM solution. Samples are heated from 10 to 60 degrees before being cooled back to 10 degrees.

Table A-3. Particle size (nm) for SDS and sodium octanoate were subjected to temperature dependent studies from 10°C to 60°C and back down in 10°C increments.

| | | Particle Size (nm) | |
|---|---|---|---|
| | Temperature (ºC) | SDS | Sodium Octanoate |
| Heating | 10 | 3.5 | 2.4 |
| | 20 | 3.4 | 2.6 |
| | 30 | 3.4 | 2.1 |
| | 40 | 2.8 | 1.6 |
| | 50 | 2.5 | 1.6 |
| | 60 | 2.7 | 1.4 |
| Cooling | 60 | 0.4 | 1.5 |
| | 50 | 1.8 | 1.6 |
| | 40 | 2.2 | 2.0 |
| | 30 | 3.1 | 2.2 |
| | 20 | 2.9 | 2.4 |
| | 10 | 3.6 | 2.6 |

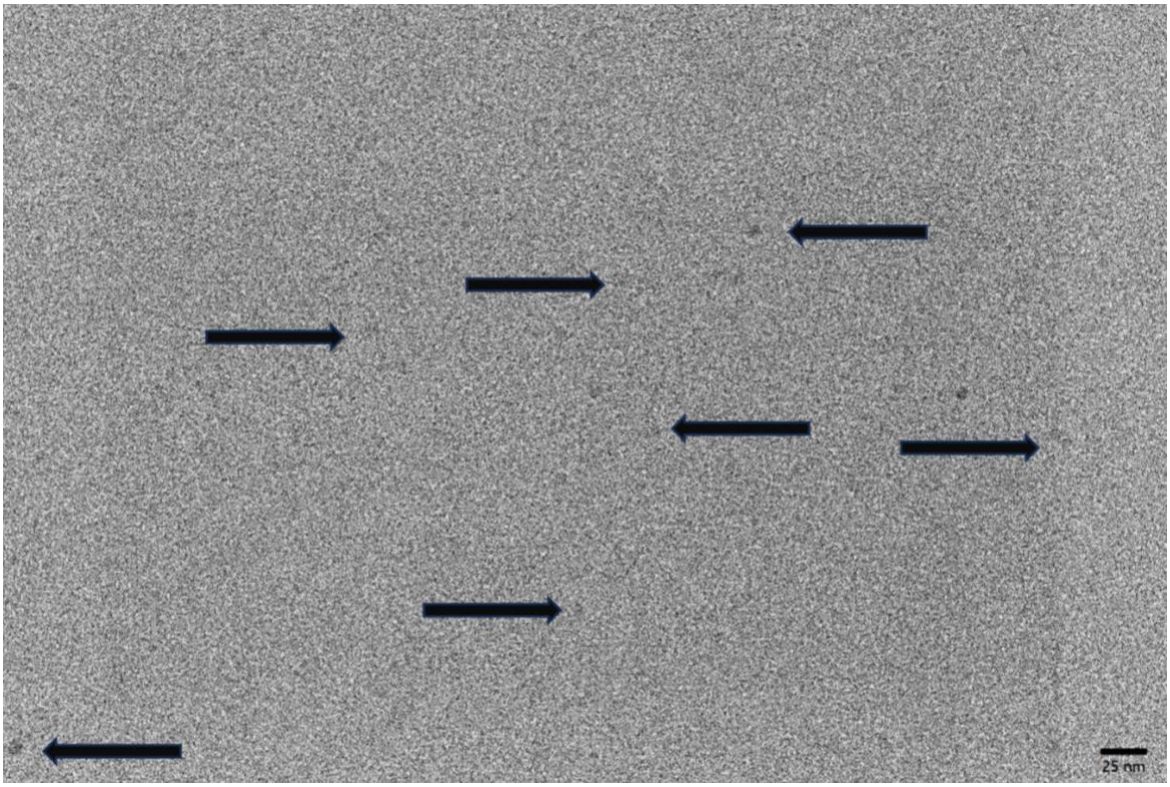



Figure A-13. A Cryo-EM image of a frozen 12 mM SDS solution with the black arrows designating SDS micelles. The micelle images range in size from 5 – 9 nm. The scale bar in the lower right corner of the image is 25 nm.

# APPENDIX B

## B. SUPPORTING INFORMATION FOR CHAPTER 3

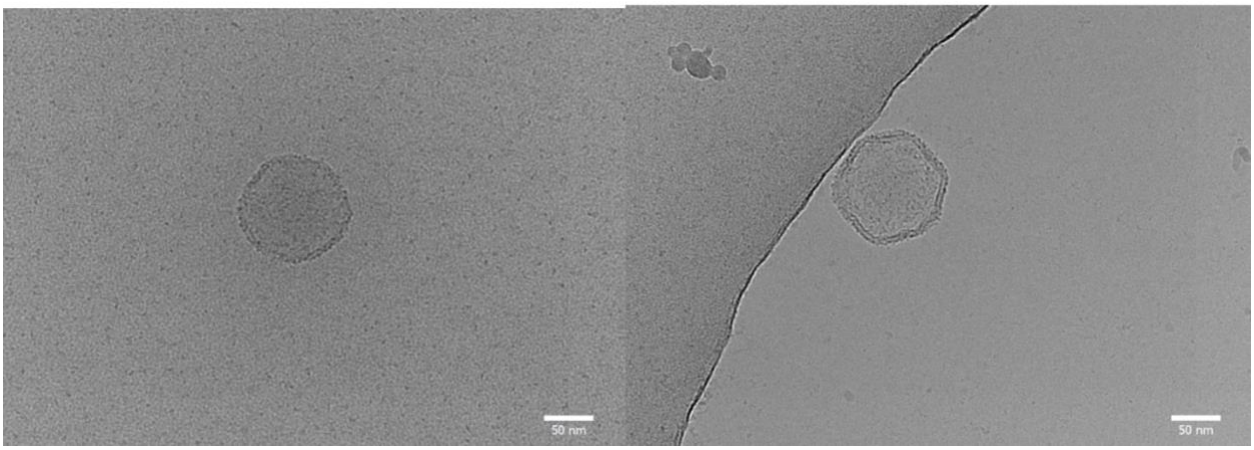



Figure B-1. Cryo-EM Images of DPPC vesicles prepared in pure buffer solutions containing no PFOA. These images can be compared directly to those in Figure 4 of the manuscript. These images are provided to demonstrate DPPC vesicle preparation generally leads to large unilamellar vesicles. Scale bars are 50 nm.

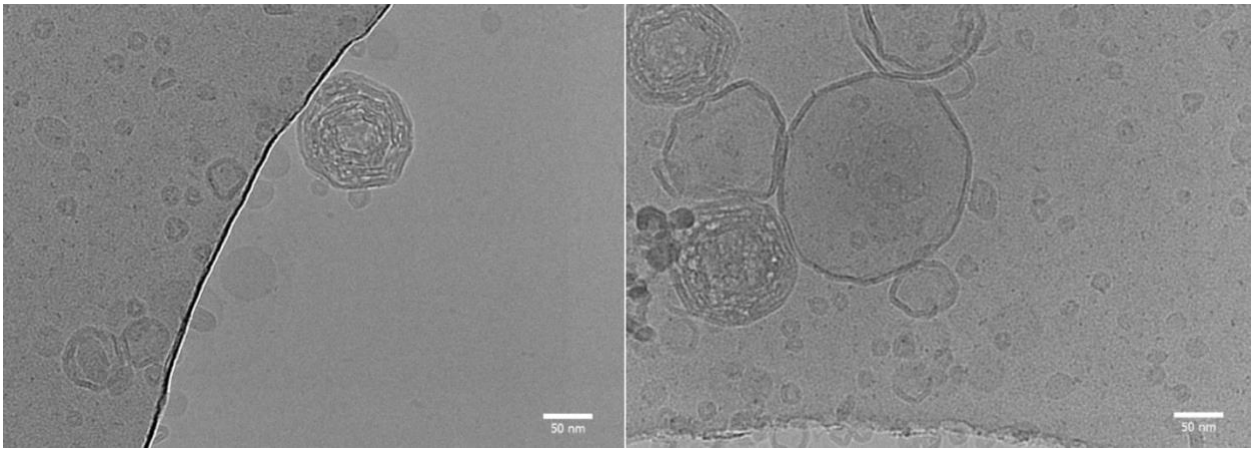



Figure B-2. Cryo-EM Images of DPPC vesicles prepared in solutions containing 100 nM PFOA. These images can be compared directly to those in Figure 5 of the manuscript. These images are provided to demonstrate generally that 100 nM PFOA introduces significant structural changes in DPPC vesicles. Scale bars are 50 nm.

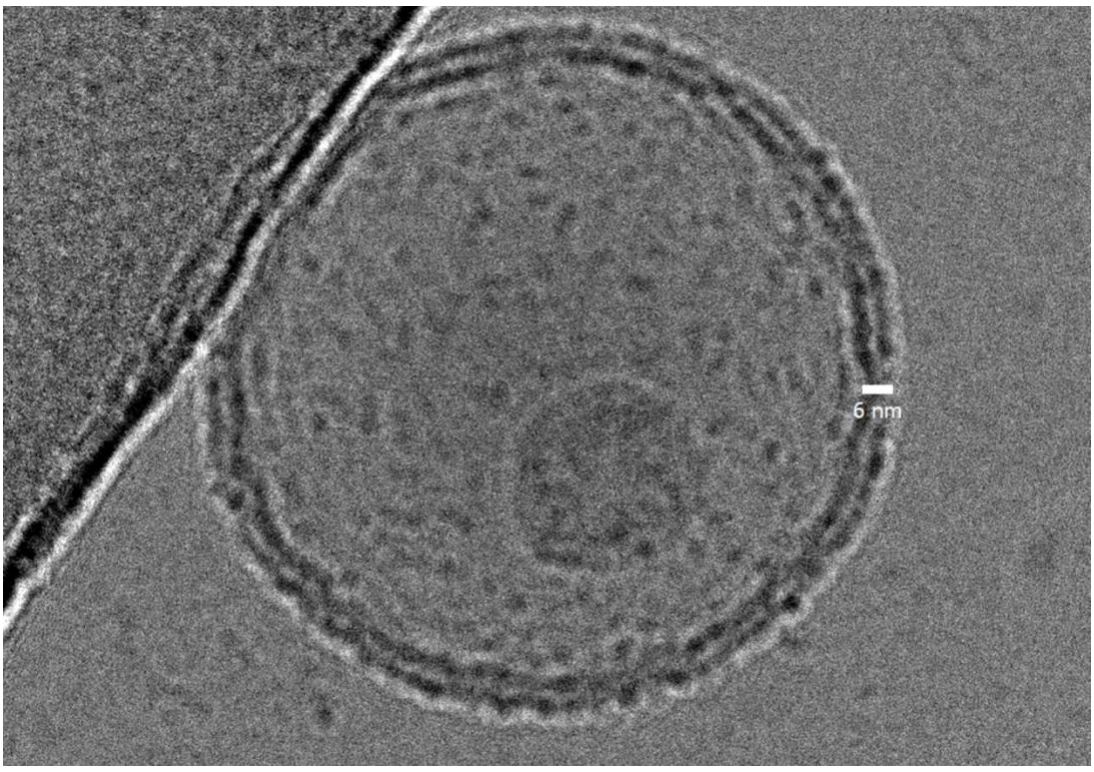



Figure B-3. Zoomed in image of a DPPC vesicle prepared in pure buffer solution. The scale bar is 6 nm and is chosen to span the bilayer width.

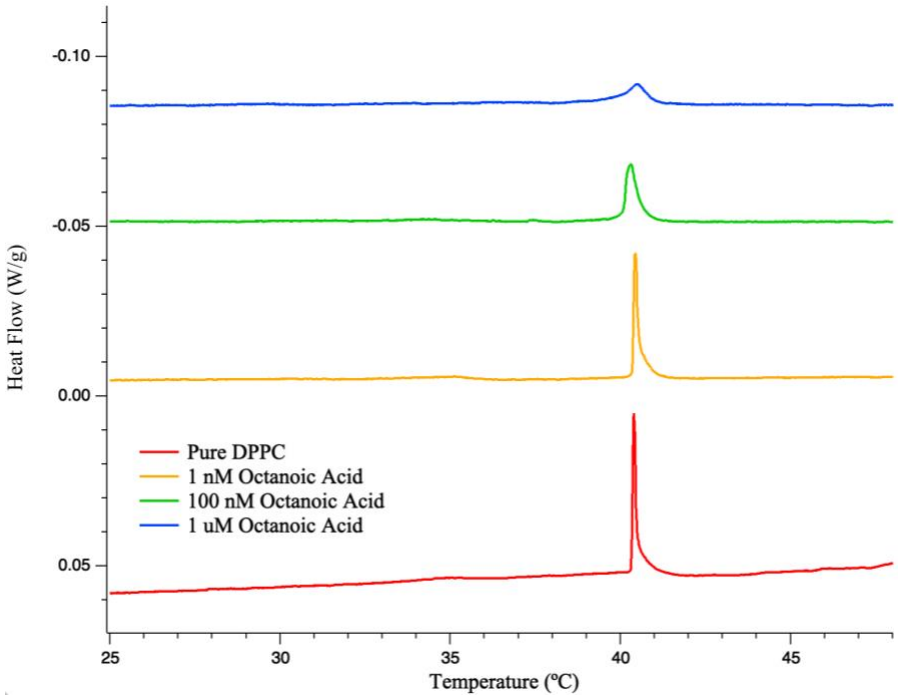



Figure B-4. DSC traces for DPPC prepared in the presence of octanoic acid.

Table B-1. DSC enthalpy values for DPPC prepared in the presence of octanoic acid.

| [Octanoic Acid] nM | Enthalpy (J/g) | Std Deviation |
|---|---|---|
| 0 | 44 | 1 |
| 1 | 40 | 3 |
| 100 | 36 | 1 |
| 1000 | 20 | 2 |

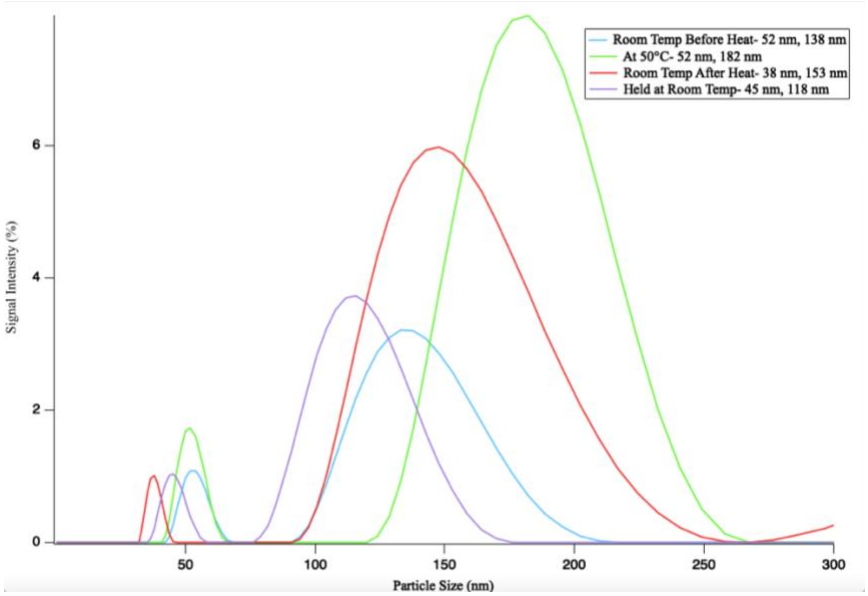



Figure A-5. DLS traces for DPPC prepared in the presence of octanoic acid at room temperature, heated to 50°C and then cooled back to room temperature.

# APPENDIX C

## C. SUPPORTING INFORMATION FOR CHAPTER 4

Table C-1. PFOA only, No DPPC (OH range)

| AVG TABLE (Avg of Two Trials) | | | | | | |
|---|---|---|---|---|---|---|
| | Peak 1 (~3200cm$^{-1}$) | | | Peak 2 (~3450cm$^{-1}$) | | |
| PFOA [uM] | FWHM | Sigma | Area | FWHM | Sigma | Area |
| 0 | 564.09 | 239.63 | 39.74 | 304.73 | 129.45 | 12.34 |
| 1 | 263.08 | 111.76 | 15.79 | 176.36 | 74.92 | 11.46 |
| 10 | 290.60 | 123.45 | 48.22 | 119.67 | 50.84 | 10.41 |
| 100 | 317.99 | 135.09 | 77.07 | 116.18 | 49.36 | 15.76 |
| 250 | 293.79 | 124.81 | 71.31 | 131.75 | 55.97 | 20.08 |
| 500 | 286.60 | 121.75 | 73.14 | 118.91 | 50.52 | 15.98 |
| 1000 | 317.77 | 134.99 | 96.06 | 111.94 | 47.56 | 19.01 |
| 8000 | 320.92 | 136.33 | 121.64 | 126.81 | 53.87 | 34.99 |

Table C-2. 40 Å$^2$/molecule DPPC with PFOA (OH range)

| AVG TABLE (averages of two tables) | | | | | | |
|---|---|---|---|---|---|---|
| | Peak 1 (~3200cm$^{-1}$) | | | Peak 2 (~3450cm$^{-1}$) | | |
| PFOA [uM] | FWHM | Sigma | Area | FWHM | Sigma | Area |
| 0 | 499.55 | 212.22 | 29.79 | 177.64 | 75.47 | 5.90 |
| 10 | 377.69 | 160.45 | 68.45 | 128.32 | 54.51 | 6.58 |
| 25 | 301.35 | 128.02 | 85.54 | 127.58 | 54.20 | 17.76 |
| 50 | 355.67 | 151.09 | 124.03 | 139.75 | 59.37 | 34.75 |
| 75 | 339.87 | 144.38 | 183.29 | 131.01 | 55.66 | 41.56 |
| 100 | 320.92 | 136.33 | 165.79 | 129.33 | 54.94 | 32.15 |

Table C-3. 55 Å$^2$/molecule DPPC with PFOA (OH range)

| AVG TABLE (averages of two tables) | | |
|---|---|---|
| | Peak 1 (~3200cm$^{-1}$) | Peak 2 (~3450cm$^{-1}$) |

| PFOA [uM] | FWHM | Sigma | Area | FWHM | Sigma | Area |
|---|---|---|---|---|---|---|
| 0 | 248.65 | 105.63 | 6.65 | 289.77 | 123.10 | 3.08 |
| 10 | 340.78 | 144.77 | 32.30 | 218.72 | 92.92 | 6.50 |
| 25 | 424.43 | 180.30 | 96.52 | 166.05 | 70.54 | 9.96 |
| 50 | 621.09 | 263.85 | 184.16 | 283.08 | 120.26 | 21.78 |
| 75 | 423.67 | 179.98 | 114.95 | 125.88 | 53.48 | 9.51 |
| 100 | 339.67 | 144.30 | 111.37 | 127.47 | 54.15 | 18.44 |

Table C-4. 40 Å$^2$/molecule DPPC with PFOA (CH Range)

| Average of Three Trials Table | | | | | | | | | |
|---|---|---|---|---|---|---|---|---|---|
| | Peak 1 ($CH_2$ SS) | | | Peak 2 ($CH_3$ SS) | | | Peak 3 ($CH_3$ SS/Fermi) | | |
| PFOA [uM] | FWHM | Sigma | Area | FWHM | Sigma | Area | FWHM | Sigma | Area |
| 0 | 14.21 | 6.04 | 1.25 | 21.83 | 9.27 | 19.69 | 25.86 | 10.99 | 18.47 |
| 10 | 16.55 | 7.03 | 1.15 | 23.13 | 9.83 | 20.49 | 29.36 | 12.47 | 20.32 |
| 25 | 15.75 | 6.69 | 1.13 | 23.18 | 9.85 | 18.82 | 29.81 | 12.66 | 17.36 |
| 50 | 13.38 | 5.68 | 0.89 | 23.97 | 10.18 | 14.17 | 27.85 | 11.83 | 17.67 |
| 75 | 13.23 | 5.62 | 0.81 | 24.14 | 10.26 | 12.06 | 26.49 | 11.25 | 16.63 |

Table C-5. 55 Å$^2$/molecule DPPC with PFOA (CH range)

| | Peak 1 ($CH_2$ SS) | | | Peak 2 ($CH_3$ SS) | | | Peak 3 ($CH_3$ SS/Fermi) | | |
|---|---|---|---|---|---|---|---|---|---|
| PFOA [uM] | FWHM | Sigma | Area | FWHM | Sigma | Area | FWHM | Sigma | Area |
| 0 | 19.23 | 8.17 | 3.86 | 18.90 | 8.03 | 3.98 | 31.87 | 13.54 | 6.84 |
| 10 | 21.24 | 9.02 | 1.99 | 26.35 | 11.19 | 8.82 | 34.51 | 14.66 | 9.70 |
| 25 | 16.24 | 6.90 | 0.69 | 25.69 | 10.91 | 10.24 | 28.43 | 12.08 | 7.60 |
| 50 | 17.65 | 7.50 | 0.57 | 26.40 | 11.22 | 8.22 | 26.63 | 11.31 | 7.35 |
| 75 | 17.87 | 7.59 | 0.30 | 26.30 | 11.17 | 7.75 | 30.95 | 13.15 | 8.73 |

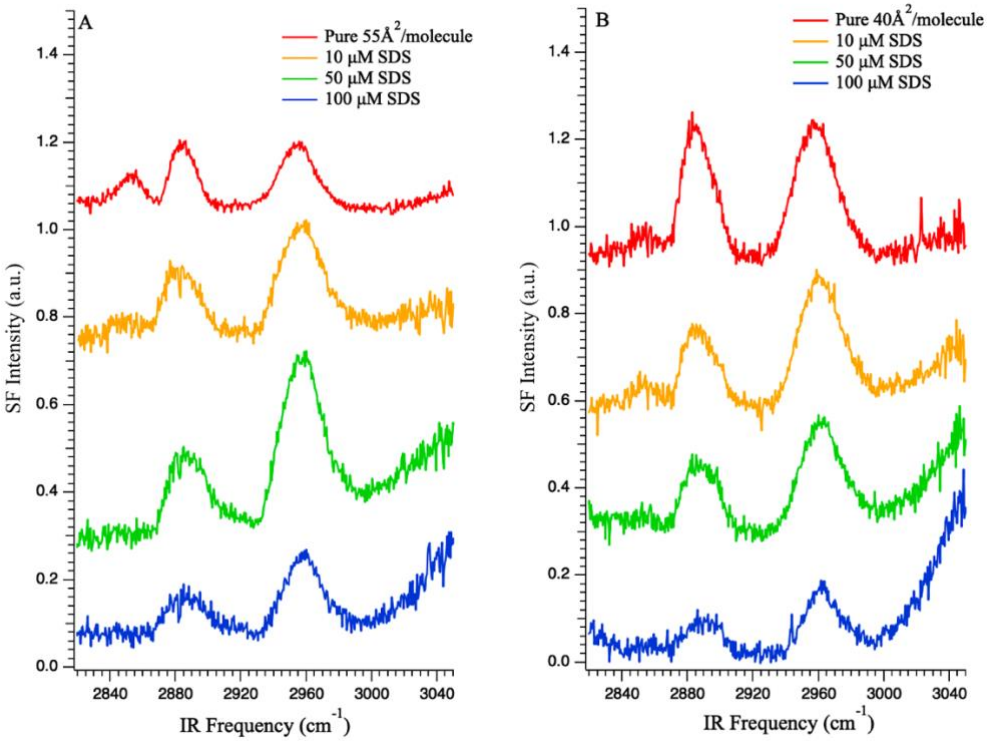



Figure C-1. (A) 55 Å$^2$/molecule DPPC with SDS (B) 40 Å$^2$/molecule DPPC and SDS deposited into the subphase (CH stretching region).

Table C-6. CH Range SDS 55 Å$^2$/molecule DPPC

| | Peak 1 ($CH_2$ SS) | | | Peak 2 ($CH_3$ SS) | | | Peak 3 ($CH_3$ SS/Fermi) | | | |
|---|---|---|---|---|---|---|---|---|---|---|
| SDS [uM] | FWHM | Sigma | Area | FWHM | Sigma | Area | FWHM | Sigma | Area | Ratio $CH_3$ SS/ $CH_2$ SS |
| 0 | 17.04 | 7.24 | 1.78 | 16.62 | 7.06 | 3.87 | 23.54 | 10.00 | 5.30 | 2.17 |
| 10 | 15.70 | 6.67 | 0.88 | 26.39 | 11.21 | 6.64 | 33.45 | 14.21 | 13.80 | 7.55 |
| 50 | 11.72 | 4.98 | 0.38 | 27.75 | 11.79 | 7.49 | 27.75 | 11.79 | 16.40 | 19.71 |
| 100 | 11.11 | 4.72 | 0.30 | 33.24 | 14.12 | 5.48 | 25.16 | 10.69 | 6.60 | 18.27 |

Table C-7. CH Range SDS 40 Å$^2$/molecule DPPC

| | Peak 1 ($CH_2$ SS) | | | Peak 2 ($CH_3$ SS) | | | Peak 3 ($CH_3$ SS/Fermi) | | | Ratio $CH_3$ SS/ $CH_2$ SS |
|---|---|---|---|---|---|---|---|---|---|---|
| SDS [uM] | FWHM | Sigma | Area | FWHM | Sigma | Area | FWHM | Sigma | Area | |
| 0 | 15.68 | 6.66 | 1.24 | 22.06 | 9.37 | 10.85 | 29.21 | 12.41 | 14.60 | 8.75 |
| 10 | 13.16 | 5.59 | 1.04 | 23.40 | 9.94 | 8.04 | 31.92 | 13.56 | 15.25 | 7.73 |
| 50 | 10.55 | 4.48 | 0.67 | 22.95 | 9.75 | 5.06 | 31.50 | 13.38 | 12.52 | 7.55 |
| 100 | 11.13 | 4.73 | 0.38 | 17.02 | 7.23 | 2.70 | 20.67 | 8.78 | 6.43 | 7.11 |

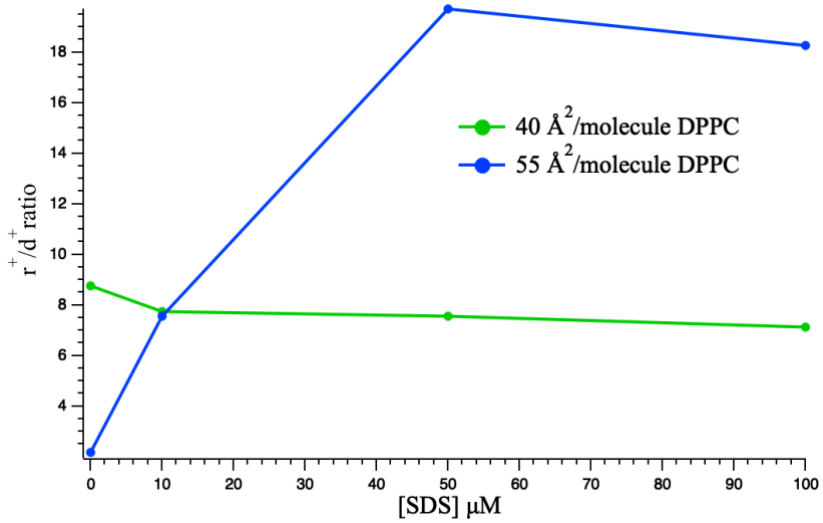



Figure C-2. The $r^+/d^+$ ratio for DPPC in the presence of SDS

Table C-8. 40 Å$^2$/molecule DPPC with SDS (OH range) Single Trial

| | Peak 1 (~3200cm$^{-1}$) | | | Peak 2 (~3450cm$^{-1}$) | | | Ratio Peaks 1:2 |
|---|---|---|---|---|---|---|---|
| SDS [uM] | FWHM | Sigma | Area | FWHM | Sigma | Area | |
| 0 | 535.39 | 227.44 | 35.62 | 99.06 | 42.08 | 2.08 | 17.13 |
| 10 | 298.65 | 126.87 | 147.49 | 126.65 | 53.80 | 11.72 | 12.58 |
| 50 | 336.06 | 142.76 | 109.30 | 115.44 | 49.04 | 12.50 | 8.74 |
| 100 | 362.68 | 154.07 | 49.12 | 112.29 | 47.70 | 8.76 | 5.61 |

Table C-9. 55 Å$^2$/molecule DPPC with SDS (OH range) Single Trial

| | Peak 1 (~3200cm$^{-1}$) | | | Peak 2 (~3450cm$^{-1}$) | | | |
|---|---|---|---|---|---|---|---|
| SDS [uM] | FWHM | Sigma | Area | FWHM | Sigma | Area | Ratio Peaks 1:2 |
| 0 | 170.97 | 72.63 | 3.45 | 308.59 | 131.09 | 16.53 | 0.21 |
| 10 | 287.26 | 122.03 | 137.10 | 99.81 | 42.40 | 8.04 | 17.05 |
| 50 | 232.88 | 98.93 | 68.30 | 111.51 | 47.37 | 9.84 | 6.94 |
| 100 | 179.37 | 76.20 | 27.83 | 125.87 | 53.47 | 9.38 | 2.97 |

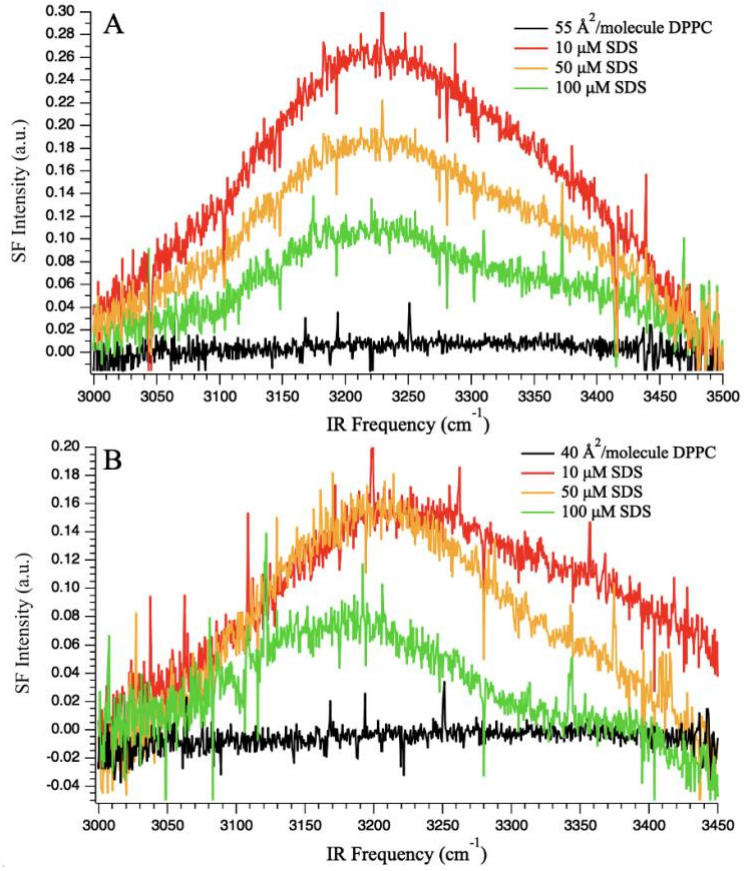



Figure C-3. 40 and 55 Å$^2$/molecule DPPC with SDS deposited into the subphase (OH stretching region).

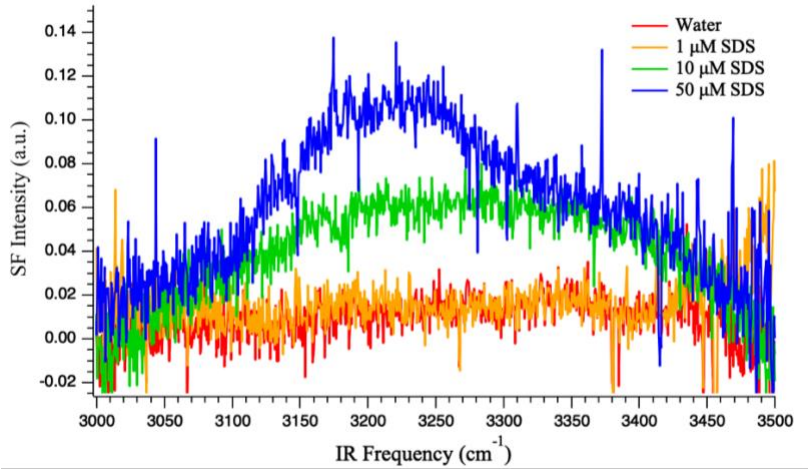



Figure C-4. OH region SDS surface activity leads to the formation of interfacial water signal.

Table C-10. SDS Only, No DPPC (OH range) Single Trial

| | Peak 1 (~3200cm$^{-1}$) | | | Peak 2 (~3450cm$^{-1}$) | | | |
|---|---|---|---|---|---|---|---|
| SDS [uM] | FWHM | Sigma | Area | FWHM | Sigma | Area | Ratio Peaks 1:2 |
| 0 | 183.78 | 78.07 | 3.16 | 309.15 | 131.33 | 15.98 | 0.20 |
| 1 | 313.51 | 133.18 | 12.46 | 114.05 | 48.45 | 14.48 | 0.86 |
| 10 | 473.30 | 201.06 | 75.09 | 311.86 | 132.48 | 42.14 | 1.78 |
| 50 | 186.53 | 79.24 | 35.16 | 125.96 | 53.51 | 28.25 | 1.24 |

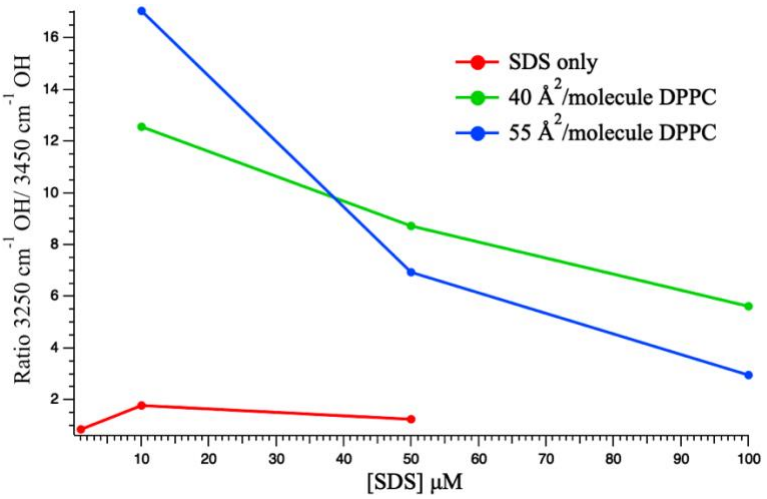



Figure C-5. OH 3200 cm$^{-1}$ ice like water to OH 3450 cm$^{-1}$ water like water ratio with no DPPC in solution, 40 Å$^2$/molecule DPPC, and 55 Å$^2$/molecule DPPC.

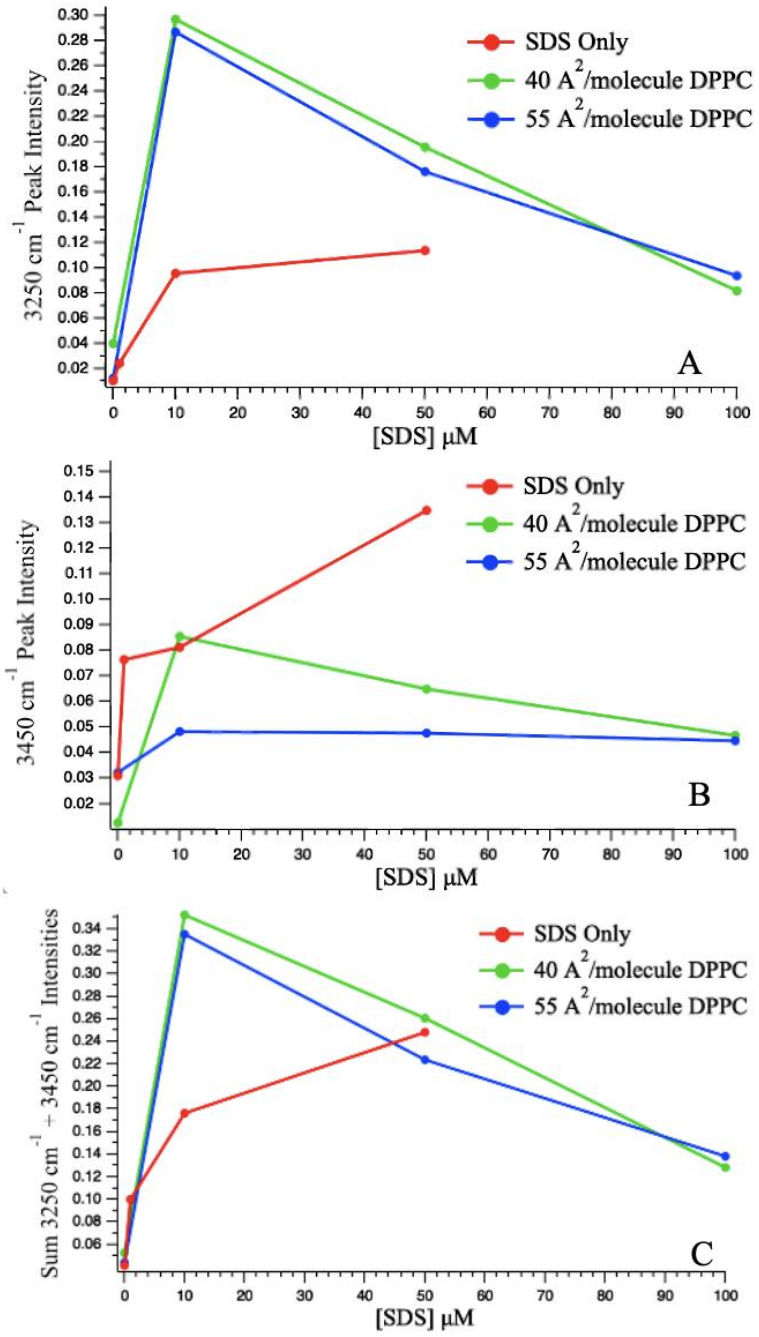



Figure C-6. Peak intensities at (A) 3200 $cm^{-1}$, (B) 3450 $cm^{-1}$, (C) sum of both peaks at 3200 $cm^{-1}$ and 3450$cm^{-1}$ showing an increasing trend with increasing concentration of SDS.

Table C-11. Peak intensities at (A) 3200 $cm^{-1}$, (B) 3450 $cm^{-1}$, (C) sum of both peaks at 3200 $cm^{-1}$ and 3450$cm^{-1}$ showing an increasing trend with increasing concentration of SDS.

| 3200 $cm^{-1}$ Peak Intensities | | | |
|---|---|---|---|
| [SDS] uM | 40 $Å^2$/molecule DPPC | 55 $Å^2$/molecule DPPC | SDS only |
| 0 | 0.04 | 0.01 | 0.01 |
| 10 | 0.30 | 0.29 | 0.10 |
| 50 | 0.20 | 0.18 | 0.11 |
| 100 | 0.08 | 0.09 | - |
| 3450 $cm^{-1}$ Peak Intensities | | | |
| [SDS] uM | 40 $Å^2$/molecule DPPC | 55 $Å^2$/molecule DPPC | SDS only |
| 0 | 0.01 | 0.03 | 0.03 |
| 10 | 0.06 | 0.05 | 0.08 |
| 50 | 0.07 | 0.05 | 0.13 |
| 100 | 0.05 | 0.04 | - |
| Sum of 3200 $cm^{-1}$ and 3450 $cm^{-1}$ Peak Intensities | | | |
| [SDS] uM | 40 $Å^2$/molecule DPPC | 55 $Å^2$/molecule DPPC | SDS only |
| 0 | 0.05 | 0.04 | 0.04 |
| 10 | 0.35 | 0.34 | 0.18 |
| 50 | 0.26 | 0.22 | 0.25 |
| 100 | 0.13 | 0.14 | - |

# APPENDIX D

## D. SUPPORTING INFORMATION FOR CHAPTER 5

**Analytical Methods**

Private well samples were analyzed by the U.S. Geological Survey National Water Quality Laboratory using two different methods. Method 2 included a preconcentration step and a slightly modified mobile phase compared to method 1 resulting in lower detection limits.

**Method 1: USGS 9660**

Concentrations of 34 PFAS analytes (Table S1) were determined in matrix-modified tap water samples by direct aqueous injection-liquid chromatography/tandem mass spectrometry (DAI-LC/MS/MS) with isotope-dilution quantification described previously Kolpin et al., 2021. Detection limits ranged from 2.0-162 ng/L for all analytes.

**Method 2: USGS 9662**

Concentrations of 56 individual PFAS analytes (Table S1) were determined in matrix-modified tap water samples with an initial preconcentration using online solid phase extraction followed by DAI-LC/MS/MS with quantification by isotope-dilution. Prior to analysis, 500 µL of the sample was loaded directly onto a Waters OASIS WAX SPE cartridge (3.9x20 mm column, 3.9µm particle diameter) with organic free water (Fisher Optima HPLC grade) at 0.5 mL/min for six minutes. Following the preconcentration step, the sample was eluted onto a reversed-phase, porous shell LC column with a water/1 % ammonium hydroxide and methanol/0.4% ammonium hydroxide gradient. Data were acquired in dynamic multiple reaction monitoring (dMRM) mode with two transitions per analyte for confirmation (except for PFBA and PFPeA that only had one confirming ion). Detection limits ranged from 0.1-22.3 ng/L for all analytes.

Table D-1. Method detection limits for individual PFAS measured by two different USGS methods. Method one is USGS 9660 (see Kolpin et al., 2021) for details and method two is USGS 9662. Detection limits are reported as ng/L for both methods. NA means the compound was not analyzed as part of the original method (9660). Six PFAS in red italic font are regulated under the Safe Drinking Water Act (SDWA) National Primary Drinking Water Regulations.

| Compound | Abbreviation | Method detection limit (ng/L) | |
|---|---|---|---|
| | | Method one (9660) | Method two (9662) |
| **Perfluoroalkyl carboxylic acids** | | | |
| Perfluorobutanoic acid | PFBA | NA | 5.0 |
| Perfluoropentanoic acid | PFPeA | 12.8 | 5.0 |
| Perfluorohexanoic acid | PFHxA | 39.8 | 1.0 |
| Perfluoroheptanoic acid | PFHpA | 43.1 | 0.2 |
| *Perfluorooctanoic acid* | *PFOA* | *5.2* | *0.2* |
| *Perfluorononanoic acid* | *PFNA* | *7.8* | *1.0* |
| Perfluorodecanoic acid | PFDA | 20.6 | 0.5 |
| Perfluorododecanoic acid | PFDoA | 51.5 | 1.0 |
| Perfluoroundecanoic acid, | PFUnDA | 16.2 | 0.2 |
| Perfluorotridecanoic acid | PFTrDA | 15.6 | 2.5 |
| Perfluorotetradecanoic acid | PFTeDA | 51.5 | 2.5 |
| **Perfluoroalkyl sulfonic acids (acid form)** | | | |
| Perfluoropropanesulfonic acid | PFPrS | NA | |
| *Perfluorobutanesulfonic acid* | *PFBS* | *12.5* | *0.5* |
| Perfluoropentansulfonic acid | PFPeS | 18.5 | 0.94 |
| *Perfluorohexanesulfonic acid* | *PFHxS* | *11.4 (linear) 22.8 (branched)* | *0.37 (linear), 0.34 (branched)* |
| Perfluoroheptanesulfonic acid | PFHpS | NA | 0.47 |
| *Perfluorooctanesulfonic acid* | *PFOS* | *14.3 (linear) 22.8 (branched)* | *0.36 (linear), 0.4 (branched)* |
| Perfluorononanesulfonic acid | PFNS | 49.5 | 0.48 |
| Perfluorodecanesulfonic acid | PFDS | 49.7 | 0.48 |
| Perfluoroundecanesulfonic acid | PFUnDS | NA | 0.48 |
| Perfluorododecanesulfonic acid | PFDoS | NA | |
| Perfluorotridecanesulfonic acid | PFTrDS | NA | 0.97 |
| **Fluorotelomer sulfonic acids** | | | |
| 1H,1H, 2H, 2H-Perfluorohexane sulfonic acid | 4:2FTS | 17.5 | 0.45 |
| 1H,1H, 2H, 2H-Perfluorooctane sulfonic acid | 6:2FTS | 52.4 | 0.5 |
| 1H,1H, 2H, 2H-Perfluorodecane sulfonic acid | 8:2FTS | 19.1 | 0.48 |
| 1H,1H,2H,2H-Perfluorododecanesulfonic acid | 10:2FTS | NA | 0.96 |
| **Perfluoroalkanesulfonamides** | | | |
| Perfluorobutanesulfonamide | FBSA | NA | 5.0 |
| Perfluorodecanesulfonamide | FDSA | NA | 0.5 |

| | | | |
|---|---|---|---|
| Perfluorohexanesulfonamide | FHxSA | 38.9 | 1.0 |
| Perfluoroheptanesulfonamide | FHpSA | NA | 0.5 |
| Perfluorooctanesulfonamide | FOSA | 101 | 1.0 |
| N-methyl perfluorooctanesulfonamide | NMeFOSA | 123 | 1.0 |
| N-ethyl perfluorooctanesulfonamide | NEtFOSA | 162 | 1.0 |
| N-methylperfluorobutanesulfonamide | NMeFBSA | NA | 5.0 |
| **Perfluorooctane sulfonamideoacetic acids** | | | |
| N-methyl perfluorooctanesulfonamidoacetic acid | NMeFOSAA | 15.4 | 0.38 |
| N-ethyl perfluorooctanesulfonamidoacetic acid | NEtFOSAA | 12.2 | 0.38 |
| **Per- and Polyfluoroether carboxylic acids** | | | |
| *Hexafluoropropylene oxide dimer acid* | *HFPO-DA* | *17.7* | *1.0* |
| 4,8-Dioxa-3H-perfluorononanoic acid | ADONA | 2.0 | 0.09 |
| **Ether sulfonic acids** | | | |
| 9-Chlorohexadecafluoro-3-oxanonane-1-sulfonic acid | 9Cl-PF3ONS | 48.1 | 0.93 |
| 11-Chloroeicosafluoro-3-oxaundecane-1-sulfonic acid | 11Cl-PF3OUdS | NA | 0.47 |
| Perfluoro(2-ethoxyethane) sulfonic acid | PFEESA | NA | 0.9 |
| **Polyfluoroalkyl Phosphate Di-esters** | | | |
| 6:2 Fluorotelomer phosphate diester | 6:2diPAP | NA | 0.97 |
| 8:2 Fluorotelomer phosphate diester | 8:2diPAP | NA | 0.98 |
| | | | |
| **Miscellaneous Compounds** | | | |
| Perfluoro-3,6-dioxaheptanoate | 3,6 OPFHpA | NA | 0.48 |
| Bis(perfluorohexyl)phosphinate | 6:6 PFPi | NA | 0.48 |
| 2H-Perfluoro-2-dodecenoate | FDUEA | NA | 2.0 |
| 3-Perfluoroheptyl propanoate | FHpPA | NA | 0.5 |
| 2H-perfluoro-2-octenoate | FHUEA | NA | 0.5 |
| 2H-Perfluoro-2-decenoate | FOUEA | NA | 0.5 |
| Perfluoro-4-oxapentanoate | PF40PeA | NA | 0.1 |
| Perfluoro-5-oxahexanoate | PF5OHxA | NA | 5.0 |
| Perfluoro(2-ethoxyethane) sulfonate | PFECHS | NA | 0.18 |
| Perfluoro(2-ethoxyethane) sulfonate | PFEESA | NA | 0.9 |
| 3-Perfluoropentyl propanoate | FPePA | NA | 10 |
| 3-Perfluoropropyl propanoate | FPrPA | NA | 20 |
| Perfluorobutane sulfonamido amin | PBSA | NA | 22.3 |

**Data Analysis:**

Table D-2. Summary of PFAS detected and the range of concentrations found in the 59 samples across the three counties. Data was obtained from Method-2.

| PFAS Compounds | Total Number of Detections | Concentration Range (ng/L) | Median Concentration Detected (ng/L) |
|---|---|---|---|
| 6:2FTS | 3 | 0.50 - 2.20 | 0.50 |
| 8:2FTS | 1 | 0.22 | 0.22 |
| FOSA | 9 | 0.21 - 5.83 | 1.03 |
| N-MeFOSAA linear | 2 | 0.25 - 0.40 | 0.32 |
| PFBA | 3 | 2.30 - 15.4 | 2.70 |
| PFBS | 13 | 0.46 - 3.36 | 1.07 |
| PFDS | 3 | 0.09 - 0.87 | 0.43 |
| PFHpA | 10 | 0.30 - 2.30 | 0.60 |
| PFHxA | 7 | 0.30 - 6.70 | 1.00 |
| PFHxS | 11 | 0.28 - 2.79 | 0.61 |
| PFOA | 7 | 1.30 - 4.40 | 2.00 |
| PFOS | 15 | 0.18 - 4.20 | 1.02 |

Table D-3. Individual Toxicity Quotients (TQs) and the ΣTQ for each site, based on six of the PFAS detected using the human-health based benchmarks in Table 2. * indicates exceedance of benchmark level (1.0) and ** indicates the exceedance of precautionary screening level of concern (0.1), respectively.

| Site ID | PFOA | PFOS | PFHxS | PFBS | PFHxA | PFBA | ΣTΘ |
|---|---|---|---|---|---|---|---|
| MJ-P30 | - | 6.0* | 0.029 | - | - | - | 6.029* |
| MJ-P49 | 35.0* | 1.8* | 0.061 | 0.0163 | 0.0335 | 0.00039 | 36.911* |
| MJ-P04 | - | 2.5* | - | - | - | 0.0022 | 2.502* |
| MJ-P13 | - | 5.4* | - | - | - | - | 5.400* |
| MJ-P48 | 19.0* | 27.4* | 0.056 | 0.0107 | 0.0045 | - | 46.471* |
| MJ-P29 | - | - | - | 0.0082 | - | - | 0.0082 |
| MJ-P37 | - | - | 0.066 | 0.0046 | - | - | 0.0706 |
| MJ-P53 | 20.0* | 42.0* | - | 0.0261 | 0.0215 | - | 62.048* |
| MJ-P52 | - | - | - | - | 0.0015 | - | 0.0015 |
| MJ-P39 | 44.0* | 40.5* | 0.095 | 0.0199 | 0.025 | - | 84.640* |
| MJ-P28 | - | 2.3* | - | - | - | - | 2.300* |
| MJ-P44 | 14.0* | 22.5* | 0.038 | 0.0336 | - | - | 36.572* |
| MJ-P41 | - | 5.8* | - | 0.0097 | 0.004 | - | 5.814* |
| MJ-P34 | 20.0* | 18.3* | - | - | - | - | 38.300* |
| MJ-P55 | - | - | - | 0.0056 | - | - | 0.0056 |
| MJ-P22 | - | - | 0.028 | - | - | - | 0.028 |
| MJ-P20 | - | - | - | - | - | 0.00033 | 0.00033 |
| MJ-P17 | - | 2.2* | - | - | - | - | 2.200* |
| MJ-P51 | - | 33.3* | 0.105 | 0.016 | - | - | 33.421 |
| MJ-P59 | - | - | 0.075 | 0.0086 | - | - | 0.0836 |
| MJ-P56 | - | 10.2* | 0.06 | 0.0301 | - | - | 10.290* |
| MJ-P45 | 13.0* | 37.7* | 0.2790** | 0.0042 | 0.005 | - | 50.988* |